

THE 8TH INTERNATIONAL CONFERENCE ON INTEGRATED MODELING AND ANALYSIS IN APPLIED CONTROL AND AUTOMATION

SEPTEMBER, 21-23 2015
BERGEGGI, ITALY

IMAACA

EDITED BY
AGOSTINO BRUZZONE
GENEVIÈVE DAUPHIN-TANGUY
SERGIO JUNCO
FRANCESCO LONGO

PRINTED IN RENDE (CS), ITALY, SEPTEMBER 2015

ISBN 978-88-97999-54-6 (Paperback)
ISBN 978-88-97999-63-8 (PDF)

© 2015 DIME UNIVERSITÀ DI GENOVA

RESPONSIBILITY FOR THE ACCURACY OF ALL STATEMENTS IN EACH PAPER RESTS SOLELY WITH THE AUTHOR(S). STATEMENTS ARE NOT NECESSARILY REPRESENTATIVE OF NOR ENDORSED BY THE DIME, UNIVERSITY OF GENOVA. PERMISSION IS GRANTED TO PHOTOCOPY PORTIONS OF THE PUBLICATION FOR PERSONAL USE AND FOR THE USE OF STUDENTS PROVIDING CREDIT IS GIVEN TO THE CONFERENCES AND PUBLICATION. PERMISSION DOES NOT EXTEND TO OTHER TYPES OF REPRODUCTION NOR TO COPYING FOR INCORPORATION INTO COMMERCIAL ADVERTISING NOR FOR ANY OTHER PROFIT - MAKING PURPOSE. OTHER PUBLICATIONS ARE ENCOURAGED TO INCLUDE 300 TO 500 WORD ABSTRACTS OR EXCERPTS FROM ANY PAPER CONTAINED IN THIS BOOK, PROVIDED CREDITS ARE GIVEN TO THE AUTHOR(S) AND THE CONFERENCE.

FOR PERMISSION TO PUBLISH A COMPLETE PAPER WRITE TO: DIME UNIVERSITY OF GENOVA, PROF. AGOSTINO BRUZZONE, VIA OPERA PIA 15, 16145 GENOVA, ITALY. ADDITIONAL COPIES OF THE PROCEEDINGS OF THE *IMAACA* ARE AVAILABLE FROM DIME UNIVERSITY OF GENOVA, PROF. AGOSTINO BRUZZONE, VIA OPERA PIA 15, 16145 GENOVA, ITALY.

ISBN 978-88-97999-54-6 (Paperback)

ISBN 978-88-97999-63-8 (PDF)

THE 8TH INTERNATIONAL CONFERENCE ON INTEGRATED MODELING AND ANALYSIS IN APPLIED CONTROL AND AUTOMATION, IMAACA 2015

SEPTEMBER 21-23 2015, BERGEGGI, ITALY

ORGANIZED BY



DIME - UNIVERSITY OF GENOA



LIOPHANT SIMULATION



SIMULATION TEAM



IMCS - INTERNATIONAL MEDITERRANEAN & LATIN AMERICAN COUNCIL OF
SIMULATION



DIMEG, UNIVERSITY OF CALABRIA



MSC-LES, MODELING & SIMULATION CENTER, LABORATORY OF ENTERPRISE
SOLUTIONS



MODELING AND SIMULATION CENTER OF EXCELLENCE (MSCOE)



LATVIAN SIMULATION CENTER - RIGA TECHNICAL UNIVERSITY



LOGISIM



LSIS - LABORATOIRE DES SCIENCES DE L'INFORMATION ET DES SYSTEMES



MIMOS - MOVIMENTO ITALIANO MODELLAZIONE E SIMULAZIONE



MITIM PERUGIA CENTER - UNIVERSITY OF PERUGIA



BRASILIAN SIMULATION CENTER, LAMCE-COPPE-UFRJ



MITIM - McLEOD INSTITUTE OF TECHNOLOGY AND INTEROPERABLE MODELING AND
SIMULATION - GENOA CENTER



M&SNET - MCLEOD MODELING AND SIMULATION NETWORK



LATVIAN SIMULATION SOCIETY



ECOLE SUPERIEURE D'INGENIERIE EN SCIENCES APPLIQUEES



FACULTAD DE CIENCIAS EXACTAS. INEGNERIA Y AGRIMENSURA



UNIVERSITY OF LA LAGUNA



CIFASIS: CONICET-UNR-UPCAM



INSTICC - INSTITUTE FOR SYSTEMS AND TECHNOLOGIES OF INFORMATION, CONTROL AND COMMUNICATION



NATIONAL RUSSIAN SIMULATION SOCIETY



CEA - IFAC



UNIVERSITY OF BORDEAUX



UNIVERSITY OF CYPRUS

I3M 2015 INDUSTRIAL SPONSORS



CAL-TEK SRL



LIOTECH LTD



MAST SRL



SIM-4-FUTURE

I3M 2015 MEDIA PARTNERS



INDERSCIENCE PUBLISHERS - INTERNATIONAL JOURNAL OF SIMULATION AND PROCESS MODELING



INDERSCIENCE PUBLISHERS - INTERNATIONAL JOURNAL OF CRITICAL INFRASTRUCTURES

INDERSCIENCE PUBLISHERS - INTERNATIONAL JOURNAL OF ENGINEERING SYSTEMS MODELLING AND SIMULATION

INDERSCIENCE PUBLISHERS - INTERNATIONAL JOURNAL OF SERVICE AND COMPUTING ORIENTED MANUFACTURING



IGI GLOBAL - INTERNATIONAL JOURNAL OF PRIVACY AND HEALTH INFORMATION MANAGEMENT



Halldale Group



HALLDALE MEDIA GROUP: MILITARY SIMULATION AND TRAINING MAGAZINE

HALLDALE MEDIA GROUP: THE JOURNAL FOR HEALTHCARE EDUCATION, SIMULATION AND TRAINING



SAGE
SIMULATION TRANSACTION OF SCS



EUROMERCI



DE GRUYTER
INTERNATIONAL JOURNAL OF FOOD ENGINEERING

EDITORS

AGOSTINO BRUZZONE

MITIM-DIME, UNIVERSITY OF GENOA, ITALY

agostino@itim.unige.it

GENEVIÈVE DAUPHIN-TANGUY

ECOLE CENTRALE DE LILLE, FRANCE

genevieve.dauphin-tanguy@ec-lille.fr

SERGIO JUNCO

UNIVERSIDAD NACIONAL DE ROSARIO, ARGENTINA

sjunco@fceia.unr.edu.ar

FRANCESCO LONGO

DIMEG, UNIVERSITY OF CALABRIA, ITALY

f.longo@unical.it

THE INTERNATIONAL MULTIDISCIPLINARY MODELING AND SIMULATION MULTICONFERENCE, I3M 2015

GENERAL CO-CHAIRS

AGOSTINO BRUZZONE, *MITIM DIME, UNIVERSITY OF GENOA, ITALY*
YURI MERKURYEV, *RIGA TECHNICAL UNIVERSITY, LATVIA*

PROGRAM CO-CHAIRS

FRANCESCO LONGO, *DIMEG, UNIVERSITY OF CALABRIA, ITALY*
EMILIO JIMÉNEZ, *UNIVERSITY OF LA RIOJA, SPAIN*

THE 8TH INTERNATIONAL CONFERENCE ON INTEGRATED MODELING AND ANALYSIS IN APPLIED CONTROL AND AUTOMATION, IMAACA 2015

CONFERENCE CHAIRS

SERGIO JUNCO, *UNIVERSIDAD NACIONAL DE ROSARIO, ARGENTINA*
GENEVIÈVE DAUPHIN-TANGUY, *ECOLE CENTRALE DE LILLE, FRANCE*

IMAACA 2015 INTERNATIONAL PROGRAM COMMITTEE

AGOSTINO BRUZZONE, *UNIVERSITY OF GENOA, ITALY*
JORGE BALIÑO, *UNIV. OF SÃO PAULO, BRAZIL*
WOLFGANG BORUTZKY, *BRS-UNIV. APPLIED SCIENCES, SANKT AUGUSTIN, GERMANY*
BELKACEM OULD BOUAMAMA, *USTL, FRANCE*
MAURO CARIGNANO, *UNR, NATIONAL UNIVERSITY OF ROSARIO, SANTA FE, ARGENTINA*
BRUNO CARMO, *DEP. ENG. MEC., UNIV. SÃO PAULO, BRAZIL*
GENEVIÈVE DAUPHIN-TANGUY, *ÉCOLE CENTRALE DE LILLE, FRANCE*
JEAN-YVES DIEULOT, *POLYTECH'LILLE, FRANCE*
ALEJANDRO DONAIRE, *THE UNIVERSITY OF NEWCASTLE, AUSTRALIA*
TULGA ERSAL, *UNIVERSITY OF MICHIGAN, USA*
A. FERRAMOSCA, *INTEC, CONICET-UNL, SANTA FE, ARGENTINA*
J.L. GODOY, *INTEC, CONICET-UNL, ARGENTINA*
A.H. GONZALEZ, *INTEC, CONICET-UNL, ARGENTINA*
JULIEN GOMAND, *ENSAM, AIX-EN-PROVENCE, FRANCE*
ADRIAN ILINCA, *UNIVERSITÉ DU QUÉBEC À RIMOUSKI, CANADA*
SERGIO JUNCO, *UNIVERSITY OF ROSARIO, SANTA FE, ARGENTINA*
FABRIZIO LEONARDI, *FEI, SÃO BERNARDO DO CAMPO, BRAZIL*
FRANCESCO LONGO, *UNIVERSITY OF CALABRIA, ITALY*
LOUCAS S. LOUCA, *UNIVERSITY OF CYPRUS, SCHOOL OF ENGINEERING, CYPRUS*
MATÍAS NACUSSE, *UNIVERSIDAD NACIONAL DE ROSARIO, ARGENTINA*
LETIZIA NICOLETTI, *CAL-TEK SRL, ITALY*
NORBERTO NIGRO, *CIMEC, SANTA FE, ARGENTINA*
RACHID OUTBIB, *LSIS, MARSEILLE, FRANCE*
P. M. PATHAK, *IIT, ROORKEE, INDIA*
RICARDO PÉREZ, *PUC, CHILE*
DRISHTYSINGH RAMDENEY, *ITMI, QUÉBEC, CANADA*
XAVIER ROBOAM, *INPT-LAPLACE, FRANCE*
CHRISTOPHE SUEUR, *ÉCOLE CENTRALE LILLE, FRANCE*
VLADIMIR TURETSKY, *ORT BRAUDE ACADEMIC COLLEGE OF ENG, ISRAEL*
DANIEL VIASSOLO, *HALLIBURTON, HOUSTON, TX, USA*
COSTAS TZAFESTAS, *NTUA, GREECE*
JUNG-MIN YANG, *KYUNGPOOK NATIONAL UNIVERSITY, REPUBLIC OF KOREA*
RAFIC YOUNES, *LEBANESE UNIVERSITY, BEIRUT, LEBANON*
ANIBAL ZANINI, *UNIV. DE BUENOS AIRES, ARGENTINA*

CONFERENCE CHAIRS' MESSAGE

IMAACA comes back after two years and moves to Bergeggi on the Italian Riviera. As in the previous years, the IMAACA conference is a unique opportunity that brings experts together for the purpose of presenting and discussing any type of application relevant control and automation problems emphasizing the role of model analysis as integral part of the complete design of the automated system. Particularly, the IMAACA conference focuses on new concepts, methods, techniques, and tools conceived in order to support an integrative interplay of modeling, identification, simulation, system analysis and control theory in all the stages of system design.

IMAACA 2015 offers a blend of interesting topics and this year includes three regular sessions and 2 joint sessions:

- Bond Graph Modeling and Analysis (regular session);
- Robot Modeling & Control (regular session);
- Modeling, Analysis and Control (regular session);
- Industrial Processes and Engineering Modeling & Simulation (joint EMSS-IMAACA-MAS session);
- Green Vehicles and Green Solutions (joint SESDE-MAS-IMAACA session).

While regular sessions focus on topics that are traditionally part of the IMAACA program (e.g. Bond Graph Modeling, Automation and Control, etc.), the joint sessions with the other I3M conferences clearly show the multi-disciplinary aim of the IMAACA conference with specific applications in the Industrial Engineering and Environmental Sustainability areas. Therefore, also this year IMACCA is co-located with the I3M multi-conference that includes 8 additional International Conferences (EMSS, HMS, MAS, DHSS, IWISH, SESDE, FOODOPS and WAMS) providing researchers, scientists, simulationists and practitioners with an ideal framework for sharing knowledge about innovative concepts and establishing new collaborations and ideas for research projects.

Finally we take this opportunity to thank all the authors as well as members of the International Program Committee and Track Chairs and we wish to all the attendees a fruitful and enjoyable IMAACA 2015 in Bergeggi.



Sergio Junco,
Universidad Nacional
de Rosario, Argentina



Geneviève Dauphin-Tanguy,
Ecole Centrale de Lille, France

ACKNOWLEDGEMENTS

The IMAACA 2015 International Program Committee (IPC) has selected the papers for the Conference among many submissions; therefore, based on this effort, a very successful event is expected. The IMAACA 2015 IPC would like to thank all the authors as well as the reviewers for their invaluable work.

A special thank goes to all the organizations, institutions and societies that have supported and technically sponsored the event.

I3M 2015 INTERNAL STAFF

AGOSTINO G. BRUZZONE, *DIME, UNIVERSITY OF GENOA, ITALY*
MATTEO AGRESTA, *SIMULATION TEAM, ITALY*
TERESA BARBIERI, *CAL-TEK SRL, ITALY*
CHRISTIAN BARTOLUCCI, *SIMULATION TEAM, ITALY*
LUIGI BRUNO, *DIMEG, UNIVERSITY OF CALABRIA*
ALESSANDRO CHIURCO, *DIMEG, UNIVERSITY OF CALABRIA, ITALY*
MARIO COSENTINI, *CAL-TEK SRL, ITALY*
RICCARDO DI MATTEO, *SIMULATION TEAM, ITALY*
CATERINA FUSTO, *DIMEG, UNIVERSITY OF CALABRIA, ITALY*
FRANCESCO LONGO, *DIMEG, UNIVERSITY OF CALABRIA, ITALY*
GIANLUCA MAGLIONE, *CAL-TEK SRL, ITALY*
MARINA MASSEI, *LIOPHANT SIMULATION, ITALY*
LETIZIA NICOLETTI, *CAL-TEK SRL*
ANTONIO PADOVANO, *DIMEG, UNIVERSITY OF CALABRIA, ITALY*
ALBERTO TREMORI, *SIMULATION TEAM, ITALY*
MARCO VETRANO, *CAL-TEK SRL, ITALY*



This International Workshop is part of the I3M Multiconference: the Congress leading **Simulation around the World and Along the Years**



Index

Predictive maintenance based on four parameters on an industrial test bench	1
Drishtysingh Ramdenee, Samuel Austin, Michel Guimond, Adrian Ilinca	
Model complexity of a cantilever beam: an energy-based approach	12
Loucas Louca	
Application of an infinite horizon MPC to a nonlinear open-loop unstable reactor system	22
André Shiguelo Yamashita, Bruno Faccini Santoro, Márcio André Fernandes Martins, Darci Odloak	
Fault accommodation by inverse simulation through solving a differential algebraic system obtained from a bond graph	29
Wolfgang Borutzky	
Steady-state power flow analysis of electrical power systems modelled by 2-dimensional multibond graphs	39
Israel Núñez-Hernández, Peter C. Breedveld, Paul B. T. Weustink, Gilberto Gonzalez-A	
Hybridization effect on fuel consumption and optimal sizing of components for HEV	48
Mauro G. Carignano, Norberto M. Nigro, Sergio Junco	
Design of a hydraulic turbine control system by numerical optimization	55
Roberto Canonico, Renato A. Aguiar, Fabrizio Leonardi	
Battery dynamic model improvement with parameters estimation and experimental validation	63
Javier M. Cabello, Eric Bru, Xavier Roboam, Fabien Lacressonniere, Sergio Junco	
Modelling, control and application of dynamic programming to a series-parallel hybrid electric vehicle	71
Ivan Miguel Trindade, Agenor de Toledo Fleury	
Modeling, identification and a first control approach on the quality of flames in oil furnaces	79
Agenor T. Fleury, Danilo S. Chui, Flavio C. Trigo, Flavius P. R. Martins	
Dynamic analysis and 3D visualization of multibody systems	89
Vjekoslav Damic, Maida Cohodar	
Fractional order $PI^{\lambda}D^{\mu}$ controller: applied to control a manipulator robot wrist	97
Youcef Zennir, Adel Makhbouche	
Obstacle avoiding strategy of a reconfigurable redundant space robot	105
Vijay Kumar Dalla, Pushparaj Mani Pathak	
Linear stability analysis for severe slugging: sensitivity to void fraction correlations	115
Gabriel Romualdo Azevedo, Jorge Luis Baliño, Karl Peter Burr	

Experimentally validated bond graph model of a brazed-plate heat exchanger (BPHE)	125
Marwa Turki, Mohamed Kebdani, Geneviève Dauphin Tanguy, Antoine Dazin, Patrick Dupont	
Gait modelling for a context-aware user-adaptive robotic assistant platform	132
Georgia G. Chalvatzaki, Xanthi S. Papageorgiou, Costas S. Tzafestas	
User front-following behaviour for a mobility assistance robot: a kinematic control approach	142
George P. Moustris, Athanasios Dometios, Costas S. Tzafestas	
Author's Index	151

PREDICTIVE MAINTENANCE BASED ON FOUR PARAMETERS ON AN INDUSTRIAL TEST BENCH

Drishtysingh Ramdennee^a, Samuel Austin^a, Michel Guimond^a, Adrian Ilinca^b

^aInstitut technologique de maintenance industrielle

^bWind Energy Research Laboratory, l'Université du Québec à Rimouski

[§]drishtysingh.ramdennee@itmi.ca

ABSTRACT

This project aims at validating the assumption of predictive maintenance based on four parameters. The economy of Northern Quebec region is highly dependent on iron and aluminium production and transformation. Related industrial activities ensure employment for a large proportion of the population. Traditional maintenance is no longer enough to ensure competitiveness of these companies. Optimised asset management and maintenance is essential to reduce production cost and machine downtime. This project has as objective the development of a high precision maintenance method embodying instrumentation, statistical and numerical modeling techniques.

The targeted technology will have as objectives to increase condition monitoring precision, reduce required maintenance interventions, improve reliability, reduce maintenance cost and allow better recognition of factors (internal and external) influencing machine element deterioration. The developed model is tested and refined on an industrially inspired test bench at Cégep de Sept-Îles. The final aim is to compare the different trends (statistical, specifications and numerical simulation) to establish a mean algorithm that will encourage the achievement of the enumerated objectives. In this paper, we establish the motivation of the work, definition of the test bench, experimental model, simulation model and manufacturer's specification model. Preliminary results are also presented as well as future work required for the final definition of this technique. Final results and technique efficiency validation will be obtained and performed once all experimental results on "in operation" test bench are obtained.

Keywords: *predictive maintenance, instrumentation, test bench, numerical simulation, wear, degradation, multiphysics.*

Abbreviations:

PM Preventive maintenance

i ordinal load cycles

$h_i(t)$ system hazard rate function prior to the i th preventive maintenance, PM, activity

T_i time interval for PM prior to the i th PM

r radius

R system reliability threshold for scheduled PM

C_{up} expected cost rate for unscheduled PM

C_{sp} expected cost rate for scheduled PM

τ_p duration of PM, same for scheduled PM and unscheduled PM

$Cost_r$ additional replacement cost

CE_r expected cost per unit time for the system in the residual life

INTRODUCTION

For most systems, failure is a dangerous or costly event. In a region like Sept-Îles, on the North Shore of Québec province, production needs to be continuous in order to ensure availability of spare parts for major mining companies of the region which operating on an incessant basis. The available information on the failure time is often not very accurate because of the great variability of elements belonging to the same population. Classical preventive maintenance policy leads to elements being replaced before complete exploitation of the useful life. Hence, failure risk is reduced but maintenance costs and maintenance frequency is increased. The need for accurate condition based maintenance, that is, predictive maintenance based on precise recognition of element health in real time is important for risk free and low cost maintenance policy application. This paper focuses on the preliminary work and results obtained within a project at developing a new predictive maintenance technique. The project aims at the validation of the assumption of predictive maintenance based on four parameters: manufacturer's specifications, statistical data, instrumentation and numerical simulation. The "Institut Technologique de Maintenance Industrielle (ITMI)" has as mission to accompany companies in achieving maximum efficiency and optimized asset management. Based in the region of Northern Quebec (Sept-Îles) and part of the Cégep de Sept-Îles (CSI), the Institute is in the heart of Northern Quebec mining industry development. Optimised asset management and maintenance is essential as it highly reduces production cost and avoids machine downtime - essential in the present economic situation. Worldwide competition is fierce and the price of iron and aluminium low. Numerous small and medium enterprises (SME) are subcontractors of the major mining and metal transformation companies and ensure employment for a large proportion of the population as well as the development of communities where they are located. Traditional maintenance is no

long enough to ensure competitiveness of these companies. This paper illustrates a project aiming the development of a high precision maintenance method that will significantly reduce cost and frequency of checks as well as better asset management.

In this paper, we establish the motivation of the work, definition of the test bench, experimental model, simulation model and manufacturer's specification model. Preliminary results are also presented as well as future work required for the final definition of this technique. Final results and technique efficiency validation will be obtained and performed once all experimental results on "in operation" test bench are obtained.

BACKGROUND

CSI has ensured training and technical help regarding traditional maintenance of the numerous industries harboured in Northern Quebec region for more than 20 years. The need for more cut edge maintenance has encouraged the college to set up ITMI which sets the path for more sophisticated and result oriented maintenance that blends itself in the present economic condition. Predictive maintenance allows scheduling maintenance with the least effect on activities and unexpected equipment breakdowns and scheduled maintenance downtime is virtually eliminated. Literature undoubtedly encourages predictive maintenance over traditional routine maintenance. Our on field evaluation supports this need. [1-5] all justify the advantages of using predictive maintenance to even quantify the relative per horsepower cost of maintenance. However, as [6] puts it – preventive or predictive maintenance is rarely performed in industries due to time pressure. Therefore, there is need to develop a tailor made approach that perfectly inscribes the maintenance measures in the activities of the industry. Furthermore,

literature shows that predictive maintenance is most of the time based on the follow up of one parameter as in [7]. The need to be more precise in predicting failure in machines and in an attempt to encourage training allowing optimised and diligent implementation of predictive maintenance routines in companies has been the motivation to the project illustrated in this paper. The methodology was developed and tested with Métal 7 Company. Located in the main industrial region for iron ore in Canada, Metal 7 has a very firm grasp of the needs of major mining companies and SME for whom, through its R&D department, manufactures durable, high-performance equipment. Metal7 dynamism and involvement in the community as well as worldwide business will propose a number of advantages on training, the local community and for knowledge improvement in the field.

PROJECT DESCRIPTION

Industrial activities rely on the proper functioning of mechanical equipment. It is necessary to control the reliability of the equipment to optimize maintenance planning and minimize costs. Various methods can be used to assess the remaining lifespan of a machine element prior to next failure. Condition based maintenance information can be inferred from:

- 1.the manufacturer's specifications, duration of operation and operating conditions;
- 2.instrumentation data from installed sensors;
- 3.statistical data on failure ;
- 4.numerical simulation results.

When maintenance is planned according to manufacturer's specifications, duration of operation and operating conditions, the equipment is replaced in accordance with manufacturer's specifications regardless of the actual wear. Manufacturer's specifications are usually built according to machine element degradation trend in

controlled environment which may differ from actual situation. When maintenance plan is based on instrumentation and statistical data, the machine element is replaced according to measured values from sensors or when the probability of failure is greater than or equal to a selected threshold. Systematic and random errors from sensors as well as installation limitations can limit sensors' accuracy. During operation, conditions vary, the probability of failure is calculated with conservative parameters and calculated life is less than the actual life. When maintenance is scheduled based on the results of numerical simulation, it is possible to take into account the variation of the operating conditions in the calculation of the probability of failure. This allows for a more precise calculation of remaining lifespan and machine element is kept in operation longer. Furthermore, simulation allows us to study the effect of modifying the design of a product over its useful life. It also allows infer the effect of chosen operating parameters on the lifespan of a product. The simulation is useful to optimize the design and operation of industrial equipment. However, numerical simulations have numerous limitations including: model precision, mesh precision, resolution scheme precision... The idea behind this project is to evaluate the correlation between degradation trends monitoring according to the four different techniques and compare the techniques within a mathematical model for error cancellation between the trends.

COST MOTIVATION

In this section, we wish to demonstrate the cost effectiveness of this four parameter damage accumulation monitoring policy versus a traditional preventive maintenance policy. Using 4 different parameters of wear and degradation monitoring, the aim is to increase the number of cycles by a more precise wear and degradation monitoring scheme – the aim is to increase the number of cycles of a given machine element whilst ensuring reliability of system.

According to [8-11], reliability can be expressed as follows:

$$\begin{aligned}
 e^{-\int_0^{T_1} h_1(t)dt} &= e^{-\int_0^{T_2} h_2(t)dt} \\
 &= \dots e^{-\int_0^{T_N} h_N(t)dt} \\
 &= R \dots \dots \dots (1)
 \end{aligned}$$

From figure 1, excerpt from [12], showing hazard rate evolution against hybrid evolution model for system hazard, we note that the relationship between hazard rate functions before and after i th PM can be expressed as:

$$h_{i+1}(t) = b_i h_i(t + a_i T_i) \quad \text{for } t \in (0, T_{i+1}) \dots \dots \dots (2)$$

$0 < a_i < 1$, $b_i > 1$ are age reduction factors and hazard rate increase factor respectively.

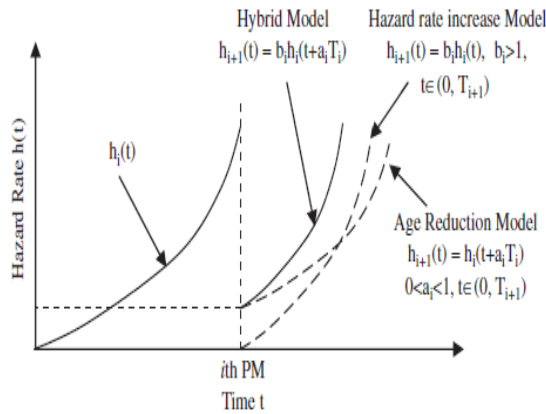


Figure 1: Hybrid evolution model for system hazard rate

Replacing equation (2) in (1), we have:

$$\begin{aligned}
 \int_0^{T_1} h_1(t)dt &= \int_0^{T_2} h_2(t)dt = \dots \dots \\
 &= \int_0^{T_N} h_{(N)}(t)dt \\
 &= -Ln R \dots \dots \dots (3)
 \end{aligned}$$

$\int_0^{T_1} h_1(t)$ represents the cumulative failure risk in maintenance cycle i . This implies that cumulative cycle is equal to $-R$.

We will now compare maintenance cost efficiency for our aimed model versus traditional preventive maintenance models.

For preventive models:

$$R = e^{-\int_0^{T_N} h_N(t)dt}$$

In our case:

$$\begin{aligned}
 R^1 &= \frac{e^{-\int_0^{T_N} h_{N'}(t)dt} + e^{-\int_0^{T_N} h_{N''}(t)dt} + e^{-\int_0^{T_N} h_{N'''(t)dt} + e^{-\int_0^{T_N} h_{N''''(t)dt}}}{4} \\
 &\dots \dots \dots (4)
 \end{aligned}$$

For the same reliability, the number of cycles can be increased and hence relative maintenance cost is reduced for same reliability as expressed by equation (5). As numerators (function of R) are logarithmic functions, and cycles as denominators, for same R, i is increased and maintenance cost is reduced:

$$C_{Eri} = \frac{C_{up} \tau_p (-\ln(R)) + C_{sp} \tau_p (1 + \ln(R))}{T_i + T_p} \dots \dots \dots (5)$$

TEST BENCH

Four parameters based predictive maintenance calibration and study was performed on an industry inspired and supported test bench at “Cegep de Sept-Îles”. The test simulated a braking system on an inertial rotating mass. The inertial start – braking system was automated using an Allen bradley programmable logic controller. Figures 2 and table 1 illustrates the test bench set up and tested for the purpose of this project.

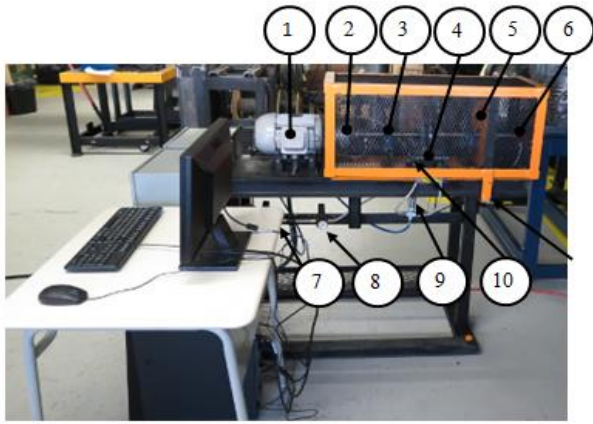


Figure 2: Test bench used for technique validation

Table 1: Test bench description:

#	Description
1	Electrical engine 208V 2hp
2	Pneumatic clutch
3	Bearing
4	Pneumatic brake
5	Inertial disc
6	Pressure power transmitter
7	Pressure regulator #1
8	Pressure regulator #2
9	Pressure sensor
10	Temperature sensor on brakes
11	Security button

A *Horton/ Nexen*[®] brand 835000 model DB caliper less brake disc was used. The brake was pneumatically activated. A Red Lion angular speed sensor was used to measure this quantity on the brake at all times. The idea is to be able to ensure reproducibility of the experiment and availability of enough information for the construction of numerical and manufacturer's specifications correlation. The *Red Lion*[®] IFMA model accepts a frequency input, and outputs an analog voltage or current in proportion to the input frequency, with 0.1% accuracy. The programmable minimum and maximum response times provide optimal response at any input frequency.

The objectives of the project, as mentioned in the abstract are not only to better predict wear level but, also, to understand wear

triggering parameters. A pressure sensor was used to evaluate the pressure applied by the brake pads on the inertial disc. This data was also used to build the numerical model. The *Dwyer*[®] 626 pressure transmitter converts a single positive pressure into a standard 4-20 mA output signal. Accuracy of instrument is specified at 0.25 to 1%.

For similar motivations as the pressure sensor, a *Phoenix*[®] brand, configurable temperature transducer for thermocouple types J and K was used (model: MINI MCR-SL-TC-UI). The sensor accuracy is specified to be 0.2 %.

Finally, in order to measure the wear on the braking pad, a *Hoskin*[®] (KL series) conductive plastic potentiometric position transducer was used. The accuracy of the sensor is specified at 0.1 %.

INSTRUMENTATION ERROR ANALYSIS

The brake pad wear measurement is dependent of 1) the accuracy of the *Hoskin*[®] sensor, 2) the quality and accuracy of the sensor fixture and 3) the alignment accuracy of the inertial disc as can be inferred from figure 3 below, which illustrates the sensor fixture relative to the inertial disc and brake pad.



Figure 3: Hoskin displacement sensor fixture

Such analysis is essential as the wear is very small for 20 000 cycles – around 0.12 mm. Hence, even minor errors in the alignment or fixture can bring large percentage errors in the wear value. This was actually the case for our measurements. Figure 4 shows results we obtained from our bench test when we compared wear (in mm) against energy developed and dissipated by the

inertial-braking system after 150 hours operation. For increasing developed and dissipated energy, simple logic will lead us to anticipate increasing wear on the pad. However, we noticed that, the wear trend is basically unchanged and we can even detect wear reduction at certain intervals of increasing dissipated energy. It is clear that this is impossible. The reason behind such irrational measurement is that alignment error increased at a comparable rate to wear rate with energy application.

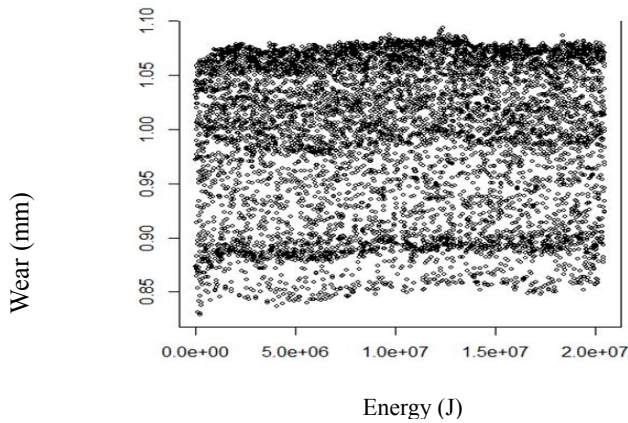


Figure 3: Results obtained after 150 hours operation

In order to cancel the errors, preliminary measurement tests were performed with pre-measured and known wear at the same energy operating regimes to evaluate the errors. The corrections were brought to minimize the errors. The interest here is that our model can, hence, be applied to high precision requirements where minor wear needs to be detected. Furthermore, it is interesting to note that statistical means exist to identify and correct such errors: figure 4 represents the probability density of the residuals of the linear regression model whereas figure 5 represents the probability density of misalignment.

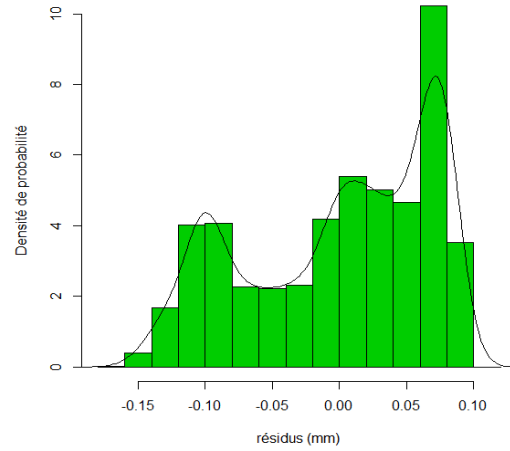


Figure 4 : Probability density of the residuals of the linear regression model

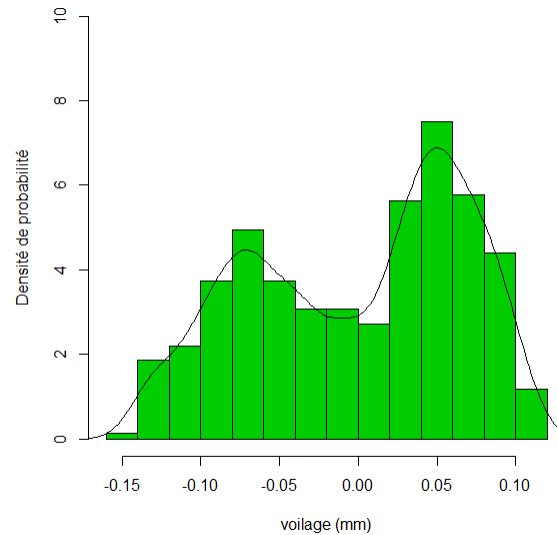


Figure 5: Probability density of misalignment

Figures 4 and 5 show that the shape of the probability density of the residuals of the linear regression model is very similar to the probability density of misalignment of the inertial disc. The difference between the minimum and maximum alignment values as well as the minimum and maximum residuals of the regression model are presented in table 2 which follows.

Tableau 2 : Comparison of the deviation of alignment value and residuals of linear regression model

Parameter	
Alignment deviation	0.254 mm
Deviation of residuals of linear regression model	0.265 mm

The two values are very close to each other. Figures 4 and 5 show that the dispersion of wear measurements can be explained mainly by the misalignment of the inertial disc.

The mode of operation of the inertial-brake system has been established by the Grafquets presented in figure 6.

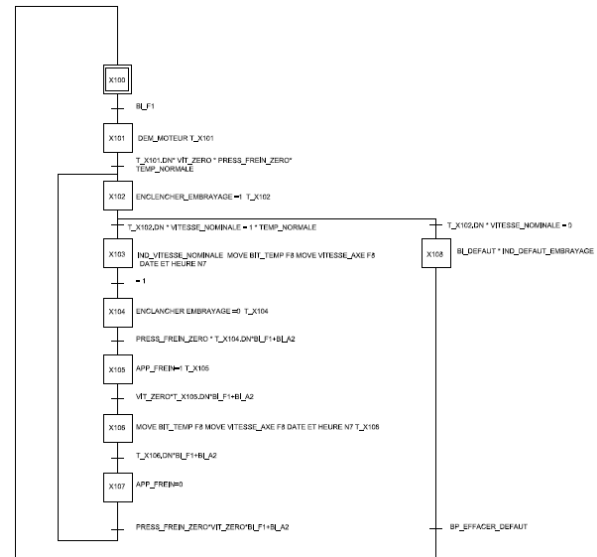
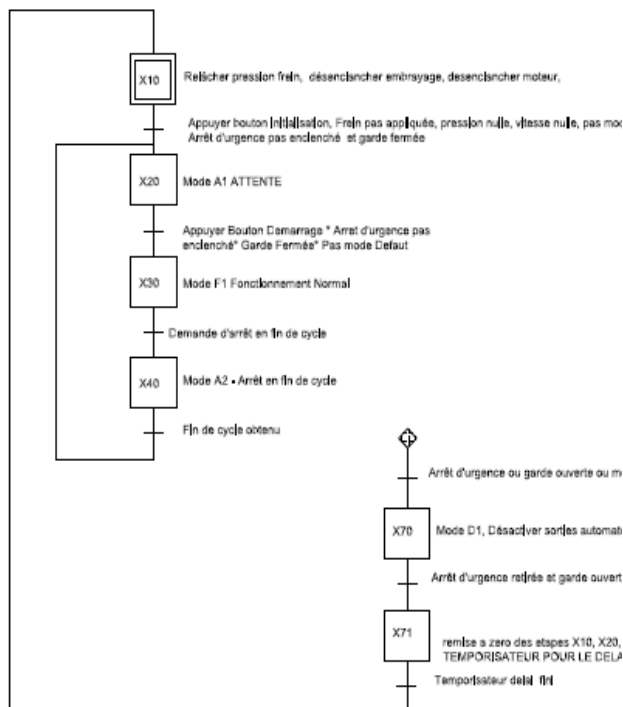


Figure 6 : Grafquets set up for operating regimedefinition of test bench in programmable logic controller



SIMULATION MODEL

Numerical simulation model as an intrinsic part of predictive maintenance can be of upmost interest. A numerical model may have numerous limitations including disturbance modelling limitations, mesh precision, resolution scheme... However, numerical models can simulate results according to any operating regime and external conditions (intrinsic of model) and becomes an excellent comparison trend to identify bad quality instrumented data, systematic and random errors. Furthermore, numerically generated degradation trend according to actual operating parameters and external conditions can be valuable data to correct manufacturers' specifications data usually generated according to different operating and external conditions.

In our case, a numerical model simulating the inertial-brake system was built using ANSYS and the model was calibrated using a Matlab based finite element model:

$$\frac{\partial \sigma_r}{\partial r \partial t} = \frac{\partial \left[E \alpha \Delta T + E \frac{\partial \omega_1}{\partial r} + F(\text{brake}) \right]}{\partial r \partial t} \dots \dots (6)$$

The system is discretized over finite elements and integrating over a rotating disk

of radius r . The applied force F is discretized over same finite elements but integrated over a smaller disk of radius r' . The area of the disk corresponds to the area of the braking pad with an error of 4%.

Therefore:

$$\int_0^{2\pi} \frac{\partial \sigma_r}{\partial r \partial t} - \frac{\partial \left[E \alpha \Delta T + E \frac{\partial \omega_1}{\partial r} \right]}{\partial r \partial t} (r dr d\theta) - \int_0^{2\pi} \frac{\partial [F(\text{brake})]}{\partial r \partial t} (r'' dr'' d\theta) = 0 \dots \dots \dots (7)$$

Local displacements are then expressed as nodal displacements:

$$\omega'(r') = \omega'_1 + (\omega'_2 - \omega'_1) \frac{r'}{r}$$

$$\omega'(r') = \left[\left(1 - \frac{r'}{r}\right) \left(\frac{r'}{r}\right) \right] \begin{Bmatrix} \omega'_1 \\ \omega'_2 \end{Bmatrix}$$

$$\omega'(r') = [N_1 \ N_2] \begin{Bmatrix} \omega'_1 \\ \omega'_2 \end{Bmatrix}$$

Hence:

$$[N] = \left[\left(1 - \frac{r'}{r}\right) \left(\frac{r'}{r}\right) \right]$$

$$\left[\frac{\partial N}{\partial r'} \right] = [N'] = \left[\left(-\frac{1}{r}\right) \left(\frac{1}{r}\right) \right]$$

Shape function development leads to the first contributing term to the matrix rigidity:

$$\int_0^r \frac{d \omega'}{d r'} EA \frac{\partial \omega'}{\partial r'} \partial r'$$

$$= \int_0^r [\partial \omega'] \{N'\} EA [N'] \{\omega'\} \partial r'$$

$$= [\partial \omega'] [S'] \{\omega'\} \dots \dots \dots (8)$$

Comparing and developing equations:

$$[S'] = EA \begin{bmatrix} \frac{1}{r} & -\frac{1}{r} \\ -\frac{1}{r} & \frac{1}{r} \end{bmatrix}$$

Similarly, other matrix rigidity terms are developed. The model allowed us to define functioning temperature and stresses for one operating ω value and applied brakes pressure. This model was used to build and calibrate an ANSYS based model used for

establishment of the 4 parameters based predictive maintenance policy.

The ANSYS based model was built and run for the following compared test bench operating parameters. Manufacturer's specifications data were also correlated to the same parameters. Figure 7 illustrates the Thermal distribution on the brake inertial disk just after zero angular velocity is attained after brake application. Table 3 describes operating parameters and conditions used for experimental measurements, numerical model design and manufacturer's data correlation.

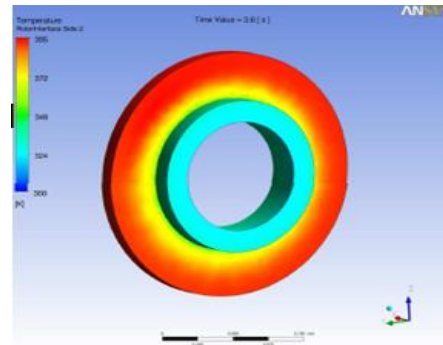


Figure 7 : Thermal distribution on inertial brake disc at establishment of zero angular velocity.

Table 3 : Operating parameters and conditions of numerical, experimental and manufacturer's models.

Working, simulated and specification corrected parameters	Value	Unit
Total inertia	507,44	lb/in ²
static torque factor	144	lbf
Dynamic torque factor	122,4	
Baking torque	520,2	lbf.in
Rotating speed, ω	180,118	rad/s
Brake disc inertia	50	lb.in ²
Specific heat capacity of brake disc	0,5	kJ/(kg°K)
Mass of braking disc	1,8	kg
Time to accelerate the drive wheel	5	s

Brake pad thickness	7,87	mm
Time to brake	0,455076549	s
Number of cycles in an hour	360	

MANUFACTURERS' SIMULATED MODEL

The life cycle of the manufacturer is defined to be 1244 hphr which is a measure of energy. The maximum power applied on the system was averaged over the disk acceleration and braking cycles and the estimated manufacturer specified life cycle is 1386388.

RESULTS

At this point, experimental data have been acquired for 18 816 cycles. The wear values obtained experimentally from the test bench were corrected to mitigate errors and compared to results generated by the numerical model and the manufacturer's specification to test bench operation correlated values. Statistical models were used to correct and improve quality of the experimental data. Table 4 presents the results obtained according to the different models.

Table 4: Wear values obtained according to instrumentation, numerical model and manufacturer's specification data correlation

cycles	wear in mm (instrumentation)	wear in mm (numerical model)	wear in mm (manufacturer's spec)
0	0	0	0
855	0,01651	0,01543	0,004787
3495	0,01651	0,01685	0,019567
4660	0,03556	0,03356	0,026089
5203	0,03683	0,03645	0,029129
6224	0,04699	0,04452	0,034846
7013	0,04826	0,046522	0,039263
7839	0,04826	0,047899	0,043887
9096	0,05715	0,05252	0,050925
10297	0,05715	0,05822	0,057649
18816	0,0889	0,089125	0,105343

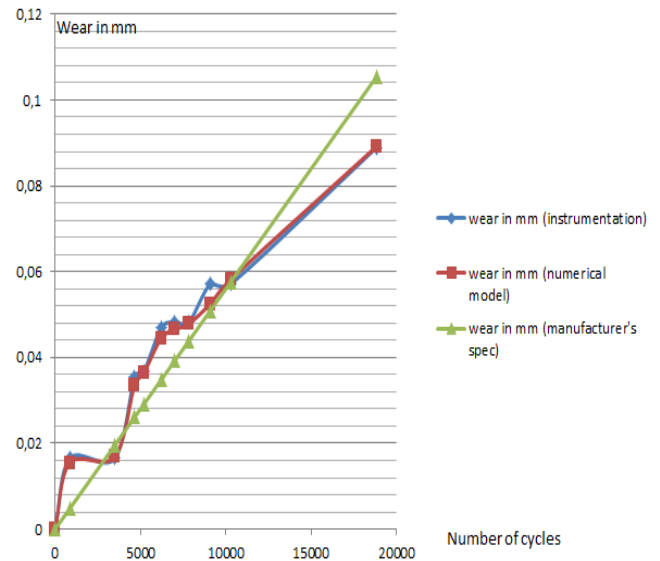


Figure 8 : Wear trend obtained according to instrumentation, numerical model and manufacturer's specification data correlation

It is interesting to note that 1) the three models provide very close values and 2) that the manufacturer's specifications data are more conservative than the data generated by the other models. This was actually anticipated and was actually the aim of the study. The idea is to develop precise degradation monitoring models that provide close values to manufacturer's specified data that are usually used for preventive maintenance. The precise but less conservative trends will allow for less frequent maintenance, lower maintenance cost but high reliability level. In order to establish an algorithm that will use the different models to establish more precise failure occurrence, the experimental tests needs to be run a few reproducible time till failure.

However, in anticipation of the experimental data availability, a preliminary function tending to identify anticipated failure has been built using Matlab[®]. The algorithm based function is expected to be an average of the different models as illustrated in figure 9 below:

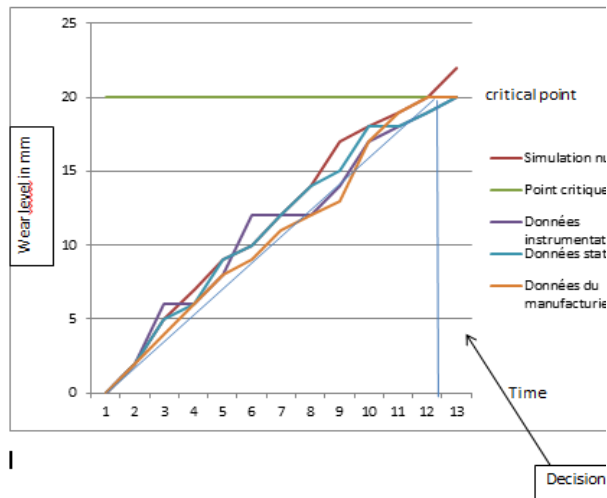


Figure 9: Expected averaged function attempting to predict failure such that reliability is maintained while maintenance frequency and cost reduced.

Using Excel and Matlab®, polynomial functions of each model were built with criterion- close fit of model data:

- 1) Numerical function model :

$$f(x) = 3.10^{-18}x^4 - 9.10^{-14}x^3 + 7.10^{-10}x^2 + 4.10^{-6}x + 0.004$$

- 2) Experimental function model :

$$f(x) = 5.10^{-18}x^4 - 2.10^{-13}x^3 + 1.10^{-9}x^2 + 3.10^{-6}x + 0.0047$$

- 3) Manufacturer's specification correlated function:

$$f(x) = -3.10^{-30}x^4 + 2.10^{-25}x^3 + 3.10^{-21}x^2 + 6.10^{-6}x + 8.10^{-14}$$

Matlab® was used to generate an average function illustrated in thicker blue which is anticipated to provide a better predictive maintenance policy according to objectives specified in this project. The generated trend is illustrated in figure 10.

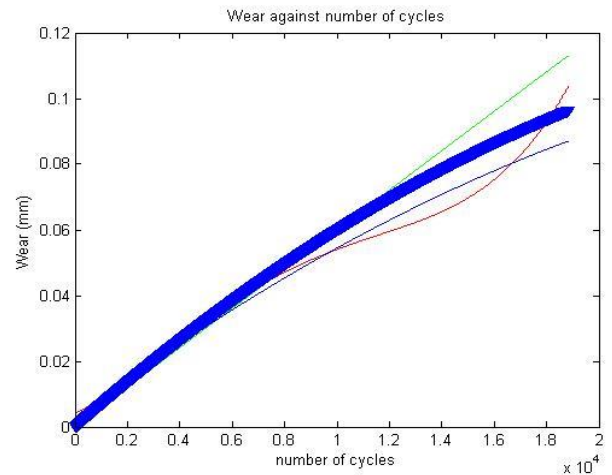


Figure 10: Matlab generated averaged wear function

Green trend: Manufacturer's specifications

Red trend: Experimental data

Purple trend: Numerical data

Thick blue trend: Averaged function

CONCLUSION AND FUTURE WORK

This paper illustrated work performed to set up a new predictive maintenance technique aiming at improving reliability whilst reducing maintenance frequency and cost. The test bench used to develop the experimental model has been illustrated and explained in this paper. Particular emphasis was laid on the need for data quality control in order to ensure accuracy of instrumented data. A numerical model was also made and illustrated. The numerical model was itself counter compared with another model to ensure accuracy. The two models were compared with manufacturer's specifications to calculate an averaged function which could be used to identify failure and help for decision taking for maintenance activities. Future work will comprise of the conclusion of experimentation on the test bench until failure. The aim will then be to improve the different models and the averaged function such that it can fit to identify the failure at the same cycle number or before but with less conservativeness than the manufacturer's specified data. Afterwards, the model will need to be validated and performance analysed for different machine element operating regimes and different machine elements.

SUPPORT

ITMI and CSI wish to thank the support of the NSERC (Natural Sciences and Engineering Research Council of Canada) for having financially supported this project and ensuring other necessary supports when needed.

REFERENCES

1. Predictive Maintenance Program « Promotes reduced maintenance cost for facility and ground support equipment » NASA technical report OPS-13
2. Lockheed Space Operations Company Predictive Engineering Technology Program Implementation Plan, 10/ 94
3. EG&G Florida, KSC Predictive Maintenance Plan. EGG-4061130, 11/20/92
4. P/PM Technology Publications (1986, 1992, 1998, 2002)
5. Maintenance Technology Publications (1995, 1997, 2001, 2002, 2004)
6. Laurent Giraud et al. “ Sécurité des outils, des machines et des procédés industriels- Étude et Recherche » Rapport R-578 IRSST
7. Thermographie infrarouge en maintenance prédictive « La thermographie infrarouge en maintenance prédictive -cas du Centre hospitalier Saint-Joseph-Espérance »
8. Malik MAK. Reliable preventive maintenance policy. AIIE Trans 1979;11(3):221–8.
9. Nakagawa T. Sequential imperfect preventive maintenance policies. IEEE Trans Reliab 1988;37(3):295–8.
10. Jayabalan V, Chaudhuri D. Cost optimization of maintenance scheduling for a system with assured reliability. IEEE Trans Reliab 1992;41(1):21–5.
11. Chan JK, Shaw L. Modeling repairable systems with failure rates that depend on age and maintenance. IEEE Trans Reliab 1993;42(4): 566–71.
12. X. Zhou et al. « Reliability-centered predictive maintenance scheduling for a continuously monitored system subject to degradation” Reliability Engineering and System Safety 92 (2007) 530–534 Science Direct

MODEL COMPLEXITY OF A CANTILEVER BEAM: AN ENERGY-BASED APPROACH

Loucas S. Louca

Department of Mechanical and Manufacturing Engineering, University of Cyprus
75 Kallipoleos Street, Nicosia 1678, Cyprus

lslouca@ucy.ac.cy

ABSTRACT

The cantilever beam is a component widely used in numerous engineering systems with its geometric and material properties varying depending on the application. Calculating the dynamic behavior of a cantilever beam is a challenging task since the critical physical phenomena and interactions vary significantly based on the geometry of the beam. There exist a number of theories/models that can be used to predict the transverse motion of a cantilever beam of which the two most commonly used are the Timoshenko and Euler-Bernoulli theories. The Euler-Bernoulli theory is simpler and thus preferred, however, depending on the beam's parameters and operating conditions this model can lead to erroneous results and thus the more complex Timoshenko theory must be used. Currently, selecting the theory to use depends on heuristics or rules that are based on experience and the accuracy requirements of the predictions. It is the purpose of this paper to address the model complexity of a cantilever beam through a systematic modeling methodology.

The paper presents a new approach for selecting the appropriate theory to use in modeling a cantilever beam. The beam is discretized through the finite segment approach and modeled using the bond graph formulation. The previously developed activity metric is then used to determine which of the inertial and stiffness effects, of the more complex Timoshenko theory, need to be included in the model in order to have accurate predictions of its dynamic behavior. An illustrative example is provided to demonstrate the new methodology.

Keywords: Cantilever beam, Timoshenko beam theory, model reduction, activity metric.

1. INTRODUCTION

Modeling and simulation have yet to achieve wide utilization as commonplace engineering tools. One reason for this is that current modeling and simulation techniques are inadequate. Specifically, a major disadvantage is that they require sophisticated users who are often not domain experts and thus lack the ability to effectively utilize the model and simulation tools to uncover the important design trade-offs. Another drawback is that models are often large and complicated with many parameters, making the physical interpretation of the model outputs, even by domain experts, difficult. This is particularly true when "unnecessary" features are included in the model.

A variety of algorithms have been developed and implemented to help automate the production of proper models of dynamic systems. Wilson and Stein (1995) developed MODA (Model Order Deduction Algorithm) that deduces the required system model complexity from subsystem models of variable complexity using a frequency-based metric. They also defined proper models as the models with physically meaningful states and parameters that are of necessary but sufficient complexity to meet the engineering and accuracy objectives. Additional work on deduction algorithms for generating proper models in an automated fashion, has been reported by Ferris et al. (1998), Ferris and Stein (1995) and Walker et al. (1996). The above algorithms have also been implemented in an automated modeling computer environment (Stein and Louca, 1996).

In an attempt to overcome the limitations of the frequency-based metrics, Louca et al. (1997) introduced a new model reduction technique that also generates proper models. This approach uses an energy-based metric (element activity) that in general, can be applied to nonlinear systems (Louca et al., 2010), and considers the importance of all energetic elements (generalized inductance, capacitance and resistance). The contribution of each energy element in the model is ranked according to the activity metric under specific excitation. Elements with small contributions are eliminated in order to produce a reduced model using a systematic methodology called Model Order Reduction Algorithm (MORA). The activity metric was also used as a basis for even further reduction, through partitioning the model into smaller and decoupled submodels (Rideout et al. 2007).

Such modeling approaches should be able to handle real mechanical systems that typically include distributed parameter (continuous) components, e.g. rods, beams, plates, etc. Frequently, modeling objectives and assumptions allow the lumping of continuous component properties into ideal energy elements that lead to a dynamic model described by a set of ordinary differential equations. However, when property lumping is not acceptable, modeling of a continuous component requires a different approach since its inertial, compliance and resistive properties are spatially distributed and cannot be lumped into single equivalent elements. The dynamic behavior of continuous components is thus described by partial differential equations with derivatives in both time and space. Another approach that is considered in this work is the modeling of a continuous component with finite segments that are spatially distributed. This is an approximation for which the accuracy is a function of the

number of segments. The model accuracy improves as the number of segments increases. Model accuracy and the required number of segments can be addressed using a frequency-based metric (Ferris et al., 1998).

Beyond the physical-based modeling, modal decomposition is also used to model and analyze continuous and discrete systems (Meirovitch, 1967). One of the advantages of modal decomposition is the ability to straightforwardly adjust (i.e., reduce) model complexity since all modes are orthogonal to each other. The reduction of such modal decomposition models is mostly based on frequency, and the user defined frequency range of interest (FROI) determines the frequencies that are important for a specific scenario. In this case, modes with frequencies within the FROI are retained in the reduced model and modes outside this range are eliminated. As expected, mode truncation introduces error in the predictions that can be measured and adjusted based on the accuracy requirements (Li and Gunter, 1981; Liu et al., 2000).

The element activity is another metric that has more flexibility than frequency-based metrics, which address the issue of model complexity by only adding compliant elements, leaving unaccounted the importance of inertial and resistive elements. In contrast, the activity metric considers the importance of all energetic elements, and therefore, the significance of all energy elements in the model can be quantified. It is the purpose of this work to develop a new methodology using the activity metric for addressing the model complexity of distributed parameter systems and specifically cantilever beams. The methodology is specifically developed using the finite segment approximation and the goal is to identify the physical phenomena to be included in each segment in order to accurately predict the dynamic behavior.

This paper is organized as follows: first, background about the energy-based activity metric is provided, along with the reduction algorithm. Next, the equation formulation for a finite segment Timoshenko beam is presented along with the closed-form expressions of the steady state activities. Then the complexity of a cantilever beam is analyzed using MORA. Finally, in the last section, discussion and conclusions are given.

2. BACKGROUND

The original work on the energy-based metric for model reduction is briefly described here for convenience. More details, extensions, and applications of this approach are given in previous publications (Louca and Stein, 2002; Louca et al., 2004; Louca and Stein, 2009; Louca et al., 2010). The main idea behind this model reduction technique is to evaluate the “element activity” of individual energy elements in a full system model under a stereotypical set of inputs and initial conditions. The activity of each energy element establishes a hierarchy for all elements. Those below a user-defined threshold of acceptable level of activity are eliminated from the model. A reduced model is then generated and a new set of governing differential equations is derived.

The activity metric has been previously formulated for systems with nonlinearities in both the element constitutive laws and junction structure. In this work, the activity metric is applied to linear systems for which analytical expressions for the activity can be derived, and therefore, avoid the use of numerical time integration that could be cumbersome. The analysis is further simplified if, in addition to the linearity assumption, the system is assumed to have a single sinusoidal excitation, and only the steady state response is examined. These assumptions are motivated from Fourier analysis where an arbitrary function can be decomposed into a series of harmonics. Using this frequency decomposition, the activity analysis can be performed as a function of frequency in order to study the frequency dependency of element activity in a dynamic system.

2.1. Element Activity for Linear Systems

A measure of the power response of a dynamic system, which has physical meaning and a simple definition, is used to develop the modeling metric, element activity (or simply “activity”). Element activity, A , is defined for each energy element as:

$$A = \int_0^{\tau} |\mathcal{P}(t)| dt \quad (1)$$

where $\mathcal{P}(t)$ is the element power and τ is the time over which the model has to predict the system behavior. The activity has units of energy, representing the amount of energy that flows in and out of the element over the given time τ . The energy that flows in and out of an element is a measure of how active this element is (how much energy passes through it), and consequently the quantity in Eq. (1) is termed activity. Activity can be defined independent of the energy domain, type of energy element or nonlinearities.

The activity is calculated for each energy element based on the system response. In the case that the system is modeled using a bond graph formulation, the state equations are derived using the multi-port bond graph representation (Borutzky, 2004; Brown, 2006; Karnopp et al., 2006; Rosenberg and Karnopp, 1983). In addition, when a system has a single input and linear junction structure and constitutive laws, the state equations are linear time invariant and have the following general form:

$$\dot{\mathbf{x}} = \mathbf{A}\mathbf{x} + \mathbf{b}u \quad (2)$$

where, $\mathbf{A} \in \mathbb{R}^{m \times m}$, $\mathbf{b} \in \mathbb{R}^m$ are the state space matrices, $\mathbf{x} \in \mathbb{R}^m$ is the state vector, $u \in \mathbb{R}$ is the input, and m is the number of independent states.

For the above system appropriate outputs are defined in order to calculate the power of each energy element in the model using the constitutive law of each element. For convenience, the outputs are selected to be generalized flow, effort, and flow for inertial, compliant, and resistive elements, respectively. The dual effort or flow needed for calculating the power is derived from the output variables

and constitutive laws. The output vector for this set of variables has the form:

$$\mathbf{y} = \begin{Bmatrix} \mathbf{f}_I \\ \mathbf{e}_C \\ \mathbf{f}_R \end{Bmatrix} \quad (3)$$

where $\mathbf{y} \in \mathbb{R}^k$ and $\mathbf{f}_I \in \mathbb{R}^{k_I}$, $\mathbf{e}_C \in \mathbb{R}^{k_C}$, and $\mathbf{f}_R \in \mathbb{R}^{k_R}$. The variables k_I , k_C , and k_R represent the number of inertial, compliant, and resistive elements, respectively. The total number of energy elements is $k = k_I + k_C + k_R$. Using the output variables set in Eq. (3), the output equations can be written as:

$$\mathbf{y} = \mathbf{C}\mathbf{x} + \mathbf{d}u \quad (4)$$

where $\mathbf{C} \in \mathbb{R}^{k \times m}$, $\mathbf{d} \in \mathbb{R}^k$ are the output state space matrices. Note that the output vector is defined such that the required variables of the inertial elements are first, followed by the variables of compliant and then resistive elements.

Given this set of output variables the missing efforts or flows, needed for calculating the element power, are computed from the linear constitutive laws of each type of energy element as shown below:

$$\begin{aligned} \mathbf{I}: p_I &= r_I f_I \Leftrightarrow e_I = \dot{p}_I = r_I \dot{f}_I \\ \mathbf{C}: q_C &= r_C e_C \Leftrightarrow f_C = \dot{q}_C = r_C \dot{e}_C \\ \mathbf{R}: e_R &= r_R f_R \end{aligned} \quad (5)$$

where r_I, r_C, r_R are known constants representing the linear constitutive law coefficients of inductance, compliance and resistance, respectively. For more compact expressions a vector, $\mathbf{r} \in \mathbb{R}^k$, with all the linear constitutive law coefficients is introduced as shown below:

$$\mathbf{r} = \begin{Bmatrix} \mathbf{r}_I \\ \mathbf{r}_C \\ \mathbf{r}_R \end{Bmatrix} \quad (6)$$

where $\mathbf{r}_I \in \mathbb{R}^{k_I}$, $\mathbf{r}_C \in \mathbb{R}^{k_C}$, and $\mathbf{r}_R \in \mathbb{R}^{k_R}$.

Finally, the power needed for calculating the activity of each element, as defined in Eq. (1), is computed as the product of generalized effort and flow. By using Eq. (5) the following expressions for the power of each element type are derived:

$$\begin{aligned} \mathbf{I}: \mathcal{P}_I &= e_I f_I = r_I f_I \dot{f}_I \\ \mathbf{C}: \mathcal{P}_C &= e_C f_C = r_C e_C \dot{e}_C \\ \mathbf{R}: \mathcal{P}_R &= e_R f_R = r_R f_R f_R = r_R f_R^2 \end{aligned} \quad (7)$$

The expressions for element power in Eq. (7) are generalized with the use of the defined structure of the output vector in Eq. (3) and parameter vector in Eq. (6). Thus, the power for energy storage elements (inertial and compliant) is given by Eq. (8) and for energy dissipation elements (resistive) in Eq. (9).

$$\mathcal{P}_i = r_i y_i \dot{y}_i, \quad i = 1, \dots, k_I + k_C \quad (8)$$

$$\mathcal{P}_i = r_i y_i^2, \quad i = k_I + k_C + 1, \dots, k \quad (9)$$

The above element power is then used to calculate the element activity based on its definition in Eq. (1). Element parameters are assumed to be constant thus the activity for each element is given by:

$$\begin{aligned} A_i &= \int_0^\tau |\mathcal{P}_i| = r_i \int_0^\tau |y_i \dot{y}_i| dt, \quad i = 1, \dots, k_I + k_C \\ A_i &= \int_0^\tau |\mathcal{P}_i| = r_i \int_0^\tau |y_i^2| dt, \quad i = k_I + k_C + 1, \dots, k \end{aligned} \quad (10)$$

2.2. Activity for Single Harmonic Excitation

The time response of the output vector, $\mathbf{y}(t)$, in Eq. (3) is required in order to complete the calculation of the element power. For nonlinear systems, numerical integration is typically used to calculate the system response; however, in this case linear system analysis can be used to obtain closed form expressions. In addition, for the purposes of this work, the excitation is assumed to be a single harmonic given by:

$$u(t) = U \sin(\omega t) \quad (11)$$

where $U \in \mathbb{R}$ is the amplitude of the excitation and ω is the excitation frequency. The steady state response of the linear system in Eq. (2) and (4), and for the excitation in Eq. (11), is calculated using linear system analysis theory. This gives the following closed form expression:

$$y_i(t, \omega) = U Y_i(\omega) \cdot \sin(\omega t + \varphi_i(\omega)), \quad i = 1, \dots, k \quad (12)$$

where $Y_i(\omega)$ and $\varphi_i(\omega)$ are the steady state amplitude and phase shift, respectively that can be easily calculated from the state space matrices using linear systems theory.

Within the context of this analysis, the output $y_i(t, \omega)$ in Eq. (12) is either an effort or a flow that is used to calculate the power of each element in Eq. (7). Finally, the activity can be calculated by Eq. (1), but first the upper bound of this integral must be specified. For this case, the steady state and periodicity of the response are exploited. A periodic function repeats itself every T seconds, and therefore, a single period of this function contains the required information about the response. Thus, the upper bound of the integral is set to one period of the excitation, $\tau = T = 2\pi/\omega$. Therefore, the steady state activity for the energy storage elements is given by:

$$\begin{aligned} A_i^{ss}(\omega) &= r_i \int_0^T |y_i \dot{y}_i| dt \\ &= \frac{1}{2} r_i U^2 Y_i^2(\omega) \omega \int_0^T \left| \sin(2(\omega t + \varphi_i(\omega))) \right| dt \quad (13) \\ &\Rightarrow A_i^{ss}(\omega) = 2r_i U^2 Y_i^2(\omega) \end{aligned}$$

and for energy dissipation elements by:

$$\begin{aligned}
A_i^{ss}(\omega) &= r_i \int_0^T |y_i|^2 dt \\
&= r_i U^2 Y_i^2(\omega) \int_0^T |\sin^2(\omega t + \varphi_i(\omega))| dt \quad (14) \\
\Rightarrow A_i^{ss}(\omega) &= \frac{\pi r_i U^2 Y_i^2(\omega)}{\omega}
\end{aligned}$$

The above simple closed form expressions can be used to calculate the activity of energy elements for a given single harmonic excitation. These expressions are proportional to the square of the amplitude, however, they have no dependency on the phase shift that is eliminated through the integration. The superscript 'ss' in Eq.(13)-(14) denotes the activity under a steady state harmonic response. Note that the activity for both energy storage and energy dissipation elements is a function of the excitation frequency but not the phase shift.

2.3. Activity Index and MORA

The activity as defined in Eq. (1) is a measure of the absolute importance of an element as it represents the amount of energy that flows through the element over a given time period. In order to obtain a relative measure of the importance, the element activity is compared to a quantity that represents the “overall activity” of the system. This “overall activity” is defined as the sum of all the element activities of the system, is termed total activity (A^{Total}) and is given by:

$$A^{Total}(\omega) = \sum_{i=1}^k A_i(\omega) \quad (15)$$

where A_i is the activity of the i^{th} element given by Eq.(1). Thus a normalized measure of element importance, called the element activity index or just activity index, is defined as:

$$AI_i^{ss}(\omega) = \frac{A_i(\omega)}{A^{Total}(\omega)} = \frac{A_i(\omega)}{\sum_{i=1}^k A_i(\omega)} \quad (16)$$

The activity index, $AI_i^{ss}(\omega)$, is calculated for each element in the model and it represents the portion of the total system energy that flows through a specific element. The input amplitude, U , does not appear in any of the element activity indices since all element activities are proportional to the square of the amplitude.

With the activity index defined as a relative metric for addressing element importance, the Model Order Reduction Algorithm (MORA) is constructed. The first step of MORA is to calculate the activity index for each element in the system for a given system excitation and initial conditions. Next, the activity indices are sorted to identify the elements with high activity (most important) and low activity (least important). With the activity indices sorted, the model reduction proceeds given the desired engineering specifications. These specifications are defined by the modeler who then converts them into a

threshold β of the total activity (e.g., 99%) that he or she wants to include in the reduced model. This threshold defines the borderline between the retained and eliminated model elements. The elimination process is shown in Figure 1 where the sorted activity indices are summed starting from the most important element until the specified threshold is reached. The element which, when included, increments the cumulative activity above the threshold, is the last element to be included in the reduced model. The elements that are above this threshold are removed from the model, e.g., when using the bond graph formulation delete the corresponding energy element and connected bond.

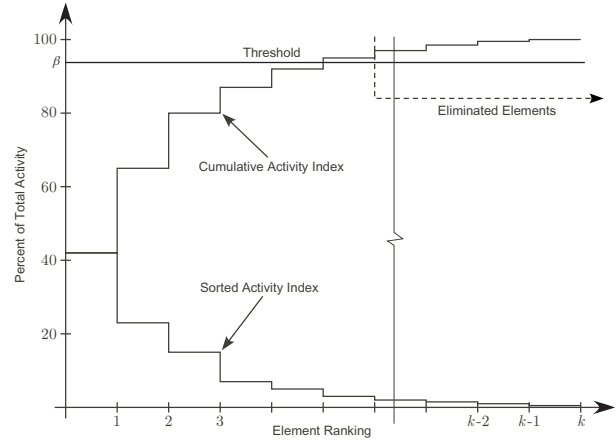


Figure 1: Activity index sorting and elimination.

3. TIMOSHENKO BEAM MODEL

The state space representation used in the previous section assumes that real components exhibit only inertial, compliant, or resistive behavior. This means that the dynamic behavior of a component can be lumped and modeled as a single inertial, compliant or resistive energy element. This can be a valid assumption for many components, however, real system components can possess all dynamic properties (inertial, compliant, resistive) simultaneously. In addition, these properties may vary or be distributed spatially. In these cases, a lumped parameter modeling approach cannot be used since it will produce erroneous predictions. These components must be considered as continuous and require a different modeling approach.

Models of continuous systems can be developed using solid mechanics techniques, which lead to Partial Differential Equations (PDE) with derivatives in both space and time (Bauchau and Craig, 2009; Genta, 2009; van Rensburg and van der Merwe, 2006; Li, 2008). The continuous cantilever beam used in this work is shown in Figure 2, where its transverse motion is considered when excited with a vertical load at its free end. The motion of a given gross section, $w(x,t)$ and $\varphi(x,t)$, from its undeformed state varies with time and location thus having PDEs describing its motion. Note that due to the rotation φ , a cross section does not remain normal to the neutral axis according to the Timoshenko beam theory that is used in this work. One method for solving these PDEs is separation of variables, which produces a modal

expansion solution (Meirovitch, 1967). This approach can also be combined with other lumped parameter elements in order to model a real system that consists of both lumped and distributed parameter components (Karnopp et al., 2006). An analysis of the advantages and disadvantages of this approach is beyond the scope of this work, however, it is safe to say that the solution of PDEs is more cumbersome than the solution of ordinary differential equations that describe the behavior of lumped parameters system.

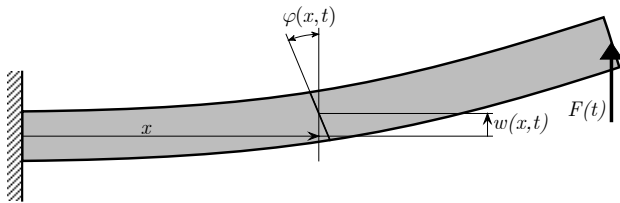


Figure 2: Cantilever beam transverse vibration.

A different approach for modeling the transverse vibration of a cantilever beam is to divide it into segments of equal length. This approach is motivated by the procedure for deriving the PDEs describing the motion of a beam. Each of these segments has linear inertial and compliant properties that can be determined from solid mechanics theory. Shear effects and rotational inertial effects are also considered, which results in a more generic model that is valid for a larger range of geometric parameters. This is known as the Timoshenko beam model, which is usually used for non-slender beams in order to get accurate model predictions. The use of this more complex model using the Timoshenko beam theory is also mandated from the use of MORA in the process of determining the appropriate model complexity. In this approach the most complex model is first developed, and then MORA is used to identify what is actually needed in order to reach a reduced model with accurate predictions.

The ideal physical model under these assumptions is shown in Figure 3 where the beam is divided into n segments. This model approaches the partial differential equations of the continuous system, as the number of segments approaches infinity. However, it is difficult to

predict the number of segments required to achieve a given level of accuracy. It is well known that a large number of segments is required for accurately predicting low frequency dynamics. For the purposes of this work the number of segments is chosen based on previous research, such that the model accurately predicts low frequency dynamics that are considered in this work (Louca, 2014; Louca, 2015). With the given number of segments, the physical phenomena to be included in each segment, for the model to accurately predict the dynamic behavior, will then be identified using the proposed methodology in this paper.

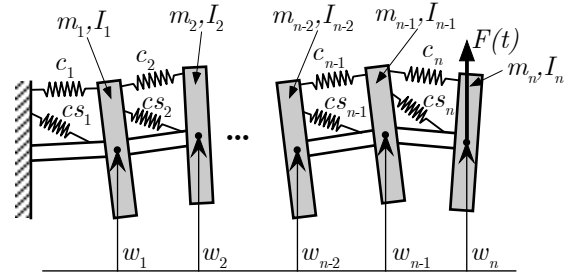


Figure 3: Ideal physical model of a Timoshenko beam.

For calculating the constitutive law parameters of the energy storage elements, the beam is assumed to have density ρ , Young's modulus E , shear modulus G , length L , cross sectional area A and cross sectional moment of inertia I . Given these physical parameters of the beam, the element parameters in the above linear model are given by the expressions below:

$$\begin{aligned} m_i &= \rho A \Delta x, \quad i = 1, \dots, n \\ I_i &= \rho I \Delta x, \\ c_i &= \frac{\Delta x}{EI} \\ cs_i &= \frac{\Delta x}{\kappa GA} \end{aligned} \quad (17)$$

where $\Delta x = L/n$ is the length of each segment, κ is a dimensionless constant that accounts for the non-uniform distribution of the shear stress and depends on the shape

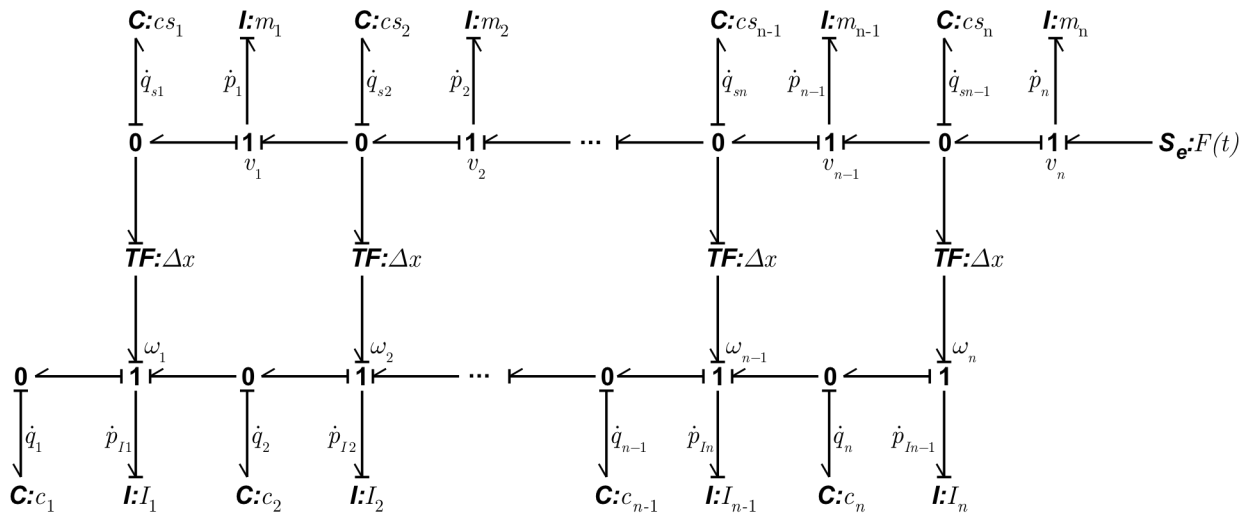


Figure 4: Bond graph model of a Timoshenko beam.

of the cross-section. The inertial parameters m_i and I_i represent the linear and rotational inertia of each segment, respectively. The parameters c_i and cs_i represent the bending and shear compliance between two segments, respectively. The beam is assumed to have no energy losses therefore there are no damping elements in the model. These parameters are used to define the parameter vector as defined in Eq. (6).

For developing the dynamic equations, the bond graph formulation is used. Bond graphs provide the power topography of the system and it is a natural selection for implementing the power-based activity metric. The bond graph model of the ideal physical model as shown in Figure 3 is developed and given in Figure 4. The bond graph has $4n$ independent state variables since each segment is modeled by 4 independent energy storage elements and its state vector has the form $\mathbf{x} = \{p_1, \dots, p_n, p_{I1}, \dots, p_{In}, q_1, \dots, q_n, q_{s1}, \dots, q_{sn}\}^T$. The transverse velocity of the each mass, v_i , represents the velocity at a given location of the continuous beam and Eq. (18) expresses the relation between the discrete and continuous variables. The other kinematic variable of the model, ω_i , is the rotation at a given location and its relation to the continuous variable is given in Eq. (19).

$$v_i(t) = \dot{w}_i = \dot{w}(i\Delta x, t) \quad (18)$$

$$\omega_i(t) = \dot{\varphi}_i = \dot{\varphi}(i\Delta x, t) \quad (19)$$

In addition, for easy calculation of the output equations that required for calculating power, the state equations are derived using the multi-port approach (Rosenberg, 1971). According to this approach, the state space and input matrices are given by:

$$\mathbf{A} = \mathbf{J}_{SS} \mathbf{S}, \quad \mathbf{b} = \mathbf{J}_{SU} \quad (20)$$

The output matrices, as defined in Eq. (4), that are required for calculating the power flow into the energy elements are given by:

$$\mathbf{C} = \mathbf{S}, \quad \mathbf{d} = \mathbf{0} \quad (21)$$

The output vector according to the analysis in the previous section is given by $\mathbf{y} = \{f_1, \dots, f_{2n}, e_1, \dots, e_{2n}\}^T$. The dimensions of the state space matrices as defined in the previous section are $m = 4n$ and $k = 4n$. Based on this set of state variables, the junction structure matrices, \mathbf{J}_{SS} and \mathbf{J}_{SU} , are derived and given in the Appendix. The above equations and junction structure matrices are simplified since the model has no resistive elements.

For the above model with n segments the steady-state response is first calculated using Eq. (12) and based on the state space equations in Eq. (20)-(21). Then the element activity is calculated from Eq. (13) and (14), which gives the following expression for the energy storage elements of the model:

$$A_i^{ss}(\omega) = 2r_i U^2 Y_i^2(\omega), \quad i = 1, \dots, 4n \quad (22)$$

The above analysis enables the calculation of the element activity for a given single harmonic excitation. The activity index that is used by MORA is independent of the excitation amplitude, as shown in Eq. (16), and therefore can be set to an arbitrary value, e.g., set to one (1) for simplicity. Model complexity and which physical phenomena need to be included can be determined given the element activity in Eq. (22) and MORA. The complexity of the beam is investigated in the next section in order to identify the significant elements based on beam length and element location. A series of analyses is performed in order to get more insight into the beam dynamics under different scenarios.

4. BEAM COMPLEXITY BASED ON ACTIVITY

The activity metric and MORA is applied to a steel cantilever beam with parameters $\rho = 7860 \text{ kg/m}^3$, $E = 210 \text{ GPa}$, $G = 80 \text{ GPa}$, $A = 3 \times 10^{-3} \text{ m}^2$, $I = 2 \times 10^{-5} \text{ m}^4$, $\kappa = 0.85$. The length of the beam is varied, $L = 0.2\text{-}2 \text{ m}$, in order to study the variation of element significance. The methodology is easy and computationally inexpensive to implement due to the simple and closed form expressions used for calculating the state space matrices, frequency response and activity.

First, the beam length is set to 2 m such that the beam is considered to be slender. The number of segments is set to $n = 30$ and therefore there are a total of 120 energy storage elements modeling the beam. The modeling target is to accurately predict static behavior to low frequency dynamics, thus the excitation frequency is set to 95% of the first natural frequency (122.68 rad/s).

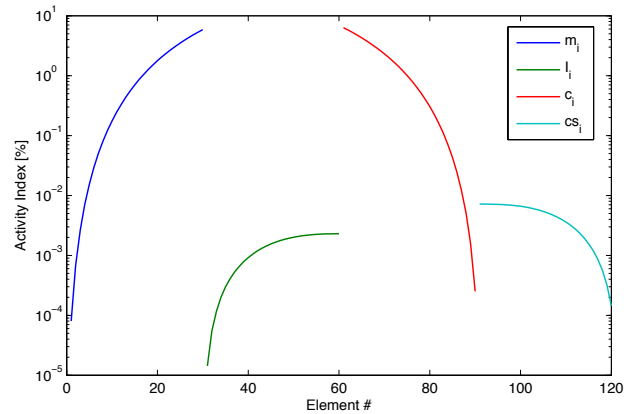


Figure 4: Element activity indices for slender beam.

The results of the activity analysis using Eq. (22) and under these assumptions are shown in Figure 4 where the activity index of all 120 elements is shown. Element numbers 1-30 represent the activity index of the linear inertia (m_i) and 31-60 the activity index of the rotational inertia (I_i) of each segment. Next, element numbers 61-90 and 91-120 represent the activity index of the bending (c_i) and shear (cs_i) compliance, respectively. For each range of elements the smallest numbers represent elements that are next to the fixed end of the beam. It is clear from the activity analysis that the most important elements are related to the linear inertia and the bending stiffness of the beam. On the contrary, the elements

related with the rotary inertia and shear stiffness have very low activity and thus are insignificant under these conditions. The activity analysis agrees with common practice, in which a slender beam is modeled using the Euler-Bernoulli theory that neglects rotational inertia and shear stress effects.

Model complexity is systematically addressed using MORA as it is described in Section 2.3. Elements are ranked according to their activity index as shown in Figure 5 where the sorted activity indices along with the cumulative activity index are plotted. According to activity analysis, 40 of the 120 elements account for almost 99% of the energy the flows through the model. This is a significant result verifying that unnecessary complexity is included in the model, however, the figure does not directly depicts the elements that are insignificant and could be eliminated from the model.

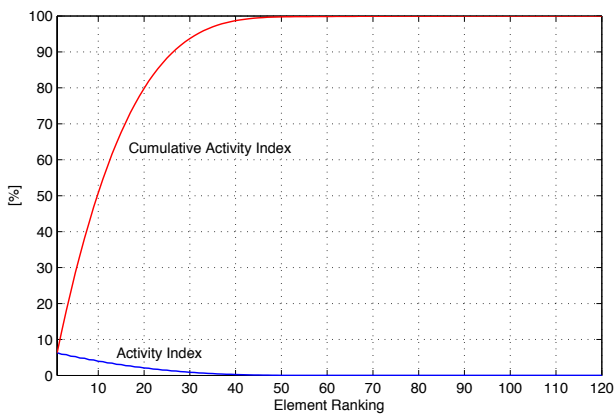


Figure 5: Element ranking for slender beam.

The important elements are next identified using MORA. Using a reduction threshold, $\beta = 99\%$, MORA identifies the elements that have a significant contribution to the system dynamic behavior. The results of this analysis are shown in Figure 6 where both the activity and elimination/inclusion in the reduced model are depicted. The '+' symbol identifies the elements with significant contribution and must be included, where the 'o' symbols identifies that an element is insignificant and must be eliminated from the full model in order to generate the reduced model. Out of the 120 elements only 42 are important and the remaining 78 can be eliminated. More specifically, MORA identifies that all rotational inertia and shear stiffness elements must be eliminated from the model. Linear inertia elements that are close to the support have low activity and can be eliminated from the model, where inertia elements towards the free end of the beam have high activity and must be retained. The reverse is true for the bending stiffness elements, where the elements towards the free end can be eliminated and the ones near the support must be retained. More specifically, 21 of the linear inertia and 21 of the bending stiffness elements have high activity and must be included in the reduced model.

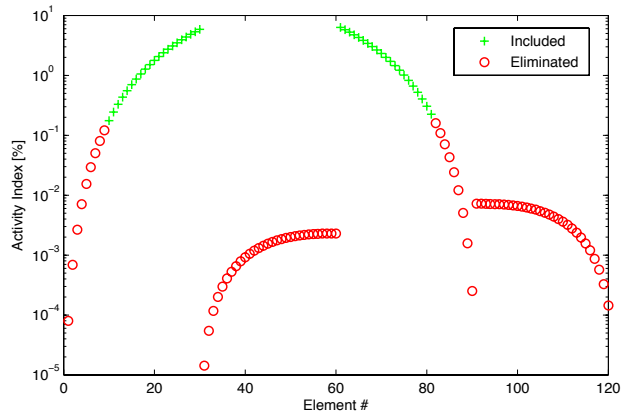


Figure 6: Model reduction for slender beam, $L = 2$ m.

The same reduction using MORA is performed with different beam lengths in order to study how element importance changes as the length is reduced. The reduction for a beam length of 0.7 m is shown in Figure 7. The same trend is observed for the elimination of linear inertia and bending stiffness elements. The activity index of all rotational inertia elements (31-60) is higher than before ($L = 2$ m) but still very low, and therefore, they are eliminated from the model. The activity of shear stiffness (91-120) also increases and some of these elements become important. The shear stiffness elements that are close to the support have higher activity index and have to be included in the reduced model, while the ones towards the free end are eliminated. A total of 59 elements are included in the reduced model with 24 linear inertia, 24 bending stiffness and 11 shear stiffness elements.

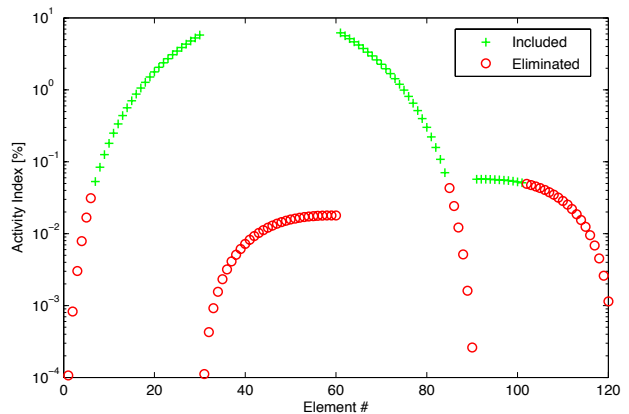


Figure 7: Model reduction for $L = 0.7$ m.

The beam length is further reduced to 0.2 m in order to examine if more elements become important. The activity index of the linear inertia and bending stiffness remains almost unchanged as shown in Figure 8. However, the activity index of the rotational inertia and shear stiffness is further increased such that some of the rotational inertia elements also become important. More specifically the rotational inertia elements that towards the free end are important and the ones near the fixed end are eliminated. A total of 89 elements out of 120 are included in the reduced model with 24 linear inertia, 17 rotational inertia, 23 bending stiffness and 25 shear stiffness elements.

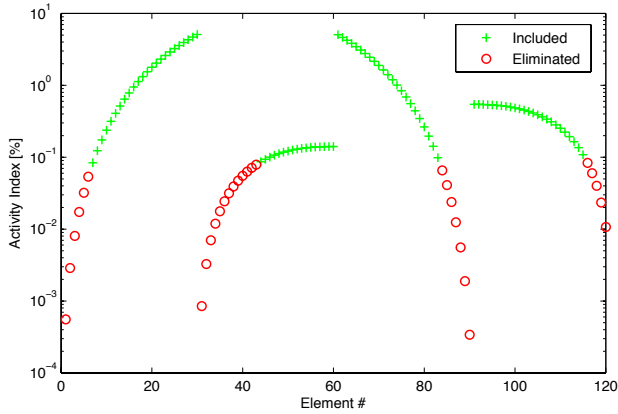


Figure 8: Model reduction for $L = 0.2$ m.

The variation of beam length showed that the total number of important elements increases as the beam length decreases. This variation is investigated in more detail by varying the beam length from 0.2 to 2 m with a step of 20 mm. The number of included linear and rotational inertia, and bending and shear stiffness is recorded along with the total number of elements. The results of this analysis are shown in Figure 9. The total number of elements is monotonically increasing as the beam length is decreased. The number of linear inertia and bending stiffness remains almost constant as the length changes. On the contrary, the number of shear stiffness elements is zero until about 0.9 m where it becomes important and starts increasing. Further reduction in length results in a monotonic increase in the number of included shear stiffness element. A similar behavior is observed for the number of the rotational inertia elements, however, they become important at a lower beam length of about 0.5 m.

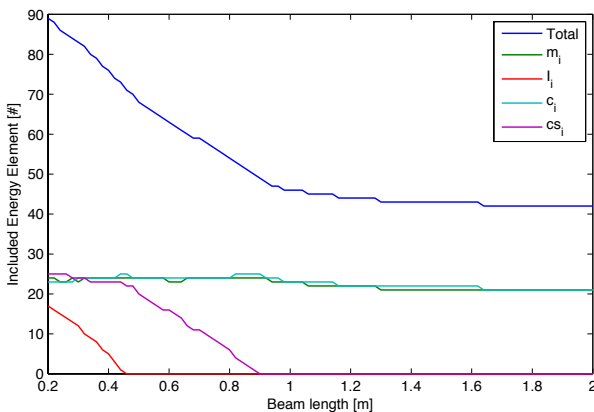


Figure 9: Model reduction for length variation.

5. DISCUSSION AND CONCLUSIONS

A new methodology is developed that reduces the complexity of a Timoshenko or Euler-Bernoulli beam model by providing more insight into the beam dynamic behavior at the same time. The proposed methodology provides a systematic modeling procedure for cantilever beams that are modeled through the finite segment approach. The previously developed activity metric is used as the basis for determining the physical phenomena that need to be included in each segment in order for the

model to accurately predict the dynamic behavior of a beam. The procedure starts with the most complicated model, Timoshenko in this case, and then eliminates insignificant elements that do not contribute to the dynamic behavior.

The results presented in this work are in agreement with the assumptions of beam theories, which propose that the Timoshenko beam model must be used for shorter rather than slender beams. The proposed methodology can be used when modeling beams, in order to decide which of the two models to use, Timoshenko or Euler-Bernoulli. In addition, the activity metric can refine the modeling assumptions by identifying what physical phenomena need to be included in each segment, i.e., linear and rotational inertia, bending and shear stiffness.

The number of segments is a significant parameter when it comes to modeling with the finite segment approach but it was considered constant in the analyses of the presented results. The methodology was also performed with various, lower and higher, number of segments, however these results are not presented in this paper for brevity. The reduced models for different number of segments are identical with the ones presented in this work. The only difference is the actual number of included elements, as shown in Figure 9, however, the ratio of included elements to the total number of elements remains constant.

The activity analysis is performed for a given single excitation frequency that is lower than the first natural frequency. This excitation is chosen since the model is expected to be used with low frequency excitations. A similar analysis with the one presented in this work can be performed for a higher frequency or range of frequencies in order to account for more realistic excitations. However, this procedure has to be formalized and this remains as an item for future research.

Because this work uses an energy-based modeling metric, it is convenient to use a model representation and formulation approach from which energy can be easily extracted/calculated. The bond graph approach explicitly presents the power topography of a dynamic system, and therefore, it is used in this work for calculating the necessary variables required for the power calculations. To be clear, the use of this methodology is not limited to systems represented by bond graphs. It can also be applied when the continuous system is modeled using any other modeling methodology, e.g., Lagrange's equations, Newton's Law, etc. However, in this case the calculation of power that is required for the proposed methodology might not be as trivial as using the bond graph formulation.

The results of this paper provide more insight into the nature of the reduced ordered models produced by MORA, and therefore, demonstrate that MORA is an even more useful tool than previously realized for the production of proper models of nonlinear systems. The activity metric effectively addresses the model complexity of distributed parameter components and in addition provides physical insight into the model.

APPENDIX: JUNCTION STRUCTURE MATRICES

$$\mathbf{S} = \begin{bmatrix} m_i \mathbf{I}_{n \times n} & \mathbf{0}_{n \times n} & \mathbf{0}_{n \times n} & \mathbf{0}_{n \times n} \\ \mathbf{0}_{n \times n} & I_i \mathbf{I}_{n \times n} & \mathbf{0}_{n \times n} & \mathbf{0}_{n \times n} \\ \mathbf{0}_{n \times n} & \mathbf{0}_{n \times n} & c_i \mathbf{I}_{n \times n} & \mathbf{0}_{n \times n} \\ \mathbf{0}_{n \times n} & \mathbf{0}_{n \times n} & \mathbf{0}_{n \times n} & cs_i \mathbf{I}_{n \times n} \end{bmatrix}^{-1}$$

$$\mathbf{J}_{SS} = \begin{bmatrix} \mathbf{0}_{n \times n} & \mathbf{0}_{n \times n} & \mathbf{0}_{n \times n} & \mathbf{J}_1 \\ \mathbf{0}_{n \times n} & \mathbf{0}_{n \times n} & \mathbf{J}_1 & \Delta x \mathbf{I}_{n \times n} \\ \mathbf{0}_{n \times n} & -\mathbf{J}_1^T & \mathbf{0}_{n \times n} & \mathbf{0}_{n \times n} \\ -\mathbf{J}_1^T & -\Delta x \mathbf{I}_{n \times n} & \mathbf{0}_{n \times n} & \mathbf{0}_{n \times n} \end{bmatrix}$$

$$\mathbf{J}_{SU} = \begin{bmatrix} \mathbf{0}_{(n-1) \times 1} \\ 1 \\ \mathbf{0}_{3 \times 1} \end{bmatrix}$$

$$\mathbf{J}_1 = \begin{bmatrix} -1 & 1 & 0 & 0 & \dots & 0 & 0 & 0 \\ 0 & -1 & 1 & 0 & \dots & 0 & 0 & 0 \\ 0 & 0 & -1 & 1 & \dots & 0 & 0 & 0 \\ \vdots & \vdots & \vdots & \vdots & \ddots & \vdots & \vdots & \vdots \\ 0 & 0 & 0 & 0 & \dots & -1 & 1 & 0 \\ 0 & 0 & 0 & 0 & \dots & 0 & -1 & 1 \\ 0 & 0 & 0 & 0 & \dots & 0 & 0 & -1 \end{bmatrix}$$

REFERENCES

- Bauchau, O.A. and J.I. Craig, 2009. *Structural Analysis*. Springer, ISBN 978-90-481-2515-9.
- Borutzky, W., 2004. *Bond Graph Methodology: Development and Analysis of Multidisciplinary Dynamic Systems*. Springer, ISBN 978-1848828810.
- Brown, F.T., 2006. *Engineering System Dynamics: A Unified Graph-Centered Approach*, Second Edition. CRC Press, ISBN 9780849396489.
- Ferris, J.B., J.L. Stein, and M.M. Bernitsas, 1998. "Development of Proper Models of Hybrid Systems." *Transactions of the ASME, Journal of Dynamic Systems, Measurement, and Control*, Vol. 120, No. 3, pp. 328-333. Published by ASME, New York, NY.
- Ferris, J.B. and J.L. Stein, 1995. "Development of Proper Models of Hybrid Systems: A Bond Graph Formulation." *Proceedings of the 1995 International Conference on Bond Graph Modeling*, pp. 43-48, January, Las Vegas, NV. Published by SCS, ISBN 1-56555-037-4, San Diego, CA.
- Genta, G., 2009. *Vibration Dynamics and Control*. Springer, Netherlands. ISBN: 978-0-387-79579-9.
- Li, D.F. and E.J. Gunter, 1981. "Study of the Modal Truncation Error in the Component Mode Analysis of a Dual-Rotor." *Transactions of the ASME, Journal of Engineering for Gas Turbines and Power*, Vol. 104, No. 3, p 525-532. Published by ASME, ISSN 0022-0825, New York, NY.
- Li, X.F., 2008. "A unified approach for analyzing static and dynamic behaviors of functionally graded Timoshenko and Euler-Bernoulli beams." *Journal of Sound and Vibration*, 318(4-5), 1210-1229.
- Liu, Dauh-Churn, Chung, Hsing-Liao and Chang, Wei-Min, 2000. "Errors Caused by Modal Truncation in Structure Dynamic Analysis." *Proceedings of the International Modal Analysis Conference - IMAC*, v 2, p 1455-1460. Published by Society for Experimental Mechanics Inc., ISSN 1046-6770, Bethel, CT.
- Louca, L.S., J.L. Stein, G.M. Hulbert, and J.K. Sprague, 1997. "Proper Model Generation: An Energy-Based Methodology." *Proceedings of the 1997 International Conference on Bond Graph Modeling*, pp. 44-49, Phoenix, AZ. Published by SCS, ISBN 1-56555-103-6, San Diego, CA.
- Louca, L.S. and J.L. Stein, 2002. "Ideal Physical Element Representation from Reduced Bond Graphs". *Journal of Systems and Control Engineering*, Vol. 216, No. 1, pp. 73-83. Published by the Professional Engineering Publishing, ISSN 0959-6518, Suffolk, United Kingdom.
- Louca, L.S., D.G. Rideout, J.L. Stein, and G.M. Hulbert, 2004. "Generating proper dynamic models for truck mobility and handling". *International Journal of Heavy Vehicle Systems (Special Issue on Advances in Ground Vehicle Simulation)*, Vol. 11, No. 3/4 pp. 209-236. Published by Inderscience Enterprises Ltd., ISSN 1744-232X, St. Helier, United Kingdom.
- Louca, L.S. and J.L. Stein, 2009. "Energy-Based Model Reduction of Linear Systems". *Proceedings of the 6th International Symposium on Mathematical Modeling*, Vienna, Austria. Published in the series ARGESIM-Reports no. 35, ISBN 978-3-901608-35-3, Vienna, Austria.
- Louca, L.S., J.L. Stein, and G.M. Hulbert, 2010. "Energy-Based Model Reduction Methodology for Automated Modeling". *Journal of Dynamic Systems Measurement and Control*, Vol. 132, No. 6, 061202 (16 pages). Published by the American Society of Mechanical Engineers, ISSN Print 0022-0434, ISSN Online 1528-9028, New York, NY.
- Louca, L.S., 2014. "Complexity of Distributed Parameter Bond Graph Models". *Proceedings of the 11th International Conference on Bond Graph Modeling and Simulation - ICGBM'2012*, Monterey, CA, USA. Published by the Society for Computer Simulation International, pp. 789-797, San Diego, CA.
- Louca, L.S., 2015. "Finite Segment Model Complexity of an Euler-Bernoulli Beam". *Proceedings of the 8th International Conference on Mathematical Modeling*, Vienna, Austria. Published by the International Federation of Automatic Control-IFAC, pp. 334-340.
- Karnopp, D.C., D.L. Margolis, and R.C. Rosenberg, 2006. *System Dynamics: Modeling and Simulation of Mechatronic Systems*, 4th Edition. Wiley, ISBN 978-0-471-70965-7.

- Meirovitch, L., 1967. *Analytical Methods in Vibrations*. Macmillan Publishing Inc., New York, NY
- Rideout, D.G., J.L. Stein, and L.S. Louca, 2007. "Systematic Identification of Decoupling in Dynamic System Models". *Journal of Dynamic Systems Measurement and Control*, Vol. 129, No. 4, pp. 503 – 513. Published by the American Society of Mechanical Engineers, ISSN Print 0022-0434, ISSN Online 1528-9028, New York, NY.
- Rosenberg, R.C., and D.C. Karnopp, 1983. *Introduction to Physical System Dynamics*. McGraw-Hill, ISBN 0070539057.
- Stein, J.L. and L.S. Louca, 1996. "A Template-Based Modeling Approach for System Design: Theory and Implementation." *TRANSACTIONS of the Society for Computer Simulation International*. Published by SCS, ISSN 0740-6797/96, San Diego, CA.
- van Rensburg, N.F.J. and A.J. van der Merwe, 2006. "Natural frequencies and modes of a Timoshenko beam." *Wave Motion*, 44(1), 58–69.
- Walker, D.G., J.L. Stein, and A.G. Ulsoy, 1996. An Input-Output Criterion for Linear Model Deduction. *Transactions of the ASME, Journal of Dynamic Systems, Measurement, and Control*, Vol. 122, No. 3, pp. 507-513. Published by ASME, New York, NY.
- Wilson, B.H. and J.L. Stein, 1995. "An Algorithm for Obtaining Proper Models of Distributed and Discrete Systems." *Transactions of the ASME, Journal of Dynamic Systems, Measurement, and Control*, Vol. 117, No. 4, pp. 534-540. Published by ASME, New York, NY.

AUTHOR BIOGRAPHY

Loucas S. Louca received his Diploma in Mechanical Engineering from the National Technical University of Athens, Greece, in 1992. He then moved to the University of Michigan where he received his M.S.E. in 1994 and Ph.D. in 1998, both in Mechanical Engineering. During his graduate studies at the University of Michigan he received a Fulbright scholarship (Cyprus-America Scholarship Program). He continued to work in the Mechanical Engineering department at the University of Michigan as a Research Fellow until 2000 when he joined the research faculty of the Mechanical Engineering department as an Assistant Research Scientist. He was contacting research and advising students in the area of intelligent vehicle system dynamics and control within the Automotive Research Center at the University of Michigan. He joined the faculty of the University of Cyprus in January 2004 and he is currently and Assistant Professor.

His research interests lie in the areas of system dynamics and control, bond graph theory, physical system modeling and model reduction of large scale systems, modeling of automotive systems, multi-body dynamics, computer aided modeling and simulation, and haptic interfaces and rehabilitation. He is the author of CAMBAS (Computer Aided Model Building Automation System), an automated modeling software that enables the rapid development of efficient models for linear systems and its used for the teaching of courses in modeling of dynamic systems.

He is an active member of the bond graph research community and organizes focused sessions at modeling related conferences. He is also a member of the American Society of Mechanical Engineers (ASME) and the vice-chairman of the Modeling and Identification technical panel of the Dynamic Systems and Control Division. He is also a member of the Institute of Electrical and Electronics Engineers (IEEE), Society for Modeling & Simulation International (SCS), and Society of Automotive Engineers (SAE).

APPLICATION OF AN INFINITE HORIZON MPC TO A NONLINEAR OPEN-LOOP UNSTABLE REACTOR SYSTEM

André Shigueo Yamashita^(a), Bruno Faccini Santoro^(a), Márcio André Fernandes Martins^(b), Darci Odloak^(a)

^(a) Department of Chemical Engineering, Universidade de São Paulo, Av. Prof. Luciano Gualberto, trv 3 380, 05424-970
São Paulo (SP), Brazil.

Phone number: +551130912261,

^(b) Department of Chemical Engineering, Universidade Federal da Bahia, Rua Aristides Novis, nº 2, 40210630, Salvador
(BA), Brazil

Phone number: +557132839811

^(a){andre.yamashita, faccini, odloak}@usp.br
^(d)marciomartins@ufba.br

ABSTRACT

A state space model for integrating and open-loop unstable systems is presented. The novel representation decomposes stable, unstable and integrating modes of the system, which in turn leads to the development of an infinite horizon MPC (IHMPC) for unstable systems. Equality constraints enforce that the system states corresponding to the integrating and unstable dynamics are zeroed whenever it is feasible. In this work, the control of a nonlinear CSTR with cooling jacket undergoing an exothermic irreversible reaction at an unstable steady state has been studied. The simulated results showed that the proposed IHMPC is capable of sustaining the system at its unstable steady state, rejecting unmeasured input disturbances and driving the system to a different steady state.

Keywords: model predictive control; nonlinear control.

1. INTRODUCTION

Model Predictive Control (MPC) is widely used in the chemical and petrochemical industries and is arguably the most advanced process control strategy to date (Garcia, Prett, & Morari, 1989). Its most interesting features are the capability to account for input, control moves and output constraints directly into the control problem, and its straightforward application to Multiple-Input and Multiple-Output (MIMO) systems. Although MPC applications to open-loop stable systems are far more common in the literature, some processes and configurations give rise to open-loop unstable systems. For instance, linearized models identified around nominal operating points of processes with recycle, mass and heat integration networks and reactions systems, such as Continuous Stirred Tank Reactors (CSTR) or batch reactors in which exothermic

reactions are taking place, CSTR operating in cascade fashion, polymerization reactors, and so on. In particular, it might be sought to operate a reactor system at its unstable point for economic reasons (Gobin, Zullo, & Calvet, 1994; Özkan & Çamurdan, 1998). In this fashion, some effort has been put on the development of control strategies for open-loop unstable systems.

Several attempts to control open-loop unstable systems have been reported in the literature. The first attempts to control such systems were done employing classic PI or PID controllers, and even though these strategies are easy to implement and yield satisfactory results for stable systems, poor performance lead to the development of alternative control strategies. (Lee, Lee, & Park, 2000). Liu, Zhang, & Gu (2005) identified the two major limitations of PID control of open-loop unstable systems as excessive overshoot and large settling time in setpoint tracking scenarios. The authors developed a two degrees of freedom (2DF) control approach, comprised of three control blocks: the first one is a proportional-only controller that stabilizes the unstable system, and the second and third blocks decouple setpoint tracking and load disturbances effects on control performance. Robust stability is demonstrated via the Small-Gain Theorem for multiplicative model uncertainty, and simulation results showed that the proposed technique performs better than classic PID control regarding both overshoot and settling time problems. Huang & Chen (1997) put forward a formal demonstration of the PID limitations on open-loop unstable set-point tracking and disturbance rejection performance observed in Liu et al. (2005), and developed a 2DF control framework capable of suppressing overshoot for both first and second order unstable processes.

It was proposed by Rotstein & Lewin (1992) an adaptive tuning algorithm for PID controllers, which takes advantage of a real-time pole placement algorithm to select the most appropriate PID controller structure. A case study depicting the control of an exothermic reaction in a batch reactor showed that, counterintuitively, the adaptive PID strategy is not always better than the classic PID approach. The proposed control strategies for open-loop unstable systems up to here are mostly limited for applications in SISO systems.

Gobin et al. (1994) controlled a styrene polymerization reaction in a two-CSTR cascade system with a Dynamic Matrix Control (DMC) algorithm. The step response coefficients were obtained from a linearized model identified at a stable operating point, and the authors reported that their approach is faster than classic PID controllers in setpoint tracking scenarios. However, it is known that such process is highly non-linear, and the reported DMC approach is limited to a restricted operating region.

Hidalgo & Brosilow (1990) developed a coordinated MPC framework, in which the control actions, for each input, are independently calculated. The control framework was applied to a free radical solution polymerization of styrene in a CSTR. The authors stated that safe control of unstable processes is only feasible when there are sufficient degrees of freedom to keep the process within a small region about the desired operating point, therefore, MIMO layouts are essential. A simulation example showed that the proposed strategy stabilized the CSTR at its unstable operating point.

A cascade control structure for open-loop unstable processes was proposed in Özkan & Çamurdan, (1998). First, a proportional-only controller stabilizes the system, then, a linearized model is identified at the stabilized operating condition, and its step response coefficients are used to design a DMC. The authors verified that once the unstable system is stabilized, the resulting control problem is trivial, and real time calculation of the DMC model, at each time step, does not improve control performance.

Demircan, Camurdan, & Postlethwaite (1999) developed a DMC based on a fuzzy relational model for open-loop unstable systems. The advantages over the classic step response coefficients model are: it is an alternative for costly and knowledge demanding first-principle model; and it represents the process accurately over a large operating range, even though the model is identified from data obtained in a limited range. The results showed that such model works well for processes with unusual dynamic behavior. The control strategies listed previously were based, to some extent, on the DMC control strategy, and alternatives to mitigate the limitations of modeling an unstable process as an input-output step response.

Muske & Rawlings (1993) developed a nominally stabilizing MPC based on a state-space model for open-loop stable and unstable systems. Equality constraints

were enforced upon the states that represent the unstable dynamics of the systems, to guarantee that such states are zeroed after the control horizon. It was shown that in case of incomplete state measurement, a stable observer and a constrained regulator guarantee a nominally stabilizing controller.

The control approach for open-loop unstable and integrating systems proposed here is based on an extension of the state-space model presented in Santoro & Odloak (2012). The redefinition of system states to accommodate the unstable dynamics is shown in Section 3, and the IHMPC for integrating and open-loop unstable systems is proposed in Section 4. It is presented a case study to illustrate the proposed approach, and for this end an exothermic irreversible reaction in a nonlinear CSTR with cooling jacket system is analyzed. Results and discussions are given in Section 5. Finally, conclusions and suggestions for future works are presented in Section 6.

2. STATE SPACE MODEL REPRESENTATION FOR OPEN-LOOP UNSTABLE PROCESSES

The state-space model for unstable systems proposed here is an extension of the state-space model for integrating and time delayed systems developed in Santoro & Odloak (2012). The original work arranges the system model matrices, separate three types of states: those related to the stable modes, the original integrating modes and finally the integrating states derived from the velocity representation. The extension of the proposed formulation includes the unstable states as well.

Considering a system with ny outputs and nu inputs, the transfer function relating input u_j and output y_i is

$$G_{i,j}(s) = \frac{(b_{i,j,0} + b_{i,j,1}s + \dots + b_{i,j,nb}s^{nb})}{s(s - r_{i,j,1}) \dots (s - r_{i,j,na'}) (s - r_{i,j,1}^{um}) \dots (s - r_{i,j,mun}^{um})} \quad (1)$$

where $\{na', nb, nun \in N \mid nb < na' + nun\}$, na' is the number of stable poles and nun is the number of unstable poles, and $r_{i,j,1}, \dots, r_{i,j,na'}$ are the distinct stable poles and $r_{i,j,1}^{um}, \dots, r_{i,j,mun}^{um}$ are the distinct unstable poles of the system. Then, for a sampling period Δt , the corresponding step response at time step k can be computed by the expression:

$$S_{i,j}(k) = \left(\begin{array}{l} d_{i,j}^0 + d_{i,j,1}^d e^{r_{i,j,1}k\Delta t} + \dots + d_{i,j,na'}^d e^{r_{i,j,na'}k\Delta t} \\ + d_{i,j,1}^{dum} e^{r_{i,j,1}^{um}k\Delta t} + \dots + d_{i,j,mun}^{dum} e^{r_{i,j,mun}^{um}k\Delta t} + d_{i,j}^i k\Delta t \end{array} \right) \quad (2)$$

in which the coefficients $d_{i,j}^0, d_{i,j,1}^d, \dots, d_{i,j,na'}^d, d_{i,j,1}^{dum}, \dots, d_{i,j,mun}^{dum}$ and $d_{i,j}^i$ are obtained from the partial fractions expansion of the transfer function $G_{i,j}(s)$. Then, the following state-space model is defined:

$$\begin{aligned} x(k+1) &= Ax(k) + B\Delta u(k) \\ y(k) &= Cx(k) \end{aligned} \quad (3)$$

$$\begin{aligned} x(k) &= \begin{bmatrix} x^s(k)^T & x^d(k)^T & x^{nm}(k)^T & x^i(k)^T \end{bmatrix}^T, \\ x &\in \mathbb{C}^{nx}, x^s \in \mathbb{R}^{ny}, x^d \in \mathbb{C}^{nd}, x^i \in \mathbb{R}^{ny}, x^{nm} \in \mathbb{C}^{nm}, y \in \mathbb{R}^{ny} \\ , \quad nx &= 2ny + nd + nm, \quad nd = ny.nu.na', \quad \text{and} \end{aligned}$$

$$A = \begin{bmatrix} I_{ny} & 0_{ny \times nd} & 0_{ny \times nm} & \Delta t I_{ny} \\ 0_{nd \times ny} & F & 0_{nd \times nm} & 0_{nd \times ny} \\ 0_{nm \times ny} & 0_{nm \times nd} & F_{nm} & 0_{nm \times ny} \\ 0_{ny} & 0_{ny \times nd} & 0_{ny \times nm} & I_{ny} \end{bmatrix}, \quad A \in \mathbb{C}^{nx \times nx},$$

$$B = \begin{bmatrix} B^s \\ B^d \\ B^{nm} \\ B^i \end{bmatrix}, \quad B \in \mathbb{C}^{nx \times nu}$$

$$C = \begin{bmatrix} I_{ny} & \Psi & \Psi_{nm} & 0_{ny \times nu} \end{bmatrix}, \quad C \in \mathbb{R}^{ny \times nx},$$

$$B^s = D^0 + \Delta t B^i, \quad B^d = D^d F N, \quad B^{nm} = D^{nm} F_{nm}$$

$$B^i = \begin{bmatrix} d_{1,1}^i & \cdots & d_{1,ny}^i \\ \vdots & \ddots & \vdots \\ d_{ny,1}^i & \cdots & d_{ny,ny}^i \end{bmatrix}, \quad B^i \in \mathbb{R}^{ny \times nu},$$

$$D^0 = \begin{bmatrix} d_{1,1}^0 & \cdots & d_{1,nu}^0 \\ \vdots & \ddots & \vdots \\ d_{ny,1}^0 & \cdots & d_{ny,nu}^0 \end{bmatrix}, \quad D^0 \in \mathbb{R}^{ny \times nu}$$

$$F = \text{diag} \left(e^{\Delta t \cdot r_{1,1,1}} \cdots e^{\Delta t \cdot r_{1,1,na'}} \cdots e^{\Delta t \cdot r_{1,nu,1}} \cdots e^{\Delta t \cdot r_{1,nu,na'}} \right)$$

$$F \in \mathbb{C}^{nd \times nd}$$

$$F^{nm} = \text{diag} \left(e^{\Delta t \cdot r_{1,1}^{nm}} \cdots e^{\Delta t \cdot r_{1,nu}^{nm}} \cdots e^{\Delta t \cdot r_{1,nu,1}^{nm}} \cdots e^{\Delta t \cdot r_{1,nu,nu}^{nm}} \right)$$

$$F^{nm} \in \mathbb{C}^{nm \times nm}$$

$$D^d = \text{diag} \left(d_{1,1,1}^d \cdots d_{1,1,na}^d \cdots d_{1,nu,1}^d \cdots d_{1,nu,na}^d \cdots \right),$$

$$D^d \in \mathbb{C}^{nd \times nd}$$

$$D^{dm} = \text{diag} \left(d_{1,1,1}^{dm} \cdots d_{1,1,nu}^{dm} \cdots d_{1,nu,1}^{dm} \cdots d_{1,nu,nu}^{dm} \cdots \right)$$

$$D^{dm} \in \mathbb{C}^{nm \times nm}, \quad N = \begin{bmatrix} J \\ J \\ \vdots \\ J \end{bmatrix} \left. \vphantom{\begin{bmatrix} J \\ J \\ \vdots \\ J \end{bmatrix}} \right\} ny, \quad N \in \mathbb{R}^{nd \times nu},$$

$$J = \begin{bmatrix} \begin{matrix} 1 & 0 & \cdots & 0 \\ na & \vdots & \ddots & \vdots \\ 1 & 0 & \cdots & 0 \end{matrix} \\ \begin{matrix} 0 & 1 & \cdots & 0 \\ \vdots & \vdots & \ddots & 0 \\ 0 & 1 & \cdots & 0 \end{matrix} \\ \vdots \\ \begin{matrix} 0 & 0 & \cdots & 1 \\ na & \vdots & \ddots & \vdots \\ 0 & 0 & \cdots & 1 \end{matrix} \end{bmatrix}, \quad J \in \mathbb{R}^{nu.na \times nu}$$

$$\Psi = \begin{bmatrix} \overbrace{1 \ 1 \ \cdots \ 1}^{nu.na} & \cdots & \overbrace{0 \ 0 \ \cdots \ 0}^{nu.na} \\ 0 \ 0 \ \cdots \ 0 & \cdots & 0 \ 0 \ \cdots \ 0 \\ \vdots & \ddots & \vdots \\ 0 \ 0 \ \cdots \ 0 & \cdots & 1 \ 1 \ \cdots \ 1 \end{bmatrix}, \quad \Psi \in \mathbb{R}^{ny \times nd},$$

$$\Psi_{nm} = \begin{bmatrix} \overbrace{1 \ 1 \ \cdots \ 1}^{nm} & \cdots & \overbrace{0 \ 0 \ \cdots \ 0}^{nm} \\ 0 \ 0 \ \cdots \ 0 & \cdots & 0 \ 0 \ \cdots \ 0 \\ \vdots & \ddots & \vdots \\ 0 \ 0 \ \cdots \ 0 & \cdots & 1 \ 1 \ \cdots \ 1 \end{bmatrix},$$

$$\Psi_{nm} \in \mathbb{R}^{ny \times nm}.$$

I_n and 0_n are the identity and null matrices of dimension n , respectively. The reader is referred to the original formulation (Santoro & Odloak, 2012) for detailed explanation about the integrating states.

3. INFINITE HORIZON MPC FOR OPEN-LOOP UNSTABLE PROCESSES

The equations below define the IHMPC proposed here.

Problem 1

$$\min_{\Delta u(k+j|k), \delta_{y,k}, \delta_{i,k}, \delta_{um,k}} V_{1,k}$$

$$\begin{aligned} V_{1,k} &= \sum_{j=1}^{\infty} \|y(k+j|k) - y^{sp} - \delta_{y,k} - (j-m)\Delta t \delta_{i,k}\|_{Q_y}^2 \\ &\quad + \sum_{j=0}^{m-1} \|\Delta u(k+j|k)\|_R^2 + \|\delta_{y,k}\|_{S_y}^2 + \|\delta_{i,k}\|_{S_i}^2 + \|\delta_{um,k}\|_{S_{um}}^2 \end{aligned} \quad (4)$$

subject to (3) and

$$x^s(k+m|k) - y_{sp,k} - \delta_{y,k} = 0 \quad (5)$$

$$x_0^j(k+m|k) - \delta_{i,k} = 0 \quad (6)$$

$$x^{um}(k+m) - \delta_{um,k} = 0 \quad (7)$$

$$\Delta u(k+j|k) \in U, j=0,1,\dots,m-1$$

$$U = \left\{ \begin{array}{l} -\Delta u_{\max} \leq \Delta u(k+j|k) \leq \Delta u_{\max} \\ \Delta u(k+j|k) = 0, j \geq m \\ u_{\min} \leq u(k-1) + \sum_{i=0}^j \Delta u(k+i|k) \leq u_{\max} \end{array} \right\} \quad (8)$$

where $Q_y \in \mathbb{R}^{m_y \times m_y}$, $Q_u \in \mathbb{R}^{m_u \times m_u}$ and $R \in \mathbb{R}^{m_u \times m_u}$ are positive semidefinite matrices; $y(k+j|k)$ is the output prediction at time step $k+j$ computed at time step k including the effects of the future control actions; $y_{sp,k}$ is the output reference; $\Delta u(k+j|k)$ is the input move ($\Delta u(k+j)=0, j>m$). Moreover, $\delta_{y,k} \in \mathbb{R}^{m_y}$, $\delta_{u,k} \in \mathbb{R}^{m_u}$, $\delta_{i,k} \in \mathbb{R}^{m_y}$, and $\delta_{um,k} \in \mathbb{R}^{m_{um}}$ are the slack variables that are introduced in the control problem in order to render the control problem always feasible, while $S_y \in \mathbb{R}^{m_y \times m_y}$, $S_u \in \mathbb{R}^{m_u \times m_u}$, $S_i \in \mathbb{R}^{m_y \times m_y}$, and $S_{um} \in \mathbb{R}^{m_{um} \times m_{um}}$ are positive definite weighting matrices associated with these slacks.

The constraint defined in (7) tries to enforce that the unstable states will be zeroed at time step $k+m$. A suitable selection of the weighting matrix S_{um} makes the control problem converge in practical situations. However, a formal nominal stability demonstration is not provided here and is a subject for future works.

4. CONTROL OF A NON-LINEAR CSTR AT ITS UNSTABLE OPERATING POINT

It is studied the control of a CSTR with cooling jacket where an elementary irreversible reaction takes place ($A \rightarrow B$). It is assumed that the physical properties and heat transfer coefficient are constant; therefore the first-principles model that represents the true plant is given by the following set of nonlinear equations (Henson & Seborg, 1997):

$$\begin{aligned} \frac{dh(t)}{dt} &= \frac{F_m(t) - F_{out}(t)}{\pi r^2} \\ \frac{dc_A(t)}{dt} &= \frac{[c_{A,m} - c_A(t)]F_m(t)}{\pi r^2 h(t)} - k_0 \exp\left[-\frac{E}{RT(t)}\right] c_A(t) \\ \frac{dT(t)}{dt} &= \frac{[T_m - T(t)]F_m(t)}{\pi r^2 h(t)} + \frac{-\Delta H}{\rho C_p} k_0 \exp\left[-\frac{E}{RT(t)}\right] c_A(t) + \frac{2U}{\rho r C_p} [T_c(t) - T(t)] \end{aligned} \quad (9)$$

The parameters associated with this system are given in Table 1. In the 3x3 control structure considered here, the controlled outputs are the liquid level in the reactor y_1 [h (m)], the reactant concentration y_2 [c_A (kmol/m³)] and the reaction temperature y_3 [T (K)]. The manipulated inputs are the inlet flow rate u_1 [F_{in}

(m³/min)], the outlet flow rate u_2 [F_{out} (m³/min)] and the cooling fluid temperature u_3 [T_c (K)].

Table 1: Nominal parameters of the CSTR system.

Description	Values
$c_{A,in}$ (reactant concentration in feed stream)	1.0 kmol·m ⁻³
T_{in} (temperature in feed stream)	350 K
r (radius of the reactor)	0.47 m
k_0 (pre-exponential factor)	6×10 ¹⁰ min ⁻¹
E/R (activation energy/universal gas constant)	8,890 K
U (overall heat transfer coefficient)	315.6 W·m ⁻² ·K ⁻¹
ρ (density of the reaction mixture)	7×10 ² kg·m ⁻³
C_p (heat capacity of the reaction mixture)	220 J·kg ⁻¹ ·K ⁻¹
ΔH (enthalpy of reaction)	-2×10 ⁷ J·kmol ⁻¹

An unstable steady state was identified solving (9) when the left hand side equals zero and the process parameters are taken from Table 1. Model equations may be linearized around this unstable steady state, resulting in the transfer function model (10).

$$G(s) = \begin{bmatrix} \frac{1.44}{s} & \frac{-1.44}{s} & 0 \\ \frac{0.44s^2 - 1.45s + 1.17}{s^3 + 0.17s^2 - 1.55s} & \frac{0.64s - 1.17}{s^3 + 0.17s^2 - 1.55s} & \frac{-0.02}{s^2 + 0.17s - 1.55} \\ \frac{-0.6s^2 + 32.13s - 46.19}{s^3 + 0.17s^2 - 1.55s} & \frac{-0.08s + 46.19}{s^3 + 0.17s^2 - 1.55s} & \frac{0.52s + 1.05}{s^2 + 0.17s - 1.55} \end{bmatrix} \quad (10)$$

The control problem defined in Problem 1 was solved in GAMS®23.6. The plant was simulated using the *ode45* algorithm in MATLAB®2010a. It was assumed that the model states are corrected by a steady-state Kalman filter, based on the deviation between the output values calculated by the state-space model (3) and the values calculated by the first-principle model (9). The IHMPC and Kalman filter tuning parameters employed in the case study are listed in Table 2.

The scenario analyzed here investigates if the IHMPC based on the proposed state-space model can keep the CSTR process at its unstable operating point. In this fashion, a simulation in which the system starts from $y_0=[0.91 \ 0.82 \ 349.54]^T$ and $u_0=[0.91 \ 0.91 \ 250]^T$ and it is driven towards the unstable steady state defined by the output values $y^{sp}=[0.91 \ 0.72 \ 350.03]^T$ is proposed. Once the system is stabilized, unmeasured impulse disturbances with intensity 5K and 0.25 m³/min affect inputs u_3 and u_2 at time instants 25min and 40min, respectively. Finally, the system is subject to a new setpoint, different from the unstable steady state: $y^{sp}_2=[0.91 \ 0.72 \ 345.03]^T$. The input upper and lower bounds and control moves maximum values are $u_{min}=[0.01 \ 0.01 \ 200]^T$, $u_{max}=[2 \ 2 \ 415]^T$, and $\Delta u_{max}=[0.065 \ 0.065 \ 15]^T$ respectively. All the variable values defined here follow the units previously defined.

Table 2: IHMPC and Kalman filter tuning parameters.

Parameter	Value
IHMPC	
Q_y	$\text{diag}([10^2 \ 5 \times 10^6 \ 10^4])$
Q_i	$\text{diag}([10^2 \ 5 \times 10^6 \ 10^4])$
S_y	$\text{diag}([10^6 \ 10^8 \ 10^4])$
S_i	$\text{diag}([10 \ 10 \ 1])$
S_{um}	$\text{diag}([10^4 \ 10^4 \ 10^4])$
R	$\text{diag}([10^{-2} \ 10^{-2} \ 10^3])$
m	7
Δt	0.1 min
Kalman Filter	
Process noise covariance matrix	$10^3 \times I_{n_x}$
Measurement noise covariance matrix	$\text{diag}([10^{-4} \ 10^{-4} \ 10^{-9}])$

Figures 1 to 4 depict the output and input responses of the system, the control cost function value, and the absolute value of the maximum component of the vector δ_{um} as a function of the simulation time, respectively. It is observed that the IHMPC stabilizes the nonlinear CSTR at its unstable operating point in less than 20 minutes. The behavior of the cost function value and the absolute value of the maximum unstable slack variable indicate that the contribution of the setpoint deviation of y_3 affects the cost function the most. In fact, its weight in the cost function ($q_{y,3}$) and its respective δ_y weight were chosen as large values because this variable can easily lead to instability. It is also observed that the impact of the feed flowrate and cooling jacket disturbances are similar on y_1 , whereas the impact of the cooling jacket temperature disturbance is larger on y_2 and y_3 . Figure 2 shows that the feed flowrate disturbance is rejected in about 5 minutes, whereas the cooling jacket temperature disturbance rejection takes twice as long. The dot-dashed curves in Figure 1 depict the system outputs related to the estimated states. The largest deviations from the plant values, shown as continuous lines are observed for variable y_1 , especially regarding the oscillatory behavior amplitude, and in y_2 , from time instants 40 min to 45 min. It indicates that the tuning parameters of the Kalman filter were well chosen, and that the linearized model was capable to accurately represent the estimated states of the plant within the operating region. Finally, it is observed that the control cost function is not a monotonically decreasing function, nonetheless, in the present simulation the unstable slacks are zeroed and the control cost converges to zero. The setpoint change at 50 min drives the system further from the region in which the linearized model represents the nonlinear system well. Nonetheless, it is observed that the amplitude of the initial peak at 50 min, in Figures 3 and 4 decreases to a constant value within two minutes, and, from that time until the end of the simulation, all the system inputs and outputs oscillate. The trend observed in Figure 4, which depicts the absolute maximum value of the unstable slacks vector, is similar to the one in Figure 3. It indicates that there is a heavy contribution of the unstable slacks to the control cost function. Moreover, it

is noted from time instants 25 to 30, 40 to 45 and 55 until the end of the simulation that the cost function of the controller proposed here is not a Lyapunov function, therefore asymptotic stability of the closed-loop is not demonstrated here.

The sampling time interval $\Delta t=0.1$ min was necessary to adequately deal with the mismatch between the nonlinear plant and the linearized model is the simulation considered here. Nonetheless, since it is merely a QP, it is reasonable to assume that Problem 1 is solvable in less than 6 seconds, and the optimum control actions are readily available.

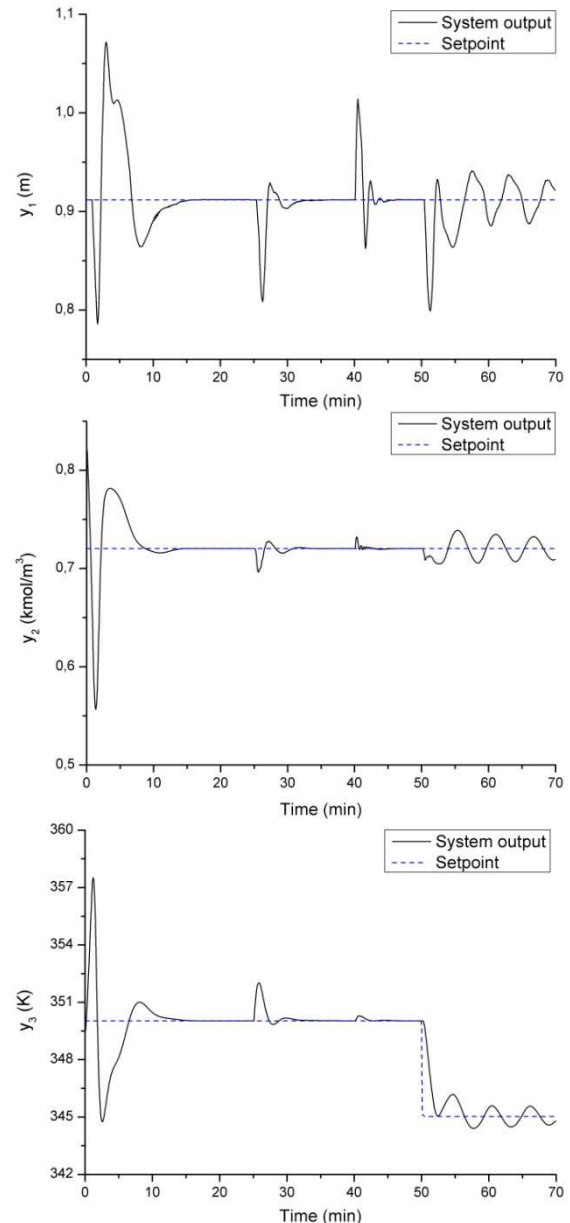


Figure 1: Simulated output responses.

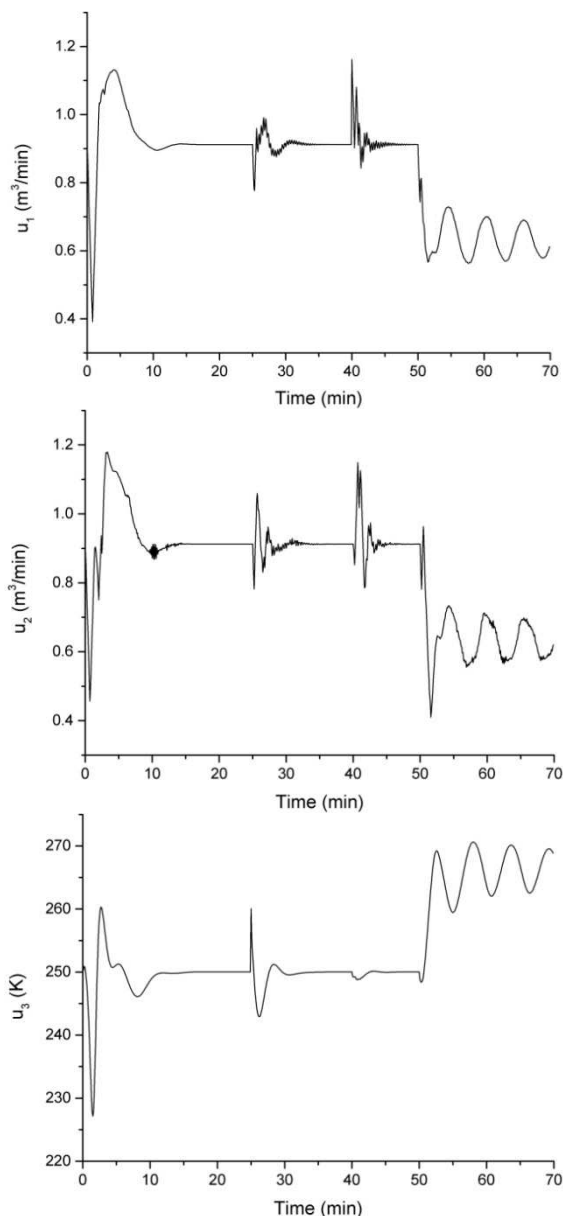


Figure 2: Simulated input responses.

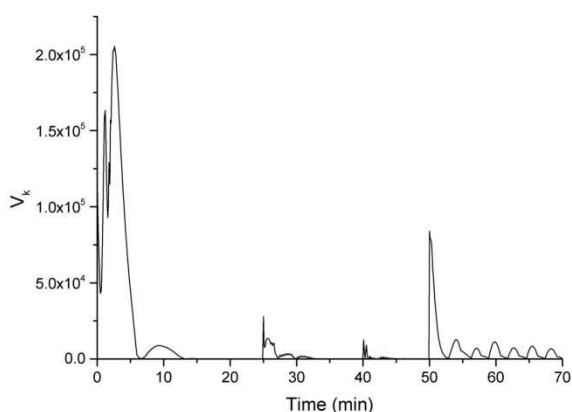


Figure 3: Control cost function.

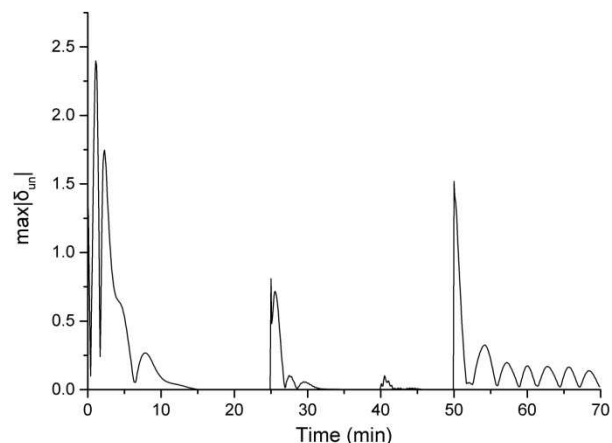


Figure 4: Maximum absolute entry of the vector of unstable slack variables, δ_{un} .

5. CONCLUSIONS

A state-space model based on the analytical step-response of the system was used to formulate an IHMPC for stable, integrating and unstable systems. The latter may arise from operating processes at unstable regions for optimum profit, for example. It is shown in a simulated case study that the proposed framework is successfully capable of controlling an exothermal irreversible reaction in a nonlinear CSTR with cooling jacket at its unstable steady state. Moreover, input disturbance rejection capabilities were observed. However, oscillatory behavior was present when the process was operating far from the region in which the linear model of the IHMPC was identified.

The work presented here does not provide formal stability guarantees, although the simulation shows that an appropriate selection of the IHMPC and Kalman filter tuning parameters can stabilize the closed-loop system as long as no constraints are violated. A formal stability demonstration, and the extension of the algorithm to account for multi-plant uncertainty are intended topics for future works.

ACKNOWLEDGMENTS

The authors would like to acknowledge the financial support by FUNDESPA and CNPq under grants 140677/2011-9 and 141418/2011-7.

REFERENCES

- Demircan, M., Camurdan, M. C., & Postlethwaite, B. (1999). On-line learning fuzzy relational model based dynamic matrix control of an openloop unstable process, 77(July).
- Gobin, F., Zullo, L. C., & Calvet, J. P. (1994). Model predictive control of an open-loop unstable train of polymerization reactors. Computers and Chemical Engineering, 18, S525–S528.
- Henson, M.A., Seborg, D.E., (1997). Nonlinear process control. Prentice-Hall, Upper Saddle River, NJ, USA.
- Hidalgo, P. M., & Brosilow, C. B. (1990). NONLINEAR MODEL PREDICTIVE CONTROL OF STYRENE POLYMERIZATION AT UNSTABLE

OPERATING POINTS. *Computers Chem. Engng*, 14(4), 481–494.

Huang, H.-P., & Chen, C.-C. (1997). Control-system synthesis for open-loop unstable process with time delay. *IEE Proceedings - Control Theory and Applications*, 144(4), 334.

Lee, Y., Lee, J., & Park, S. (2000). PID controller tuning for integrating and unstable processes with time delay. *Chemical Engineering Science*, 55, 3481–3493.

Liu, T., Zhang, W., & Gu, D. (2005). Analytical design of two-degree-of-freedom control scheme for open-loop unstable processes with time delay. *Journal of Process Control*, 15, 559–572.

Muske, K. R., & Rawlings, J. B. (1993). Linear model predictive control of unstable processes. *Journal of Process Control*, 3(2), 85–96.

Özkan, L., & Çamurdan, M. (1998). Model predictive control of a nonlinear unstable process. *Computers & chemical engineering*, 22(1989).

Rotstein, G. E., & Lewin, D. R. (1992). Control of an unstable batch chemical reactor. *Computers and Chemical Engineering*, 16(1), 27–49.

Santoro, B. F., & Odloak, D. (2012). Closed-loop stable model predictive control of integrating systems with dead time. *Journal of Process Control*, 22(7), 1209–1218.

AUTHORS BIOGRAPHY

André Shiguelo Yamashita is currently a postdoctoral fellow at the Department of Chemical Engineering of the Polytechnic School of the University of São Paulo. He earned a Ph.D. from the University of São Paulo in 2015. His research interests include model predictive control, model predictive control tuning, and robust control.

Bruno Faccini Santoro is currently a postdoctoral fellow at the Department of Chemical Engineering of West Virginia University. He received a M. Sc. (2011) and Ph. D. (2015) in Chemical Engineering from the University of Sao Paulo, Brazil. His current research interests include model predictive control, stochastic process and state estimation.

Márcio André Fernandes Martins holds a position as an Assistant Professor within the Department of Chemical Engineering at the Federal University of Bahia (UFBA). He received the M.Sc. in Industrial Engineering from UFBA (2010) and the Ph.D. in Chemical Engineering from the University of São Paulo (2014). His research interests include tuning methods for model predictive control, robust integration of model predictive control and real time optimization, Bayesian statistical inference.

Darci Odloak is a Professor at the Department of Chemical Engineering of the Polytechnic School of the University of São Paulo. He received a M.Sc. from the University of Rio de Janeiro (COPPE) in 1977 and a Ph.D. from the University of Leeds-UK in 1980. He worked for Petrobras from 1973 to 1990 as a process engineer and from 1991 to 1996 as the head of the Advanced Control Group that developed and

implemented an in-house advanced control package in the main oil refineries of Brazil. His present research interest are robust model predictive control, fault-tolerant control and integration of control and real time optimization.

FAULT ACCOMMODATION BY INVERSE SIMULATION THROUGH SOLVING A DIFFERENTIAL ALGEBRAIC SYSTEM OBTAINED FROM A BOND GRAPH

W. Borutzky

Department of Computer Science

Bonn-Rhein-Sieg University of Applied Sciences, St. Augustin Germany

ABSTRACT

When an abrupt parametric fault occurs in a system, active fault tolerant control (FTC) aims at reconstructing the system input after the fault has been isolated and estimated so that the fault is compensated and the system output follows a desired trajectory despite the fault.

Input reconstruction by *inverse simulation* is a quite general approach to active FTC which can be supported by existing sophisticated simulation software for the solution of DAE systems. Desired outputs are obtained by computing a forward model of the healthy system. Values of the reconstructed input into the faulty systems needed at the next time instant are obtained by computing the DAE system of the inverse model *simultaneously*.

The proposed approach assumes a single fault hypothesis and is illustrated by application to averaged models of simple examples of power electronic systems. Differentiation of the inverse model equations with respect to time results in a semi-explicit ordinary differential equation (ODE) system.

Keywords: Active fault tolerant control, fault isolation and estimation, fault accommodation, input reconstruction, inverse simulation, power electronic systems, averaged bond graph models.

1. INTRODUCTION

The increasing equipment of mechatronic systems with communicating smart sensors, actuators, embedded digital circuitry and software renders them into what is sometimes called intelligent systems and enables them to operate autonomously to some extent. This includes to detect and isolate faults and to recover from faults by accommodating them autonomously. Approaches to fault detection and isolation (FDI) can be roughly categorised into data-driven and model-based methods Borutzky (2015). Among the latter ones are techniques based on bond graphs that derive analytical redundancy relations (ARRs) from a bond graph (BG) and check their residuals against thresholds Djeziri et al. (2007); Samantaray and Ould Bouamama (2008); Y. Touati et al. (2012); Wang et al. (2013); Borutzky (2015). As to fault tolerant con-

trol (FTC), passive and active techniques are known. Passive approaches use a controller with a fixed control law that ensures stability and the control objectives in the presence of faults of a certain class of anticipated faults. In an active approach, the control law is changed without changing the controlled system after a fault has been detected and isolated so that an acceptable system performance in the presence of a persisting fault can be maintained. Changing the control law and the system is often termed reconfiguration. An elaborated presentation of fault tolerant control may be found in Blanke et al. (2006). A bibliographical review on reconfigurable fault-tolerant control systems is given in Y. Zhang and J. Jiang (2008). Bond graph model-based approaches to passive as well as to active FTC have been presented in Nacusse, M. and Junco, S.J. (2011); Samantaray and Ould Bouamama (2008); Loureiro, R. (2012); Allous, M. and Zanzouri, N. (2014). In active FTC, changing the controller law after a fault has occurred requires system inversion, i.e. to find an input so that the faulty system produces a desired output. One way to decide whether a model is invertible and to determine an input required to produce a desired output is to assign bicausalities to a BG Gawthrop (1995); Ngwompo et al. (2001a,b); Loureiro, R. (2012).

In this paper, input reconstruction is based on the solution of the DAE system of a forward model of the healthy system deduced from a BG and considered as a system for the required input into the faulty system. This way, existing sophisticated software for the solution of DAEs such as OpenModelica OpenModelica Consortium (nd) can be used for nonlinear inverse simulation, though, in general, the solution of a DAE system is not guaranteed and stability issues may arise.

The paper is organised in the following manner. The next section briefly addresses the problem of isolating and estimating a fault as this step is a prerequisite for FTC. In Section the construction of an input that compensates for a fault is confined to linear time-invariant multiple input multiple output (MIMO) systems as forward models and assumes a single fault hypothesis. The output of the healthy system is considered the desired output for which an input must be reconstructed after a fault has happened. Differentiation of

the inverse model equations with respect to time results in a semi-explicit ODE system for the required input. An example demonstrates that the matrix pre-multiplying the state vector of this semi-explicit ODE system is not necessarily a matrix with constant coefficients in contrast to the forward model.

The procedure is applied to a boost converter and to a buck converter driven DC motor as two simple examples of power electronic systems. The dynamic behaviour of the healthy systems is represented by a BG model with variables averaged over the switching cycle time. In Section , a case study considers as a fault scenario the leakage of the capacitor in the buck converter driven DC motor system and the recovery from this fault. Simulation runs have been performed by means of the open source software Scilab Scilab Enterprises (nd).

2. PARAMETRIC FAULT ISOLATION AND ESTIMATION

In bond graph model-based fault detection and isolation (FDI), analytical redundancy relations (ARRs) are deduced from a diagnostic bond graph (DBG). Their evaluation gives so-called ARR residuals that are close to zero in the case of a healthy system and exceed given thresholds in the case a fault has happened. If nonlinear constitutive component equations permit to eliminate unknown variables so that ARR can be obtained in closed form, their structure is usually captured by a structural fault signature matrix (FSM). If a single fault hypothesis can be adopted, and if the fault can be mapped onto a faulty parameter, and if the parameter has a unique component fault signature, then the fault can be isolated by just inspecting the FSM.

In case two components with parameters Θ_1 and θ_2 respectively have got the same structural component fault signature in the FSM, then, given the single fault hypothesis still holds, parameter sensitivities of ARR can be used to isolate the fault Y. Touati et al. (2012).

Furthermore, multiple faults may happen simultaneously but the ARR residuals sensitive to them may not be structured, i.e. the component fault signatures are not linear independent. As a result, faults cannot be isolated by inspection of the FSM. In this case, parametric faults can be identified by comparing actual parameters obtained by parameter estimation with their nominal values (Samantaray and Ould Bouamama, 2008; Wang et al., 2013; Borutzky, 2015). However, iterative parameter estimation takes time which may be an issue in online fault diagnosis. Solving a nonlinear least squares problem by means of a gradient based algorithm may be faster than an algorithm that uses function evaluations only but convergence is not guaranteed.

Finally, even if the system itself stays healthy, sensor and actuator faults may degrade its control and thus the perfor-

mance of the closed loop system. Given a single fault hypothesis, sensor and actuator faults assumed to be additive can be easily isolated and estimated. ARR residuals can be used to determine their size. In (Y. Touati et al., 2012), bicausality assigned to a DBG is used for the estimation of isolatable faults. Alternatively, the magnitude of a, say sensor fault, can be obtained directly from the ARR established for the sensor junction.

3. INPUT RECONSTRUCTION

Assume that an abnormality in the dynamic behaviour of a multiple input, multiple output (MIMO) system is observed at time instant t_1 and that it is due to a single parametric fault. Once the fault has been isolated and its size has been estimated, it can be accommodated by designing a new input into the faulty system so that the fault is compensated and the system produces a desired output behaviour despite the fault. The required input can be determined by constructing an inverse model. There are various approaches to system inversion. The required input may be obtained by

- designing a feedback system,
- numerical solution of a DAE system,
- application of bicausality to a bond graph Gawthrop (1995); Ngwompo et al. (1996)

A review of inverse simulation methods may be found in (Murray-Smith, 2012, Chapter 4). All of them have their pros and cons.

3.1 Model inversion by numerical solution of a DAE system

In the following, an approach based on the solution of a DAE is considered. Assume that the dynamic behaviour of a healthy system may be captured by a linear time-invariant multiple input, multiple output (MIMO) forward model deduced from a BG.

$$\dot{\mathbf{x}}(t) = \mathbf{A}\mathbf{x}(t) + \mathbf{B}\mathbf{u}(t) \quad (1a)$$

$$\mathbf{y}(t) = \mathbf{C}\mathbf{x}(t) \quad (1b)$$

where $\mathbf{x}(t)$ denotes the vector of state variables, $\mathbf{u}(t)$ the input vector, and $\mathbf{y}(t)$ the output vector. The constant coefficient matrices $\mathbf{A}, \mathbf{B}, \mathbf{C}$ are of appropriate dimensions. Suppose that the single parametric fault that has occurred at t_1 is isolated and identified as of $t_2 > t_1$. Then for $t > t_2$ an input $\mathbf{u}_{\text{req}}(t)$ is required that forces the faulty system to produce the output of the healthy system as the desired output in the presence of the

fault, i.e. $\mathbf{y}_{\text{des}}(t) = \mathbf{y}(t)$. The equations of the faulty system then read

$$\dot{\tilde{\mathbf{x}}}(t) = \tilde{\mathbf{A}}\tilde{\mathbf{x}}(t) + \tilde{\mathbf{B}}\mathbf{u}_{\text{req}}(t) \quad (2a)$$

$$\mathbf{y}_{\text{des}}(t) = \tilde{\mathbf{C}}\tilde{\mathbf{x}}(t) \quad (2b)$$

where $\tilde{\mathbf{x}}(t)$ denotes the unknown state of the faulty system and $\mathbf{u}_{\text{req}}(t)$ the input to be determined. As the faulty parameter may affect the coefficients of all matrices, the latter ones are distinguished from the ones of the healthy system by a tilde.

Differentiation of the algebraic constraint (2b) with respect to time and substitution of (2a) into the result gives the DAE system

$$\begin{bmatrix} \mathbf{I} & \mathbf{0} \\ \mathbf{0} & \mathbf{0} \end{bmatrix} \begin{bmatrix} \dot{\tilde{\mathbf{x}}} \\ \dot{\mathbf{u}}_{\text{req}} \end{bmatrix} = \begin{bmatrix} \tilde{\mathbf{A}} & \tilde{\mathbf{B}} \\ \tilde{\mathbf{C}}\tilde{\mathbf{A}} & \tilde{\mathbf{C}}\tilde{\mathbf{B}} \end{bmatrix} \begin{bmatrix} \tilde{\mathbf{x}} \\ \mathbf{u}_{\text{req}} \end{bmatrix} + \begin{bmatrix} \mathbf{0} \\ -\dot{\mathbf{y}} \end{bmatrix} \quad (3)$$

where \mathbf{I} denotes the $n \times n$ identity matrix. DAE (3) is of index 1 if $(\tilde{\mathbf{C}}\tilde{\mathbf{B}})^{-1}$ exists and can be numerically computed by a BDF-based solver. The algebraic constraint in (3) can be solved for \mathbf{u}_{req} and substituted into the ODE for $\tilde{\mathbf{x}}$.

$$\dot{\tilde{\mathbf{x}}}(t) = (\tilde{\mathbf{A}} - \tilde{\mathbf{B}}(\tilde{\mathbf{C}}\tilde{\mathbf{B}})^{-1}\tilde{\mathbf{C}}\tilde{\mathbf{A}})\tilde{\mathbf{x}}(t) + \tilde{\mathbf{B}}(\tilde{\mathbf{C}}\tilde{\mathbf{B}})^{-1}\dot{\mathbf{y}}(t) \quad (4)$$

Differentiation of the algebraic constraint in (3) with respect to time results in another DAE system.

$$\begin{bmatrix} \mathbf{I} & \mathbf{0} \\ \tilde{\mathbf{C}}\tilde{\mathbf{A}} & \tilde{\mathbf{C}}\tilde{\mathbf{B}} \end{bmatrix} \begin{bmatrix} \dot{\tilde{\mathbf{x}}} \\ \dot{\mathbf{u}}_{\text{req}} \end{bmatrix} = \begin{bmatrix} \tilde{\mathbf{A}} & \tilde{\mathbf{B}} \\ \mathbf{0} & \mathbf{0} \end{bmatrix} \begin{bmatrix} \tilde{\mathbf{x}} \\ \mathbf{u}_{\text{req}} \end{bmatrix} + \begin{bmatrix} \mathbf{0} \\ \dot{\mathbf{y}} \end{bmatrix} \quad (5)$$

DAE (5) can be turned into an explicit ODE system if $(\tilde{\mathbf{C}}\tilde{\mathbf{B}})^{-1}$ exists. The input required to accommodate the fault reads

$$\mathbf{u}_{\text{req}}(t) = (\tilde{\mathbf{C}}\tilde{\mathbf{B}})^{-1}[-\tilde{\mathbf{C}}\tilde{\mathbf{A}}\tilde{\mathbf{x}}(t) + \dot{\mathbf{y}}(t)] \quad (6)$$

It may happen that some states of the faulty system can be expressed as a function of the remaining states, the input \mathbf{u}_{req} to be determined, the desired output \mathbf{y}_{des} and its time derivatives. The result is an inverse model of reduced order. This is illustrated by means of the example in the next section. See also the appendix.

3.2 Example: Buck-converter driven DC motor

Fig. 1 displays a circuit schematic of a buck-converter-driven DC motor and Fig. 2 shows a corresponding averaged forward BG model, where R_L denotes the resistance of the inductor, R_a and L_a the resistance and the inductance of the motor's armature winding, b a friction parameter and τ_{load} an external load torque. The transistor Q and the diode have been modelled as a non-ideal switch with an ON-resistance R_{on} , $m := 1 - d$, where d denotes the duty cycle of the signal $u(t)$

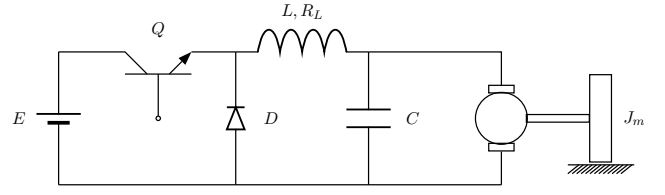


Figure 1: Schematic of a buck-converter-driven DC motor

controlling the transistor Q . The MTF and the Se source on the left side may be combined into a modulated source MSe.

From the BG in Fig. 2, the following equations of the healthy system are obtained.

$$1_1 : 0 = mE - (R_{\text{on}} + R_L)i_L - L\frac{di_L}{dt} - u_C \quad (7)$$

$$0_1 : 0 = i_L - C\frac{du_C}{dt} - i_a \quad (8)$$

$$1_2 : 0 = u_C - R_a i_a - L_a \frac{di_a}{dt} - k\omega \quad (9)$$

$$1_3 : 0 = k i_a - b\omega - J_m \frac{d\omega}{dt} - \tau_{\text{load}} \quad (10)$$

$$y = \omega \quad (11)$$

Let the identified parametric fault be the resistance of the motor inductance, $\tilde{R}_a := R_a + \Delta R_a$, and let $\tau_{\text{load}} = 0$ for simplicity. If the load torque is different from zero it must be measured or estimated. Accordingly, a load torque estimator would be required in a practical implementation. Furthermore, let $y_{\text{des}} = \omega_{\text{des}} = y = \omega$, $u := mE$, $u_{\text{req}} = \tilde{m}E = (1 - \tilde{d}(t))E$, $\tilde{x}_1 := \tilde{i}_L$, $\tilde{x}_2 := \tilde{u}_C$, $\tilde{x}_3 := \tilde{i}_a$, $\tilde{x}_4 := \tilde{\omega} = \omega$ and $R := R_{\text{on}} + R_L$. Then the DAE system determining u_{req} reads

$$0 = u_{\text{req}} - R\tilde{x}_1 - L\dot{\tilde{x}}_1 - \tilde{x}_2 \quad (12)$$

$$0 = \tilde{x}_1 - C\dot{\tilde{x}}_2 - \tilde{x}_3 \quad (13)$$

$$0 = \tilde{x}_2 - \tilde{R}_a\tilde{x}_3 - L_a\dot{\tilde{x}}_3 - k\tilde{x}_4 \quad (14)$$

$$0 = k\tilde{x}_3 - b\tilde{x}_4 - J_m\dot{\tilde{x}}_4 \quad (15)$$

$$y = \tilde{x}_4 \quad (16)$$

Substituting (16) into (15) gives

$$k\tilde{x}_3 = by + J_m\dot{y} \quad (17)$$

Comparison with (10) yields $\tilde{x}_3 = x_3$. Accordingly,

$$\begin{aligned} \tilde{x}_2 &= \tilde{R}_a x_3 + L_a \dot{x}_3 + ky \\ &= (R_a + \Delta R_a)x_3 + L_a \dot{x}_3 + ky \\ &= R_a x_3 + L_a \dot{x}_3 + ky + (\Delta R_a)x_3 \\ &= x_2 + (\Delta R_a)x_3 \end{aligned} \quad (18)$$

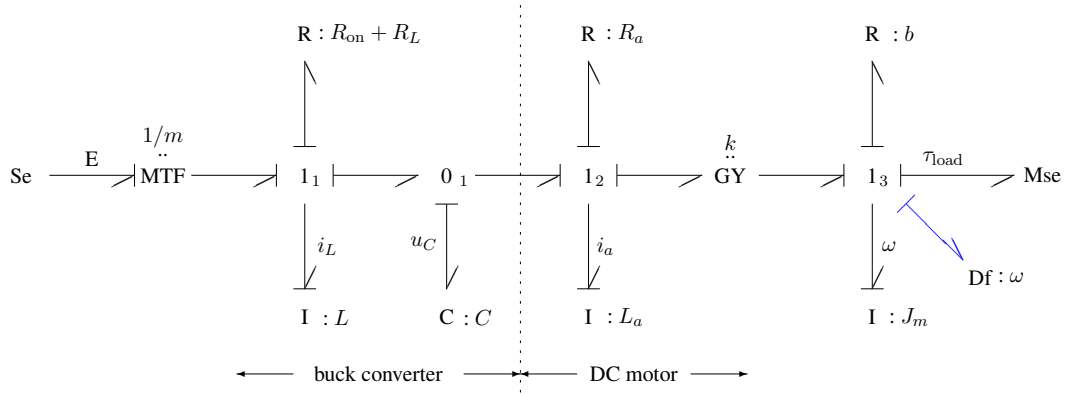


Figure 2: Averaged BG model of the healthy buck-converter-driven DC motor

Furthermore,

$$\begin{aligned}\tilde{x}_1 &= C\tilde{\dot{x}}_2 + \tilde{x}_3 \\ &= C\dot{x}_2 + C(\Delta R_a)\dot{x}_3 + x_3 \\ &= x_1 + C(\Delta R_a)x_3\end{aligned}\quad (19)$$

Finally,

$$\begin{aligned}u_{\text{req}} &= R(x_1 + C(\Delta R_a)\dot{x}_3) + L(\dot{x}_1 + C(\Delta R_a)\ddot{x}_3) \\ &\quad + x_2 + (\Delta R_a)x_3 \\ &= \underbrace{R\dot{x}_1 + L\dot{x}_1 + x_2}_u \\ &\quad + (x_3 + RC\dot{x}_3 + LC\ddot{x}_3)(\Delta R_a) \\ &= u + \frac{1}{k}(by + J_m\dot{y} + RC(\dot{y} + J_m\ddot{y}) \\ &\quad + LC(b\ddot{y} + J_m y^{(3)}))\Delta R_a\end{aligned}\quad (20)$$

As a result, in this example, all unknown states of the faulty system, $\tilde{\mathbf{x}}(t)$, can be eliminated. The required input u_{req} is a function of the initial input u , the desired output y and its derivatives. In the case of no fault ΔR_a , the required input equals the initial input.

The result obtained in this example may be confirmed by assigning bicausalities to the BG, by following the propagation of bicausality from the output source-sensor element SS to the input SS element and by deducing equations from the bicausal inverse BG model depicted in Fig. 3. As there is a unique causal path from the output $y_{\text{des}} = \omega$ to the input $u_{\text{req}} = \tilde{m}E$, the forward model is structurally invertible Ngwompo et al. (2001a). Note that bicausalities force all storage elements into derivative causality. Hence, the inverse model will be of order zero.

From the bicausal inverse BG in Fig. 3, the following equations may be deduced and solved for the required input $u_{\text{req}} = \tilde{m}E$.

$$1_3 : \quad e_2 = b\omega_{\text{des}} + J_m\dot{\omega}_{\text{des}} + \tau_{\text{load}} \quad (21)$$

$$GY : \quad e_3 = k\omega_{\text{des}} \quad (22)$$

$$\tilde{i}_a = f_3 = \frac{1}{k}e_2 \quad (23)$$

$$1_2 : \tilde{u}_C = e_4 = \tilde{R}_a\tilde{i}_a + L_a\frac{d\tilde{i}_a}{dt} + e_3 \quad (24)$$

$$0_1 : \tilde{i}_L = f_5 = f_3 + C\dot{e}_4 \quad (25)$$

$$1_1 : \quad e_6 = Rf_5 + L\frac{df_5}{dt} + e_5 \quad (26)$$

$$MTF : \quad e_6 = \tilde{m}E \quad (27)$$

3.3 Scheme of the active FTC procedure

Fig. 4 displays the scheme of the active FTC procedure based on system inversion by solving a DAE system. The real system may be subject to a fault as of some time instant t_1 . Its input $\mathbf{u}(t)$ and measured quantities are delivered into a DBG model. Its computation generates ARR residuals. On the basis of these ARR residuals a diagnosis module decides whether a fault has happened. If a parametric fault has occurred, it is isolated and quantified. At time $t_2 > t_1$, the faulty parameter \tilde{p} is provided into an input reconstruction module that takes the output $\mathbf{y}(t)$ of a forward model of the healthy system as the desired output $\mathbf{y}_{\text{des}}(t)$ and determines an input $\tilde{\mathbf{u}}(t)$ into the faulty system by solving a DAE system so that the output of the faulty system recovers after the fault and matches the one of the healthy system.

3.4 Nonlinear problems

In the previous section, it was assumed that a power electronic system may be represented by an averaged linear time-invariant model. For model inversion, a semi-linear DAE system with a constant coefficient matrix premultiplying the descriptor vector could be turned into an explicit ODE sys-

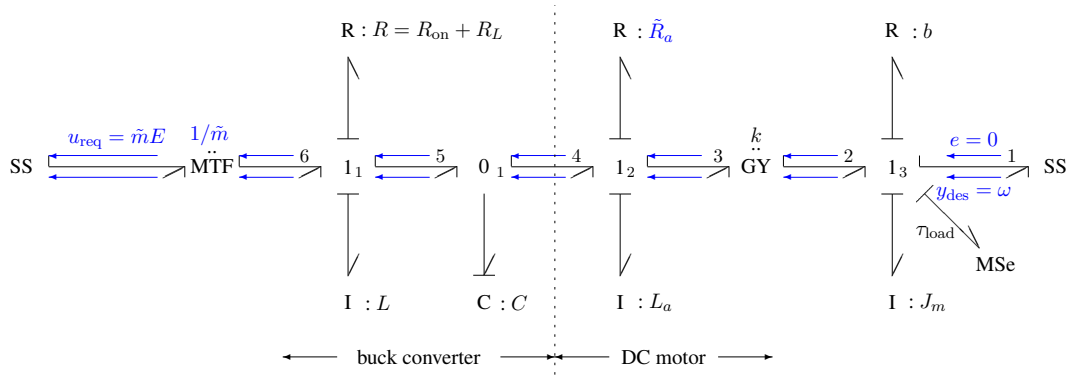


Figure 3: Inverse BG model of the buck-converter-driven DC motor

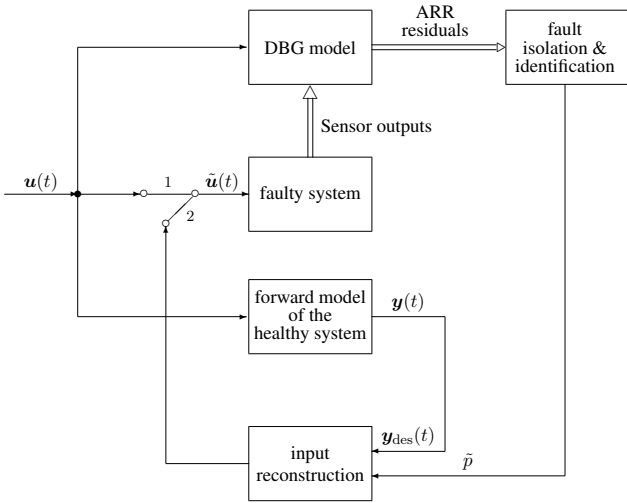


Figure 4: Scheme of the active FTC procedure

tem given $(\tilde{\mathbf{C}}\tilde{\mathbf{B}})^{-1}$ exists. For systems of slightly different structure, however, the forward model may be linear, while model inversion leads to a nonlinear problem. This is illustrated by the simple example of a boost-converter. Fig. 5 depicts its circuit schematic and Fig. 6 shows an averaged linear time-invariant forward BG model. The transistor and the diode have been considered as non-linear switches with ON-resistance R_{on} that commute oppositely in a healthy system. Furthermore, the equivalent series resistance of the capacitor has been neglected.

Let $R := R_L + R_{on}$. The equations of the averaged linear forward model deduced from the BG in Fig. 6 read

$$L \frac{di_L}{dt} = -Ri_L - m u_C + E \quad (28a)$$

$$C \dot{u}_C = m i_L - \frac{u_C}{R_l} \quad (28b)$$

$$y = u_C \quad (28c)$$

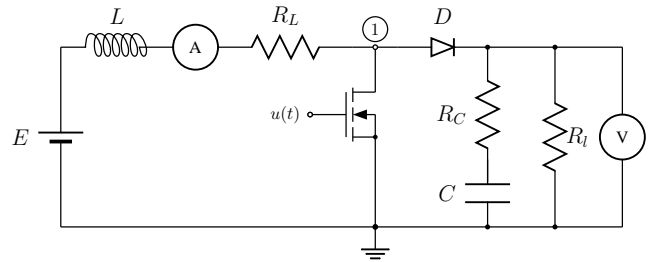


Figure 5: Circuit schematic of a boost converter

Now, suppose that the resistance, R_L , of the inductor becomes faulty as of some time instant t_1 . Given a constant voltage supply, E , the question then is how to change the duty cycle, d , of the signal $u(t)$ controlling the MOSFET transistor so that the output voltage $\tilde{V}(t) = \tilde{u}_C(t)$ of the faulty systems follows the output voltage $V(t) = u_C(t)$ of the healthy system despite the faulty resistance \tilde{R}_L . Changing the duty cycle, d , into a time dependent variable, $\tilde{d}(t)$ as of some time instant turns the signal $u(t)$ into a pulse width modulated (PWM) signal.

Let $\tilde{x}_1 := \tilde{i}_L$, $\tilde{x}_2 := \tilde{u}_C$, $y_{des} := y$ and $\tilde{R} := \tilde{R}_L + R_{on}$. Then the nonlinear DAE system that determines $m_{req}(t) := 1 - \tilde{d}(t)$ read

$$L \dot{\tilde{x}}_1 = -\tilde{R} \tilde{x}_1 - m_{req} y + E \quad (29)$$

$$C \dot{y} = m_{req} \tilde{x}_1 - \frac{1}{R_l} y \quad (30)$$

$$y = \tilde{x}_2 \quad (31)$$

Differentiation of the algebraic constraint (30) with respect to time and (29) give the semi-explicit ODE system

$$\begin{bmatrix} L & 0 \\ m_{req} & \tilde{x}_1 \end{bmatrix} \begin{bmatrix} \dot{\tilde{x}}_1 \\ \dot{m}_{req} \end{bmatrix} = \begin{bmatrix} -\tilde{R} & -y \\ 0 & 0 \end{bmatrix} \begin{bmatrix} \tilde{x}_1 \\ m_{req} \end{bmatrix} + \begin{bmatrix} E \\ \frac{y}{R_l} + C \dot{y} \end{bmatrix} \quad (32)$$

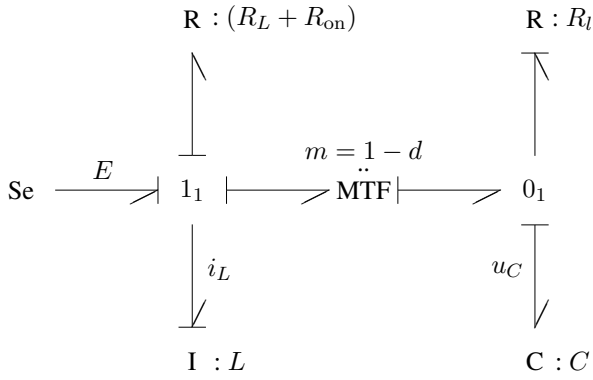


Figure 6: Averaged linear forward BG model of a boost converter

The unknown m_{req} can be eliminated from the first equation of the inverse model by means of the equations of the forward model. As $\tilde{u}_C = \tilde{x}_2 = y = u_C = x_2$, the following relation may be obtained.

$$m_{\text{req}} \tilde{x}_1 = C \dot{\tilde{x}}_2 + \frac{1}{R_l} \tilde{x}_2 = C \dot{x}_2 + \frac{1}{R_l} x_2 = m x_1 \quad (33)$$

Substituting $m_{\text{req}} = m x_1 / \tilde{x}_1$ into the first ODE of the inverse model yields

$$\frac{1}{2} L 2 \tilde{x}_1 \dot{\tilde{x}}_1 = -\tilde{R} \tilde{x}_1^2 - m x_1 y + E \tilde{x}_1 \quad (34)$$

Let $x := \tilde{x}_1^2$, then one obtains the explicit nonlinear ODE

$$\dot{x} = -\frac{2\tilde{R}}{L} x + \frac{2E}{L} \sqrt{|x|} - \frac{2m x_1 y}{L} \quad (35)$$

The last term on the right hand side of this ODE is known from a solution of the forward model. The values $x(t)$ can be used to determine $m_{\text{req}}(t)$.

Suppose that the fault in R_L occurred at $t = t_1$ and that it is isolated and quantified as of $t > t_2$. Then, the fault can be accommodated by switching from d to $\tilde{d}(t)$.

4. CASE STUDY

In this case study, the buck converter driven DC-motor (Fig. 1) is considered again. As a fault scenario, some leakage in the capacitor as of some time t_1 is assumed. As a result, the voltage across the capacitor C driving the motor will drop and so will the angular velocity ω . Given a constant voltage supply of the buck converter, the duty cycle of the signal controlling the transistor must be changed to keep up the angular velocity of the healthy system considered the desired output y_{des} .

4.1 Input Reconstruction

The leakage may be captured by a small resistance R_s in parallel to the capacitance that becomes effective as of some time t_1 . Again, let $\tau_{\text{load}} = 0$. For $t > t_1$, the DAE system for the inverse model then reads

$$0 = u_{\text{req}} - R \tilde{i}_L - L \frac{d\tilde{i}_L}{dt} - \tilde{u}_C \quad (36)$$

$$0 = \tilde{i}_L - C \dot{\tilde{u}}_C - \frac{\tilde{u}_C}{R_s} - \tilde{i}_a \quad (37)$$

$$0 = \tilde{u}_C - R_a \tilde{i}_a - L_a \frac{d\tilde{i}_a}{dt} - k y \quad (38)$$

$$0 = k \tilde{i}_a - b \omega - J_m \dot{\omega} \quad (39)$$

$$y = \omega \quad (40)$$

where $u_{\text{req}} = \tilde{m}E$ is to be determined, $y(t)$ is known (measured) and $R = R_L + R_{\text{on}}$.

Let i_a and u_C denote the armature current and the capacitor voltage in the healthy system obtained by solving the forward model. Equation 39 then entails $\tilde{i}_a = i_a$ and $\tilde{u}_C = u_C$. Substitution of equations yields for the required input

$$\begin{aligned} u_{\text{req}} &= \tilde{m}E \\ &= R \left(C \dot{u}_C + \frac{u_C}{R_s} + R i_a \right) \\ &\quad + L \frac{d}{dt} \left(C \dot{u}_C + \frac{u_C}{R_s} + i_a \right) + u_C \\ &= mE + \frac{R}{R_s} u_C + \frac{L}{R_s} \dot{u}_C \end{aligned} \quad (41)$$

In steady state, (41) reduces to

$$\begin{aligned} u_{\text{req}} = \tilde{m}E &= R \left[\frac{1}{R_s} \left(R_a \frac{b}{k} + k \right) + \frac{b}{k} \right] \omega \\ &\quad + \left(R_a \frac{b}{k} + k \right) \omega \end{aligned} \quad (42)$$

As long as the leakage in the capacitor has not occurred, $R_s \rightarrow \infty$ and $\tilde{m}E = mE$. This gives an equation the steady state value of the desired angular velocity must fulfill.

$$mE = \left[(R + R_a) \frac{b}{k} + k \right] \omega \quad (43)$$

If the fault is not accommodated by a changed input $\tilde{m}E$, then the angular velocity reaches a faulty steady state value $\tilde{\omega}$ that is given by the equation

$$\begin{aligned} mE &= R \left[\frac{1}{R_s} \left(R_a \frac{b}{k} + k \right) + \frac{b}{k} \right] \tilde{\omega} \\ &\quad + \left(R_a \frac{b}{k} + k \right) \tilde{\omega} \end{aligned} \quad (44)$$

The parameters listed in Table 1 give the steady state values $\omega = 69.63 \text{ rad/s}$ and $\tilde{\omega} = 35.57 \text{ rad/s}$.

Table 1: Parameters of the system buck converter - DC-motor

Parameter	Value	Units	Meaning
E	12.0	V	Voltage supply
L	20	mH	Inductance
R_L	0.1	Ω	Resistance of the coil
R_{on}	0.1	Ω	ON resistance (switch, diode)
d	0.5	–	Duty ratio
C	40	μF	Capacitance
L_a	2.6	mH	Armature inductance
R_a	2.0	Ω	Armature resistance
k	0.046	Vs/rad	Motor constant
J_m	$7.0 \cdot 10^{-4}$	kgm ²	Moment of inertia
b	$8.4 \cdot 10^{-4}$	Nms/rad	Friction coefficient
τ_{load}	0	Nm	Load moment
R_s	0.2	Ω	Resistance accounting for capacitor leakage

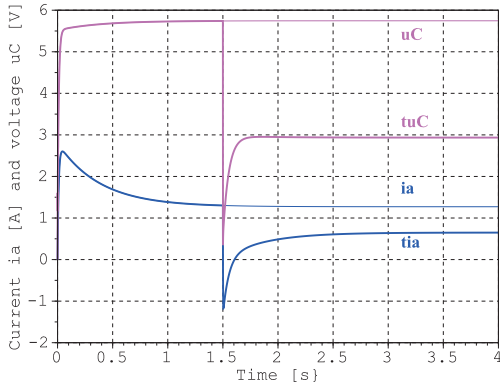


Figure 7: Time evolution of the armature current and the output voltage of the buck converter

4.2 Simulation of the fault

Simulation runs have been performed by means of the open source software Scilab Scilab Enterprises (nd) and have used the parameters given in Table 1.

Fig. 7 shows the time evolution of the armature current and the output voltage of the buck converter if the capacitor leakage is not compensated by a reconstructed input. The analytically computed steady state values for the healthy system read $i_a = 1.27A$, $u_C = 5.75V$ and for the faulty not accommodated system $\tilde{i}_a = 0.65A$, $\tilde{u}_C = 3.0V$. In Fig. 7, the tilde is indicated by the prefixed letter t.

Fig. 8 depicts the time history of the desired angular velocity, ω_{des} , the faulty velocity $\tilde{\omega}$ (denoted as $\tilde{\omega}$ in the figure) and the accommodated faulty velocity ω_{acc} . Again, the simulation run confirms the analytically computed steady state

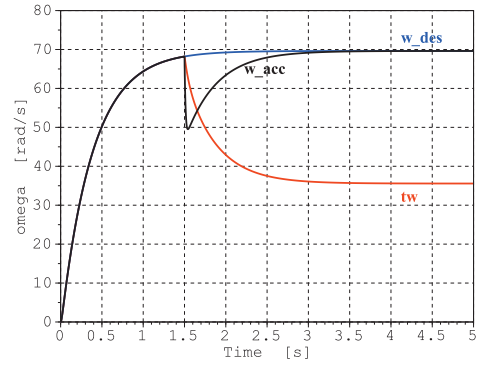


Figure 8: Time histories of the desired, the faulty and the accommodated faulty angular velocity

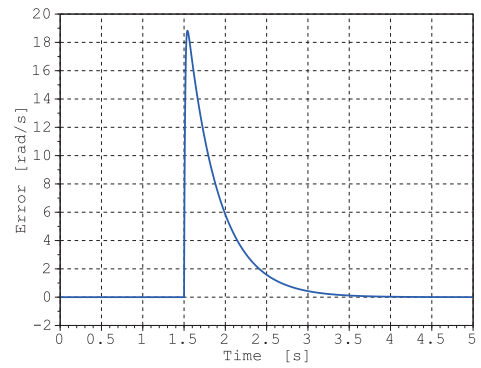


Figure 9: Time history of the error between the desired, the faulty angular velocity

values.

As of $t_1 = 1.5s$, a small resistance of $R_s = 0.2\Omega$ in parallel to the capacitor becomes effective. As a result of the capacitor leakage modelled this way, the capacitor voltage drops sharply and so does the angular velocity. If this fault is not compensated, the faulty steady state value is roughly half of the desired one.

It is assumed that detection and isolation of this fault takes about $0.02s$ so that fault accommodation can start at $t_2 = 1.52s$. Computing the reconstructed input by numerically solving the DAE system of the inverse model on a multi-processor, multi-core computer also takes some time. As can be seen, after the leakage of the capacitor has happened, the reconstructed input $u_{req}(t)$, in fact, forces the faulty angular velocity, $\tilde{\omega}(t)$, to follow the desired velocity $\omega_{des}(t)$. The dynamics of the recovery depends on how much the capacitor voltage has dropped and on the parameters of the systems. Given the parameters in this case study, it takes about $1.5s$ to recover from this sharp drop of the angular velocity (Fig. 9). Finally, Fig. 10(a) shows that the armature current i_a in the accommodated system, apart from a peak at $t = 1.5s$ caused

by the abrupt leakage of the capacitor, in fact, remains unchanged as it is determined by the desired angular velocity.

Fig. 10(b) indicates that the voltage u_C in the accommodated system does not drop to the steady state value of 3.0V but is forced in a very short time to regain the value of the healthy system so that the motor continues operating with the desired angular velocity despite the leakage of the capacitor. As a result, the inductor current i_L increases significantly (Fig. 10(c)). The steady state value rises from 1.27A to 30.07A.

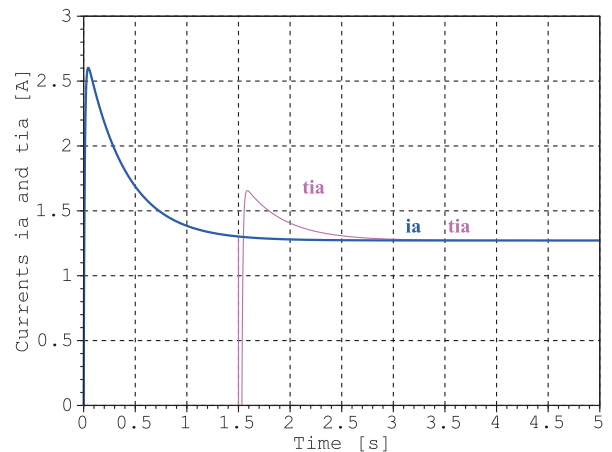
CONCLUSION

Once an abrupt parametric fault that has occurred in a system at some time instant is isolated and its magnitude is estimated, the system input can be reconstructed so that the system returns to a desired output after some delay. In this paper, a forward model deduced from a BG is considered a DAE system of the inverse model that may be solved by inverse simulation for the unknown required input that forces the faulty system to produce the output of the healthy one. The inverse simulation uses values of output variables that are provided by numerical computation of the forward model of the healthy system.

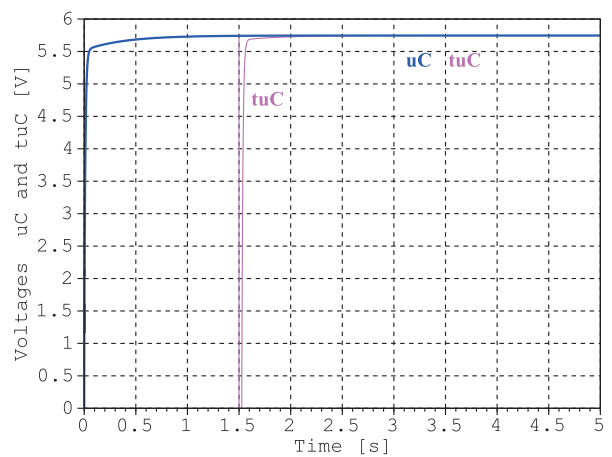
The analysis has been confined to linear time-invariant forward models. It is shown that after differentiation of the algebraic output equation a semi-explicit ODE system can be obtained that determines the required input. The approach to active FTC is applied to two simple examples of power electronic systems which have been represented by an averaged BG model. In a case study, a fault scenario in a buck converter driven DC motor has been considered.

The reconstruction of the system input in response to abrupt faults by inverse simulation is quite general. Existing sophisticated software for solving nonlinear DAE systems can be used. Analytical determination of the reconstructed system input is not necessary if possible at all. For complex systems with fast dynamics, the time needed for computing a reconstructed input after a fault has occurred may become an issue. This time adds to the time needed to detect and to isolate a fault and increases the time delay until the reconstructed input becomes effective. Exploitation of parallelism in the system model and computation on a multiprocessor system may reduce the time delay.

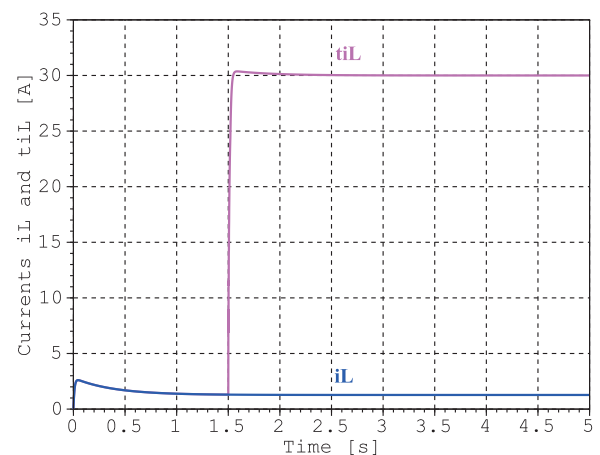
An advantage of input reconstruction by means of inverse simulation is that it is applicable to cases in which an analytical determination of the input required to accommodate a fault is not possible. Subjects of further research may be the application to systems with nonlinearities and to hybrid systems other than switched power electronic systems. Hybrid systems operate in various modes and their dynamic behaviour in one mode may be quite different from that in an-



(a) Time history of the currents i_a and \tilde{i}_a



(b) Time history of the voltages u_C and \tilde{u}_C



(c) Time history of the currents i_L and \tilde{i}_L

Figure 10: Time history of the currents i_a , i_L and the voltage u_C in the accommodated system

other mode. This affects FDI as well as input reconstruction for active FTC.

REFERENCES

- Allous, M. and Zanzouri, N. (2014). Active fault tolerant control based on bond graph approach. *Advances in Electrical Engineering 2014*, Article ID 216153.
- Blanke, M., M. Kinnaert, J. Lunze, and M. Staroswiecki (2006). *Diagnosis and Fault-Tolerant Control*. Berlin: Springer.
- Borutzky, W. (2015). *Bond Graph Model-based Fault Diagnosis of Hybrid Systems*. Springer International Publishing Switzerland.
- Djeziri, M., R. Merzouki, B. Ould Bouamama, and G. Dauphin-Tanguy (2007, 11–13 July). Bond Graph Model Based For Robust Fault Diagnosis. In *Proceedings of the 2007 American Control Conference*, New York City, U.S.A., pp. 3017–3022. IEEE.
- Gawthrop, P. (1995). Bicausal Bond Graphs. In F. Cellier and J. Granda (Eds.), *ICBGM'95, International Conference on Bond Graph Modeling and Simulation*, Volume 27(1) of *Simulation Series*, pp. 83–88. SCS Publishing.
- Loureiro, R. (2012). *Bond Graph Model Based on Structural Diagnosability and Recoverability Analysis: Application to Intelligent Autonomous Vehicles*. PhD thesis, L' Université Lille 1.
- Murray-Smith, D. (2012). *Modelling and simulation of integrated systems in engineering – Issues of methodology, quality, test and application*. Woodhead Publishing.
- Nacusse, M. and Junco, S.J. (2011, September). Passive fault tolerant control: A bond graph approach. In Bruzzone, A., Dauphin-Tanguy, G., Junco, S., and Piera, M.A. (Eds.), *Proc. 5th International Conference on Integrated Modelling and Analysis in Applied Control and Automation (IMAACA 2011)*, Rome, Italy, pp. 75–82. DIPTM UNIVERSITÀ DI GENOVA.
- Ngwompo, R., S. Scavarda, and D. Thomasset (1996). Inversion of Linear Time-invariant SISO Systems Modelled by Bond Graph. *Journal of the Franklin Institute* 333(B)(2), 157–174.
- Ngwompo, R., S. Scavarda, and D. Thomasset (2001a). Physical model-based inversion in control systems design using bond graph representation part 1: theory. *Proceedings of the IMechE Part I Journal of Systems and Control Engineering* 215(2), 95–103.
- Ngwompo, R., S. Scavarda, and D. Thomasset (2001b). Physical model-based inversion in control systems design using bond graph representation part 2: applications. *Proceedings of the IMechE Part I Journal of Systems and Control Engineering* 215(2), 105–112.
- OpenModelica Consortium (n.d.). OpenModelica.
- Samantaray, A. and B. Ould Bouamama (2008). *Model-based Process Supervision – A Bond Graph Approach*. Advances in Industrial Control. Springer, London.
- Scilab Enterprises (n.d.). Scilab. 78000 Versailles, France.
- Wang, D., M. Yu, C. Low, and S. Arogeti (2013). *Model-based Health Monitoring of Hybrid Systems*. Springer.
- Y. Touati, R. Merzouki, and B. Ould Bouamama (2012, August 29–31). Fault estimation and isolation using bond graph approach. In *8th IFAC Symposium on Fault Detection, Supervision and Safety of Technical Processes (SAFEPROCESS)*, Mexico City, Mexico, pp. 138–143.
- Y. Touati, R. Merzouki, B. Ould Bouamama, and R. Loureiro (2012, August 29–31). Detectability and Isolability Conditions in Presence of Measurement and Parameter Uncertainties Using Bond Graph Approach. In *8th IFAC Symposium on Fault Detection, Supervision and Safety of Technical Processes (SAFEPROCESS)*, Mexico City, Mexico, pp. 958–963.
- Y. Zhang and J. Jiang (2008, December 2008). Bibliographical review on reconfigurable fault-tolerant control systems. *Annual Reviews in Control* 32(2), 229–252.

APPENDIX

In order to keep the presentation concise consider a linear time-invariant single input single output (SISO) system with three states. Let u denote the input and y the output.

$$\dot{x}_1 = a_{11}x_1 + a_{12}x_2 + a_{13}x_3 + b_1u \quad (45)$$

$$\dot{x}_2 = a_{21}x_1 + a_{22}x_2 + a_{23}x_3 + b_2u \quad (46)$$

$$\dot{x}_3 = a_{31}x_1 + a_{32}x_2 + a_{33}x_3 + b_3u \quad (47)$$

$$= f_3(x_1, x_2, x_3, u) \quad (48)$$

$$y = c_1x_1 + c_2x_2 + c_3x_3 \quad (49)$$

Let $c_1 \neq 0$ without loss of generality. Then (49) may be solved for x_1 .

$$x_1 = \frac{1}{c_1}(-c_2x_2 - c_3x_3 + y) = f_1(x_2, x_3, y) \quad (50)$$

Differentiation of (49) with respect to time gives

$$\dot{y} = c_1\dot{x}_1 + c_2\dot{x}_2 + c_3\dot{x}_3 \quad (51)$$

$$\ddot{y} = c_1\ddot{x}_1 + c_2\ddot{x}_2 + c_3\ddot{x}_3 \quad (52)$$

Substitution of (45) – (47) into (51) and (52) results in two equations that may be written as

$$\dot{y} = f_2(x_1, x_2, x_3, u) \quad (53)$$

$$\bar{b}\dot{u} = f_4(x_1, x_2, x_3, u, \dot{y}) \quad (54)$$

where $\bar{b} = c_1b_1 + c_2b_2 + c_3b_3$.

Substitute (50) into (53) and assume that the resulting linear equation can be solved for x_2 , i.e. the coefficient premultiplying x_2 does not vanish.

$$x_2 = \bar{f}_2(x_3, u, y, \dot{y}) \quad (55)$$

Substituting x_1 and x_2 into (47) and (54) then yields

$$\dot{x}_3 = \bar{f}_3(x_3, u, y, \dot{y}) \quad (56)$$

$$\bar{b}\dot{u} = \bar{f}_4(x_3, u, y, \dot{y}, \ddot{y}) \quad (57)$$

As a result, the required input is a function of a reduced number of states, the desired output and its derivatives.

STEADY-STATE POWER FLOW ANALYSIS OF ELECTRICAL POWER SYSTEMS MODELLED BY 2-DIMENSIONAL MULTIBOND GRAPHS

Israel Núñez-Hernández^(a), Peter C. Breedveld^(b), Paul B. T. Weustink^(c), Gilberto Gonzalez-A^(d)

^{(a),(b)} Robotics and Mechatronics Group, University of Twente, Enschede, Netherlands

^(c) Controllab Products B.V, Hengelosestraat 500, 7521 AN Enschede, Netherlands

^(d) Faculty of Electrical Engineering, University of Michoacan, Morelia, Michoacán, Mexico

^(a) i.nunezhernandez@utwente.nl, ^(b) p.c.breedveld@utwente.nl
^(c) paul.weustink@controllab.nl, ^(d) gilmichga@yahoo.com.mx

ABSTRACT

The steady-state analysis of electrical circuits is frequently done by means of phasors. This paper focuses on the use of multiport elements with two-dimensional multibond as representation of the real and imaginary part of a phasor. This set of two-dimensional multibonds forms, together with elements that are adapted likewise, a so-called phasor bond graph model. A procedure is presented to derive a symbolic function of the steady-state of a user-defined output from a phasor bond graph model. The application of a phasor bond graph model in power flow studies of an electrical power system are presented as an example.

Keywords: steady-state; power flow; phasor; bond graph, electrical power systems

1. INTRODUCTION

An electrical power system (EPS) consists of many individual elements connected together to form a large, complex and dynamic system capable of generating, transmitting and distributing electrical energy over a large geographical area (Machowski et al., 2008).

Power system stability (PSS) may be defined as the ability to retrieve an equilibrium state of such a system after being subjected to a physical disturbance. Three quantities are important for power system operation: i) phase-angles of nodal voltages, also called power or load angles; ii) frequency; and iii) nodal voltage magnitude (Machowski et al., 2008; Kundur, 1994).

In the stability analysis of practical power systems consisting of thousands of buses and hundreds of generators. It is common to assume all machines to be in a steady-state condition prior to a disturbance (Kundur, 1994; Anderson and Fouad, 2003).

The sinusoidal analysis by means of phasors is an elegant way to analyze electrical circuits with sinusoidal inputs and responses with a given constant frequency, i.e. when the system is in steady-state, without the need to solve differential equations (Steinmetz, 1893).

At the other hand, bond graph (BG) methodology deals with a graphical approach to system modelling, the essential feature of the bond graph approach is the

concise representation of energy storage, dissipation, and exchange in a system. It describes how the power flows through the system. The overall purpose of this methodology is the domain-independent representation of any engineering system which is involved in different domains (Paynter, 1961).

Previous studies have reported how steady-state values can be obtained from BG models of dynamic systems. An algorithm to determine the equilibrium state of a system with constant inputs by direct inspection of its BG is proposed in (Breedveld, 1984a). A BG model in a derivative causality assignment is proposed to determine the steady-state of a linear system in (Gonzalez-A, 2003). However, the previously mentioned approaches are mainly focus on the final amplitude value of the defined output. They do not give in a direct manner information about the phase shift of the signals. As mentioned above, for the case of EPS, the phase-angle of a nodal voltage is important since the power flow depends on it.

This paper attempts to show the use of phasors together with bond graphs by means of two-dimensional (2D) multibonds. The main issues addressed in this paper are: i) the formulation of regular BG elements into phasor bond graph (PhBG) elements; ii) the procedure to obtain a symbolic function in the complex plane of a given output; and iii) the power flow analysis of EPS's.

The paper has been organized in the following way. In order to inform the reader about phasor theory and BG methodology, Section 2 and Section 3 respectively present a brief background of these topics, including references for further reading. If the reader has previous knowledge of the topics these sections can be skipped without any trouble. Section 4 presents the theoretical background to obtain the PhBG elements. In Section 5, the methodology proposed to determine a symbolic function of the steady-state from a PhBG model is described. Furthermore, the proposed methodology is applied to a passive band pass filter in order to obtain a symbolic function of its steady state as an example. Section 6 addresses the application of PhBG to the analysis of power flow of a simple EPS. Finally, the conclusions are stated in Section 7.

2. PHASOR REPRESENTATION

2.1. Introduction

A phasor represents a periodic waveform as a “rotary vector”. This is illustrated in Fig. 1. Suppose a vector \mathbf{F} rotating with angular velocity ω with respect to a stationary reference frame. Its position at any instant of time is given by $\mathbf{F}(t) = \hat{A}e^{j(\omega t + \theta)}$, where \hat{A} is the amplitude and θ is the phase shift with respect to the reference frame Re-Im. The projection of vector \mathbf{F} onto the fixed horizontal axis is a sinusoidal function expressed as $f(t) = \hat{A} \cos(\omega t + \theta)$.

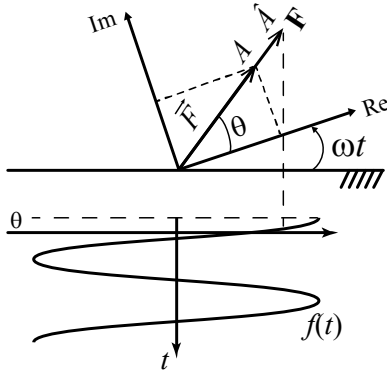


Fig. 1 Illustration of definition of phasors

The amplitude \hat{A} may be expressed in rms value, A . For sinusoidal waves $\hat{A} = \sqrt{2}A$. Then, it is possible rewrite the vector position in the following way:

$$\mathbf{F}(t) = \sqrt{2}Ae^{j\theta}e^{j\omega t} \quad (1)$$

The part that does not depend on time $Ae^{j\theta}$ in (1) is known as a phasor (Veltman, 2007). A phasor \vec{F} may also be written as,

$$\vec{F} = Ae^{j\theta} = A \angle \theta = A(\cos \theta + j \sin \theta) \quad (2)$$

The time integral and time derivative of $\mathbf{F}(t)$ are

$$\int \mathbf{F}(t) dt = \sqrt{2}Ae^{j\theta} \int e^{j\omega t} dt = -j \frac{1}{\omega} \sqrt{2} \vec{F} e^{j\omega t} \quad (3)$$

$$\frac{d}{dt} \mathbf{F}(t) = \sqrt{2}Ae^{j\theta} \frac{d}{dt} e^{j\omega t} = j\omega \sqrt{2} \vec{F} e^{j\omega t}$$

which implies that the integral of the phasor is lagged by $\pi/2$ radians, and scaled by $1/\omega$. At the other hand, the derivative of a phasor is leaded by $\pi/2$ radians, and multiplied by ω . This means that in phasor notation the integration and differentiation operations can be performed by scaling and phase shifting.

2.2. Analysis of Electrical Networks with Phasors

Phasors are an efficient method for steady-state analysis of AC circuits with a given constant frequency. When the system operates in a steady-state condition, differential equations are not necessary since all variables are either

constants or sinusoidal variations with time. With these terms neglected, equations appear as algebraic equations. In an electrical network, let the instantaneous voltage and the instantaneous current be

$$\begin{aligned} v(t) &= v \cos(\omega t + \theta_v) \\ i(t) &= i \cos(\omega t + \theta_i) \end{aligned} \quad (4)$$

The phasor representation of (4) may be obtained by using (1) and (2), thus

$$\begin{aligned} \vec{V} &= V e^{j\theta_v} = V \angle \theta_v \\ \vec{I} &= I e^{j\theta_i} = I \angle \theta_i \end{aligned} \quad (5)$$

The impedance, Z , is the relationship between the voltage and current. Since this relationship is between two phasors, it will be a phasor too. The impedance may be expressed as

$$\vec{Z} = \vec{V} / \vec{I} = Z \angle \theta = R + j(X_L - X_C) \quad (6)$$

where $\theta = \theta_v - \theta_i$ is called the impedance angle. The real part is given by the resistive elements R , and the imaginary or reactive part, is given by the inductive and capacitive reactances in the system, respectively X_L and X_C . Table 1 shows a list of the three basic elements (resistor, inductor, and capacitor) in an electrical network and their impedances.

Table 1: Impedances

Time	Phasor	Impedance
$v(t) = R \cdot i(t)$	$\vec{V} = R \cdot \vec{I}$	R
$v(t) = L \frac{d}{dt} i(t)$	$\vec{V} = jX_L \vec{I}$	$jX_L = j\omega L$
$v(t) = \frac{1}{C} \int i(t) dt$	$\vec{V} = -jX_C \vec{I}$	$-jX_C = 1/j\omega C$

In power engineering, voltages, and currents are often represented in a phasor diagram. A phasor diagram is a “picture” at any instant of these rotary vectors, which represents the phase relationship between them at that time.

2.3. Complex Power

The instantaneous power consumed by the network may be written as,

$$\begin{aligned} p(t) &= v(t) \cdot i(t) = v \cdot i \cos(\omega t + \theta_v) \cos(\omega t + \theta_i) \\ &= P(1 + \cos 2(\omega t + \theta_v)) + Q \sin 2(\omega t + \theta_v) \end{aligned} \quad (7)$$

with $P = VI \cos \theta$, $Q = VI \sin \theta$, and $\theta = \theta_v - \theta_i$. The variable P is called real or *active power* defined in watts (W). It represents the absorbed power by the resistive elements in the load. At the other hand, Q is referred as *reactive power*, defined in volt-ampere reactive (*var*), and this power supplies the stored energy in reactive elements. Since $\cos \theta$ plays an important role in the

amount of real power in the system, it is called *power factor* (Saadat, 1999; El-Hawary, 1995).

Real, and reactive power are represented together as a complex or *apparent power*, S , its unit is volt-ampere (VA) (Chapman, 2005). The apparent power may be represented as,

$$\begin{aligned}\vec{S} &= P + jQ = \vec{V}\vec{I}^* = \vec{Z}|\vec{I}| \\ &= R|\vec{I}|^2 + jX|\vec{I}|^2 \\ &= (V_{Re}I_{Re} + V_{Im}I_{Im}) + j(V_{Im}I_{Re} - V_{Re}I_{Im})\end{aligned}\quad (8)$$

where \vec{I}^* is the conjugate current. These three powers are normally described in a so-called power triangle.

3. BOND GRAPHS

The port-based approach with regard to modeling of physical systems is an effective way to split a system model into conceptual elements that are interacting with each other via (power) ports. As it is based on energy, port-based modelling offers a unified way to model physical systems from different physical domains, such as electrical, magnetic, mechanical, hydraulic, thermal, etc.

A BG is a graphical notation of such a port-based description. The BG conceptual framework was originated by Paynter in (Paynter, 1961).

This graphical technique is based on representing power transfer between elements as labelled nodes, which are linked to each other by means of oriented edges called *bonds*. In each physical domain, the power can be written as the product of two variables, *effort* $e(t)$ and *flow* $f(t)$. This pair of variables is called *power variables*. Conserved physical variables can either be the time integral of a flow (generalized *displacement* $q(t)$) or the time integral of an effort (generalized *momentum* $p(t)$) and can be considered as stored quantities, *state variables* or *energy variables*, as the stored energy is a function of these variables. By making the distinction between displacement-like states and momentum-like states, the mechanical framework of variables is used as opposed to the more general, but less known, generalized framework of variables (Breedveld, 1984b).

In a bond graph, the way in which these variables need to be computed are specified as input and output to the constitutive relation that characterizes a port is indicated by means of a so-called causal stroke. It is a perpendicular line put at one end of a bond indicating the direction of the effort signal, also called the causality.

The port-based approach is in principle an object-oriented approach to modeling. This permits different realizations of an object by directly replacing a portion of it with another bond graph system with a different degree of dynamic details.

The basic elements (nodes) of the bond graph language can be classified as follows:

- 1-port elements, which dissipate (free) energy (resistor R), store energy (inertia I , capacitor C) and supply power (sources S_e, S_f).

- 2-port elements (transformers TF and gyrators GY) are used when it is necessary to interconnect submodels in different domains in a power conservative way. However, transformers can also be used for scaling variables in a power conserving manner.
- Multiport elements that represent the conceptual structure of the model. The 0-junction is a BG node with common effort; the 1-junction describes a common flow node.

A BG model can be organized into interconnected blocks (modulated sources, storage block, dissipation block, junction structure, ideal sensors). It is possible to obtain the state-space equations of the system using a BG model. Fig. 2 shows a multiport linear time-invariant (LTI) system, which includes the key vectors of BG variables by the input-output role they play in the causal problem (Rosenberg, 1971).

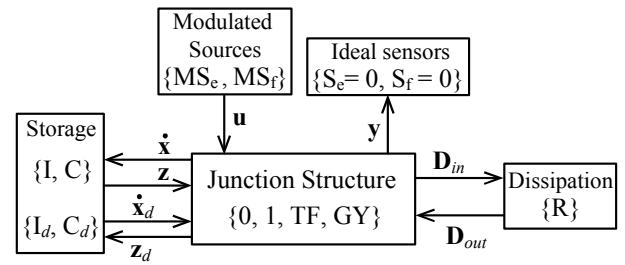


Fig. 2 Block representation and key vectors of a bond graph model

In Fig. 2, the state vector $\mathbf{x} \in \mathfrak{R}^n$ is composed of generalized state variables; $\mathbf{z} \in \mathfrak{R}^n$, the vector of power variables (C-port efforts and I-port flows); $\mathbf{u} \in \mathfrak{R}^p$ denotes the vector of system input variables; $\mathbf{D}_{in} \in \mathfrak{R}^r$, and $\mathbf{D}_{out} \in \mathfrak{R}^r$ contain mixed sets of efforts and flows and their inner product represent the energy exchange between the dissipation multiport and the junction structure; $\mathbf{x}_d \in \mathfrak{R}^q$ is the state vector associated with elements in derivative causality; $\mathbf{z}_d \in \mathfrak{R}^q$, the vector of power variables in derivative causality (I-port efforts and C-port flows); finally, the vector $\mathbf{y} \in \mathfrak{R}^k$ is the system output variables. The outputs can be measured by means of ideal sensors. As the amount of power the ideal sensors take out of the system is zero, then the device can be modelled by an energy sink that provides a zero effort or a zero flow. As a result, an effort sensor can be represented by a zero flow sink and a flow sensor can be modelled by a zero effort sink.

The storage and dissipation block relationships are,

$$\mathbf{z} = \mathbf{F}\mathbf{x}; \quad \mathbf{z}_d = \mathbf{F}_d \mathbf{x}_d; \quad \mathbf{D}_{out} = \mathbf{L}\mathbf{D}_{in} \quad (9)$$

where \mathbf{F} is a diagonal matrix composed of the elements in integral causality, \mathbf{F}_d is a diagonal matrix composed of the elements in derivative causality, and \mathbf{L} is a diagonal matrix composed of the dissipative elements.

The junction structure matrix deduced from Fig. 2 has the following form:

$$\begin{bmatrix} \dot{\mathbf{x}} \\ \mathbf{D}_{in} \\ \mathbf{y} \\ \mathbf{z}_d \end{bmatrix} = \begin{bmatrix} \mathbf{S}_{11} & \mathbf{S}_{12} & \mathbf{S}_{13} & \mathbf{S}_{14} \\ \mathbf{S}_{21} & \mathbf{S}_{22} & \mathbf{S}_{23} & \mathbf{0} \\ \mathbf{S}_{31} & \mathbf{S}_{32} & \mathbf{S}_{33} & \mathbf{0} \\ \mathbf{S}_{41} & \mathbf{0} & \mathbf{0} & \mathbf{0} \end{bmatrix} \begin{bmatrix} \mathbf{z} \\ \mathbf{D}_{out} \\ \mathbf{u} \\ \dot{\mathbf{x}}_d \end{bmatrix} \quad (10)$$

Because of some usual hypotheses the matrix \mathbf{S} , satisfies the following properties (Karnopp et al., 1990; Rosenberg, 1971):

- no connection between the dissipation block and elements in derivative causality: $\mathbf{S}_{24} = \mathbf{S}_{42} = \mathbf{0}$,
- no connection between the sources/sensors and the elements in derivative causality: $\mathbf{S}_{34} = \mathbf{S}_{43} = \mathbf{0}$,
- \mathbf{S}_{11} and \mathbf{S}_{22} are square skew-symmetric matrices
- if there is no causal connection between dissipative elements, then: $\mathbf{S}_{22} = \mathbf{0}$,
- causal connection between elements with integral and derivative causality: $\mathbf{S}_{14} = -\mathbf{S}_{41}^T$,
- \mathbf{S}_{12} and \mathbf{S}_{21} are each other's negative transpose.

The entries of the \mathbf{S} matrix take values inside the set $\{0, \pm 1, \pm m, \pm n\}$, where m , and n are transformer, and gyrator modules. Conveniently representing the state equations as

$$\begin{aligned} \dot{\mathbf{x}} &= \mathbf{A}\mathbf{x} + \mathbf{B}\mathbf{u} \\ \mathbf{y} &= \mathbf{C}\mathbf{x} + \mathbf{D}\mathbf{u} \end{aligned} \quad (11)$$

where

$$\begin{aligned} \mathbf{A} &= \mathbf{E}^{-1}(\mathbf{S}_{11} + \mathbf{S}_{12}\mathbf{M}\mathbf{S}_{21})\mathbf{F} \\ \mathbf{B} &= \mathbf{E}^{-1}(\mathbf{S}_{13} + \mathbf{S}_{12}\mathbf{M}\mathbf{S}_{23}) \\ \mathbf{C} &= (\mathbf{S}_{31} + \mathbf{S}_{32}\mathbf{M}\mathbf{S}_{21})\mathbf{F} \\ \mathbf{D} &= \mathbf{S}_{33} + \mathbf{S}_{32}\mathbf{M}\mathbf{S}_{23} \end{aligned} \quad (12)$$

being $\mathbf{M} = (\mathbf{I} - \mathbf{L}\mathbf{S}_{22})^{-1}\mathbf{L}$, $\mathbf{E} = \mathbf{I} + \mathbf{S}_{14}\mathbf{F}_d^{-1}\mathbf{S}_{14}^T\mathbf{F}$, and \mathbf{I} the identity matrix of appropriate dimension. The reader interested in more details about BG, may refer to (Karnopp et al., 1990; Borutzky, 2010).

4. PHASOR BOND GRAPHS ELEMENTS

The Laplace transform can also be applied to the BG models (Borutzky, 2010; Kypuros, 2013). With this transformation, the regular passive BG elements become impedances, or admittances.

As shown in Fig. 3a), if a 1-port element has effort-out causality can be characterized by an impedance, while a 1-port element with flow-out causality is modelled as an admittance, see Fig. 3b). In order to represent dynamic systems using impedances, it must be assumed that the constitutive relationships of the components are linear.

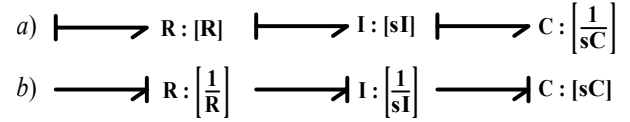


Fig. 3 1-port elements a) impedances, and b) admittances

Impedance bond graphs are synthesized by following the same procedure that in the case of dynamic models. If the Laplace operator is substituted by the Fourier operator, i.e. $s = j\omega$, the PhBG elements may be obtained. Thus, an impedance BG model becomes a PhBG model.

The proposed PhBG model expresses the impedances in matrix form. In this way, the phasor elements may be represented using 2D multibonds (Bonderson, 1975; Breedveld, 1985). While one bond represents the real part of the phasor, the second bond represents the imaginary part of the phasor. The impedances from Table 1 are rewritten in matrix form, see Table 2.

Table 2: 1-Port Impedances in Phasor Bond Graph Form

Element	Phasor	2D multibond
Resistive	$\begin{bmatrix} V_{Re} \\ V_{Im} \end{bmatrix} = R \begin{bmatrix} 1 & 0 \\ 0 & 1 \end{bmatrix} \begin{bmatrix} I_{Re} \\ I_{Im} \end{bmatrix}$	$\Rightarrow \mathbf{R}$
Inductive	$\begin{bmatrix} V_{Re} \\ V_{Im} \end{bmatrix} = X_L \begin{bmatrix} 0 & -1 \\ 1 & 0 \end{bmatrix} \begin{bmatrix} I_{Re} \\ I_{Im} \end{bmatrix}$	$\Rightarrow \mathbf{X}_L$
Capacitive	$\begin{bmatrix} V_{Re} \\ V_{Im} \end{bmatrix} = X_C \begin{bmatrix} 0 & 1 \\ -1 & 0 \end{bmatrix} \begin{bmatrix} I_{Re} \\ I_{Im} \end{bmatrix}$	$\Rightarrow \mathbf{X}_C$

The 2-port elements are modelled in the same way as in case of 2D multibonds (Breedveld, 1985), see Table 3.

Table 3: 2-Port Elements in Phasor Bond Graph Form

Element	Phasor	2D multibond
Transformer	$\begin{bmatrix} \vec{V}_1 \\ \vec{I}_2 \end{bmatrix} = \begin{bmatrix} 0 & \mathbf{T}^T \\ \mathbf{T} & 0 \end{bmatrix} \begin{bmatrix} \vec{I}_1 \\ \vec{V}_2 \end{bmatrix}$, $\mathbf{T} = \begin{bmatrix} m & 0 \\ 0 & m \end{bmatrix}$	$\Rightarrow \mathbf{TF} \Rightarrow$
Gyrator	$\begin{bmatrix} \vec{V}_1 \\ \vec{V}_2 \end{bmatrix} = \begin{bmatrix} 0 & \mathbf{G}^T \\ \mathbf{G} & 0 \end{bmatrix} \begin{bmatrix} \vec{I}_1 \\ \vec{I}_2 \end{bmatrix}$, $\mathbf{G} = \begin{bmatrix} n & 0 \\ 0 & n \end{bmatrix}$	$\Rightarrow \mathbf{GY} \Rightarrow$

m and n are the scalar modulus of the transformer and gyrator, respectively

The 2D multibond sources from (5) can be changed into its matrix form using (2). See Table 4.

Table 4: Sources in Phasor Bond Graph Form

Source	Phasor	2D multibond
Voltage	$\vec{V} = V[\cos \theta_v \quad \sin \theta_v]^T$	$\mathbf{V} \angle \theta \Rightarrow$
Current	$\vec{I} = I[\cos \theta_i \quad \sin \theta_i]^T$	$\mathbf{I} \angle \theta \Leftarrow$

V and I are the rms value of voltage and current, respectively

5. PHASOR BOND GRAPH ANALYSIS

This section presents the analysis required to obtain a symbolic function from a PhBG model that represents the steady-state of user-defined output. In a PhBG model there is not difference between elements in integral or derivative causality, since they are replaced by their equivalent admittance or impedance. In other words, a PhBG model only contains passive elements with indifferent causality. Nevertheless, in order to maintain the familiarity between regular BG and PhBG models, the Standard Causality Assignment Procedure (SCAP) introduced in (Karnopp and Rosenberg, 1968) is applied to the PhBG models. Similar to the regular BG analysis. The block representation of a PhBG is depicted in Fig. 4.

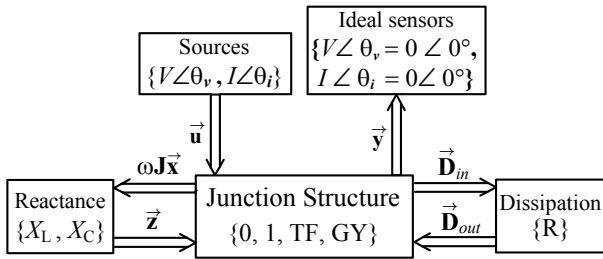


Fig. 4 Block representation of a phasor bond graph model

The reactance, and dissipation blocks contain the power demanding elements of the system, and may be defined as

$$\bar{\mathbf{z}} = \bar{\mathbf{F}}(\omega \mathbf{J} \bar{\mathbf{x}}); \quad \bar{\mathbf{D}}_{out} = \bar{\mathbf{L}} \bar{\mathbf{D}}_{in} \quad (13)$$

where

$$\mathbf{J} = \begin{bmatrix} 0 & -1 \\ 1 & 0 \end{bmatrix} \quad (14)$$

and $\bar{\mathbf{F}}$ is a diagonal matrix filled with the impedance, or admittance of the reactive elements. The diagonal matrix $\bar{\mathbf{L}}$ contains the impedance, or admittance of the resistive elements.

The junction structure relationships of a PhBG model can be defined as follows:

$$\begin{bmatrix} \omega \mathbf{J} \bar{\mathbf{x}} \\ \bar{\mathbf{D}}_{in} \\ \bar{\mathbf{y}} \end{bmatrix} = \begin{bmatrix} \bar{\mathbf{S}}_{11} & \bar{\mathbf{S}}_{12} & \bar{\mathbf{S}}_{13} \\ \bar{\mathbf{S}}_{21} & \bar{\mathbf{S}}_{22} & \bar{\mathbf{S}}_{23} \\ \bar{\mathbf{S}}_{31} & \bar{\mathbf{S}}_{32} & \bar{\mathbf{S}}_{33} \end{bmatrix} \begin{bmatrix} \bar{\mathbf{z}} \\ \bar{\mathbf{D}}_{out} \\ \bar{\mathbf{u}} \end{bmatrix} \quad (15)$$

After some algebraic manipulations, the system output is given by

$$\bar{\mathbf{y}} = (\bar{\mathbf{C}}(\bar{\mathbf{F}}^{-1} - \bar{\mathbf{A}})^{-1} \bar{\mathbf{B}} + \bar{\mathbf{D}}) \bar{\mathbf{u}} \quad (16)$$

with

$$\begin{aligned} \bar{\mathbf{A}} &= \bar{\mathbf{S}}_{11} + \bar{\mathbf{S}}_{12} \bar{\mathbf{M}} \bar{\mathbf{S}}_{21} \\ \bar{\mathbf{B}} &= \bar{\mathbf{S}}_{13} + \bar{\mathbf{S}}_{12} \bar{\mathbf{M}} \bar{\mathbf{S}}_{23} \\ \bar{\mathbf{C}} &= \bar{\mathbf{S}}_{31} + \bar{\mathbf{S}}_{32} \bar{\mathbf{M}} \bar{\mathbf{S}}_{21} \\ \bar{\mathbf{D}} &= \bar{\mathbf{S}}_{33} + \bar{\mathbf{S}}_{32} \bar{\mathbf{M}} \bar{\mathbf{S}}_{23} \end{aligned} \quad (17)$$

being $\bar{\mathbf{M}} = (\mathbf{I} - \bar{\mathbf{L}} \bar{\mathbf{S}}_{22})^{-1} \bar{\mathbf{L}}$, and \mathbf{I} the identity matrix of appropriate dimension.

5.1. Example: Passive Filter

To clarify the application of the PhBG analysis, it will be shown an example. Consider the passive band pass circuit depicted in Fig. 5a).

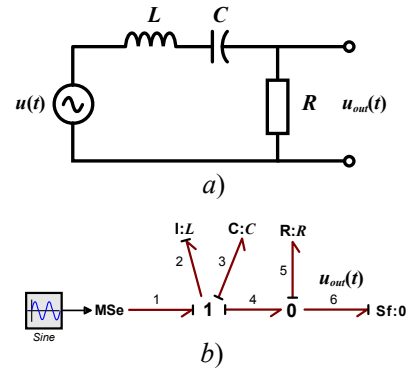


Fig. 5 Passive band pass filter

In Fig. 5b) is possible to observe the BG model of the filter. As illustrated in Fig. 6, the BG model was changed into a PhBG model by using the 2D multibonds, the SCAP and the impedance/admittance of each element.

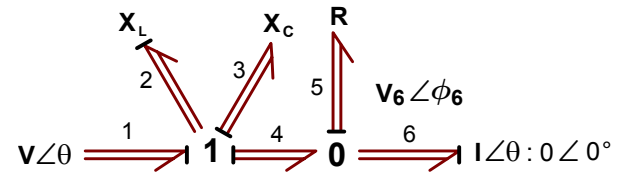


Fig. 6 PhBG model of the band pass filter

The key vectors obtained from the PhBG model are,

$$\begin{aligned} \omega \mathbf{J} \bar{\mathbf{x}} &= \begin{bmatrix} \bar{e}_2 \\ \bar{f}_3 \end{bmatrix} = \begin{bmatrix} e_{2 \text{ Re}} \\ e_{2 \text{ Im}} \\ f_{3 \text{ Re}} \\ f_{3 \text{ Im}} \end{bmatrix}; \quad \bar{\mathbf{z}} = \begin{bmatrix} \bar{f}_2 \\ \bar{e}_3 \end{bmatrix} = \begin{bmatrix} f_{2 \text{ Re}} \\ f_{2 \text{ Im}} \\ e_{3 \text{ Re}} \\ e_{3 \text{ Im}} \end{bmatrix} \\ \bar{\mathbf{D}}_{in} = \bar{f}_5 &= \begin{bmatrix} f_{5 \text{ Re}} \\ f_{5 \text{ Im}} \end{bmatrix}; \quad \bar{\mathbf{D}}_{out} = \bar{e}_5 = \begin{bmatrix} e_{5 \text{ Re}} \\ e_{5 \text{ Im}} \end{bmatrix} \\ \bar{\mathbf{u}} = \bar{e}_1 &= \begin{bmatrix} e_{1 \text{ Re}} \\ e_{1 \text{ Im}} \end{bmatrix}; \quad \bar{\mathbf{y}} = \bar{e}_6 = \begin{bmatrix} e_{6 \text{ Re}} \\ e_{6 \text{ Im}} \end{bmatrix} \end{aligned} \quad (18)$$

Note that in (18) the chosen output is the voltage difference over the resistor. The constitutive relations of the 2D multibond elements are

$$\bar{\mathbf{F}} = \text{diag}\{X_C \mathbf{J}^{-1}, 1/X_L \mathbf{J}\}; \quad \bar{\mathbf{L}} = R \mathbf{I}_{2 \times 2} \quad (19)$$

The submatrices of junction structure \mathbf{S} given by (15) are

$$\begin{aligned} \bar{\mathbf{S}}_{11} &= \begin{bmatrix} \mathbf{0}_{2 \times 2} & \mathbf{I}_{2 \times 2} \\ -\mathbf{I}_{2 \times 2} & \mathbf{0}_{2 \times 2} \end{bmatrix}; & \bar{\mathbf{S}}_{32} &= \mathbf{I}_{2 \times 2}; \\ \bar{\mathbf{S}}_{13} &= \begin{bmatrix} \mathbf{0}_{2 \times 2} \\ \mathbf{I}_{2 \times 2} \end{bmatrix}; & \bar{\mathbf{S}}_{12} &= -\bar{\mathbf{S}}_{21}^T = \begin{bmatrix} \mathbf{0}_{2 \times 2} \\ -\mathbf{I}_{2 \times 2} \end{bmatrix} \\ \bar{\mathbf{S}}_{22} &= \bar{\mathbf{S}}_{23} = \bar{\mathbf{S}}_{31} = \bar{\mathbf{S}}_{33} = \mathbf{0}_{2 \times 2} \end{aligned} \quad (20)$$

Finally, (20) is substituted into (16) to obtain the steady-state symbolic function in the complex plane of the output:

$$\begin{bmatrix} e_{6 \text{ Re}} \\ e_{6 \text{ Im}} \end{bmatrix} = \frac{1}{\Delta} \begin{bmatrix} R^2 & -R(X_C - X_L) \\ R(X_C - X_L) & R^2 \end{bmatrix} \begin{bmatrix} e_{1 \text{ Re}} \\ e_{1 \text{ Im}} \end{bmatrix} \quad (21)$$

where $\alpha = R^2 + (X_C - X_L)^2$. In order to verify the proposed methodology, consider the following parameters $u(t) = \sqrt{2} \sin(2\pi ft)$ for the dynamic model and $\bar{\mathbf{u}} = \bar{\mathbf{e}}_1 = [1 \ 0]^T$ for the PhBG model, $C = 0.5F$, $R = 10\Omega$, $L = 1H$, $f = 50\text{Hz}$. By substituting the numerical parameters into (21) the steady-state value of the output is given by

$$\begin{bmatrix} e_{6 \text{ Re}} \\ e_{6 \text{ Im}} \end{bmatrix} = \begin{bmatrix} 0.0010 \\ -0.0318 \end{bmatrix} \quad (22)$$

It is necessary to obtain the magnitude and the argument of the complex number in (22), so

$$\begin{aligned} e_6 &= \sqrt{e_{6 \text{ Re}}^2 + e_{6 \text{ Im}}^2} = 0.0318 V_{\text{rms}} \\ \phi_6 &= \arctan(e_{6 \text{ Im}} / e_{6 \text{ Re}}) = -88.1988^\circ \end{aligned} \quad (23)$$

As can be seen in Fig. 7, the magnitude value of (23) represents the rms voltage at the output,

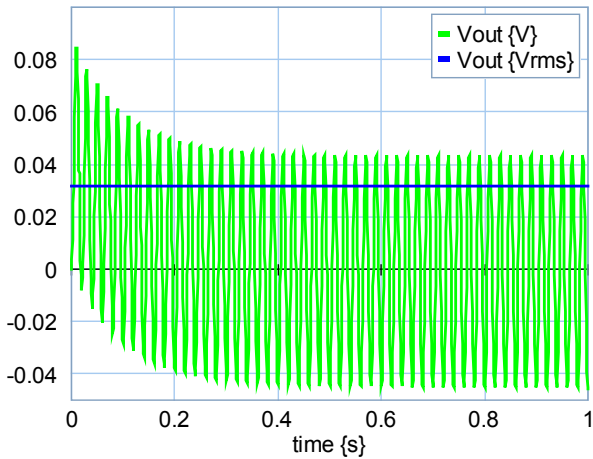


Fig. 7 Comparison between instantaneous output and steady-state value from the PhBG

One advantage of PhBG models arise at this point. As was described before, the impedance depends of the

frequency. If the impedances of a PhBG are rewritten as functions of the frequency (see Table 1) is possible to obtain the steady-state response of the output under different frequencies, i.e. Bode, Nichols, and Nyquist plots. Equation (21) may be expressed as

$$\begin{bmatrix} e_{6 \text{ Re}} \\ e_{6 \text{ Im}} \end{bmatrix} = \frac{1}{\Delta} \begin{bmatrix} R^2 & -R(1/\omega C - \omega L) \\ R(1/\omega C - \omega L) & R^2 \end{bmatrix} \begin{bmatrix} e_{1 \text{ Re}} \\ e_{1 \text{ Im}} \end{bmatrix} \quad (24)$$

where $\Delta = R^2 + (1/\omega C - \omega L)^2$. By calculating the output magnitude in decibels, $e_{6 \text{ dB}} = 20 \log_{10}(e_6)$, and varying the frequency is possible to obtain the Bode magnitude and phase plot of the band pass filter, see Fig. 8.

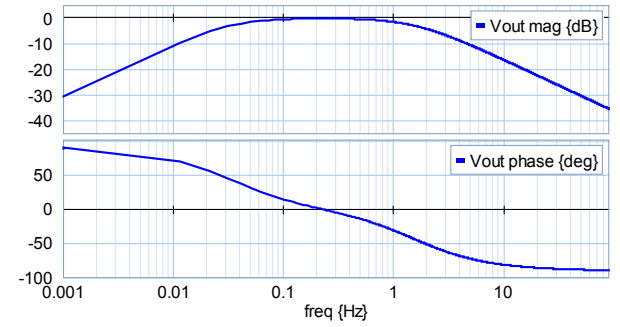


Fig. 8 Bode plot obtained from the PhBG

6. APPLICATION OF PHASOR BOND GRAPHS ON POWER FLOW ANALYSIS

This section deals with the steady-state analysis of an interconnected EPS during normal operation. The system is assumed to be operating under balanced condition and is represented by a single-phase network.

Power flow studies are the backbone of EPS analysis and design. They are necessary for planning, operation, economic scheduling and exchange of power between utilities. The principal information obtained from a power-flow study is the magnitude and phase angle of the voltage at each bus and the real and reactive power flowing in each line (Saadat, 1999).

The system buses are generally classified into three types: i) slack bus, it is taken as reference where the magnitude and phase angle of the voltage are specified; ii) load bus, the magnitude and the phase angle of the bus voltages are unknown; and iii) regulated bus, the real power and the voltage magnitude are specified. Clearly the conditions imposed by the different types of nodes make the problem nonlinear and therefore power-flow equations are commonly solved iteratively using techniques such as the Gauss-Seidel or Newton-Raphson method (Machowski, 2008; Kundur, 1994; Saadat, 1999; El-Harawy, 1995). A detailed description of these algorithms is beyond the scope of this paper but can be found in most textbooks on numerical methods or on power system analysis.

In order to demonstrate the application of PhBG in EPS analysis and to compare results the example illustrated in page 213 of (Saadat, 1999) is used. Fig. 9 shows the one-line diagram of a simple three-bus power system with

generation at bus a (slack bus). The magnitude of voltage at bus a is adjusted to 1.05 per-unit and 0° . The scheduled loads at buses b and c are as marked on the diagram. Line impedances and complex loads are marked in per-unit on a 100-MVA base and the line charging susceptances are neglected (Saadat, 1999).

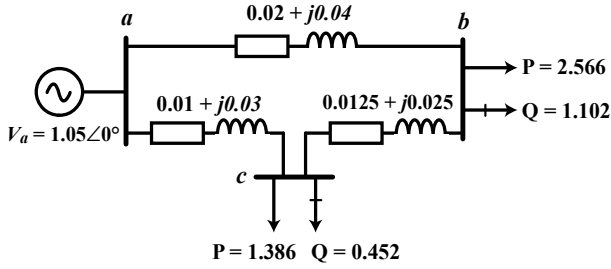


Fig. 9 One-line diagram of a three-bus EPS

The PhBG model of the EPS is shown in Fig. 10.

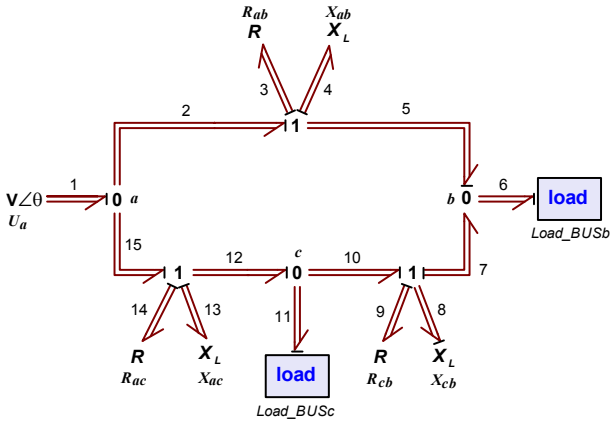


Fig. 10 PhBG model of the three-bus power system

The two load buses are modelled as flow sinks $(\vec{f}_6, \vec{f}_{11})$ because of the following reasons:

- it is necessary to determine the phasor values of the voltages at the load buses b and c , thus voltages at bonds 6 and 11 are defined as outputs,
- if the real and reactive powers are specified, then it is possible to rewrite (8) in the form

$$\begin{bmatrix} I_{\text{Re}} \\ I_{\text{Im}} \end{bmatrix} = \begin{bmatrix} V_{\text{Re}} & V_{\text{Im}} \\ V_{\text{Im}} & -V_{\text{Re}} \end{bmatrix}^{-1} \begin{bmatrix} P \\ Q \end{bmatrix} \quad (25)$$

- the complex voltage may be calculated by iterations.

The causality in the PhBG is propagated through the junction structure following the SCAP. The regular BG model of the power system would have had two elements in derivative causality, in this case (X_{ac}, X_{ab}) . Nevertheless, in the PhBG these two elements are simply modeled by the impedance of both inductive reactances. The key vectors are defined as,

$$\begin{aligned} \omega \mathbf{J} \bar{\mathbf{x}} &= \begin{bmatrix} \vec{f}_4 \\ \vec{e}_8 \\ \vec{f}_{13} \end{bmatrix} = \begin{bmatrix} f_{4 \text{ Re}} \\ f_{4 \text{ Im}} \\ e_{8 \text{ Re}} \\ e_{8 \text{ Im}} \\ f_{13 \text{ Re}} \\ f_{13 \text{ Im}} \end{bmatrix}; \quad \bar{\mathbf{z}} = \begin{bmatrix} \vec{e}_4 \\ \vec{f}_8 \\ \vec{e}_{13} \end{bmatrix} = \begin{bmatrix} e_{4 \text{ Re}} \\ e_{4 \text{ Im}} \\ f_{8 \text{ Re}} \\ f_{8 \text{ Im}} \\ e_{13 \text{ Re}} \\ e_{13 \text{ Im}} \end{bmatrix} \\ \bar{\mathbf{D}}_{\text{in}} &= \begin{bmatrix} \vec{f}_3 \\ \vec{f}_9 \\ \vec{f}_{14} \end{bmatrix} = \begin{bmatrix} f_{3 \text{ Re}} \\ f_{3 \text{ Im}} \\ f_{9 \text{ Re}} \\ f_{9 \text{ Im}} \\ f_{14 \text{ Re}} \\ f_{14 \text{ Im}} \end{bmatrix}; \quad \bar{\mathbf{u}} = \begin{bmatrix} \vec{e}_1 \\ \vec{f}_6 \\ \vec{f}_{11} \end{bmatrix} = \begin{bmatrix} e_{1 \text{ Re}} \\ e_{1 \text{ Im}} \\ f_{6 \text{ Re}} \\ f_{6 \text{ Im}} \\ f_{11 \text{ Re}} \\ f_{11 \text{ Im}} \end{bmatrix} \\ \bar{\mathbf{D}}_{\text{out}} &= \begin{bmatrix} \vec{e}_3 \\ \vec{e}_9 \\ \vec{e}_{14} \end{bmatrix} = \begin{bmatrix} e_{3 \text{ Re}} \\ e_{3 \text{ Im}} \\ e_{9 \text{ Re}} \\ e_{9 \text{ Im}} \\ e_{14 \text{ Re}} \\ e_{14 \text{ Im}} \end{bmatrix}; \quad \bar{\mathbf{y}} = \begin{bmatrix} \vec{e}_6 \\ \vec{e}_{11} \end{bmatrix} = \begin{bmatrix} e_{6 \text{ Re}} \\ e_{6 \text{ Im}} \\ e_{11 \text{ Re}} \\ e_{11 \text{ Im}} \end{bmatrix} \end{aligned} \quad (26)$$

The constitutive relations of the transmission line elements are

$$\begin{aligned} \bar{\mathbf{F}} &= \text{diag} \left\{ X_{ab} \mathbf{J}^{-1}, \frac{1}{X_{cb}} \mathbf{J}, X_{ac} \mathbf{J}^{-1} \right\} \\ \bar{\mathbf{L}} &= \text{diag} \left\{ R_{ab} \mathbf{I}_{2 \times 2}, R_{cb} \mathbf{I}_{2 \times 2}, R_{ac} \mathbf{I}_{2 \times 2} \right\} \end{aligned} \quad (27)$$

For this system, the following junction structure matrices can be constructed:

$$\begin{aligned} \bar{\mathbf{S}}_{11} &= \begin{bmatrix} \mathbf{0}_{2 \times 2} & -\mathbf{I}_{2 \times 2} & \mathbf{0}_{2 \times 2} \\ \mathbf{I}_{2 \times 2} & \mathbf{0}_{2 \times 2} & -\mathbf{I}_{2 \times 2} \\ \mathbf{0}_{2 \times 2} & \mathbf{I}_{2 \times 2} & \mathbf{0}_{2 \times 2} \end{bmatrix} \\ \bar{\mathbf{S}}_{12} &= \begin{bmatrix} \mathbf{0}_{2 \times 2} & \mathbf{0}_{2 \times 2} & \mathbf{0}_{2 \times 2} \\ \mathbf{I}_{2 \times 2} & -\mathbf{I}_{2 \times 2} & -\mathbf{I}_{2 \times 2} \\ \mathbf{0}_{2 \times 2} & \mathbf{0}_{2 \times 2} & \mathbf{0}_{2 \times 2} \end{bmatrix} = -\bar{\mathbf{S}}_{21}^T \\ \bar{\mathbf{S}}_{13} &= \begin{bmatrix} \mathbf{0}_{2 \times 2} & \mathbf{I}_{2 \times 2} & \mathbf{0}_{2 \times 2} \\ \mathbf{0}_{2 \times 2} & \mathbf{0}_{2 \times 2} & \mathbf{0}_{2 \times 2} \\ \mathbf{0}_{2 \times 2} & \mathbf{0}_{2 \times 2} & \mathbf{I}_{2 \times 2} \end{bmatrix} = \bar{\mathbf{S}}_{23} \\ \bar{\mathbf{S}}_{31} &= \begin{bmatrix} -\mathbf{I}_{2 \times 2} & \mathbf{0}_{2 \times 2} & \mathbf{0}_{2 \times 2} \\ \mathbf{0}_{2 \times 2} & \mathbf{0}_{2 \times 2} & -\mathbf{I}_{2 \times 2} \end{bmatrix} = \bar{\mathbf{S}}_{32} \\ \bar{\mathbf{S}}_{33} &= \begin{bmatrix} \mathbf{I}_{2 \times 2} & \mathbf{0}_{2 \times 2} & \mathbf{0}_{2 \times 2} \\ \mathbf{I}_{2 \times 2} & \mathbf{0}_{2 \times 2} & \mathbf{0}_{2 \times 2} \end{bmatrix} \end{aligned} \quad (28)$$

Substituting (28) into (16), the steady-state symbolic function of the outputs is expressed by

$$\begin{aligned} \bar{\mathbf{y}} &= (\bar{\mathbf{C}}(\bar{\mathbf{F}}^{-1} - \bar{\mathbf{A}})^{-1} \bar{\mathbf{B}} + \bar{\mathbf{D}}) \bar{\mathbf{u}} \\ &= \frac{1}{\Delta} \begin{bmatrix} 1 & 0 & H_{13} & H_{14} & H_{15} & H_{16} \\ 0 & 1 & H_{23} & H_{24} & H_{25} & H_{26} \\ 1 & 0 & H_{33} & H_{34} & H_{35} & H_{36} \\ 0 & 1 & H_{43} & H_{44} & H_{45} & H_{46} \end{bmatrix} \bar{\mathbf{u}} \end{aligned} \quad (29)$$

where,

$$\begin{aligned}
H_{13} &= (r_{ab}^2 - X_{ab}^2)\alpha - r_{ab}(\Delta - 2X_{ab}\beta) \\
H_{14} &= (r_{ab}^2 - X_{ab}^2)\beta + X_{ab}(\Delta - 2r_{ab}\alpha) \\
H_{15} &= (X_{ab}X_{ac} - r_{ab}r_{ac})\alpha - (r_{ac}X_{ab} + X_{ac}r_{ab})\beta \\
H_{16} &= (r_{ac}X_{ab} + X_{ac}r_{ab})\alpha + (X_{ab}X_{ac} - r_{ab}r_{ac})\beta \\
H_{35} &= (r_{ac}^2 - X_{ac}^2)\alpha - r_{ac}(\Delta - 2X_{ac}\beta) \\
H_{36} &= (r_{ac}^2 - X_{ac}^2)\beta + X_{ac}(\Delta - 2r_{ac}\alpha) \\
H_{23} &= -H_{14}; \quad H_{24} = H_{13}; \quad H_{25} = -H_{16} = H_{43} \\
H_{26} &= H_{15} = H_{44} = H_{33}; \quad H_{34} = H_{16} \\
H_{45} &= -H_{36}; \quad H_{46} = H_{35}
\end{aligned} \tag{30}$$

with $\alpha = r_{ab} + r_{ac} + r_{cb}$, $\beta = X_{ab} + X_{ac} + X_{cb}$, and $\Delta = \alpha^2 + \beta^2$. After substituting the numerical parameters is possible to generate the iterative equation necessary to obtain the node voltage magnitude and angle. Thus,

$$\bar{\mathbf{y}}^{(k+1)} = \begin{bmatrix} 1 & 0 & -0.011 & 0.023 & -0.005 & 0.013 \\ 0 & 1 & -0.023 & -0.011 & -0.013 & -0.005 \\ 1 & 0 & -0.005 & 0.013 & -0.008 & 0.021 \\ 0 & 1 & -0.013 & -0.005 & -0.021 & -0.008 \end{bmatrix} \bar{\mathbf{u}}^k \tag{31}$$

where,

$$\begin{aligned}
\bar{\mathbf{y}}^{(k+1)} &= \begin{bmatrix} e_{6 \text{ Re}}^{(k+1)} \\ e_{6 \text{ Im}}^{(k+1)} \\ e_{11 \text{ Re}}^{(k+1)} \\ e_{11 \text{ Im}}^{(k+1)} \end{bmatrix}; \quad \bar{\mathbf{u}}^k = \begin{bmatrix} 1.05 \\ 0 \\ f_{6 \text{ Re}}^k \\ f_{6 \text{ Im}}^k \\ f_{11 \text{ Re}}^k \\ f_{11 \text{ Im}}^k \end{bmatrix} \\
\begin{bmatrix} f_{6 \text{ Re}}^k \\ f_{6 \text{ Im}}^k \end{bmatrix} &= \begin{bmatrix} e_{6 \text{ Re}}^k & e_{6 \text{ Im}}^k \\ e_{6 \text{ Im}}^k & -e_{6 \text{ Re}}^k \end{bmatrix}^{-1} \begin{bmatrix} 2.566 \\ 1.102 \end{bmatrix} \\
\begin{bmatrix} f_{11 \text{ Re}}^k \\ f_{11 \text{ Im}}^k \end{bmatrix} &= \begin{bmatrix} e_{11 \text{ Re}}^k & e_{11 \text{ Im}}^k \\ e_{11 \text{ Im}}^k & -e_{11 \text{ Re}}^k \end{bmatrix}^{-1} \begin{bmatrix} 1.386 \\ 0.452 \end{bmatrix}
\end{aligned} \tag{32}$$

with the number of iterations $k = 0, \dots, n$. The updated voltages immediately replace the previous values in the solution of the subsequent equations. The process is continued until changes in the real and imaginary components of bus voltages between successive iterations are within a specified accuracy, typically 1×10^{-5} to 5×10^{-5} per-unit.

Starting from an initial value of $e_{6 \text{ Re}}^{(0)} = 1$, $e_{6 \text{ Im}}^{(0)} = 0$ and $e_{11 \text{ Re}}^{(0)} = 1$, $e_{11 \text{ Im}}^{(0)} = 0$, and after seven iterations the final solution in per-unit is

$$\begin{bmatrix} e_{6 \text{ Re}} \\ e_{6 \text{ Im}} \\ e_{11 \text{ Re}} \\ e_{11 \text{ Im}} \end{bmatrix} = \begin{bmatrix} 0.98 \\ -0.0599 \\ 1.0 \\ -0.0499 \end{bmatrix} \tag{33}$$

The solution given by (33) is the same than the one given in (Saadat, 1999). The above result was obtained by both matrix equations in MATLAB® and PhBG model in 20-sim®. Note that, if the reader wish to implement the PhBG model on 20-sim® is necessary to write (32) in the load blocks by means of a delay command.

7. CONCLUSIONS

This study has found that the implementation of 2D multibonds as description of a complex plane successfully may describe a phasor into the BG methodology, which is important because the widespread use of phasors in the analysis of EPS.

One of the significant findings to emerge from this study is that this approach may be implemented in a software tool like, for instance, 20-sim®, which was used in this paper. Thus, it is not only possible to obtain a symbolic function that describes a phasor but also to obtain a numerical simulation. Moreover, the characteristics of BG methodology allow us to maintain the topology of the EPS, and because BG is a form of object-oriented modelling the user may change the complexity of the submodels, e.g. transmission lines models may be easily changed.

When a PhBG model is applied to EPS analysis, the node voltages and angles may be obtained. The usage of delay commands in the simulation allow us to have an iterative PhBG model.

Further research might explore the application of PhBG in other domains where the steady-state is necessary. Other field of research could be the model order reduction in the steady-state. In (Louca, 2014) is proposed to measure the activity (an energy-metric) in steady-state of a quarter car model under different input frequencies. The steady-state activity equations proposed therein may be related to PhBG models.

ACKNOWLEDGMENT

The authors wish to thank CONACYT (Mexican National Council of Science and Technology) and SEP (Mexican Secretary of Public Education) for the funding of this research. We are also immensely grateful to the reviewers for their comments on the draft version of this paper.

REFERENCES

- Anderson P.M., Fouad A.A., 2003, Power System Control and Stability. 2nd edition, John Wiley & Sons, USA.
- Bonderson L.S., 1975, "Vector Bond Graphs Applied to One-Dimensional Distributed Systems", J. Dyn. Sys. Meas. Control 97(1), 75-82.
- Borutzky W. (Ed.), 2010, Bond Graphs: A Methodology for Modelling Multidisciplinary Dynamic Systems, Springer, London.
- Breedveld P.C., 1984a, "A Bond Graph Algorithm to Determine the Equilibrium State of a System", Journal of the Franklin Institute, vol. 318, No. 2, pp.71-75.

- Breedveld P.C., 1984b, "Physical systems theory in terms of bond graphs", Thesis (PhD), University of Twente, Netherlands, ISBN 90-9000599-4.
- Breedveld P.C., 1985, "Multibond graph elements in physical systems theory", *Journal of the Franklin Institute*, 319(1/2):1-36.
- Chapman S.J., 2005, *Electric Machinery Fundamentals*, 4th edition, McGraw-Hill, New York.
- El-Hawary M.E., 1995, *Electrical Power Systems*, John Wiley & Sons, New York.
- Gonzalez-A G., 2003, "Steady-State Values for a Physical System with Bond Graph Approach", 9th IEEE International Conference on Methods and Models in Automation and Robotics, pp. 25-28, Miedzyzdroje, Poland.
- Karnopp D.C., Margolis D.L., and Rosenberg R.C., 1990, *System Dynamics: A Unified Approach*. John Wiley & Sons, Inc., New York, USA.
- Karnopp D.C., and Rosenberg R.C., 1968, *Analysis and Simulation of Multiport Systems - The Bond Graph Approach to Physical System Dynamics*. MIT Press, Cambridge, MA.
- Kundur P., 1994, *Power System Stability and Control*. Mc-GrawHill, California, USA.
- Kypuros J.A., 2013, *System Dynamics and Control with Bond Graph Modeling*, Taylor & Francis Group, USA.
- Louca L.S., 2014, "Power Conserving Bond Graph Based Modal Representations and Model Reduction of Lumped Parameter Systems", *J. Dyn. Sys., Meas., Control* 136(6), 061007 (13 pages).
- Machowski J., Bialek J.W., Bumby J.R., 2008, *Power System Dynamics: Stability and Control*. 2nd edition, John Wiley & Sons, Great Britain.
- Paynter H.M., 1961, *Analysis and Design of Engineering Systems*, The M.I.T. Press, Cambridge, Massachusetts.
- Rosenberg R.C., 1971, "State-space formulation for bond-graph models of multiport systems", *J. Dyn. Syst. Meas. Control*, 93(1): 35-40.
- Saadat H., 1999, *Power System Analysis*, McGraw-Hill, New York.
- Steinmetz C.P., 1893, "Complex Quantities and their use in Electrical Engineering", *Proceedings of the International Electrical Congress, AIEE Proceedings*, pp. 33-74.
- Veltman A., Pulle D.W.J., and De Doncker R.W., 2007, *Fundamentals of Electrical Drives*, Springer.

HYBRIDIZATION EFFECT ON FUEL CONSUMPTION AND OPTIMAL SIZING OF COMPONENTS FOR HEV

Mauro G. Carignano^(a), Norberto M. Nigro^(b), Sergio Junco^(c)

^(a) EIM, Escuela de Ingeniería Mecánica, Facultad de Ciencias Exactas, Ingeniería y Agrimensura, Universidad Nacional de Rosario, Berutti 2109, Rosario, Argentina.

^(b) CIMEC, Centro Internacional de Métodos Computacionales en Ingeniería, INTEC-CONICET-UNL, Güemes 3450, Santa Fe, Argentina.

^(c) LAC, Laboratorio de Automatización y Control, Facultad de Ciencias Exactas, Ingeniería y Agrimensura, Universidad Nacional de Rosario, Riobamba 250bis, Rosario, Argentina.

^(a)mauroc@fceia.unr.edu.ar, ^(b)norberto.nigro@cimec.santafe-conicet.gov.ar, ^(c)sjunco@fceia.unr.edu.ar

ABSTRACT

Reductions of fuel consumption and gas emissions count among the main advantages of hybrid electric vehicles (HEV). It is well known that the level of hybridization has a large influence on the fuel consumption. On the other hand, the cost of manufacturing HEV increases since at least two power sources are required. Therefore, a proper selection of the hybridization factor (HF) could be the result of a tradeoff between fuel consumption and cost. This paper shows how HF affects fuel consumption of a HEV. The work was realized using Series and Parallel architectures, with an internal combustion engine and electrochemical batteries as thermal machine and storage system respectively. Simulations with different HF are evaluated using urban and road driving profiles. In order to achieve optimal power split, dynamic programming was applied. The results show that there exists an optimal HF which generates the minimum fuel consumption for each architecture. According that, the optimal size of components are found for each case analyzed.

Keywords: hybrid electric vehicle, hybridization factor, fuel consumption, optimization

1. INTRODUCTION

Hybrid electric vehicles have had a great saving fuel compared with conventional internal combustion engine vehicles due to both, recovering braking energy and higher efficiency operation of the internal combustion engine (ICE). Accordingly, hybridization power-train of conventional vehicles makes them more efficient and cleaner. The hybridization factor (HF) is an important feature of the HEV, which points out the ratio between the installed power coming from electric source and total installed power. Commercial HEV have shown improved fuel consumption as HF is increased. Improving up to 45% efficiency can be achieved with full-HEV (Tie and Tan 2013). Contrasting to the advantages mentioned above, HEVs have higher costs than conventional vehicles because extra components such as electric machines and energy storage systems are required.

Depending on the kind of HEV, the battery cost can reach one-third of the total vehicle cost (Tie and Tan 2013). Other issues like security, space, and life cycle are associated with some components of HEV. Therefore, proper election of the HF for a HEV has no trivial answer, but rather it will result from a complex tradeoff taken into account the fuel consumption, manufacturing costs and lifecycle, among others.

This work shows how HF affects the fuel consumption of the HEV. Energetic approach and backward models (Chan, Bouscayrol and Chen 2010) are used to perform the study. Specifically, Series and Parallel-HEV architectures with different HF are analyzed using urban and road driving cycle. Electrochemical batteries and internal combustion engine are used as energy storage system and thermal machine respectively.

Previous works from other authors addressed similar issues. Lukic et al. (Lukic and Emadi 2004) and Holder and James (Holder and Gover 2006) worked with Parallel-HEVs using ADVISOR. Capata and Coccia (Capata and Coccia 2010) tests Series-HEV with a gas turbine as thermal engine. Cuddy and Wipke (Cuddy and Wipke 1997) evaluate Series and Parallel-HEVs consumption through ADVISOR simulation. In all of them the power split was realized through suboptimal strategy of Supervisory Control (SC). It is known that SC has a large effect on fuel consumption (Sciarretta, Serrao, Dewangan, Tona, Bergshoeff, Bordons and Wu 2014). In this work, unlike the above, an optimal instead of suboptimal SC strategy is applied in order to achieve a better comparison. Specifically, dynamic programming is used to reach the minimal fuel consumption for each configuration.

The paper is organized as follows. First, models of the HEV components are described in Section II. Then, component sizing, backward approach and SC strategy are presented in Section III. Details and results of simulations are summarized in Section IV. Finally, some conclusions, comments and futures works are pointed out in Section V.

2. HYBRID ELECTRIC VEHICLE MODEL

2.1. Architectures

HEVs are frequently classified regarding drive-train architecture. The most popular and widely used are Series, Parallel and Series/Parallel. The two first are discussed in this work. Although there exist different possibilities inside each drivetrain architecture, only those shown in Figure 1 will be utilized.

As shown, most of the typical HEV components are present in both architectures. The generator is only present in the Series architecture, whereas in the Parallel two gear boxes are required. Main difference is in the way of interconnection. Each component is related to the rest through a power flow. As mentioned in introduction, this approach leads to an energetic and power analysis.

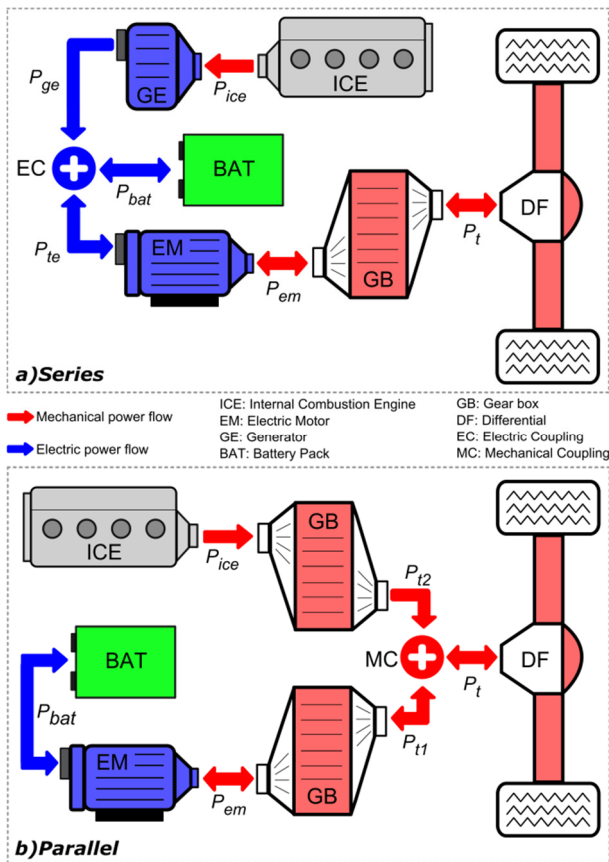


Figure 1: Architectures a) Series b) Parallel

Some components shown in Fig. 1 are considered to be ideal, i.e. power lossless. This group includes differential, mechanical and electric coupling. The ideal Electrical and mechanical coupling are represented by the following power balance equations:

$$\text{Electrical Coupling: } P_{te} = P_{bat} + P_{ge} \quad (1)$$

$$\text{Mechanical Coupling: } P_t = P_{t1} + P_{t2} \quad (2)$$

On the other hand, for electric motor, internal combustion engine, generator, battery and gear box, efficiency values are considered as simplified models. This will be explained in detail in Section III.

2.2. Hybridization Factor (HF)

In order to evaluate the influence of HF on the fuel consumption, this concept would be defined explicitly for both architectures. For Parallel and Series/Parallel-HEV, HF is the relation between the maximum power of the electric motor and the total installed power (Lukic, Cao, Bansal, Rodríguez and Emadi, 2008). This is:

$$HF \triangleq \frac{P_{em_max}}{P_{em_max} + P_{ice_max}} \quad (3)$$

Where P_{x_max} is the maximum power that component "x" is able to deliver and/or receive. This definition is not suitable for Series-HEV. For example, if maximum power from battery tend to zero, $P_{em_max} \cong P_{ice_max}$ and HF tend to 0.5 (see Fig.1a). HF should tend to zero 0 when maximum power from electric source tends to zero (like conventions vehicles or vehicles with electric drive-train without electric storage). Inversely, HF should tend to 1 when maximum power of fuel source tends to 0 (like purely electric vehicle).

In this work a slight modification to HF for Series-HEV is proposed. It is deduced following the idea that HF expresses the relation between maximum mechanical power coming from electric source and the maximum mechanical power coming from fuel + electric source. Accordingly, in case of Parallel-HEV (considering equal efficiency for both GBs), HF is correctly defined by Eq. 3. However, in case of Series-HEV, HF results:

$$HF \triangleq \frac{P_{bat_max} \cdot \eta_{em} \cdot \eta_{gb}}{P_{bat_max} \cdot \eta_{em} \cdot \eta_{gb} + P_{ice_max} \cdot \eta_{ge} \cdot \eta_{em} \cdot \eta_{gb}}$$

Assuming $P_{ice_max} \cdot \eta_{ge} = P_{ge_max}$ and simplifying leads to:

$$HF \triangleq \frac{P_{bat_max}}{P_{bat_max} + P_{ge_max}} \quad (4)$$

Eq. (3) and Eq. (4) could be seen as a relation between the maximum powers involved in coupling component (see Fig.1). These expressions will be used in Section III to define the size of the components.

2.3. Electric motor, Generator, Internal combustion engine and Gear box

Fuel consumption and global efficiency of a HEV depend on the efficiency of each drive-train component. EM, GE, ICE and GB are the main components that contribute to overall efficiency. Due to the high complex phenomena present in each of these components, detailed analytical model should be employed to obtain its efficiency. A common practice is testing each of them and obtaining an efficiency surface as a function of port variables (voltage, current, speed and torque) (Sciarretta, Serrao, Dewangan, Tona, Bergshoeff, Bordons and Wu 2014). Processing this surface it is possible to extract a curve of best efficiency as function of output power. It

other words, each value on the curve represents the best possible efficiency for each power value. It is assumed that GB is automatic and able to position the ICE and EM on a speed that generates the best efficiency. Here, data from EM, GE, ICE and GB similar to those used on the Toyota Prius are considered as reference (Wipke, Cuddy and Burch 1999; Olszewski 2005). Because GB shows low efficiency variations, a constant $\eta_{GB} = 0.95$ is considered in all power range.

The maximum power of each component changes according to the architecture and HF selected. So it is useful in these cases to work with normalized efficiency curves. Once defined the maximum power of the components, final efficiency tables are generated scaling linearly these curves. Figure 2 shows normalized curves of efficiency for EM, GE and ICE respectively.

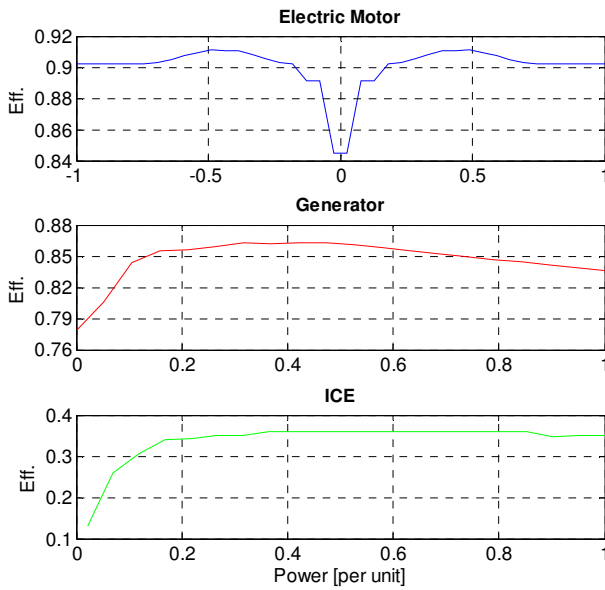


Figure 2: Efficiency of components

Notice that the EM can work both as motor and generator, whereas GE and ICE only work as power suppliers. Efficiency of power electronics converters as rectifiers or inverters are included in these curves.

2.4. Battery model

In this subsection, in contrast with previous ones, an explicit expression of battery efficiency and energy storage will be deducted.

Generally a battery is composed by a number of electrochemical cells (N_{cell}). However, it can be idealized as a system composed of a single component. Accordingly, a model of battery used to get its efficiency is presented in Fig. 3. It consists on an ideal voltage source and an internal resistance connected in series, so only ohmic losses are considered. Variations of voltage and resistance in function of state of charge of battery are neglected.

$P_{0bat} \triangleq I_{bat} U_{0bat}$ is the power flow from the ideal electric source, and $P_{bat} \triangleq U_{bat} I_{bat}$ is the power flow as seen from battery terminals. The power balance leads to:

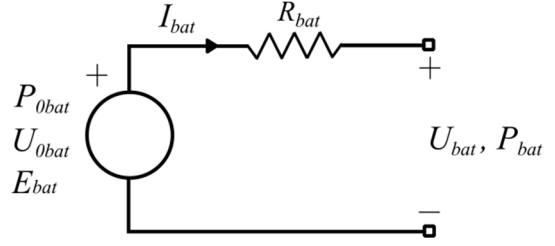


Fig. 3: Battery circuit model

$$P_{0bat} - I_{bat}^2 R_{bat} - P_{bat} = 0 \quad (5)$$

The battery energy storage and state of charge can be expressed as:

$$E_{bat}(t) = E_{t0bat} - \int_0^t P_{0bat}(\tau) d\tau \quad (6)$$

$$SoC(t) = \frac{E_{bat_max} - E_{bat}(t)}{E_{bat_max}} \quad (7)$$

Where E_{bat_max} and E_{t0bat} are full energy capacity and initial energy of battery respectively.

As will be seen later, P_{bat} will be a control variable and E_{bat} a state variable. So it is necessary to obtain an expression to evaluate $E_{bat}(t)$ using P_{bat} as input. The battery efficiency is defined as:

$$\eta_{bat}(P_{bat}) \triangleq \frac{P_{bat}}{P_{0bat}} \quad (8)$$

Using eq. (5) and $I_{bat} = \frac{P_{0bat}}{U_{0bat}}$, P_{bat} can be written as:

$$P_{bat} = P_{0b} - \left(\frac{P_{0bat}}{U_{0bat}} \right)^2 R \quad (9)$$

Then, P_{0bat} can be written as function of P_{bat} as follows:

$$P_{0bat} = \frac{U_{0bat}^2}{2R} \left(1 + \sqrt{1 - \left(\frac{4R P_{bat}}{U_{0bat}^2} \right)} \right) \quad (10)$$

Using eq. (9) and eq. (10) in (8), the efficiency results:

$$\eta_{bat}(P_{bat}) = \frac{1}{2} \left(1 + \sqrt{1 - \left(\frac{4R P_{bat}}{U_{0bat}^2} \right)} \right) \quad (11)$$

This is an expression of battery efficiency, with R_{bat} and U_{0bat} as parameters. It will be useful to further analysis to use the maximum battery power (P_{bat_max}) as parameter instead of the previous two.

P_{bat_max} could be calculated from the maximum allowed voltage variation ΔU_{bat_max} . It can see that using $\Delta U_{bat_max} \triangleq 0.2 U_{0bat}$, the maximum battery power results:

$$P_{bat_max} = 0.16 \frac{U_{0bat}^2}{R} \quad (12)$$

Using eq. (12) in eq. (11) the battery efficiency results:

$$\eta_{bat}(P_{bat}) = \frac{1}{2} \left(1 + \sqrt{1 - \left(\frac{0.64 P_{bat}}{P_{bat_max}} \right)} \right) \quad (13)$$

This is the final expression desired. It is worth noticing that this efficiency expression only depends on the maximum battery power. Figure 4 shows battery efficiency as function of P_{bat} per unit.

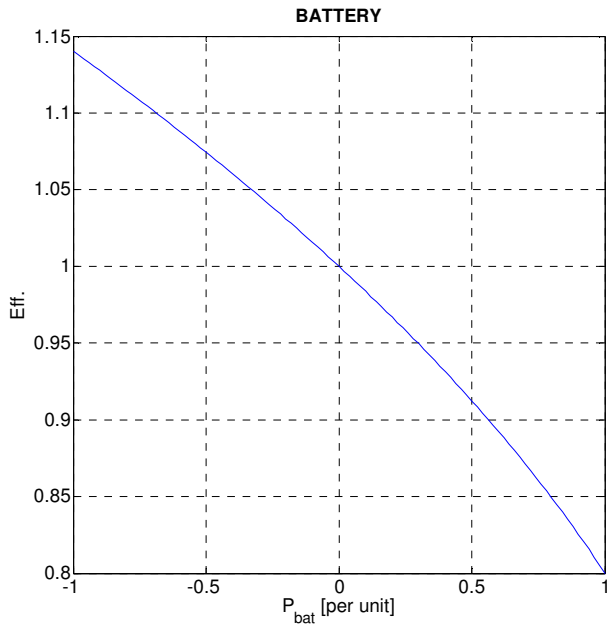


Fig. 4: Battery efficiency

Finally, from eq. (6), E_{bat} can be expressed as follows:

$$E_{bat}(t) = E_{t0bat} - \int_0^t \frac{P_{bat}(\tau)}{\eta_{bat}(P_{bat}(\tau))} d\tau \quad (14)$$

Returning to the idea of a battery as a set of cells, for a given electrochemical cell, the relation between P_{bat_max} and N_{cell} can be calculated as:

$$N_{cell} = \frac{P_{bat_max}}{P_{cell_max}} \quad (15)$$

Where, similar to eq. (12):

$$P_{cell_max} = \frac{0.16 U_{0cell}^2}{R_{cell}} \quad (16)$$

Then, N_{cell} can be evaluated from these two equations at each configuration proposed.

3. METHODOLOGY

3.1. Sizing components

The size of a component in a HEV is generally expressed by the maximum power the component is able to deliver or receive. In this subsection power requirements and constraints will be defined and used to size the components of the HEV. This allows to perform reasonable comparisons between different configurations and architectures.

In the batteries, the size could be defined by either the maximum power flow allowed or the storage capacity (Carignano, Cabello and Junco 2014). Results obtained in current paper have shown that, in all cases of HEV simulated, the battery size is conditioned by the maximum flow power. This means that the minimum charge level is never reached if the battery has been sized according to the maximum power flow.

Main requirement to take into account for sizing is the maximum total power of HEV, i.e. the maximum power available at wheels (P_{t_max}). For this work the value $P_{t_max} = 75 \text{ kW}$ was considered.

Moreover, some power constraints must be fulfilled for each architecture. These can be easily derived from Figure 1. In case of Series-HEV:

$$P_{em_max} = \frac{P_{t_max}}{\eta_{gb}} \quad (17)$$

$$P_{ge_max} + P_{bat_max} = \frac{P_{em_max}}{\eta_{em}(P_{em_max})} \quad (18)$$

$$P_{ice_max} = \frac{P_{ge_max}}{\eta_{ge}(P_{ge_max})} \quad (19)$$

For the Parallel-HEV the power constraints are:

$$P_{em_max} + P_{ice_max} = \frac{P_{t_max}}{\eta_{gb}} \quad (20)$$

$$P_{bat_max} = \frac{P_{em_max}}{\eta_{em}(P_{em_max})} \quad (21)$$

Notice that for Series-HEV there are 3 equations and 4 unknowns (P_{em_max} ; P_{ge_max} ; P_{bat_max} ; P_{ice_max}), while for parallel-HEV there are 2 equations and 3 unknowns (P_{em_max} ; P_{bat_max} ; P_{ice_max}). The remaining equation in both cases is provided by the HF definitions presented in subsection 2.2.

Finally, a constraint from minimum road speed imposes that the HEV must be able to maintain a constant speed of 120Km/h without using electric source, i.e. working only with ICE. This restriction will limit the minimum size of the ICE.

3.2. Backward approach and Supervisory control

As mentioned in the introduction, backward models (Chan, Bouscayrol and Chen 2010) are used in this work. This approach avoids using low level controllers (typically PID) in order to follow speed references. This

obtained. This procedure was repeated for each architecture and for each HF proposed. The results obtained are shown in the following section.

4. SIMULATION RESULTS

Two different driving cycles, an urban and a road cycle were selected to perform simulations (André 2004). Each of the described architectures was tested with different HF using these cycles. Table 1 summarizes the parameters common to all HEV configurations.

Table 1: Parameters of HEV

Vehicle Model	Total mass, m	1400 Kg
	Frontal area, A_f	2 m^2
	Drag coefficient, D_c	0.3
	Rolling resistance, $r_0 ; r_1$	$0.015; 7 \cdot 10^{-6} \text{ m}^2/\text{s}^2$
Battery's cells	Nominal voltage, U_{ocell}	1.25 V
	Internal resistance, R_{cell}	0.002Ω
	Nominal energy, E_{ocell}	8.12 Wh
Gear box	Efficiency, η_{gb}	0.95
Fuel	Lower heating value, Q_{LHV}	42.6 kJ/g

For each configurations tested, the following sequence was employed: setting HF and sizing component according to Section 3; updating efficiency of component according to the model presented in Section 2; running the DP algorithm; running simulation using backward model.

Fig. 6 shows the effect of HF on fuel consumption, which is expressed in liters per 100km. $HF = 0$ correspond to conventional ICE-vehicles, whereas $HF = 0.83$ corresponds to the minimum possible size of ICE that assures sustained charge of battery at the end of the cycle. Vertical dotted red line denotes HF_{max} , which expresses maximum HF according to the road speed constraint mentioned in Subsection 2-1.

In all cases it can be seen that the fuel consumption curve is concave, which ensures the existence of a minimum. Specifically there exists an optimum HF for which the fuel consumption reaches a minimum value (HF_{opt}). It is worth noticing that in all cases $0 < HF_{opt} < HF_{max}$. Furthermore, Fig. 6 shows that effect of reductions in fuel consumption decreases as HF increases until reaching HF_{opt} , then the fuel consumptions is kept approximately constant or slightly increased as HF increases.

Comparing optimal HEV with conventional vehicles (i.e. $HF = 0$) it can be seen that reduction of the fuel consumption reaches 43% for urban profile and 20% for road profile, approximately.

Finally, comparing both architectures, it can be seen that the parallel configuration has the lowest fuel

consumption. Table 2 summarizes optimal size of components for each of the simulated cases.

It is worth noticing that in Series architecture HF_{opt} is the same for both driving profiles. This is different to the Parallel architecture although their values are close to each other.

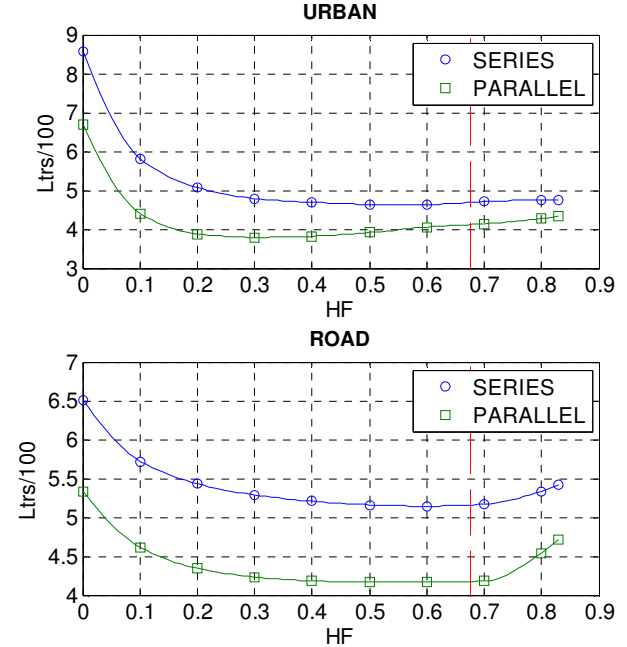


Fig. 6: Hybridization effect on fuel consumption

Table III: Optimal HEV configuration

		SERIES	PARALLEL
URBAN	HF_{opt}	0.6	0.3
	Lts/100 km	4.636	3.790
	$P_{bat \ max}$	52.6 kW	26.3 kW
	N_{cell}	421	210
	$P_{ice \ max}$	42.3 kW	55.3 kW
ROAD	HF_{opt}	0.6	0.5
	Lts/100km	5.145	4.164
	$P_{bat \ max}$	52.6 kW	43.9 kW
	N_{cell}	421	350
	$P_{ice \ max}$	42.3 kW	39.5 kW

5. CONCLUSION

In this paper, hybridization effect on the fuel consumption of HEVs has been analyzed through simulations. Series and Parallel architectures were tested using urban and road driving profile. Architectures, models and sizing procedure were described along the work.

The results show similar behavior in all cases simulated. A great reduction in fuel consumption is achieved with low hybridization levels. Then, as HF increases, the fuel consumptions changes slightly until reaching a minimum. Beyond this value the consumption increases again. In all cases the optimum HF is placed in a region of the curve with a reduced slope. Besides these results, which are valid only for the particular cases simulated, it

is worth mentioning that the methodology presented in this paper is general enough to cover a wide range of problems concerning the optimization of HEVs. Following this line, we are working on improving current strategies of high level supervisory control applicable to HEVs in real-time.

REFERENCES

- André, M., 2004. The ARTEMIS European driving cycles for measuring car pollutant emissions. *Science of the total Environment*, 334, 73-84.
- Capata, R., & Coccia, A., 2010. Procedure for the design of a hybrid-series vehicle and the hybridization degree choice. *Energies*, 3(3), 450-461.
- Carignano, M. G., Cabello, J. M., & Junco, S., 2014. Sizing and performance analysis of battery pack in electric vehicles. In *Biennial Congress of Argentina (ARGENCON)*, 2014 IEEE (pp. 240-244). IEEE.
- Chan, C. C., Bouscayrol, A., & Chen, K., 2010. Electric, hybrid, and fuel-cell vehicles: Architectures and modeling. *Vehicular Technology, IEEE Transactions on*, 59(2), 589-598.
- Cuddy, M. R., & Wipke, K. B., 1997. Analysis of the fuel economy benefit of drivetrain hybridization (No. 970289). SAE Technical Paper.
- Holder, C., & Gover, J., 2006. Optimizing the hybridization factor for a parallel hybrid electric small car. In *Vehicle Power and Propulsion Conference, 2006. VPPC'06. IEEE* (pp. 1-5). IEEE.
- Kirk, D. E., 2012. *Optimal control theory: an introduction*. Courier Corporation.
- Lukic, S. M., & Emadi, A., 2004. Effects of drivetrain hybridization on fuel economy and dynamic performance of parallel hybrid electric vehicles. *Vehicular Technology, IEEE Transactions on*, 53(2), 385-389.
- Lukic, S. M., Cao, J., Bansal, R. C., Rodríguez, F., & Emadi, A., 2008. Energy storage systems for automotive applications. *IEEE Transactions on*, 55(6), 2258-2267.
- Olszewski, M., 2005. Evaluation of 2004 TOYOTA PRIUS Hybrid electric drive system. *Energy Efficiency and Renewable Energy, FreedomCAR and Vehicle Technologies, Vehicle Systems Team, Oak Ridge*.
- Pérez, L. V., Bossio, G. R., Moitre, D., & García, G. O., 2006. Optimization of power management in an hybrid electric vehicle using dynamic programming. *Mathematics and Computers in Simulation*, 73(1), 244-254.
- Sciarretta, A., Serrao, L., Dewangan, P. C., Tona, P., Bergshoeff, E. N. D., Bordons, C., ... & Wu, M., 2014. A control benchmark on the energy management of a plug-in hybrid electric vehicle. *Control Engineering Practice*, 29, 287-298.
- Tie, S. F., & Tan, C. W., 2013. A review of energy sources and energy management system in electric vehicles. *Renewable and Sustainable Energy Reviews*, 20, 82-102.
- Vinot, E., Trigui, R., Cheng, Y., Espanet, C., Bouscayrol, A., & Reinbold, V., 2014. Improvement of an EVT-based HEV using dynamic programming. *Vehicular Technology, IEEE Transactions on*, 63(1), 40-50.
- Wipke, K. B., Cuddy, M. R., & Burch, S. D., 1999. ADVISOR 2.1: a user-friendly advanced powertrain simulation using a combined backward/forward approach. *Vehicular Technology, IEEE Transactions on*, 48(6), 1751-1761.

AUTHORS BIOGRAPHY

Mauro G. Carignano received the Mechanical Engineering degree from Facultad de Ciencias Exáctas Ingeniería y Agrimensura de la Universidad Nacional de Rosario, Rosario, Argentina, in 2011. He is currently working toward the Ph.D. degree.

His research interests include optimal sizing of components and strategies of high level supervisory control for hybrid electric vehicles.

Norbeto M. Nigro received the Mechanical Engineer at Universidad Tecnológica Nacional de Buenos Aires in 1985, Got his doctorate in Engineering Sciences in Universidad Nacional de Cordoba during 1993 under the direction of Sergio Idelsohn in topics related to FEM solutions to CFD problems, especially stabilization. In 1994-1995 a postDoc in Minnesota Supercomputer Institute under the advisory of Tayfun Tezduyar. Since 1996 Researcher at CONICET (National Council of Science and Technology in Argentina). At present Principal Researcher of CONICET and Associate Professor of Universidad Nacional del Litoral at Santa Fe, Argentina in topics related with multiphase reactive flow problems by CFD with applications in energy management, in particular internal combustion engines, oil & gas and nuclear industries. Also his interest lies on external aerodynamics of vehicles.

Sergio Junco received the Electrical Engineer degree from the Universidad Nacional de Rosario in 1976. He joined the National University of Rosario in 1982, where he currently is a Full-time Professor of System Dynamics and Control and Head of the Automation and Control Systems Laboratory. His current research interests are in modeling, simulation, control and diagnosis of dynamic systems, with applications in the fields of motion control systems with electrical drives, power electronics, mechatronics, vehicle dynamics and smart grids. He has developed, and currently teaches, several courses at both undergraduate and graduate level on System Dynamics, Bond Graph Modeling and Simulation, Advanced Nonlinear Dynamics and Control of Electrical Drives, as well as Linear and Nonlinear Control with Geometric Tools.

DESIGN OF A HYDRAULIC TURBINE CONTROL SYSTEM BY NUMERICAL OPTIMIZATION

Roberto Canonico, Renato A. Aguiar, Fabrizio Leonardi

Centro Universitário da FEI, São Bernardo do Campo, Brazil

canonico.roberto@gmail.com, preraguiar@fei.edu.br, fabrizio@fei.edu.br

ABSTRACT

This work proposes the use of numerical optimization based on Direct Transcription as a method for the design of the control system for hydroelectric turbines. The control design for this application involves constraints but the usual control techniques do not allow explicitly to incorporate constraints in its formulation or are very sensitive to initial estimates of the optimization problem implying in convergence issues. The Direct Transcription is an alternative optimization-based design where the dynamics are discretized and included as constraints of the optimization problem causing the errors due to the quality of the initial estimate to be diluted over the discretization nodes. The constraints considered are related to the actuator and other operating limits during a change maneuver of operating point.

Keywords: Hydraulic Turbines Governors, Numerical Optimization, Direct Transcription.

1. INTRODUCTION

The majority of existing hydroelectric plants use Francis type turbines, and among these, the most of them use speed governors equipped with electro-hydraulic controllers, usually processing algorithms PID. In recent years, new techniques are under analysis to improve the regulation of the speed and power of the hydroelectric turbines.

Jiang, Ma and Wang (2006) proposed an evolutionary programming method based on a mutating factor for determining the optimized parameters of a PID controller of a speed governor for power hydroelectric turbines. The authors argue that it is possible to optimize the PID parameters efficiently and the system keeps stability characteristics, low variations and quick responses.

Qian, Yi and Liu (2011), using the order reduction feature, applied the Sliding Mode Control (SMC) technique. The authors present a case study emphasizing the robustness of the control problem.

In their paper, Ding and Sinha (2011) combined the SMC and H_∞ control techniques. The result are compared with those of traditional PI and LQR controllers, demonstrating that the proposed control technique improves system performance against load

disturbances and parametric uncertainties, with significant advantage.

Liu, Li and Huang (2012), in turn, propose a robust nonlinear controller based on a high gain observer. The process of adjusting the controller parameters is simplified and only one control parameter needs to be tuned. The objective function defined reflects the regulatory system characteristics of hydroelectric turbines, i.e., the actuator, the electric power generator and the rotor dynamics. The simulations showed that this method can provide a good and robust dynamic response.

The work of Hamarashed, Haris and Nopiah (2012) presents an adaptive multiple control technique. The controllers used are the LQG/LTR and the PI, optimized to meet the plant requirements. From the results obtained, the LQG/LTR control showed good performance for smooth changes of disturbance, but exhibiting oscillating response in situations of sudden changes. The PI controller, in turn, showed good performance for both, i.e., for smoothly or sudden disturbances.

The work of Singh, Naresh and Gupta (2013) proposes the use of genetic algorithms to determine the tuning parameters of a controller for compensation of the temporary droop in the regulation of hydroelectric turbines. The authors tested four different performance indices. The goals were to minimize the variation in speed, in face of two different steps sizes. After the tests, the ITAE performance index was chosen as the best option, so its associated parameters were adopted.

Anbo, Xiangang and Hao (2013) proposed a distributed multi-agent genetic algorithm applied in optimizing parameters of a self-adaptive PID, to be used in world's largest hydroelectric power plant located in China. The results show that the proposed simulation performed better when compared to the conventional genetic optimization algorithm, and furthermore reduced significantly the optimization time.

This work proposes an alternative solution to the control problem found in many installations of hydroelectric plants by means of an optimization strategy called Direct Transcription involving the parameters of a PID controller.

2. METHOD

The parametric optimal control problem of a hydraulic turbine was formulated as a nonlinear optimization problem and solved with the technique of direct transcription.

2.1. Dynamical Model

The hydroelectric plant facilities may have different settings related to the characteristics of each situation in which they are designed. In general, hydroelectric plants are composed of the items shown in Figure 1.

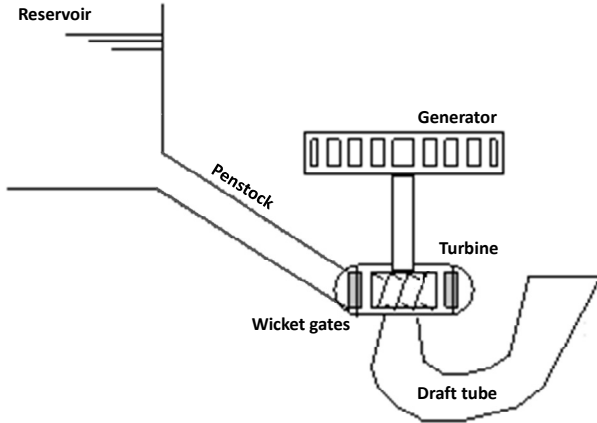


Figure 1: Typical hydroelectric plant.

For this work it was considered a plant without intake tunnel and surge tank. Based on the diagram of Jaeger *et al.* (1994), the block diagram of Figure 2 shows the typical control system for this kind of hydroelectric plant.

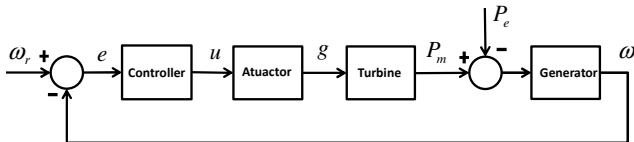


Figure 2: Control system of a hydraulic turbine.

The actuator is driven by a servo system which acts on the wicket gates ring of the turbine and its position determines the flow of water through the turbine. Based on the work of Qian, Yi and Liu (2011), the actuator can be expressed as a first order transfer function (1), disregarding the effects of the pilot valve and the dead-zone.

$$\frac{g}{u} = \frac{1}{1 + sT_G} \quad (1)$$

The block diagram in Figure 3 represent the hydraulic actuator transfer function of Equation (1). From that diagram, it is immediate to write Equation (7) to represent it in state space.

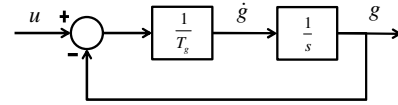


Figure 3: Block diagram of the hydraulic actuator.

For a Francis turbine connected to the reservoir via a single penstock without intake tunnel, the model suggested by Kundur (1993) and Machowski, Bialek and Bumby (2008) is given by

$$\frac{P_m}{g} = \frac{1 - sT_W}{1 + s\frac{T_W}{2}} \quad (2)$$

that is, a first order transfer function with a non-minimum-phase zero. The zero here models the inverse response, typical on maneuvers with hydraulic turbines.

The block diagram in Figure 4 also represent the turbine transfer function of Equation (2). The auxiliary variable x was chosen at output of the integrator so that the turbine can be fully represented in state space by means of Equations (9) and (12).

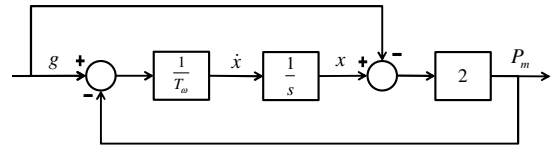


Figure 4: Detailed block diagram of the turbine.

As described by Kundur (1993), the generator receives the mechanical torque from the turbine by the rotor shaft and produces an electromagnetic torque. In a simplified manner, the dynamics of the generator is of first order

$$\frac{\omega}{(M_m - M_e)} = \frac{1}{K_D + sT_M} \quad (3)$$

where M_m is the mechanical torque and M_e is the equivalent torque related to the electrical load. For studies of frequency and load, it is preferred to express the equation (3) in terms of mechanical and electrical power, rather than torque. Based on the development Kundur (1993) and Machowski, Bialek and Bumby (2008), the torque deviation ($M_m - M_e$) is equivalent to the power deviation ($P_m - P_e$). Thus, the model of the generator can be represented by the block diagram in Figure 5 so that its model in state space results in Equation (10).

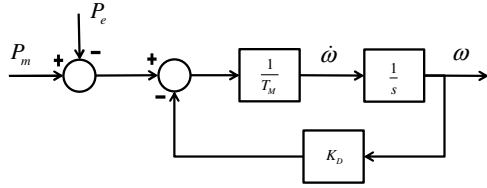


Figure 5: Detailed block diagram of the generator.

In real applications, the controller is typically a PID compensator whose transfer function is

$$\frac{u}{(\omega_r - \omega)} = K_p + \frac{K_i}{s} + \frac{K_d s}{T_d s + 1}, \quad (4)$$

The block diagram in Figure 6 also represent the PID transfer function of Equation (4) in a detailed way. The auxiliary variables z and v were chosen at outputs of the integrators so that the control law can be fully represented in state space by means of Equations (5), (6) and (11).

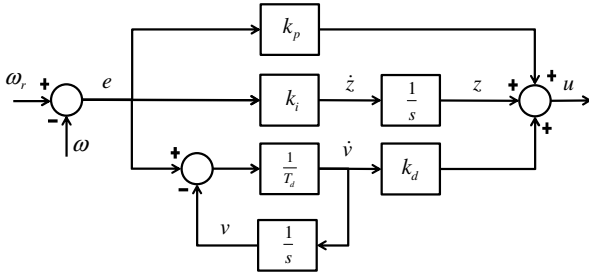


Figure 6: Detailed block diagram of the PID controller.

The model of the closed loop control system of the Figure 2 has five states when the controller is a PID with filtering of the derivative. Equations (5) to (12) summarize the system model.

$$\dot{z} = K_i (\omega_r - \omega) \quad (5)$$

$$\dot{v} = \frac{1}{T_d} ((\omega_r - \omega) - v) \quad (6)$$

$$\dot{g} = \frac{1}{T_G} (u - g) \quad (7)$$

$$2P_m + T_w \dot{P}_m = 2(g - T_w \dot{g}) \quad (8)$$

$$\dot{x} = \frac{1}{T_w} (g - P_m) \quad (9)$$

$$\dot{\omega} = \frac{1}{T_M} ((P_m - P_e) - K_D \omega) \quad (10)$$

$$u = K_p (\omega_r - \omega) + (z) + K_d (\dot{v}) \quad (11)$$

$$P_m = 2(x - g) \quad (12)$$

2.2. Optimal Control

The numerical solution of an optimal control problem can be classified into two methods, the indirect and the direct one. The indirect method, in practice, is often inefficient, as in the case described by Murty (2008) where an application of the optimal control was designed to control the frequency of a hydraulic turbine constituted by one generator unit. The system was represented in the state space and it was solved a linear regulator problem by means of the algebraic matrix Riccati. However, the author reveals few concerns about the application effectiveness.

In the direct method it is necessary to transform the original optimal control problem into a nonlinear programming problem by means of the discretization of the state and control, and then solving the resulting nonlinear programming problem. Based on the discretization of the state and control, direct methods can be classified into two different types:

- Discretization of both the state variables and control and then the resulting model is solved by an algorithm for nonlinear programming problems. A variety of these direct methods was developed and applied, including the method of direct transcription. We highlight the work of Subchan and Zbikowsky (2009) and Betts (2010). It can be pointed out that this method has a large domain of convergence (Stryk and Schlemmer, 1994).
- Discretization of control so that the states and the performance index can be obtained by numerical integration of the state equations. This approach is known as Shooting technique. Although this method may suffer of convergence issues it provides normally a highly accurate solution (Stryk and Schlemmer, 1994).

The controller design can therefore be done by means of a nonlinear optimization problem in which the system dynamic appear as constraint. We argue that the use of direct transcription technique is most suitable for this application.

In this work it was used PROPT (Rutquist and Edval, 2010) which automates the conversion of an optimal control problem into an equivalent problem of parametric optimization to be solved by Sparse Nonlinear Optimization (SNOPT) that is an appropriate solver for nonlinear systems with sparse matrices. It is worth mentioning that sparsity is an intrinsic characteristic in Direct Transcription problem caused by model discretization in time.

Considering a quadratic objective function, the optimal control problem we are interested in solving, can be written as follows:

$$\min_p J = \int_0^t (\omega_r - \omega)^2 + \lambda (g)^2 dt \quad (13)$$

This objective function is used to try to make the rotor speed ω follow the reference ω_r where λ represents the balance between control and speed error.

The system is subject to the dynamic constraints of equations (5) to (10), the algebraic constraints of equations (11) and (12), and also subject to the operational constraints (14) and (15). Note that equations (5) to (12) are equalities constraints whereas (14) and (15) are inequalities ones of the nonlinear optimization problem. Since the objective function is quadratic and all constraints are linear, this problem is classified as a quadratic optimization problem. However, even being a convex problem, the success finding the global minimum depends mainly on the features of the solver.

$$g_{\min} \leq (g) \leq g_{\max} \quad (14)$$

$$\dot{g}_{\min} \leq (\dot{g}) \leq \dot{g}_{\max} \quad (15)$$

The operational constraints (14) and (15) refer primarily to the The actuator is driven by a servo system which acts on the wicket gates ring of the turbine and its position determines the flow of water through the turbine. Based on the work of Qian, Yi and Liu (2011), the actuator can be expressed as a first order transfer function (1), disregarding the effects of the pilot valve and the dead-zone.

The minimum and maximum aperture constraints are physical limits. The speed constraint is the also physical limitation that the actuator can impose during the transient response, but can also represent a resource one may use to mitigate the effect of inverse response of the turbine. The inverse response of the turbine appears by the presence of non-minimum-phase zero in its transfer function. The consequence of this is that the rapidly changing the position of the wicket gates, the flow does not change immediately because of the inertia of the moving fluid, but the pressure changes rapidly. After that the forces are balanced and the pressure goes back to the steady state value and the change in the flow promotes the change of mechanical power and, as a result, changing the rotation of the generator. Therefore, making a slow variation of the wicket gates can help reduce the effect of inverse response.

Note that other operating constraints can be easily incorporated into the optimization problem. Some of them that are relevant to the problem are related to the time domain performance during a maneuver of changing the operating condition such as maximum overshoot, settling time, maximum peak of the inverse response, etc.

Notice that the constraints (5) and (11) of the optimization problem are nonlinear because in them the controller gains appear multiplying the state ω or the state v , that are also parameters of the problem. However, although there are nonlinear constraints, the

partial derivatives of these constraints on optimization parameters (Jacobian) are linear. This is because the nonlinearity is due to the product of optimization parameters. As a result, the optimization problem lies in the quadratic programming class that is easier to solve than other problems with more stringent nonlinearity. However, even quadratic programming problems can suffer numerical problems as is often happens with integration method of the dynamic equations (Shooting). In the Shooting method the nonlinearities of the dynamic model does not appear in constraints as in the Direct Transcription but affect the integration of the model that will then allow to calculate the objective function and also its gradient and constraints. That is, the objective function and constraints are a nonlinear function of the controller parameters. Note that a small change in the initial value of a parameter may involve a high cumulative error at the end of integration, which can compromise the convergence of optimization.

3. RESULTS

The objective in this work is to evaluate the suitability of direct transcription method as an alternative to the design of a hydraulic turbine control system for power generation since usual shooting method is often very troublesome regarding convergence. To test the ability of the method, typical maneuvers with power generation systems are considered. They refer to the change of the angular rotor speed and load disturbance rejection caused by the variation in power consumption.

Based on the work of Kundur (1993), normally the typical values of T_W are within the range of 0.5 to 4.0 s, and values T_G are close to 0.5 s. The T_M values are within in the range of 5.0 to 10.0 s as can be seen in Qian, Yi and Liu (2011), Fang and Shen (2005). The nominal values of the plant parameters used in this study were selected based on the work of Kundur (1993) and are presented in the Table 1. The constant $T_d = 0.1$ s was chosen as suggested by Fang and Shen (2005).

Table 1 – Plant Parameters

T_G	T_W	T_M	K_D
0.5 s	2.0 s	10 s	1

Although the design method proposed in this work is not similar to the tuning method proposed by Hagihara *et al.* (1979), the initial estimates for the controller gains are based on this method to avoid a trivial estimate. The suggested values are:

$$K_p = \frac{0.8T_M}{T_w} \quad (16)$$

$$K_i = \frac{0.24T_M}{T_w^2} \quad (17)$$

$$K_d = 0.27T_M \quad (18)$$

Since the control effort is explicitly being considered by operational constraints, it was adopted $\lambda = 0$ in all the situations discussed in this paper.

3.1. Nominal Constraints

In the first simulation, the values considered arise from operational restrictions and are similar to those used by Sansevero (2006):

$$-0.5 \leq g \leq 0.5 \quad pu \quad (19)$$

$$-0.2 \leq \dot{g} \leq 0.2 \quad pu/s \quad (20)$$

The constraint (19) associated with the opening of the wicket gates reflects the assumption that the linear model for deviations was obtained for about 50% of the opening of the wicket gates, so that it can be changed by +/- 50%. The constraint (20) implies that the opening speed of the wicket gates can be changed up to 20% from nominal opening.

The optimization problem was solved by the direct transcription method using 200 nodes (discretization). The model has five states and without an explicit input variable, resulting 5 parameters per node, that is, 1000 parameters to be optimized, in addition to the three gains of the PID controller. The Jacobian results in a matrix of 1,000,000 of elements. The resulting dimension is only treatable because the direct transcription problem implies in a sparse Jacobian and the used solver (SNOPT) disregard the large number of null elements. It would probably be impractical to solve this problem of direct transcription with a dense matrix solver.

Solving the optimization problem, the gains for the PID controller are $K_p = 1.444$, $K_i = 0.226$, $K_d = -0.109$ and the cost function resulted in $J = 0.124$.

The Figure 7 illustrates the performance obtained with the system during two maneuvers: the first maneuver consists in the reduction of rotation ω of 0.1 pu at $t = 0$ s and, the second maneuver consists of a disturbance rejection to a load power variation P_e of 0.2 pu at $t = 50$ s.

The graph (a) of the Figure 7 shows the performance of the maneuver. The steady value of the rotation speed was reached after about 30 seconds and with an overshoot of approximately 25% with an inverse response of 0.013 pu. In the graph (b), during the first maneuver, it can be observed that the mechanical power exhibited a maximum variation of roughly the same percentage value of the corresponding opening of the wicket gates, but exhibited an inverse response during about 2 s reaching 0.125 pu. This percentage value is much larger than the inverse response of power and, moreover, is significant, since the change in the power was only 0.1 pu. In the maneuver of disturbance rejection, the inverse response of the power exhibited a maximum deviation of 0.026 pu for a variation of 0.2 pu, that is, with a very low inverse response. The graph (c) shows that the opening of the wicket gates had a maximum variation of

about 0.23 pu considering both maneuvers, i.e., far below of the operating limit.

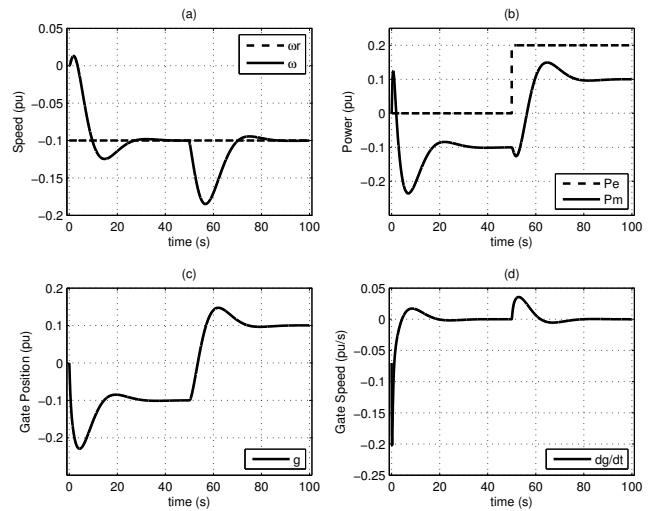


Figure 7: Time Response with Optimal PID.

Finally, the graph (d) shows that the wicket gates speed variation had operational constraint active only at the beginning of the maneuver because of the abrupt change in the wicket gates caused by the change with the reference step. In summary, the control system design via optimization produced responses satisfying all performance specifications.

3.2. Milder Constraints

Assuming now that the hydraulic actuator is such that the rate of change of position of the wicket gates can be increased in twice, that is

$$-0.4 \leq \dot{g} \leq 0.4 \quad pu/s \quad (21)$$

Solving the original optimization problem with this less restrictive bond, the optimal gains are $K_p = 2.54$, $K_i = 0.24$, $K_d = 0.06$ and the cost function resulted $J = 0.10$.

The new controller represents a more aggressive system with values of gain higher than original values. The graphs of the Figure 8 confirm what was expected, that is, the system responds more quickly with less settling time compared to the original system, but with a larger control effort and higher overshoot in the response. Similarly, to the original case, the actuator speed limit was only active during the beginning of the first maneuver with the application of the reference step.

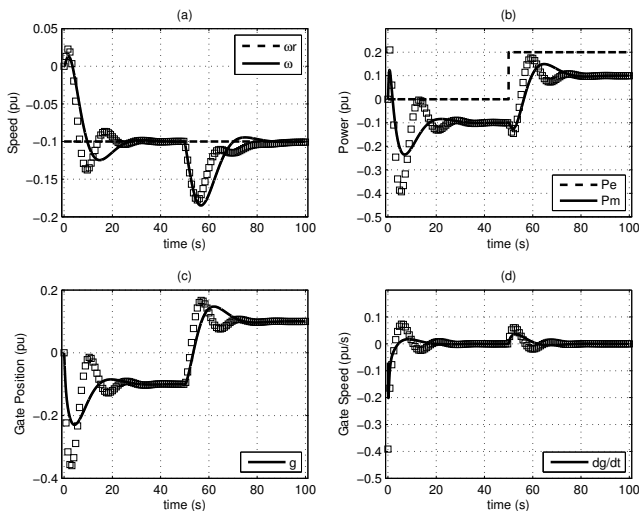


Figure 8: Response for mild constraints.

3.3. Severe Constraints

Consider now that the wicket gates opening bound is changed to

$$-0.1 \leq g \leq 0.1 \quad pu \quad (22)$$

The graphs of the Figure 9 summarize the result of the maneuvers after the optimal control problem has been resolved for the constraint (22), whose optimal gains are $K_p = 0.74$, $K_i = 0.07$, $K_d = 0.03$ and the cost function resulted $J = 0.28$.

The plots with solid line are the original results for the limit of wicket gates opening equal to 0.5 pu, while the plots with square markers are the results with the same constraint reduced to 0.1 pu. Note that the constraints are satisfied and, as consequence, the system presented response less oscillatory and smaller overshoot.

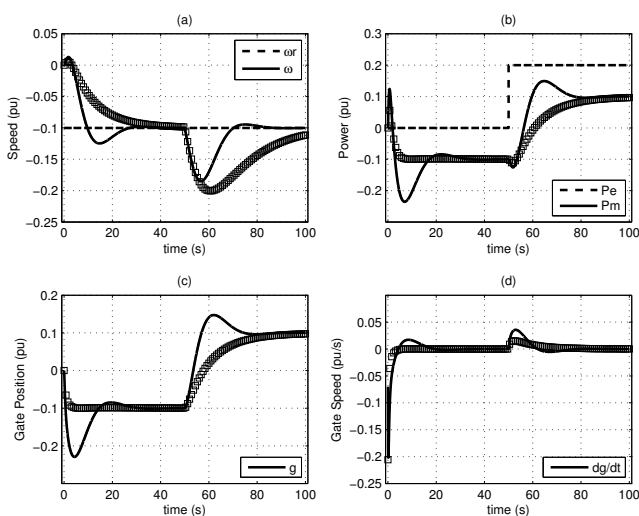


Figure 9: Response for severe constraints.

3.4. Design via Shooting

Here it was utilized the optimization method of integration of differential equations (Shooting) for comparison purpose. The only change was the inclusion of a state variable α in the dynamic model, so, the cost function can be rewritten as

$$\min_p J = \alpha, \quad (23)$$

such that

$$\dot{\alpha} = (\omega_r - \omega)^2. \quad (24)$$

Compared with the direct transcription, which was implemented with 200 nodes and about 1000 parameters to be optimized, in the Shooting there are only 3 parameters, that is, only the PID controller gains. However, in opposition to this apparent advantage, this method presents a high sensitivity, because a small change in the parameters at the beginning of the solution may result in large differences at the end of integration. This feature can generate difficulties of convergence as seen in different scenarios of this work.

As expected, the Shooting method was quite sensitive to the initial estimate and, only for values close of the optimal values, there was convergence in the response. Table 2 illustrates some of these cases, and in all cases that converged, the value of the cost function was $J = 0.1247$.

Unlike Shooting method, the direct transcription rarely presented convergence problems according to initial estimates, always converging to the global minimum whatever is the initial guess. It's emphasized that the direct transcription had always the same good performance despite of its 1008 parameters in contrast to the 3 parameters of Shooting method.

Table 2 – Convergence of the Shooting.

Initial Estimate			Convergency	
K_p	K_i	K_d	Yes	No
1.44	0.23	-0.11	●	
1.83	-0.06	1.20	●	
1.40	0.20	0	●	
-0.43	0.62	-1.32	●	
10	10	10		○
-10	-10	-10		○
1	1	0		○
1.86	-1.37	1.89		○

In the work presented by Stryk and Schlemmer, (1994), the authors combine the two methods, Direct Transcription and Shooting, joining the advantages of each method: large domain of convergence and highly accurate solutions. Might be that this hybrid approach could be a good choice for this application to be investigated next.

4. CONCLUSIONS

This work analyzed the optimal control technique Direct Transcription in order to optimize the tuning parameters of a controller used in the regulation of speed and power of hydroelectric turbines. It was elected a PID controller because of its large acceptance in industrial application although the method can be adapted to other types of controllers.

Some numerical examples were considered by changing the operational constraints related to the opening bound of the wicket gates and also to the maximum opening speed. The proposed technique was compared with the usual technique, the Shooting. The findings were compatible, however, the Shooting technique proved to be very sensitive to initial estimates, presenting convergence problems, even processing a much smaller number of parameters than those processed by direct transcription. The numerical results suggest that direct transcription technique is well suited to the control system design for hydroelectric turbines.

As a proposal for further study an alternative is to investigate the performance of the control system considering improvements in the plant model, such as nonlinearities; considering water compressibility phenomena; including tunnel and expanding tanks. Also multiple generating units in parallel can be considered.

It is proposed to investigate the extent of the project method to investigate the problem of modeling errors, producing a robust controller.

REFERENCES

- Anbo, M.; Xiangang, P.; Hao, Y., 2013. Multi-agent Based Distributed Genetic Algorithm Applied to the Optimization of Self-Adaptive PID Parameters of Hydro-turbine. *Proc. Of the 2nd International Conference on Intelligent System Design and Engineering Application (ISDEA)*. p.359 - 363, Sanya, Hainan, China.
- Betts, J.T; Practical, 2010. Methods for Optimal Control and Estimation Using Nonlinear Programming – Second Edition. *Society for Industrial and Applied Mathematics*.
- De Jaeger, E. *et al.*, 1994. Hydro turbine model for system dynamic studies. *IEEE Transactions on Power Systems*. v.9, n.4, p.1709 - 1715, November.
- Ding, X; Sinha, A. Sliding Mode/Hinf Control of a Hydro-power Plant, 2011. *Proc. of the American Control Conference*, San Francisco, CA.
- Fang, H.; Shen, Z., 2005. Modeling and Simulation of Hydraulic Transients for Hydropower Plants.. *IEEE/PES Transmission and Distribution Conference & Exhibition: Asia and Pacific*, Dalian, China.
- Hagihara, S. *et al.*, 1979. Stability of a hydraulic Turbine Generating Unit Controlled by P.I.D. Governor. *IEEE Transactions on Power Apparatus and Systems*. v.PAS-98, n.6, p. 2294 – 2298.
- Hamarasheed, C.; Haris, S. M.; Nopiah, Z. M., 2012. Weighted Multiple Model Adaptive LQG and PI Control for a Hydro Turbine Plant. *International Conference on Advanced Mechatronic Systems (ICAMechS)*.p. 656-661. Tokyo.
- Jiang, C.; Ma, Y.; Wang, C., 2006. PID controller parameters optimization of hydro-turbine governing systems using deterministic-chaotic-mutation evolutionary programming (DCMEP). *Energy Conversion and Management- Elsevier*. v. 47, n. 9-10, p. 1222-1230.
- Kundur, P., 1993. Power System Stability and Control. McGraw-Hill.
- Liu, S.; Li, D. L.; Huang, C., 2012. Nonlinear robust control with high gain observer for governor of hydro-turbine generator sets. *10th World Congress on Intelligent Control and Automation (WCICA)*. p.2752 - 2757, Beijing, China.
- Machowski, J.; Bialek, J. W.; Bumby, J. R., 2008. *Power System Dynamics: Stability and Control – 2nd. Ed.* John Wiley & Sons, Ltd.
- Murty, P. S. R., 2008. Operation and Control in Power Systems. B.S. Publications, India.
- Stryk, O. V.; Schlemmer, M. Optimal Control of the Industrial Robot Manutec r3, 1994. *International Series of Numerical Mathematics*, v. 115, p. 367-382
- Qian, D.; Yi, J.; Liu, X., 2011. Design of reduced order sliding mode governor for hydro-turbines. *American Control Conference (ACC)*. p.5073-5078. San Francisco, CA, USA.
- Sansevero, G., 2006. Controle Preditivo Baseado em Modelo para Turbo-geradores Hidráulicos Tipo Francis.. 96p. *Dissertação* (Mestrado em Engenharia Elétrica) - UNICAMP, Campinas, SP.
- Singh, M. K; Naresh, R.; Gupta, D.K., 2013. Optimal tuning of temporary droop governor of hydro power plant using genetic algorithm. *International Conference on Energy Efficient Technologies for Sustainability (ICEETS)*. p.1132 - 1137, Nagercoil, TN, India.
- Subchan, S.; Zbikowsky, R., 2009. Computacional Optimal Control – Tools and Practice. *John Wiley and Sons, Ltd*, Publications.
- Rutquist, Per E.; Edval, M. M., 2010. PROPT - Matlab Optimal Control Software. *Tomlab Optimization Inc.* WA, USA.

AUTHORS BIOGRAPHY

Roberto Canonico received the Master degree in Mechanical Engineering from FEI University, in September 2014. In the last 15 years, he has engaged mainly in control engineering design and commissioning of Hydroelectric plants. He is currently teaching in Mechanical Engineering course at UNIP University, located in São Paulo.

Fabrizio Leonardi received the PhD from University of Sao Paulo, in 2002. He has industrial and academic experience in the control system area and worked in the industry during 10 years. He is in the academia since 1987 teaching control systems and operations research and his research areas are related to control, optimization and applications. He is currently with the graduate program in Mechanical Engineering at FEI University, located in the main industrial pole in Brazil.

Renato A. Aguiar received the B.Sc. degree in Electrical Engineering from the FEI University in 1996, and the M.Sc. and Ph.D. degrees in Systems Engineering from the Department of Electrical Engineering of the Polytechnic School of the University of São Paulo in 2003 and 2007, respectively. Currently is full Professor of the Department of Electrical Engineering at FEI University. His research interests include Pattern Recognition, Fuzzy Sets and Control System.

BATTERY DYNAMIC MODEL IMPROVEMENT WITH PARAMETERS ESTIMATION AND EXPERIMENTAL VALIDATION

Javier M. Cabello ^(a), Eric Bru ^(b), Xavier Roboam ^(b), Fabien Lacressonniere ^(b), Sergio Junco ^(a)

^(a) LAC, Facultad de Ciencias Exactas, Ingeniería y Agrimensura, Universidad Nacional de Rosario, Argentina

^(b) Université de Toulouse, LAPLACE, UMR CNRS-INP-UPS, ENSEEIHT, Toulouse, France

jcabello,sjunco@fceia.unr.edu.ar, eric.bru,xavier.roboam,fabien.lacressonniere@laplace.univ-tlse.fr

ABSTRACT

The knowledge of the dynamic behavior of batteries is essential for their correct operation and management, to which aim mathematical models are invaluable tools. This paper presents an improvement of an already existing, commonly used dynamic battery model. The modification allows a better reproduction of the battery output voltage during charge and discharge processes without increasing the model complexity. Three parameter estimation methods are presented for both models. Also results of experimental tests are presented, which were performed in order to provide data for these three estimation methods and for validation purposes.

Keywords: Battery modeling, parameter estimation, battery testing.

1. INTRODUCTION

Nowadays energy storage systems are key elements in electrical systems. They allow for increased integration of renewable energy sources connected to the grid as well as to increase reliability and stability of various systems (Du and Lu 2015) like, for instance, in electric vehicles (Tie and Tan 2013).

Electrochemical batteries are the most widely used (Tie and Tan 2013) and special attention is paid to model them. There are several battery models of diverse complexity and accuracy (Dumbs 1999). A commonly used model was proposed by Tremblay-Dessaint (Tremblay and Dessaint 2009) which allows accurately representing the dynamic behavior of the battery with an easy parameterization method.

This model, implemented in the Matlab-Simulink SimPowerSystems library, takes the charge drain over time and battery current to represent the voltage behavior with an error typically lower than 5%. Its main shortcoming is its performance deterioration when reaching the end of discharge zone and for high current demands.

The objective of this paper is to propose a modification of Tremblay-Dessaint's battery Model (TDM) which overcomes the above mentioned shortcomings. The new model features a better reproduction of the battery dynamic performance. This modification, here designated as Expanded Battery

Model (EBM), does not increase the model complexity nor the parameter estimation process.

An estimation method, which preserves the simplicity of parameter estimation, extended from the method contributed by Tremblay and Dessaint (2009) is presented. In addition, two other new parameterization methods are addressed. The first two are based on the typical constant-current discharge characteristic or "Typical discharge characteristic", usually provided by manufacturers; in that case, no battery testing is needed. If more accuracy is required and if battery testing is possible, a final estimation method is proposed.

We had focused our work on Li-Ion batteries but the results should be applicable to electrochemical batteries based on other technologies.

The rest of this paper is organized as follows: In section 2, the battery models are described. Section 3 presents the estimation methods. In section 4, the tests performed over the battery in order to estimate the model parameters are addressed and, in section 5, the validation of the EBM as well as the parameters estimations methods are shown. Finally, section 6, presents the conclusions.

2. BATTERY MODELS

An electrochemical battery is an element capable of transforming electrical energy into chemical energy (charging) and vice versa (discharging) through electrochemical reactions. For simulating them, several application-dependent models of varying complexity can be used. The following models use the State of Charge (*SoC*) and the filtered output current i^* as state variables.

2.1. Tremblay-Dessaint's Model

The Tremblay-Dessaint's Model (TDM) is a semi-empirical battery model based on Shepherd's work (Shepherd 1965) and consisting in two voltage equations (discharge and charge) as a function of the charge drain over time it (Ah), the actual current i , and the filtered current i^* .

A Li-Ion cell will be utilized along this work. For this type of cell, the battery voltage given by Tremblay and Dessaint (2009) is:

Discharge:

$$V_{batt-dch} = E_0 + Ae^{-B.it} - K \frac{Q}{Q-it} it - Ri - Ki^* \frac{Q}{Q-it} \quad (1)$$

Charge:

$$V_{batt-ch} = E_0 + Ae^{-B.it} - K \frac{Q}{Q-it} it - Ri - Ki^* \frac{Q}{it - 0.1Q} \quad (2)$$

where the variables are the battery voltage V_{batt} (V), the charge drain over time from full charge state $it = \int i dt$ (Ah), the output current i (A), and the filtered current i^* (A); and the parameters are the battery constant voltage E_0 (V), the polarization constant or polarization resistance K (V/Ah or Ω), exponential zone amplitude A (V), the exponential zone time constant inverse B (Ah⁻¹), the internal resistance R (Ω) and the battery capacity Q (Ah).

To complete the model the filtered current equation is needed:

$$T_f \frac{d}{dt} i^* + i^* = i \quad (3)$$

where T_f is the filter time constant.

The State of Charge, SoC , is a widely used variable of battery systems (Zhang and Lee 2011). It is used as an indicator of battery charge left and also to calculate other variables for more complex models such as ageing effect. The SoC can be calculated as:

$$SoC = SoC_0 - \frac{\int idt}{Q} \quad (4)$$

Where SoC_0 is the State of Charge initial.

Equations 1 and 2 could be expressed as functions of the SoC , remembering that the SoC_0 is 1, resulting in the Equation 5.

$$V_{batt}(SoC, i, i^*) = E_0 + Ae^{-BQ(1-SoC)} - KQ \left(\frac{1}{SoC} - 1 \right) - Ri - Ki^* \left(\frac{iS_{dch}}{SoC} + \frac{iS_{ch}}{1.1 - SoC} \right) \quad (5)$$

where the variables iS_{dch} and iS_{ch} values were introduced to capture both battery voltage equations in only one expression. iS_{dch} is 1 when the battery is discharging and 0 otherwise and iS_{ch} is 1 when the battery is charging and 0 otherwise.

2.2. Expanded Battery Model.

Analyzing the TDM's voltage Equation 5, two types of terms can be identified. Those depending solely on the SoC and those depending also on the actual current. The three first terms represent the Open Circuit Voltage (OCV). Special attention is given to the third term modeling the abrupt fall of the voltage for low SoC which contains the parameter K .

The fourth and fifth terms represent the battery resistance. The last term, polarization-resistance voltage drop, models the abrupt increase of the internal resistance at low SoC while discharging and at high SoC while charging. The parameter K appears also as a multiplying factor.

Even though both effects which involve the K parameter (OCV voltage drop and polarization resistance) during discharge could likely be due to the active material current density (Shepherd 1965), the fact that both parameters have different units leads to the idea of distinguishing them. This separation, which is proposed in the Expanded Battery Model (EBM), does not increase the parameter estimation complexity and provides better dynamic model performance especially for low SoC .

The voltage state with the EBM is expressed as:

$$V_{batt}(SoC, i, i^*) = E_0 + Ae^{-BQ(1-SoC)} - K_1 Q \left(\frac{1}{SoC} - 1 \right) - Ri - K_2 i^* \left(\frac{iS_{dch}}{SoC} + \frac{iS_{ch}}{1.1 - SoC} \right) \quad (6)$$

This Expanded Battery Model differentiates K_1 and K_2 parameters.

3. PARAMETER ESTIMATION METHODS

One of the main advantages of TDM is its easy parameterization needing only one "Typical discharge characteristic", normally given by manufacturers. This estimation method will be reviewed and a first modification will be proposed in order to estimate K_1 and K_2 without increasing its complexity.

Next, a second method for estimating parameters for both models is presented. In this case, 3 complete constant-current discharge characteristics are used. These characteristics are also normally given by the manufacturer.

Finally, a third method based on the Hybrid Pulse Power Characterization test (HPPC) will be introduced, where all model parameters are estimated. This characterization test excites the frequency spectrum of electrochemical batteries in order to achieve a correct parameter fitting.

Independently of the selected parameterization method the number of parameters to be estimated are 7 for the TDM and 8 for the EBM: E_0 , K_1 , A , B , R , K_2 , Q and T_f where the constraint $K_1 = K_2 = K$ is applied for the TDM.

3.1. Method of the Minimal Equation System (M1)

This method, fully described in Tremblay and Dessaint (2009), can be summarized as follows. From the datasheet provided by manufacturer, the maximum capacity Q , and the internal resistance R , are directly obtained.

A ‘‘Typical discharge characteristic’’ at a constant discharge current (generally $i_{dch} = 0.2C$) is also provided and three points are extracted. The Full voltage ($0, V_{full}$), the End of exponential zone (Q_{exp}, V_{exp}) and the Nominal (Q_{nom}, V_{nom}) when the voltage begins to fall abruptly (see Figure 1).

The parameter B could be approximated to $3/Q_{exp}$ which is the end of the exponential term.

The steady state of the discharge test (constant current) allows considering $i = i^* = i_{dch}$ at the two points (Q_{exp}, V_{exp}) and (Q_{nom}, V_{nom}). And for ($0, V_{full}$) the initial as well as the filtered currents, are zero.

These leads to the following equation system:

$$\begin{aligned} V_{full} &= E_0 + A \\ V_{exp} &= E_0 + A\alpha_{(SoC_{exp})} - K(\beta_{(SoC_{exp})} + \gamma_{(SoC_{exp}, i_{dch})}) - Ri_{dch} \\ V_{nom} &= E_0 + A\alpha_{(SoC_{nom})} - K(\beta_{(SoC_{nom})} + \gamma_{(SoC_{nom}, i_{dch})}) - Ri_{dch} \end{aligned} \quad (7)$$

where

$$\begin{aligned} \alpha_{(SoC)} &= e^{-BQ(1-SoC)} \\ \beta_{(SoC)} &= Q \left(\frac{1}{SoC} - 1 \right) \\ \gamma_{(SoC, i^*)} &= \frac{i^*}{SoC} \end{aligned} \quad (8)$$

Considering B as known, the previous equation could be easily solved and the parameters E_0 , A and K can be obtained.

Finally the time constant T_f is not given by the manufacturer but experimental tests have shown that it can be approximated to 30s (Tremblay and Dessaint 2009).

This completes the 7 parameter estimation method for the TDM.

When relaxing the constraint of equality between the K parameters, the system of equations became under-determined. This is easily solved by adding a new equation through selecting another point. By choosing a point from a ‘‘Typical discharge characteristic’’ at a higher current (e.g. 1C) and at a low SoC the influence of non-linear resistance is augmented. The point (Q_{nom1C}, V_{nom1C}) is selected resulting in Eq. (9),

$$\begin{aligned} V_{full} &= E_0 + A \\ V_{exp} &= E_0 + A\alpha_{(SoC_{exp})} - K_1\beta_{(SoC_{exp})} - Ri_{dch} - K_2\gamma_{(SoC_{exp}, i_{dch})} \\ V_{nom} &= E_0 + A\alpha_{(SoC_{nom})} - K_1\beta_{(SoC_{nom})} - Ri_{dch} - K_2\gamma_{(SoC_{nom}, i_{dch})} \\ V_{nom1C} &= E_0 + A\alpha_{(SoC_{nom1C})} - K_1\beta_{(SoC_{nom1C})} - Ri_{dch1C} - K_2\gamma_{(SoC_{nom1C}, i_{dch1C})} \end{aligned} \quad (9)$$

This complete the 8 parameter estimation method for the EBM extended from the TDM estimation method.

3.2. Method of Over-determined Equation System (M2)

The previous method is strongly dependent of the selected discharge characteristic curve and the selected points, especially the nominal point. Moreover, only 3 points (4 in the EBM) are used from several complete discharge characteristic curves.

This second estimation method proposes to use the complete discharge characteristic curve to create an over-determined equation system while estimating the parameters B , Q and T_f as for the previous method.

The system of equations for the TDM is

$$\begin{bmatrix} V_1 \\ \vdots \\ V_n \end{bmatrix} = \begin{bmatrix} 1 & \alpha_{(SoC_1)} & -\beta_{(SoC_1)} - \gamma_{(SoC_1, i_1)} & -i_1 \\ \vdots & \vdots & \vdots & \vdots \\ 1 & \alpha_{(SoC_n)} & -\beta_{(SoC_n)} - \gamma_{(SoC_n, i_n)} & -i_n \end{bmatrix} \begin{bmatrix} E_0 \\ A \\ K \\ R \end{bmatrix} \quad (10)$$

The system of equations for the EBM is

$$\begin{bmatrix} V_1 \\ \vdots \\ V_n \end{bmatrix} = \begin{bmatrix} 1 & \alpha_{(SoC_1)} & -\beta_{(SoC_1)} & -i_1 & -\gamma_{(SoC_1, i_1)} \\ \vdots & \vdots & \vdots & \vdots & \vdots \\ 1 & \alpha_{(SoC_n)} & -\beta_{(SoC_n)} & -i_n & -\gamma_{(SoC_n, i_n)} \end{bmatrix} \begin{bmatrix} E_0 \\ A \\ K_1 \\ R \\ K_2 \end{bmatrix} \quad (11)$$

For both equation systems, the method of ordinary least squares was used to find an approximate solution. This method states that for a system $Ax = b$ the least squares formula for solving:

$$\min_x \|Ax - b\|$$

is

$$x = (A^T A)^{-1} A^T b$$

3.3. Optimization Method for Estimation of the Complete Parameter Set (M3)

Both previous methods are easily processed from experiments or from data sheets but several assumptions were made in order to simplify the estimation problem. If more precise models were needed and if the necessary tests could be performed, the following method could be used for parametric estimation.

Given voltage measures from data testing, the problem can be formulated as:

$$\min_x \left\| V_n - V_{batt(SoC_n, i_n, i_n^*)} \right\|_2^2 \quad (12)$$

where x is the parameters vector (E_0, K, A, B, R, Q, T_f for the TDM, and replace K for K_1 and K_2 for EBM), V_n is the measured voltage vector and i_n the measured current vector. SoC_n is calculated according to Equation 4, i_n^* according to Equation 3 and V_{batt} according to Equation 5 or Equation 6 for TDM and EBM respectively.

In order to solve the previous minimization problem, a Trust Region Reflective Method (Coleman and Li 1996) is used. This method needs a suitable starting point to converge. One solution of the previous estimation method is used to initialize the process.

The HPPC test provides a full scope in terms of SoC span and input current.

Based on the constant current discharge characteristics (see Figure 1) for methods M1 and M2 and on the HPPC test (see Figure 2) for the third (M3) method, all parameter results are gathered in Table 1:

Table 1: Battery parameters for the Tremblay Dessaint Model (TDM) and the Extended Battery Model (EBM) using the three estimations methods (M1,M2,M3)

	TDM			EBM		
	M1	M2	M3	M1	M2	M3
E_0 [V]	3,311	3,297	3,320	3,312	3,284	3,275
K_1 [mVAh ⁻¹]	0,470	0,370	0,507	0,435	0,255	0,277
A [V]	0,034	0,100	0,023	0,032	0,096	0,058
B [Ah ⁻¹]	6,010	6,010	3,879	6,010	6,010	0,036
R [mΩ]	5,000	6,511	6,718	5,000	5,543	6,474
K_2 [mΩ]	0,470	0,370	0,507	0,632	0,624	0,788
Q [Ah]	36	36	36,91	36	36	36,42
T_f [s]	30	30	108,6	30	30	94,1

4. BATTERY TESTS

The battery test bench consists in a DC Power Supply and an Electronic DC Load functioning alternately in order to allow two quadrants operation. Data acquisition of voltage, current and temperature was done with a sampling time of 10ms.

A Lithium Iron Phosphate battery was tested (LiFePo4 3.2V-36Ah).

4.1. Typical discharge characteristic

Usually provided by the manufacturer, this test was reproduced in order to achieve parametric estimation of the two first estimation methods.

The “typical discharge characteristic” consists in discharging a fully charged battery at a constant current

until minimal voltage is reached. Three different current intensities were selected (0.2C, 0.5C and 1C).

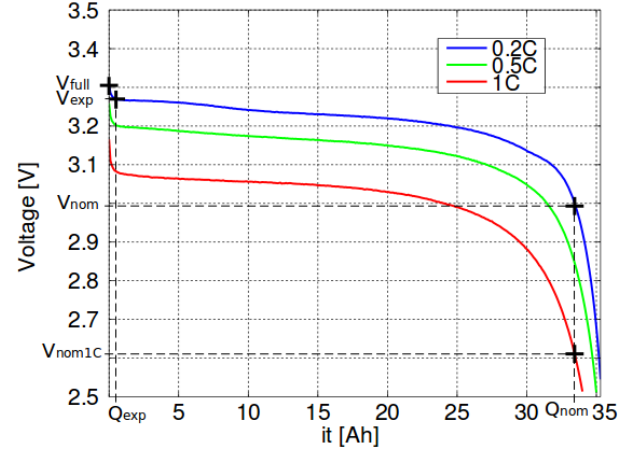


Figure 1: Typical discharge characteristic (1C, 0.5C and 0.2C)

In figure 1 the “Typical discharge characteristic” for the three different discharge currents is shown allowing extraction of the four points used in the first estimation method.

4.2. Hybrid Pulse Power Characterization (HPPC)

The HPPC profile was designed in order to measure the dynamic power capability over a device’s usable charge and voltage range (Hunt 2001, Shim and Striebel 2003). It consists in a series of discharge and charge pulses of constant current at different SoC. Pulse duration and intensity depends of test objectives.

In this particular case, because non-linear resistance identification is intended and because battery time constant is approximately 30s, a series of consecutive pulses increasing in intensity were considered with a duration of 45s followed by 45s pause intervals. The phase of pulses is followed by a constant current discharge to change the battery SoC of 10%.

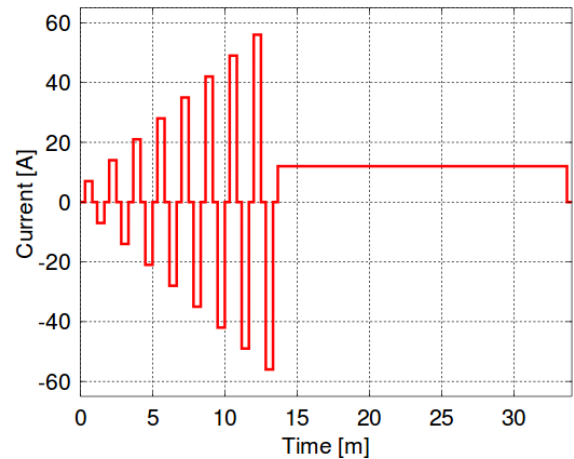


Figure 2: A cyclic charge/discharge process followed by *SoC* variation.

4.3. Typical Electric Vehicle profile (FTP)

Based on the work presented by Carignano, Cabello and Junco (2014) a likely current profile from a battery-powered electric vehicle (BEV) subject to the FTP-75 driving cycle was extracted and adapted for the present battery.

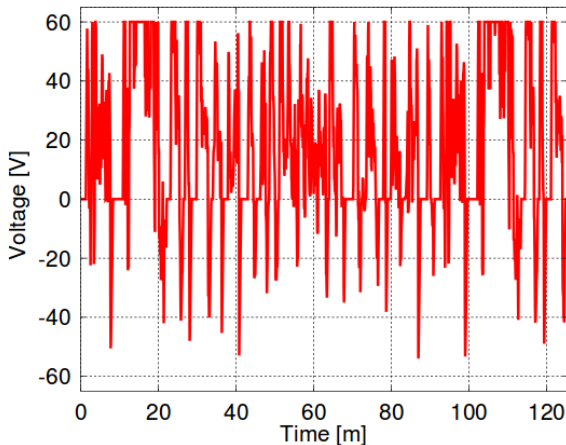


Figure 3: Current profile demanded to the battery system of a BEV to complete FTP-75 speed profile.

This last profile will be used in the next section dedicated to the validation of estimated models.

5. VALIDATION

An important feature of this paper is the validation of the two models discussed with the corresponding three estimation methods.

The two first tests, “Typical discharge characteristic” and HPPC profile cannot really be used as validation test because they were used to estimate and fit parameters in the three methods. However, comparisons with these two profiles are displayed in Figures 5, 6 and 7 for “Typical discharge characteristic” and then in Figures 8, 9 and 10 for HPPC profile. In these figures model and experimental battery voltage behavior are compared. The FTP profile is also used to compare and validate the model accuracies. Note that this profile was never used to fit parameters in the estimation methods.

The Normalized Root Mean Square Error (NRMSE) relative to the nominal voltage was used to compare models accuracies. In all tests the error increase notoriously when approaching to a low *SoC*. Error calculation is distinguished between low *SoC* (<20%) and the rest of the *SoC* span (see Table 2).

5.1. Typical discharge characteristic

Figure 5 compares the TDM and the EBM using the first method (M1) to estimate parameters. It can be seen that the maximal error is reduced from 2.5% to 1.3% for

maximal discharge current while remaining almost the same for the two other discharge currents.

Comparing the model simulations of the second method (M2), see Figure 6, it can be seen that the TDM error is lower than 1% for a *SoC* > 20% as well as the EBM. Also comparing the NRMSE from Table 2 not a remarkable improvement is seen for this test. As expected, both models improve estimations regarding M1.

For the models estimated with the third method (M3) the errors increase. This was expected because the “typical discharge characteristic” was not used by the third method for estimation.

Table 2: Normalized Root Mean Square of the TDM and EBM models using the 3 parameterization methods.

	Estimation				Validation	
	Typ. Dis. Char.		HPPC		FTP	
<i>SoC</i>	>20%	<20%	>20%	<20%	>20%	<20%
TDM-M1	1,01	1,97	0,68	1,51	1,03	2,37
EBM-M1	0,86	1,74	0,79	1,49	0,92	1,70
TDM-M2	0,42	1,44	1,12	0,97	0,66	1,40
EBM-M2	0,40	1,32	1,33	0,97	0,56	1,11
TDM-M3	0,40	2,13	0,41	0,74	0,49	1,47
EBM-M3	0,49	1,70	0,35	0,44	0,36	1,39

5.2. HPPC profile

In Table 2, the reduction of the NRMSE can be seen while using the 2nd estimation method (M2) instead of the M1 while *SoC* is lower than 20% but, on the contrary, an increment is seen for *SoC* higher than 20%.

The best simulation result is obtained by the 3rd estimation method (M3) of the EBM. These results are expectable because it was the fitting data for this method.

5.3. Typical Electric Vehicle profile (FTP)

For the M1 estimation method, the maximal error for the TDM is 5% while it is reduced to 4% for the EBM (Figure 11). This improvement is also visible in Table 2 as the reduction of the NRMSE (1.03% to 0.92% for typical *SoC* and from 2.37% to 1.70% for low *SoC*).

The performance obtained for the EBM with the method M3 of parameter estimation improves the models estimated using M1 in at least 40% (1.03% to 0.36% for typical *SoC* and from 2.37% to 1.39% for low *SoC*).

6. CONCLUSION

In conclusion, this paper shows a battery model improvement from the Tremblay-Dessaint’s Model which does not increase model complexity or parameter estimation difficulty and provides a better prediction of voltage behavior. For *SoC* higher than 20%, the NRSME indicator is reduced by 10% while for typical *SoC* is reduced by 28% in the validation (FTP) test.

In addition, two novel estimation methods for both models were developed. One uses the normally given “Typical discharge characteristic”, where no battery tests are needed, and the other uses the “HPPC” profile. Each of these new methods improves the previous one.

ACKNOWLEDGMENTS

The authors wish to thanks CONICET (the Argentine National Council for Scientific and Technological Research), SeCyT-UNR (the Secretary for Science and Technology of the National University of Rosario), ANPCyT (PICT 2012 Nr. 2471) and the scholarship program *Saint-Exupery* for their financial support as well as the *Facultad de Ciencias Exactas Ingeniería y Agrimensura* for providing workplace. Authors would like to thanks to Ing. Daniel Alba for the fruitful discussions related to battery modeling and testing.

APPENDIX



Figure 4: Battery Test Bench developed in the LAPLACE.

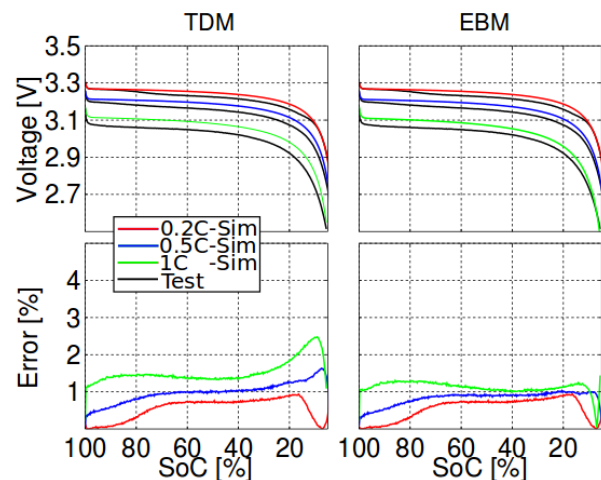


Figure 5: Comparison of typical discharge characteristic of TDM and EM with parametric estimation using method M1 §3.1 and test data.

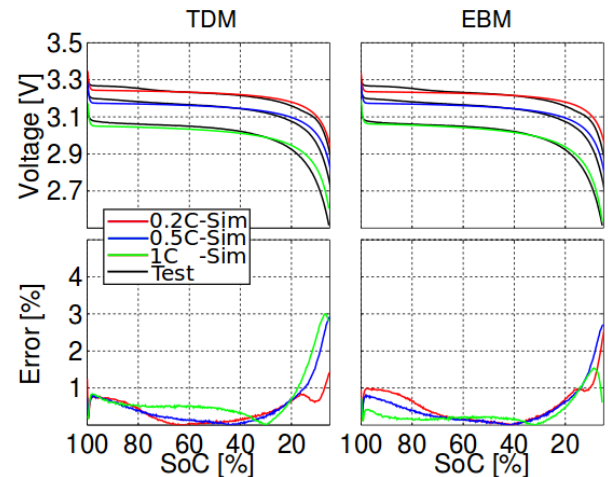


Figure 6: Comparison of typical discharge characteristic of TDM and EM with parametric estimation using method M2 §3.2 and test data.

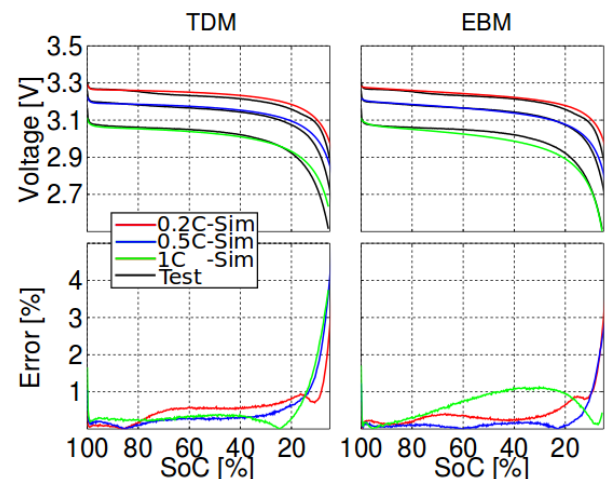


Figure 7: Comparison of typical discharge characteristic of TDM and EM with parametric estimation using method M1 §3.3 and test data.

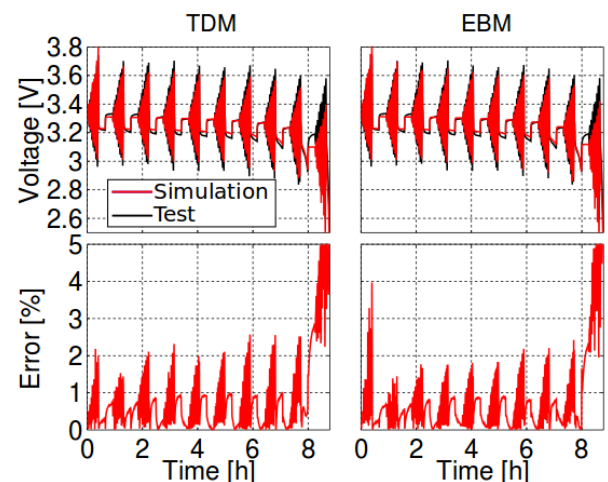


Figure 8: Comparison of HPPC profile of TDM and EM with parametric estimation using method M1 §3.1 and test data.

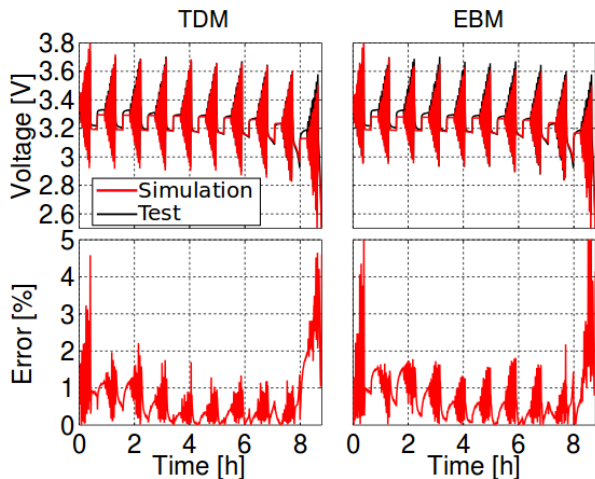


Figure 9: Comparison of HPPC profile of TDM and EM with parametric estimation using method M2 §3.2 and test data.

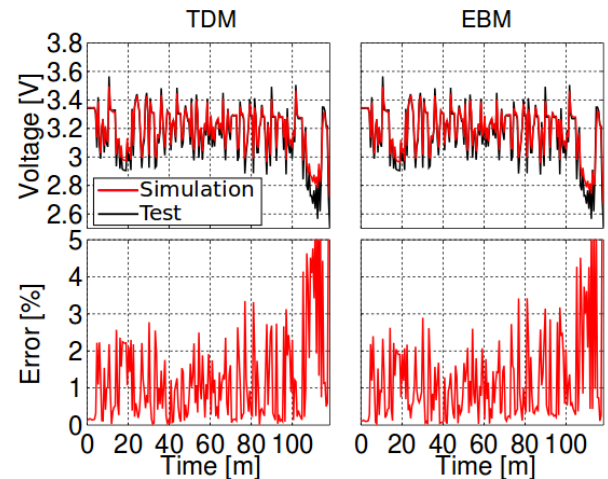


Figure 12: Comparison of FTP profile of TDM and EM with parametric estimation using method M2 §3.2 and test data.

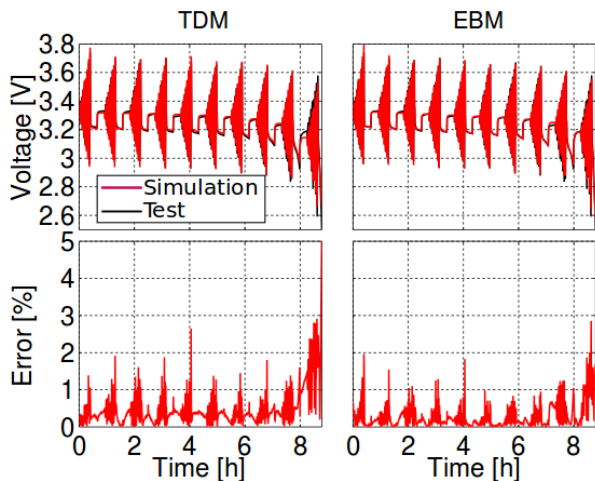


Figure 10: Comparison of HPPC profile of TDM and EM with parametric estimation using method M3 §3.3 and test data.

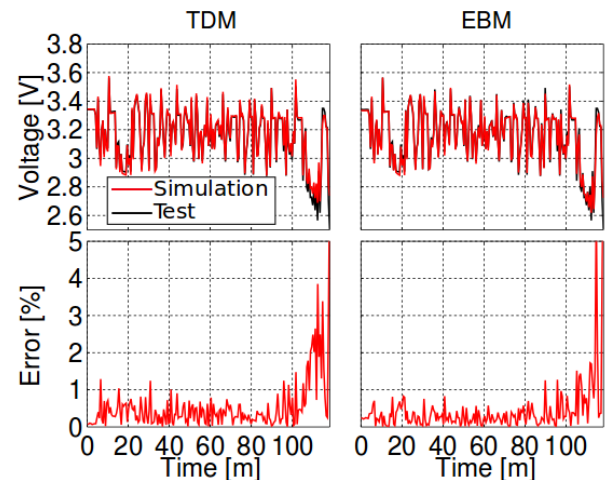


Figure 13: Comparison of FTP profile of TDM and EM with parametric estimation using method M3 §3.3 and test data.

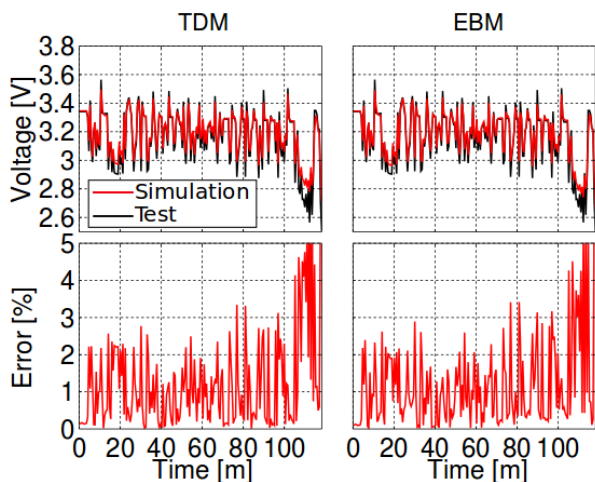


Figure 11: Comparison of FTP profile of TDM and EM with parametric estimation using method M1 §3.1 and test data.

REFERENCES

- Carignano M., Cabello J. M., Junco S., 2014. Sizing and performance analysis of battery pack in electric vehicles. *Biennial Congress of Argentina (ARGENCON) 2014 IEEE*. pp. 240-244.
- Coleman T.F., Li Y., 1996. An Interior, Trust Region Approach for Nonlinear Minimization Subject to Bounds. *SIAM Journal on Optimization*. Vol. 6, pp. 418-445.
- Du P., Lu N., 2015. *Energy Storage for Smart Grids*, Boston, Academic Press.
- Dumbs C. 1999. *Développement d'outils pour l'analyse des systèmes hybrides photovoltaïque-diesel*. Ph.D. Ecole National Supérieure de mines de Paris.
- Hunt G., 2001. *PNGV battery test manual*. INEEL, DOE/ID-10597, Rev. 3.
- Shepherd C. M., 1965. Design of Primary and Secondary Cells - Part 2. An equation describing battery

discharge. *Journal of Electrochemical Society*, Vol. 112, pp 657-664.

Shim J., Striebel K. A., 2003. Characterization of high-power lithium-ion cells during constant current cycling: Part I. Cycle performance and electrochemical diagnostics. *Journal of Power Sources*. Vol. 122, pp 188–194.

Tie S. F., Tan C. W., 2013 A review of energy sources and energy management system in electric vehicles. *Renewable and Sustainable Energy Reviews*. Vol. 20, pp. 82–102.

Tremblay O., Dessaint L. A., 2009. Experimental validation of a battery dynamic model for ev applications. *World Electric Vehicle Journal*. Vol. 3, no. 1, pp. 1–10.

Zhang J., Lee J., 2011. A review on prognostics and health monitoring of Li-ion battery. *Journal of Power Sources*, 196(15), 6007-6014.

AUTHORS BIOGRAPHY

Javier M. Cabello received the Electronic Engineering degree from the *Facultad de Ciencias Exactas Ingeniería y Agrimensura* of *Universidad Nacional de Rosario*, Rosario, Argentina, in 2012. He is currently working toward the Ph.D. degree. His research interests include optimal sizing of components and energy management strategies in Smart Grids applications.

Eric Bru received the MSc electric engineering degree from *l'École d'ingénieurs du Cnam*, Toulouse, France, in 2005. He joined the LAPLACE as test engineer in 2006. He develops test benches devoted to HVDC networks, renewable energy systems, hybridization devices with electrical storage such as ultracapacitor or electrochemical accumulators in the GENESYS-Team.

Xavier Roboam received the Ph.D. Degree of *Université de Toulouse*, France in 1991. He is full-time researcher (Directeur de Recherches CNRS) in the

Laboratory of Plasma and Conversion of electrical Energy (LAPLACE) of Toulouse since 1992 where he develops design methodologies specifically oriented towards multi-fields devices for embedded or renewable energy systems.

Fabien Lacressonniere received the Ph.D degree in Electrical Engineering from the *Université d'Artois*, Béthune, France, in 2005. Since 2007, he is currently an Associate Professor at the Université de Toulouse – Université Paul Sabatier – IUT de Tarbes where he teaches the electric actuators and power electronics. His research activity takes place in Laboratoire Plasma et Conversion d'Énergie, Toulouse. His major research interest is the modeling of electrochemical accumulators, and more particularly that of Li-ion batteries.

Sergio Junco received the Electrical Engineer degree from the *Universidad Nacional de Rosario* in 1976. He joined the *National University of Rosario* in 1982, where he currently is a Full-time Professor of System Dynamics and Control and Head of the Automation and Control Systems Laboratory. His current research interests are in modeling, simulation, control and diagnosis of dynamic systems, with applications in the fields of motion control systems with electrical drives, power electronics, mechatronics, vehicle dynamics and smart grids. He has developed, and currently teaches, several courses at both undergraduate and graduate level on System Dynamics, Bond Graph Modeling and Simulation, Advanced Nonlinear Dynamics and Control of Electrical Drives, as well as Linear and Nonlinear Control with Geometric Tools.

MODELLING, CONTROL AND APPLICATION OF DYNAMIC PROGRAMMING TO A SERIES-PARALLEL HYBRID ELECTRIC VEHICLE

Ivan Miguel Trindade^(a), Agenor de Toledo Fleury^(b)

^{(a),(b)} Mechanical Engineering Department, Polytechnic School, University of Sao Paulo, Brazil

^(b) Mechanical Engineering Department, FEI University, Sao Bernardo do Campo, Brazil

^(a)ivan.trindade@usp.br, ^(b)agfleury@fei.edu.br

ABSTRACT

Hybrid Electric Vehicles (HEVs) present a wide range of powertrain configurations, degrees of hybridization and added costs when compared to conventional powertrains. From the point of view of control system, the major problem is the reduction of fuel consumption and pollutant emission. A method for determining the strategy that best suits this problem relies on minimization methods that find the optimal control variables depending on the system states and cost functions.

This paper presents the modelling of the powertrain of a series-parallel HEV and control strategies with focus on fuel consumption reduction. As energy management strategy, a rule based (sub optimal) and dynamic programming (optimal) methods were implemented. Results obtained with both models are compared with real dynamometer test.

Keywords: hybrid electric vehicle, dynamic programming, fuel consumption, optimization

1. INTRODUCTION

The major powertrain losses in a conventional vehicle are inherited by the relatively low average fuel efficiency of combustion engines (around 33% for spark ignited) and the very low efficiency at part loads, typical of operation in urban driving cycles. On the other hand, an electric vehicle (EV) provides high energy conversion efficiency when combining battery, electric motor and motor electronics which can be as high as 80% for the complete power path. The main disadvantage of EVs is the low energy density possessed by chemical batteries, which ranges around 1% of combustible fuels (Ehsani and Emadi 2005). This characteristic makes EVs applicable for a very specific usage of short range drive. In this case the cost trade-off for the different component configurations and size is off course a major issue.

The main purpose of a hybrid electric vehicle (HEV) in terms of fuel efficiency is to overcome the typical losses of conventional powertrains by accomplishing the following principles:

- Usage of electric motor for propulsion at low speeds and low power requests
- Internal combustion engine (ICE) deactivation when vehicle is stopped
- Regeneration of energy during braking events
- Optimization of engine operation region during mechanical only traction and when in generator mode

Different drivetrain configurations for HEVs can accomplish the task of minimizing fuel consumption. Series-parallel hybrids are well known for providing different modes of operation allowing either pure electrical, pure mechanical propulsion or a combination of both. The powertrain configuration of this study is a series-parallel electric hybrid which uses a planetary gear set as torque-split device by interconnecting ICE and two electric motors. In order to study the operation of this system, a detailed mathematical model was built in MATLAB/Simulink. For this system a non-optimal control strategy was implemented using rule-based control and a charge sustaining strategy. The results of this model were correlated with data from dynamometer testing in order to assure the quality of the powertrain and control model.

The main step of the problem of minimizing fuel consumption consists in finding the optimum power-split between ICE and battery power for a given driver's request. Dynamic programming (dp) uses Hamilton-Jacobi-Bellman equation to solve the problem and find the global optimum solution and has a suitable application for motor vehicles. The use of dynamic programming for the HEV problem is well described in the literature (Lin, Peng, Grizzle, and Kang 2003; Delprat, Lauber, Guerra, and Rimaux 2004) where the accumulated fuel consumption over a driving cycle is used as cost function with addition of a penalty term due to final variation of battery state of charge (SOC). Dynamic programming requires prior information of the driving cycle and, therefore, the simulation is run in backward mode. Moreover, a simplified model representing the dynamic system has to be used which may create a response that deviates from the detailed model using non-optimal control. The time step size and sampling of state and control variables are also factors

that can impact in the results of the optimization. For these reasons, there is the need of having two different models using optimum and non-optimum control.

2. DESCRIPTION OF THE POWERTRAIN SYSTEM

The configuration of the powertrain is shown in Figure 1 where a planetary gear set is used to connect motor-generator 1 (MG1), ICE and motor-generator 2 (MG2) to solar, carrier and ring gears, respectively. The ring gear is connected through the differential and final reduction to the wheels. The ratio of torque amplification from the ICE to the wheels is fixed, however, different ICE speeds can be realized for a given vehicle speed. This is possible by controlling MG1 speed so that it compensates for the ICE torque transferred to the shaft of the solar gear. The main traction motor is MG2, which is also the responsible for regenerative braking.

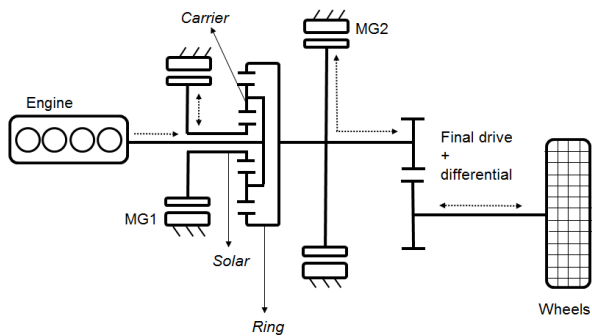


Figure 1: Diagram Of The Power-Split Hybrid Topology With Energy Flow Defined By Arrows.

The 2nd generation of Toyota Prius is used as base from where the main parameters were taken for this study. Data available for this powertrain is widely literature in the literature (Sekimori 1998; Kamiya 2006; Abe 2000). The lever diagram in Figure 2 shows different operation modes of the powertrain. At low speed driving, the traction motor speed is increased while the engine remains stopped with the generator accelerating in the reverse direction (red line). At higher vehicle speeds and loads, the generator accelerates towards the positive direction in order to start the engine (green line). The engine can also operate in fuel cut off and drag along the planetary, with the effect of engine friction lowered due to the overdrive ratio to the wheels. The engine can still be started at standstill in order to generate electricity or in order to warm-up the exhaust system.

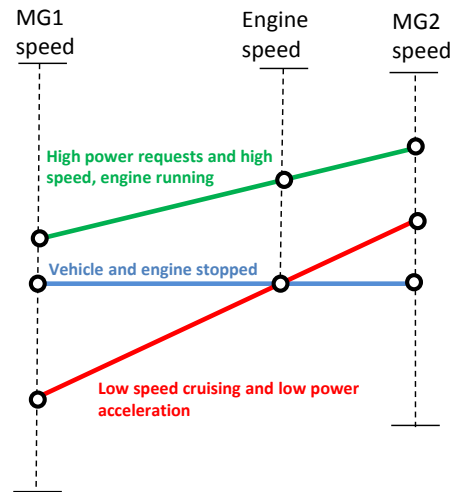


Figure 2: Lever Diagram Of The Power-Split Device.

Table 1: Characteristics of the vehicle model.

Engine	
Displacement	1.5 cm ³
Torque	115 Nm @ 4200 rpm
Power	57 kW @ 5000 rpm
Traction motor	
Type	Brushless Permanent Magnet motor
Torque	400 Nm
Power	50 kW
Maximum speed	6500 rpm
Generator	
Type	Brushless Permanent Magnet motor
Power	30 kW
Maximum speed	10000 rpm
Battery	
Type	Ni-MH
Nominal voltage	201.6 V
Rated capacity	6.5 Ah

An inherent feature of the power-split powertrain is that electrical energy is always consumed in order to control engine speed by MG1 attached to the sun gear. As explained in (Abe 2000; Muta, Yamazaki, and Tokieda 2004) at certain vehicle speeds where the engine has to be started, MG1 has negative speed and has to decelerate in order to start the engine, therefore generating energy which is used by the traction motor for torque assist. However, when the engine has to be started at low speeds, MG1 operates as a motor and afterwards uses traction power to control engine speed. At this point, MG2 has to operate as a generator decreasing torque at the output shaft. This constant recirculation of energy on the high voltage bus is beneficial for city driving, where electric traction is

more efficient, so that the energy is not directed in and out of the battery, consequently reducing conversion losses. On the other hand, on highway driving the overall efficiency is reduced as mechanical only traction is not possible. The general characteristics of the vehicle are shown in Table 1.

3. SYSTEM MODELLING

The power-split configuration shown in Figure 1 allows the system to operate as an electric continuous variable transmission (CVT), as the generator is used to control the ICE speed. The torque relationship in the planetary carrier is fixed by the ratio between the diameters of each gear and a general gear ratio of the planetary gear set, i_{PGS} , is defined as the ratio between the number of teeth of ring and sun gears. The dynamic equations for the system are shown in Eq.(1) and Eq.(2), where subscripts C, S, R, represent carrier, sun and ring gear parameters. The torque demand of ICE, MG1 and MG2 described by T_{ICE} , T_{MG1} and T_{MG2} are related to the torque demanded at the wheels. Inertia terms from the planetary are represented by I_S, I_R and I_C , while $I_{ICE}/\alpha_{ICE}, I_{MG1}/\alpha_{MG1}$ and I_{MG2}/α_{MG2} represent inertia and angular acceleration of ICE, MG1 and MG2, respectively. The equivalent rotational inertia of the vehicle mass on the ring shaft is represented by I_{R-EQ} .

$$T_{MG1} - I_S \alpha_{MG1} = - \left(\frac{1}{i_{PGS} + 1} \right) \cdot (T_{ICE} - I_C \alpha_{ICE}) \quad (1)$$

$$\begin{aligned} & \left(\frac{i}{i_{PGS} + 1} \right) \cdot (T_e - I_{ICE} \alpha_{ICE}) + T_{MG2} - I_R \alpha_{MG2} = \\ & = \frac{T_{W-R}}{i_{MG2-wheel}} - I_{R-EQ} \alpha_{MG2} \end{aligned} \quad (2)$$

The ratio of the planetary gear set of the system under study is 2.6, meaning that 72% of engine torque is transferred to the driveshaft and 28% to the electric generator at any condition. This is in line with the equations above. A comparison to a manual transmission can be made such that in this case the engine has an overdrive gear ratio to the wheels. The ratio of angular speed between the sun, carrier and ring gear is derived by the following equation:

$$(i_{PGS} + 1) \cdot \omega_{ICE} = \omega_{MG1} + i_{PGS} \cdot \omega_{MG2} \quad (3)$$

The equation above indicates that there are two independent variables in the system, therefore, for a given wheel speed there will be a number of possibilities for engine and generator speeds. In this way, MG1 will be responsible for controlling the engine speed and electrical power will likely to always be consumed when the engine is on. From Eq. (1), MG1 will always have a negative torque in order to control the ICE speed in a constant level but exceptions can happen in case of transients of engine speed.

4. VEHICLE PLANT MODEL

The ICE model does not incorporate thermo-mechanical or combustion phenomena, therefore, behaviors during catalyst and coolant warm-up are neglected. The model works with an external torque request for the ICE from the main control strategies and incorporates the maximum torque limitation across speed, a friction model and idle controller. Engine friction is based on the model proposed by Chen and Flynn (1965) where the resistance load is subject to a constant term, and two terms dependent on the rotational speed and its square. An important aspect of the simulation with impact on the fuel economy is the efficiency map of the engine. Duoba, Ng, and Larsen (2000) a torque sensor was added to the engine output shaft and torque measurements were executed in the vehicle at steady state speeds. The results, however, don't cover the whole operation range of the engine, instead, only the points resultant from the control strategy.

In order to reproduce the efficiency map of the engine, a thermodynamic engine model was created in the GT-Power software and combustion characteristics were calibrated throughout the engine speed and torque in order to result in the brake specific fuel consumption map (BSFC) shown in Figure 3. The optimum operation line (OOL) for this efficiency map is also shown in the graph and it presents a high correlation to the OOL presented by Kim, Rousseau, and Rask (2012) from real vehicle testing.

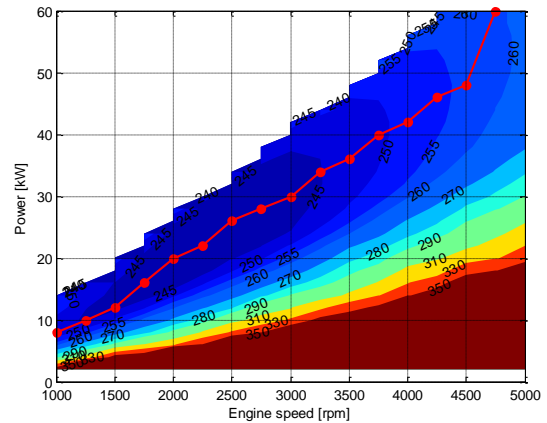


Figure 3: Engine BSFC Map And Optimum Operation Line.

Regarding ICE start and shutdown behavior, (Duoba, Henry, and Larsen 2001; Ayers, Hsu, Marilino, Miller, Ott, and Oland 2004) show test results with a maximum acceleration of 4000rpm/s during startup and -2000rpm/s during shut down. Those are important parameters for determining the ICE start torque from MG1.

The model of traction motor and generator incorporates the torque limitation characteristics of each motor with a look-up table. An investigation was conducted by (Hsu, Nelson, Jallouk, Ayers, Campbell, Coomer, Lowe, and Burrell 2005) in order to determine the

continuous torque values of the traction motor that produces a limited winding and oil temperature for a certain inlet coolant temperature. Results show a continuous torque of 167Nm for an inlet coolant temperature of 34.6°C. Moreover, the peak rated capacity generates a rise in winding temperature of 2.1 °C/s.

From the OOL in Figure 3, which produces a fixed relation between engine speed and torque, the system from Eq. (3) is reduced to only one degree of freedom. For the transmission model, the losses were incorporated from (Ayers, Hsu, Marlino, Miller, Ott, and Oland 2004) which shows a maximum total system loss of 2500W at 170 km/h.

5. BATTERY MODEL

The battery model is simulated using a capacitor as voltage source with internal and parasitic losses. As shown in Ehsani and Emadi (2005), the terminal voltage of such a battery is defined as:

$$V_T = V_{OC} - R_i \cdot I \tag{4}$$

Where V_{OC} , R_i and I are the open circuit voltage, internal resistance and terminal current, respectively. The sum of terminal current and leakage current of the battery can be expressed as:

$$I + I_L = -C \frac{dV_{OC}}{dt} \tag{5}$$

Where C is the capacitance of the battery. The leakage current is defined by V_{OC} / R_L and, when substituted in Eqs (4) and (5), leads to:

$$\frac{dV_{OC}}{dt} = - \left(\frac{V_{OC}}{CR_L} + \frac{I}{C} \right) \tag{6}$$

The resultant battery model in Simulink from this system of equations is shown in Figure 4. The electrical circuit is shown in Figure 14 from the Appendix.

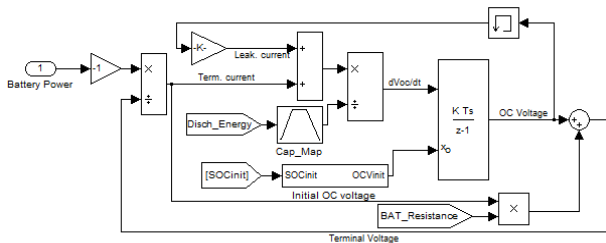


Figure 4: Battery Model In Simulink.

The validation of the battery model was done against data from tests performed by Gray and Shirk (2010) in which the battery was discharged with a constant rate of 1C (Figure 15 from the Appendix). The value used in the validation corresponds to a new battery. The battery

capacity was then calibrated in order to match the test data. The resulting battery terminal voltage of the validation model is shown in Figure 5.

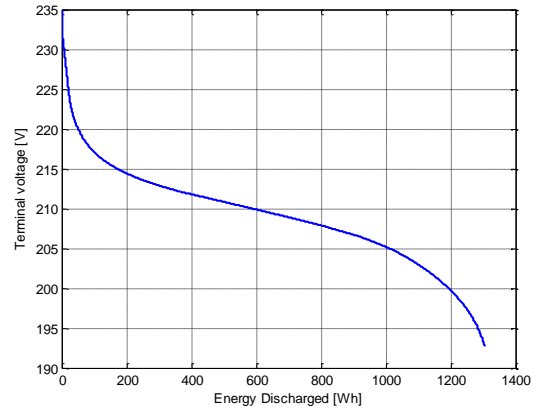


Figure 5: Validation Of The Battery Model.

6. DRIVER MODEL

The main function of the driver model is to set the desired traction torque target to be used in the forward simulation. This model contains a PID controller which compares the target speed from the input driving cycle to the actual vehicle speed. The output of the PID is the torque demand on the driveshaft, which is directly proportional to the accelerator pedal request. The driver model performance is such that the difference between followed and targeted vehicle speed must lie within a margin of 1 km/h. Figure 6 shows the difference between target and simulated speed for the NEDC cycle. The absolute difference throughout the cycle is below 0.3 km/h which indicates proper modelling not only for the driver model but also for the complete powertrain control system.

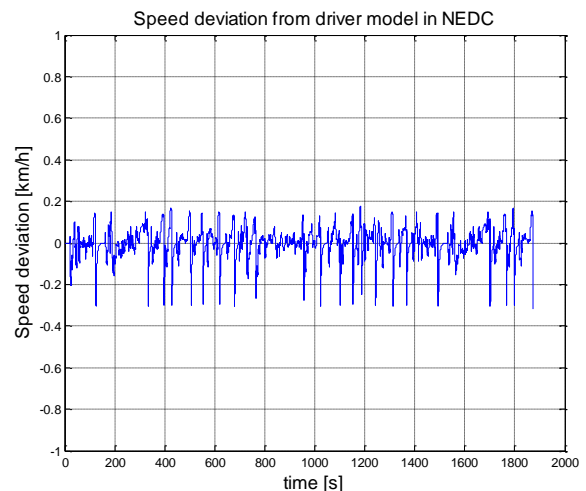


Figure 6: Absolute Speed Error From PID In Driver Model.

7. TEST DATA

Data from tests performed with Toyota Prius Gen 3 are available from Argonne National Laboratory (2013). Although the powertrain configuration has small

differences in comparison with the one presented here, the data provides a good base for validating the system. These data correspond to chassis dynamometer testing of the vehicle operating under the urban cycle FTP75.

8. GENERAL GUIDELINES

The basis for the control system design relies on the test measurements described below. The graph of Figure 7 shows the driver's request power at which the engine is turned on during the driving cycle. One can see that the ICE usually starts in a region between 8kW and 9kW.

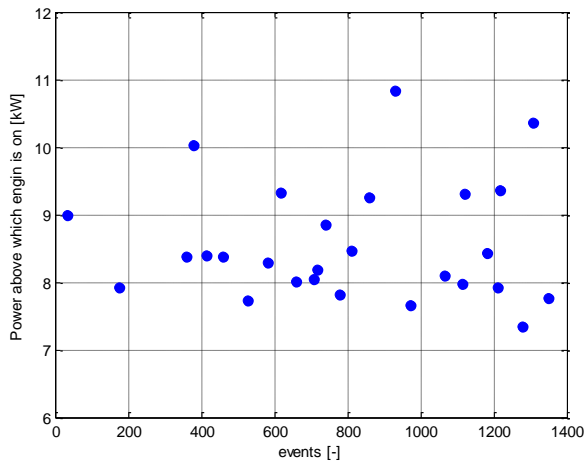


Figure 7: Engine-On Condition From Test Data.

When the engine is running, it should provide the full power demand of the road plus the battery power demand. The battery power demand is shown in Figure 8 where additional power is added to the ICE power demand in order to charge the battery when the SOC is low, or to help discharging the battery in case SOC is high. This strategy was observed by Kim, Rousseau, and Rask (2012) during vehicle tests.

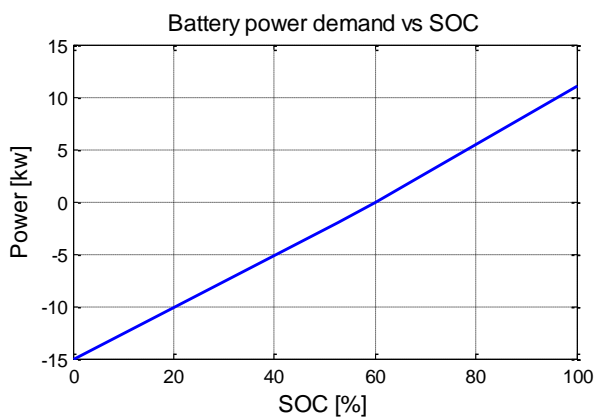


Figure 8: Battery Power Demand Added To Engine Power.

9. SIMULATION RESULTS

As mentioned before, the simulation runs in forward mode with the load request set by the driver model. Figure 9 shows vehicle and ICE speed for the simulation and test data results under the FTP75 cycle.

At this point, no emission strategy is considered what makes the ICE operates with start stop profile in the beginning of the cycle. The results show that even at speeds around 50 km/h, the traction is purely electrical and the engine basically assists the vehicle during accelerations and high speed cruising. One constrain is that above 68 km/h the engine has to be turned on in order to prevent the generator speed becoming too high, what would lead to little torque reserve to perform an engine start.

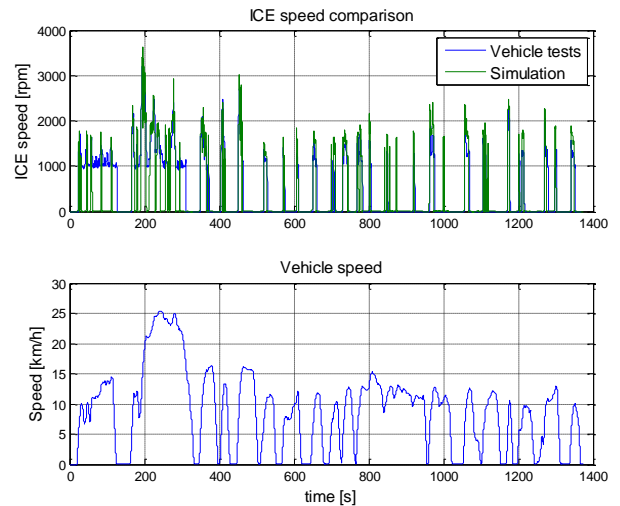


Figure 9: Results For ICE Speed.

Battery SOC and fuel consumption are shown in Figure 10, in this case for the extended FTP75 cycle, which includes the initial 500s of the cycle again at it's end. The net change in SOC at the end of the cycle was around -1%, which means that the compensated fuel consumption should be slightly higher. The final value of the non-corrected fuel economy of the simulation is 2.93l/100km which is close to the experimental data of 3.11l/100km with hot engine and 3.73l/100km with a cold engine. In the tests from Argonne National Laboratory (2013), the net variation of integrated battery current is very close to zero.

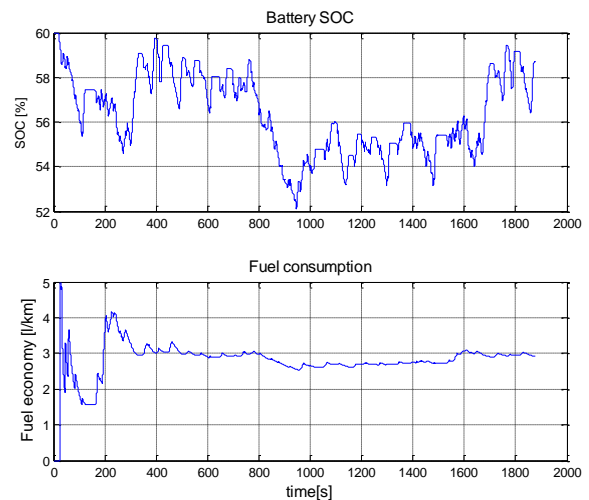


Figure 10: Results For Battery SOC And Fuel Consumption.

10. OPTIMAL CONTROL

Dynamic programming is an optimization algorithm which aims to finding the solution that generates the global minimum result for a determined cost function. This means that for a given driving cycle, the optimized solution will be a vector of control values against time. A time continuous function represent the current system can be represented by:

$$\dot{x}(t) = f(x(t), u(t), t) \quad (9)$$

where $u(t)$ is the control variable, in this case the power-split (PS), and $x(t)$ is the vector of state variables of the system, in this case the battery SOC. The cost function for this system is:

$$J(u(t)) = G(x(t_f)) + \int H(x(t), u(t), t) dt \quad (10)$$

where $G(x(t_f))$ is the final cost and the second term represents a penalty to ensure that a dynamic constrain should be satisfied, in this case that the SOC at the beginning and at the end are the same. The following cost function represent the fuel consumption in the vehicle over the driving cycle:

$$J(u(t)) = \int \dot{m}_{fuel}(u(t), t) dt \quad (11)$$

The constrains for the optimization have to be set in order to prevent that the system drift out of its boundaries:

$$T_{min} < T_{req} < T_{max} \quad (12)$$

$$SOC_{min} < SOC < SOC_{max} \quad (13)$$

$$SOC_{end,min} < SOC_{end} < SOC_{end,max} \quad (14)$$

$$u_{min}(SOC, t) < u(SOC, t) < u(SOC, t)_{max} \quad (15)$$

where T are torque requests in the system for all three power sources and SOC_{end} represent the variation of SOC from beginning to the end of the cycle.

The DP routine developed by Sundström and Guzzella (2009) was used in this analysis. The range of the PS control variable was divided in 0.1 intervals from [-1, 1], where 1 means pure electric, values between 0 and 1 mean electric assist drive, 0 means pure ICE traction, and negative values mean electric generation (no electric assist drive). The moment of ICE start could also have been inserted as a control variable but was made the same as in the detailed model. The SOC was divided in 61 steps between the range of 50% to 70% where it is allowed to vary. The constraint on the final SOC is a net variation of 1% against the initial SOC.

The detailed model in Simulink is not appropriate to this optimization due to the increase of computational power that would be necessary and also due to the difficulty of implementation. A backward looking simplified model was therefore implemented. It

incorporates the same efficiency maps for the power sources of the model presented above and has a 1s time step while the detailed model runs at 0.01s.

Figure 11 shows the PS result of the DP algorithm corresponding to the ratio of traction power from MG1 and MG2 by total power demand. The first graph shows the dependency against power demand at wheels. The traction is purely electrical until around 8kW (PS = 1), between 8kW and 12kW there is no assist drive but only charging (negative values of PS), which means that the ICE power is increased in order to go to higher efficiency islands. At further higher power values, the ICE is also set to generate in most of the events with very few events of electric assist ($1 < PS < 0$). The second graph of PS against vehicle speed shows similar results with the trend of having limited generation at higher speeds towards a pure ICE traction.

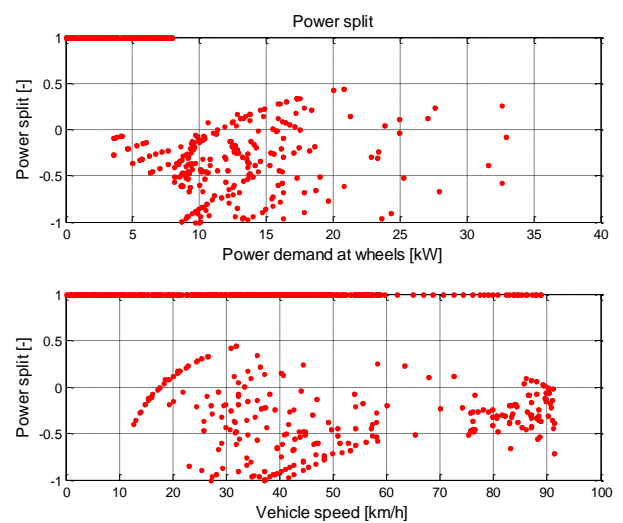


Figure 11: Power-Split (Control Variable) Result From The Dynamic Programming.

The fuel consumption result from the DP was 3.73l/km which is higher than the result of the detailed model, 2.93l/100km, with non-optimal control. Figure 12 shows battery power for a section of the driving cycle resultant from the detailed model and DP. Peaks around 25kW correspond to engine start events which take around 0.4s (Duoba, Henry, and Larse 2001). Although the trend of both curves is similar, one can see that the major differences come from the coarse time step size of 1s used in the DP routine. Behaviors such as engine start are then not taken into account as they happen in a smaller time frame. As a consequence, the total energy demand at the driveshaft and the results of the PS present high deviation when compared to the detailed model.

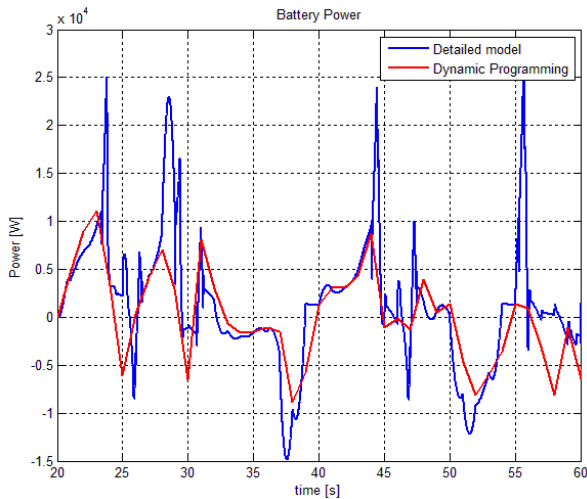


Figure 12: Battery Power For Detailed Model And DP.

The main task of the dynamic programming was building a PS map where the intended distribution of power between ICE, MG1 and MG2 could be optimally scheduled. The behavior of the state variable is shown in Figure 13 and it tells the response of the system to the variations in the control input variable.

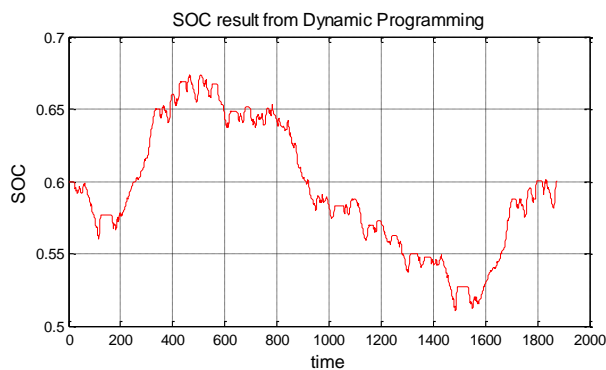


Figure 13: Dynamic Programming Result For SOC (State Variable).

11. CONCLUSION AND FUTURE WORK

Due to the differences between detailed model and the DP model, comparable results will only be possible when the DP routine runs with similar time step sizes as the detailed model. Until now this was not possible due to exponential increase in computational load and time required for convergence in the DP routine. Other optimal control programs could be used and this will be investigated further. The dynamic programming routine should be adapted so that it also decides on the moment that the ICE should be turned on. For a practical application of the results from the DP, either local optimization or a look-up table based control would have to be implemented in the detailed model as the implementation of DP in real-time is not possible.

ACKNOWLEDGMENTS

The authors greatly appreciate the data made available by Argonne National Laboratory. Without this data, the validation of the vehicle model and control strategy

would not be possible. Also, the DP routine made available by ETH and Olle Sundström was of essential contribution.

APPENDIX

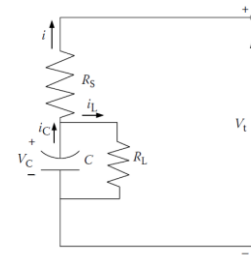


Figure 14: Equivalent Battery Circuit. Courtesy Of Ehsani and Emadi (2005).

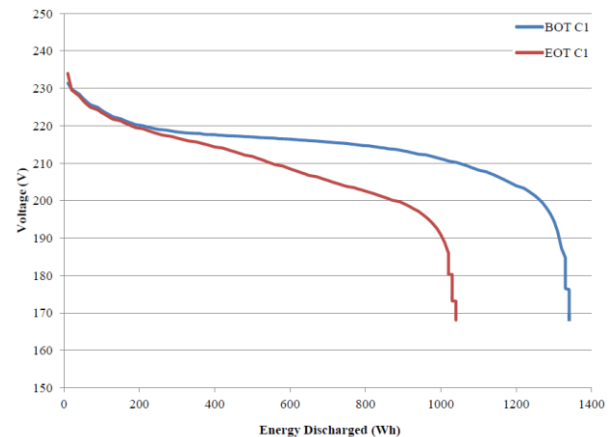


Figure 15: Voltage Variation During Battery Discharge Tests (BOT indicates new battery, EOT indicates used battery). Courtesy Of Gray and Shirk (2010).

REFERENCES

- Ehsani M., Gao Y., Emadi A., 2005. Modern Electric, Hybrid Electric, and Fuel Cell Vehicles, Fundamentals, Theory, and Design. 2nd ed. Florida: CRC Press.
- Lin C., Peng H., Grizzle J., Kang J., 2003. Power management strategy for a parallel hybrid electric truck. IEEE Trans. Control Systems Technol., 11(6), 839–849.
- Delprat S., Lauber J., Guerra T., Rimaux J., 2004. Control of a parallel hybrid powertrain: Optimal control. IEEE Transactions on Vehicular Technology, 53(3), 872–881.
- Sekimori T., 1998. Development of Toyota's Electric and Hybrid Vehicle. SAE Technical Paper 98C053, 355-361.
- M. Kamiya, 2006. Development of traction drive motors for the toyota hybrid system. IEEE Transactions on Industry Applications, 126(4), 473-479.
- Abe S., 2000. Development of the Hybrid Vehicle and its Future Expectation. SAE Technical Paper 2000-01-C042.
- Muta K., Yamazaki M., Tokieda J., 2004. Development of New-Generation Hybrid System THS II -

- Drastic Improvement of Power Performance and Fuel Economy. SAE Technical Paper 2004-01-0064.
- Duoba M., Ng, Henry, Larse R., 2001. Characterization and Comparison of Two Hybrid Electric Vehicles (HEVs) – Honda Insight and Toyota Prius. SAE Technical Paper 2001-01-1335.
- Rask E., Duoba M., Busch H., Bocci D., 2010. Model Year 2010 (Gen 3) Toyota Prius Level-1 Testing Report. Argonne National Laboratory. Report ANL/ES/RP-67317.
- Chen S. and Flynn P., 1965. Development of a Single Cylinder Compression Ignition Research Engine. SAE Technical Paper 650733.
- Duoba M., Ng H., Larsen R., 2000. In-Situ Mapping and Analysis of the Toyota Prius HEV Engine. SAE Technical Paper 2000-01-3096.
- Kim N., Rousseau A., Rask, E., 2012. Autonomie Model Validation with Test Data for 2010 Toyota Prius. SAE Technical Paper 2012-01-1040.
- Hsu J.; Nelson S., Jallouk P., Ayers C., Campbell S., Coomer C., Lowe K., Burress T., 2005. Report on Toyota Prius motor thermal management. Oak Ridge National Laboratory, ORNL/TM-2005/33.
- Gray T., Shirk M., 2013. Toyota Prius VIN 0462 Hybrid Electric Vehicle Battery Test Results. Idaho National Laboratory INL/EXT-13-28025.
- Ayers C., Hsu J., Marlino L., Miller C., Ott Jr.G., Oland C., 2004. Evaluation of 2004 Toyota Prius Hybrid Electric Drive System Interim Report. ORNL/TM-2004/247.
- Argonne National Laboratory, 2013. All Data- 2010 Toyota Prius, Available from: <http://www.anl.gov/energy-systems/group/downloadable-dynamometer-database/hybrid-electric-vehicles/2010-toyota-prius>, [Accessed 17 February 2015].
- Sundström O., Guzzella L., 2009. A Generic Dynamic Programming Matlab Function. Proceedings of the 18th IEEE International Conference on Control Applications, 1625–1630, Saint Petersburg, Russia.

AUTHORS BIOGRAPHY

Agenor de Toledo Fleury has a degree in mechanical engineering from ITA - Technological Institute of Aeronautics (1973), a MSc (1978) and a PhD degree in Mechanical Engineering from the University of São Paulo (1985). He is currently full-time professor at FEI University and a part-time PhD professor at Polytechnic School, University of Sao Paulo. He has led various projects with emphasis on Dynamics and Control Systems. His most recent projects address modeling and control of nonlinear systems, optimal control and estimation, in applications of Biomechanics, Robotics and Automotive Engineering.

Ivan Miguel Trindade is a Master student at Polytechnic School of University of São Paulo and has a degree in mechanical engineering (2008) from the same university. He has worked on various projects

with internal combustion engine and hybrid powertrain development. Nowadays he works in Punch Powertrain N. V. with control systems development for hybrid and electric powertrains.

MODELING, IDENTIFICATION AND A FIRST CONTROL APPROACH ON THE QUALITY OF FLAMES IN OIL FURNACES

Agenor T. Fleury^(a,b), Danilo S. Chui^(b), Flavio C. Trigo^(b), Flavius P. R. Martins^(b)

^(a) Centro Universitário da FEI, São Bernardo do Campo, SP, Brazil

^(b) Escola Politécnica da Universidade de São Paulo, SP, Brazil

^(a) agfleury@fei.edu.br, ^(b) danilochui@usp.br, ^(b) trigo.flavio@usp.br, ^(b) martins.flavius@usp.br

ABSTRACT

In industrial oil furnaces, unstable flames can lead to potentially dangerous conditions. Elaborate control systems are used to monitor the parameters of the process to avoid those problems. Current trends in research seek to identify *a priori* anomalous behavior of the flames, thus improving the time response of the control system. Controller performance is directly affected by the accuracy of the system model. Unfortunately, due to the complexity of the process, physical models of flame propagation are still not faithful enough for control purposes. Conversely, could the complex dynamics of flame propagation be described in terms of an identified assumed model, the control strategy could be improved. In this work, a control technique based on an Operational Modal Analysis model identification of a state-space description of oil flame dynamics in a prototype furnace is designed. Results obtained suggest that the proposed approach might be used in an automated control system.

Keywords: Flame modelling, Operational Modal Analysis, LQ control systems.

1. INTRODUCTION

The monitoring of oil-flame conditions in industrial petrochemical plants is of capital importance in terms of economy, environment-friendly operation, and safety. Currently, a wide array of sensors performs the task of measuring and informing the plant staff who, ultimately, judges the necessity of intervening to alter control parameters. This process has two drawbacks: firstly, sensors like thermocouples, flow meters, opacity meters, pressure sensor or even air-fuel ratio gauges are normally expensive and require frequent maintenance interventions; secondly, the judging ability of distinct operators is not the same, which might lead to below-standard functioning condition, including potentially dangerous ones. The first drawback pointed above should be tackled by replacing the specialized sensors by a frame-grabber and a set of low-cost CCD video cameras properly inserted in the furnace; those cameras can produce a continuous flow of flame images exhibiting luminance patterns that are well correlated to the physical combustion variables. The second drawback can be handled with computer vision routines able to

identify normal or abnormal combustion states through the analysis of the sequence of flame images grabbed by the cameras. However, such an aim can not be successfully achieved unless the decision-making be supported by reliable inferences on the image processed data. That is why the computer vision based systems for combustion processes monitoring usually apply a heterogeneous set of statistical and artificial intelligence techniques, especially multivariate statistics, artificial neural networks and fuzzy logics.

Expert systems with these attributes are getting more and more importance for the oil and gas industries in the last years because of the potential impact to clean combustion. A key feature that must be monitored in order to maintain optimal burning conditions of oil flames is the vapor to fuel rate (VFR), which directly affects fuel nebulization and flame quality. Fleury *et al.* (2013) proposed a method based on computer vision and Kalman filtering to monitor nebulization quality of oil flames in a prototype refinery furnace. In short, the authors show that CCD-grabbed images of the flames at a priori known nebulization quality can be used to devise characteristic vectors that generate a set of fuzzy classification rules. Then, the components of a characteristic vector obtained from grabbed images of unknown a priori nebulization quality are assumed to be state-variables of a random-walk state-space model which, through a Kalman filter, effectively estimates the state and the nebulization quality when there is a statistically-proven convergence to a state that matches one of the classification rules. The researchers also state that the method could be improved once, instead of a random-walk model for the evolution of the state, a more accurate description of the system dynamics was employed. The difficulty that arises concerns the fact that phenomenological models available in the literature are poorly capable of encompassing both micro and macro scales occurring in flame propagation. As a consequence, a description based on either one would not cover the wide range of phenomena in between limiting conditions, thus resulting in a poor model under the estimation perspective.

Another important issue for the adequate operation of refinery furnaces is the early detection of flame instability. This phenomenon may cause the extinction of

the flame, resulting in an undesirable dangerous condition. Models for combustion instability in the literature (Bouziani *et al.*, 2005) based on coupled van der Pol equations state that unstable conditions can be detected under certain controlled situations; however, perturbations may induce false instability diagnosis near theoretically stable operation setups. Therefore, a description of the dynamics of the system based purely on data from observations of flames under actual operating conditions could possibly enhance the predictability of AI algorithms in general. A technique that suits this purpose is Operational Modal Analysis (OMA) in the time domain and, in a second paper (Silva *et al.*, 2015), authors proposed a new approach to estimate flame dynamics using OMA.

Overall, OMA seeks to identify parameters of an assumed model of the system dynamics using information from measurements of the system response to known particular inputs, namely, either step or impulse excitations, in real operating environment. The so called Ibrahim Time-Domain Method (ITDM), one of the tools available to perform the task, is widely employed in the identification of frequencies and modes of vibration in structures like stayed bridges (Liu *et al.*, 2012; Wu *et al.*, 2012), offshore platforms (Wang *et al.*, 2010), and components of rotating mechanisms (Grange *et al.*, 2009), just to cite some of the most recent publications.

An unconventional application of the ITDM was presented by Moura *et al.* (2010). Those researchers employed the technique to identify the discrete state transition matrix in electrical impedance tomography, one of the instances for which analytical models do not suffice to describe the evolution of the state, the resistivity distribution in a domain of interest, with the required accuracy. This suggests the power of the ITDM, in the sense of surpassing its original scope, once the modal decomposition approach enables avoiding complex (and, sometimes, quite inaccurate) modeling, even of highly non-linear systems.

Considering the previous discussion and the importance of combustion condition monitoring, this work proposes an extension of the paper by the same authors (Silva *et al.*, 2015) which addresses the problem of detecting evidence of the beginning of flame unstable behavior and automatically act to avoid such condition. The state transition matrix from a four-degree of freedom second order model of this phenomenon in a prototype furnace was already identified and a Linear Quadratic controller (LQ) is designed based on this dynamic model. This is a quite usual control approach, as should be done, for example, for the control of a flexible structure, except for the fact that the control system has to sustain flames in a nonzero condition, since this would imply flame extinguishment.

In the next sections, data collection and processing, a brief description of the ITDM, the LQ design and the first control results, with emphasis on the current approach are presented.

2. METHODS

Since modeling is a crucial requirement for a good control design, this section brings a discussion on the most important parts of author's previous work (Silva *et al.*, 2015). First aspect, experimental data were taken on a small-scale refinery furnace. Image data acquisition equipment is the same as mentioned by Fleury *et al.* (2013). The CCD camera for image grabbing is placed in a shielded and cooled compartment in the central cross-section of the furnace cylindrical wall. Burner inlets of primary and dry air, steam and oil enable the control of combustion parameters.

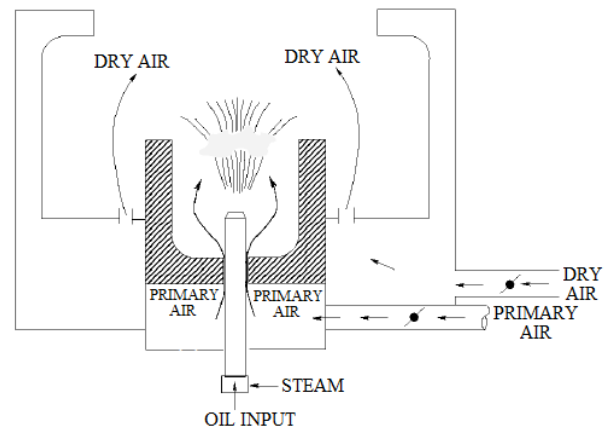
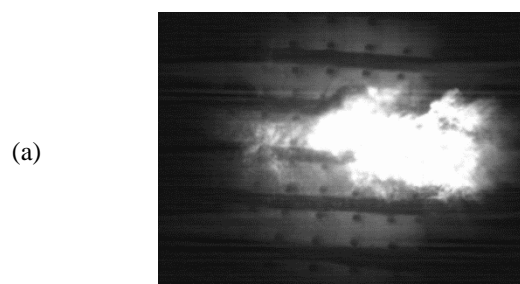


Figure 1: Burner Nozzle Schematics (modified from Fleury *et al.* (2013))

In order to correlate the visual appearance of the flames with the stability of the combustion process, three series of operational tests were carried out. Typical stability states, ranked according to a specialist, were obtained through proper regulation of the primary/secondary air rate (PSAR) at the burner nozzle, as depicted in the detail of Figure 1. Those series, encompassing an amount of 280 images, will be nominated hereafter as 'stable flames (PSAR=1.0)', 'unsteady flames (PSAR=1.86)' and 'unstable flames (PSAR=4.0)'. As illustrated by Figure 2 (a)-(b)-(c), the visual appearance of those image flames are clearly distinct, since the spatial distribution and arrangement of their pixel gray levels give rise to different types of texture.

The previous assertion was taken into account to construct a discriminant characteristic vector \vec{v}_i based on 13 properties directly related to the texture and spatial distribution of the pixel gray levels of the flame image I_i . The components of \vec{v}_i correspond to the following image properties:



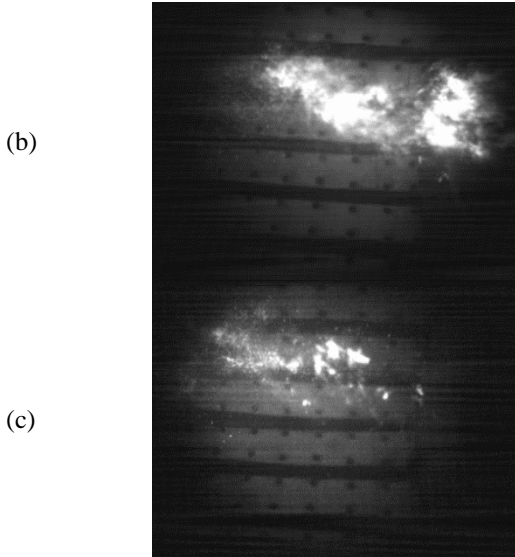


Figure 2: Flame Images. (a) PSAR=1.0; (b) PSAR=1.86; (c) PSAR=4.0.

- $v_i[1]$ is the average pixel gray level;
- $v_i[2]$ is the image entropy;

$$v_i[2] = -\sum_{j=1}^N p_j \log_2(p_j), \text{ where } p_j \text{ is the}$$

frequency occurrence of gray level j ;

- $v_i[3]$ is the average local maximum pixel gray level difference observed through a complete image scanning by a 3x3 window;
- $v_i[4]$ is the average local maximum mean standard deviation observed through a complete image scanning by a 3x3 window;
- $v_i[5]$ to $v_i[13]$ are texture characteristics based on the co-occurrence matrix (Gonzalez and Woods, 1992) of the image I_i , relative to two horizontally neighbor pixels whose gray levels are separated by either 1, 3 or 5 units. This way, $v_i[5]$, $v_i[6]$, and $v_i[7]$ are the correlation indexes of the number of occurrences of sequences of two pixels i and j whose gray levels are separated by 1, 3 and 5 units, respectively. Those indexes are calculated according to:

$$\sum_{i,j} \frac{(i - \mu_i)(j - \mu_j) p(i, j)}{\sigma_i \sigma_j} \quad (1)$$

where $p(i, j)$ is the frequency occurrence of two horizontally pixels exhibiting gray levels i and j , μ_i and μ_j are the average number of occurrences of gray level pixels i and j , and σ_i, σ_j are their corresponding mean standard deviation. Similarly, $v_i[8]$, $v_i[9]$, and $v_i[10]$ are the contrast values of the number of occurrences of sequences of two pixels i and j whose gray levels are separated by 1, 3 and 5 units, respectively. Those indexes are calculated according to:

$$\sum_{i,j} |i - j|^2 p(i, j) \quad (2)$$

Finally, $v_i[11]$, $v_i[12]$, and $v_i[13]$ are the homogeneity values of the number of occurrences of sequences of two pixels i and j whose gray levels are separated by 1, 3 and 5 units, respectively. Those measures are calculated according to:

$$\sum_{i,j} \frac{p(i, j)}{1 + |i - j|} \quad (3)$$

3. IBRAHIM TIME-DOMAIN METHOD

The ITDM was conceived in the 1970s and has, since then, been developed and successfully applied. The methodology here presented is a concise version of a work by Pappa and Ibrahim (1981), which reviews a series of previous research since Ibrahim and Mikulcik (1973).

Essentially, as originally devised, the method infers modal properties of a n -degree of freedom 2nd order assumed model from the free-response of a system to either impulsive or other excitation function (Ewins, 2000). By hypothesis, the dynamics of the system is represented by the equation:

$$M \ddot{y} + C \dot{y} + Ky = f \quad (4)$$

in which M is the mass matrix, C is the damping matrix and K is the stiffness matrix, y , \dot{y} , \ddot{y} respectively represent displacement, velocity and acceleration vector, while f stands for the exogenous forcing vector. Once this model is mapped into a state-space framework and the resulting $2n$ first order differential equations are written in matrix form, a so called $2n \times 2n$ system matrix conveys all information concerning inertia, stiffness and damping characteristics of the system under analysis.

As it is known from dynamic system theory, the *eigenvalues* of the system matrix are used to compute natural frequencies and damping factors, whereas its *eigenvectors* provide mode shapes, for each degree-of-freedom of the assumed model. Thus, provided that the system undergoes free vibration, Ibrahim's method estimates the above-mentioned matrix. Thus, naming x the state vector and A the system matrix, for a certain instant t_i , a set of displacements, velocities and acceleration measurements of the free-response of the system yield n linear equations to solve for $2n^2$ unknowns according to Eq. (5),

$$\dot{x}_j = Ax_j \quad (5)$$

When measurements for $2n$ instants t_1, t_2, \dots, t_{2n} , are made, then one comes up with $2n^2$ equations, as follows:

$$[\dot{x}_1 \ \dot{x}_2 \ \dots \ \dot{x}_{2n}] = A[x_1 \ x_2 \ \dots \ x_{2n}] \quad (6)$$

$$\dot{X} = AX \rightarrow A = \dot{X}X^{-1} \quad (7)$$

Hence, considering that all the components of X and dX/dt are available, matrix A is unambiguously obtained, as it can be realized from Eq. (7). Regarding that the characteristic equation for the free-response of the system in Eq. (4) is:

$$\lambda^2 M + \lambda C + K = 0 \quad (8)$$

the solution of Eq. (7), at any measuring spot j , may be written as the sum of the contribution of each individual mode at that spot; for a given instant t_j ,

$$x_j(t_i) = \sum_{k=1}^{2n} \psi_{jk} e^{\lambda_k t_i} \quad (9)$$

in which ψ_{jk} represents the free-response of the mode associated to the k^{th} eigenvector at the j^{th} spot, and λ_k the corresponding eigenvalue, solution of the characteristic equation, in general, both complex numbers. When $2n$ points are measured at several time instants, after some algebraic manipulation, Pappa and Ibrahim (1981) prove that the sought system matrix A is part of an eigenvalue problem. It follows that the eigenvalues of matrix A , complex numbers of the form $\lambda_k = \beta_k + i\gamma_k$, and the roots of the characteristic equation, the eigenvalues of the spatial model of Eq. (1) (Ewins, 2000) $s_k = \sigma_k + i\omega_{d,k}$, are related by

$$\beta_k + i\gamma_k = e^{\{\sigma_k + i\omega_{d,k}\}\Delta t_1} \quad (10)$$

In the above equation, Δt_1 represents an arbitrary time-shift and, in view of Eq. (9), the scalars β_k and γ_k can be used to obtain the damped natural frequency, natural frequency and damping factor for each mode according to Eqs. (11)-(14) which, once associated to the eigenvectors, completely characterize the system dynamics.

$$\omega_{d,k} = \tan^{-1} \left(\frac{\gamma_k / \beta_k}{\Delta t_1} \right) \quad (11)$$

$$\zeta_k = \frac{\sigma_k}{(\sigma_k^2 + \omega_{d,k}^2)^{1/2}} \quad (12)$$

$$\omega_{n,k} = \frac{\omega_{d,k}}{(1 - \zeta_k^2)^{1/2}} \quad (13)$$

$$\sigma_k = \frac{1}{2\Delta t_1} \ln(\beta_k^2 + \gamma_k^2) \quad (14)$$

An important issue that avoids straightly employing either the original or the modified ITDM is the demand of data from the free-response of the system under evaluation. This problem arises in several field situations, for instance, the identification of large structures like buildings and bridges, whose free-response is virtually impossible to obtain since, at least, random excitation coming from the environment (wind,

ground vibration transmitted to the structure *via* mechanical constraints) is always present. In the case of the present scope, a free-response would imply extinguishing the flame, a potentially dangerous operational condition. This difficulty can be surmounted when the ITDM is employed in conjunction with the Random Decrement Technique (Cole, 1971), also known as RANDOMDEC, since demonstrated by Ibrahim and Mikulcik (1977).

The RANDOMDEC technique uses data from random excitation to estimate the free-response of the system. Cole (1971) asserts that, for a system vibrating under random stationary excitation, when the average of numerous samples of the displacements response are computed, the contribution of velocities and accelerations on the measured signal gradually vanish; consequently, the free-response is obtained. The *RANDOMDEC signature* of the system, as named by Cole, is computed using segments of the measured displacement signal delimited by the same boundary condition (a chosen amplitude, for instance). First, N equal time-length τ segments of the measured signal $y(t)$, starting at instants t_j ($j=1, 2, \dots, N$) provided that $y(t_j) = \alpha$ (the boundary condition) are sampled. Subsequently, the signature is obtained according to Eq. (15), the sought free-response of the system.

$$\delta(\tau) = \frac{1}{N} \sum_{j=1}^N y(t_j + \tau) \quad (15)$$

In this work, the RANDOMDEC signature is computed from averages of segments with initial value (boundary condition) ranging from 60 to 80% of the maximum amplitude. A four degree-of-freedom second order system model with viscous damping was admitted for the application of the ITDM. Owing to the availability of only one measuring station (the housing for the camera in the furnace wall), the procedure outlined by Pappa and Ibrahim (1981) was employed to fill the response matrix and the time-shifted response matrix, in the following way: lines at the upper half of the response matrix received data collected at lagging intervals of 1/24 and 1/8 seconds; data on the upper four lines, further delayed in 7/24 seconds, completed the lower four lines. The lagged response matrix, on the other hand, was obtained through a time-shift of 5/6 seconds of the elements of the response matrix. Finally, 12 time-instants were used by the ITDM.

4. MODELING RESULTS AND DISCUSSION

Grabbed images from the unstable flame condition (PSAR=4.0) were processed according to the description of Section 2, providing a set of vectors $v_i(t_k)$, $i=1, \dots, 13$, $k=1, \dots, 100$, corresponding to a temporal sequence from available data of short-period trials for each of the 13 image characteristics. This reduced number of results poses another difficulty to the utilization of the RANDOMDEC technique: according to

Cole (1971), the procedure is as accurate as the number of averages in Eq. (12) increases. One manner to deal with this problem is by vectorizing v_i so as to obtain a longer sequence and improve algorithm performance, an artifice whose justification is based on the rationale that follows.

In the first place, the stationarity hypothesis was admitted as a requirement to the RANDOMDEC scheme, which implies that grabbed data (images) represents a stochastic process. The instantaneous components of each of the characteristic vectors v_i are obtained from the same data sample through strictly deterministic algorithms; furthermore, this sample contains information concerning the whole process at that instant. Therefore, it is fair to admit that the process is also wide-sense ergodic. As a consequence, the proposed vectorization will preserve the two first moments of the entire process. Offset cancellation and normalization of each sequence of parameters were performed before the vectorization process, whose outcome for the PSAR=4,0 is featured in Figure 3. The 'relative amplitude' instead of physical units at the ordinates label is thereof justified. The RANDOMDEC/ITDM was, then, employed to compute the modal parameters of the model, which can be seen in the second and third columns of Table 1.

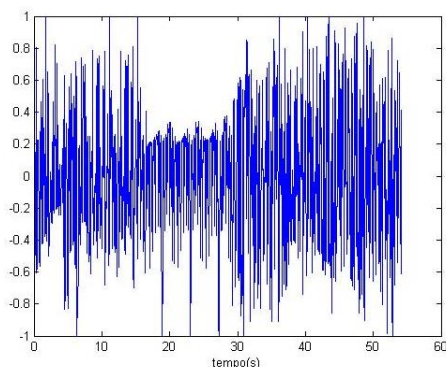


Figure 3: Vectorized Time-History of Characteristic Parameters for the 'Unstable' Flames ($PSAR = 4.0$)

In order to corroborate the above results, a spectral analysis of the temporal sequence of Figure 3 was performed and provided the power spectrum depicted in Figure 4, on which is possible to realize the spreading of the signal power throughout the whole range of identifiable frequencies, namely, from 0 to 12 Hz, including peaks at the four frequencies obtained by the ITDM/RANDOMDEC technique. The occurrence of several spurious frequencies among those identified can be explained by leakage arising from the convolution with a rectangular window before the spectral analysis. Nevertheless, the four frequencies of interest do present higher relative amplitudes. For the sake of comparison, the third and fourth columns of Table 1 show, respectively, natural frequencies computed by Fast Fourier Transform (FFT) and their relative discrepancy to the ones obtained with by the proposed approach.

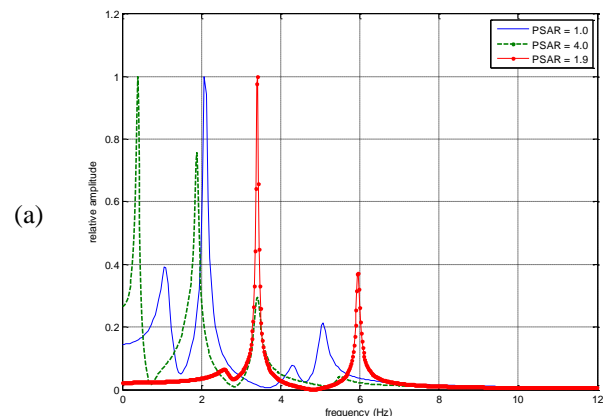
Overall, the errors may be considered negligible except for the second natural mode.

Table 1: Damped Natural Frequencies/ Damping Factors for Each Identified mode and Discrepancy Among Frequencies Computed from ITDM/ RANDOMDEC and Spectral Analysis.

Natural mode	ITDM-Rd damped natural frequency f (Hz)/ damping factor ζ	FFT damped natural frequency f (Hz)	$\frac{f_{FFT} - f_{Rd/MI}}{f_{Rd/MI}} \times 100$
1	1.88/0.072	1.88	0.0
2	2.41/0.740	2.88	19.5
3	3.60/0.791	3.40	-5.5
4	5.03/0.005	5.07	-0.8

The next step concerns the validation of the proposed approach; to this end, it suffices to verify whether data from stable ($PSAR = 1.0$) and partially stable ($PSAR = 1.9$) flame conditions, once processed according to ITDM/RANDOMDEC technique with parameters tuned for the unstable condition, can be distinguished from the latter. A further ratification is possible by reversing the process, *i.e.*, using the ITDM/RANDOMDEC to identify stable flames and check the parameters thus found against partially stable and unstable flames. The results of both analyses are described below.

Spectra of signals reconstructed from the identified models, normalized by each relative amplitude, are depicted in Figure 4(a) and Figure 4(b), whose reference spectra are respectively the curves for $PSAR = 4$ and $PSAR = 1.0$. According to common sense reasoning, one should expect closer resemblance between curves of PSARs 1.9 and 4.0 in Figure 4(a) whereas, in Figure 4(b), curves of PSARs 1.9 and 1.0 would presumably look more alike. This qualitative analysis, however, does not provide solid ground for a definitive validation of the method since, in the first case, a clear match occurs once, at the 3.41 Hz frequency; on the other hand, in the second case, frequency matches occur close to abscissae 1.3 and 5.7 Hz.



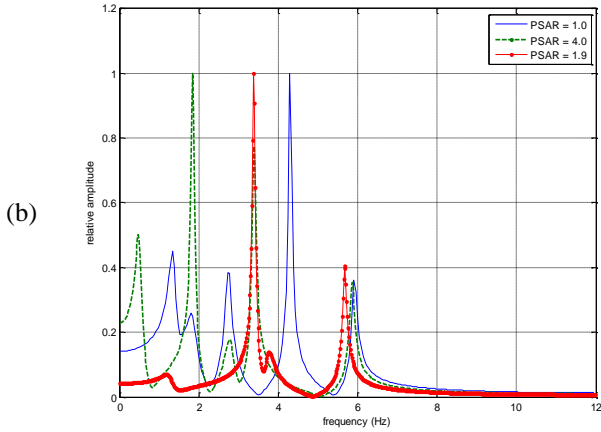


Figure 4: Comparative Relative Power Spectra for Identified Models of (a): Unstable ($PSAR = 4.0$); and (b): Stable ($PSAR = 1.0$) Reference Flames.

A quantitative measure of the adherence between an estimated mode and a reference mode which is normally used in OMA is the Modal Assurance Criterion - MAC (Ewins, 2000). The MAC essentially computes cumulative least-squares differences of all the combinations of pairs of data from distinct sets into a single scalar, despite that mode shapes and frequencies may be complex-valued. In the present case, the MAC has been modified to provide separate summations of the squared differences among frequencies and amplitudes of the reference and the other spectra in both cases under consideration.

Upon naming Nr : number of reference signals; Nt : number of test signals; Nrp : number of peaks of the reference signals; Ntp : number of peaks of the test signals; t : superscript related to test; r : superscript related to reference; F computation index related to frequency; and A : computation index related to amplitude, the criterion can be mathematically stated according to:

$$(MAC_F)_{Nr} = \sum_{i=1}^{Nt} \sum_{j=1}^{Nrp} \sum_{k=1}^{Ntp} (F_{j,k}^t - F_{j,k}^r)^2, \quad (16)$$

$$Nr = 1,2$$

$$(MAC_A)_{Nr} = \sum_{i=1}^{Nt} \sum_{j=1}^{Nrp} \sum_{k=1}^{Ntp} (A_{j,k}^t - A_{j,k}^r)^2, \quad (17)$$

$$Nr = 1,2$$

$$MAC = 1 - \frac{MAC_F \times MAC_A}{\max(MAC_F, MAC_A)} \quad (18)$$

Eq. (16) and Eq. (17) represent a quantitative measure of the scattering of frequencies and relative amplitudes around respective their references, whereas Eq. (18) expresses, in a single scalar, the combined effect of both dispersions. Thus, stable or partially stable flames, when tested using parameters computed from unstable flames, are expected to exhibit increasing values of MAC (partially stable > stable); conversely, unstable or partially stable flames should present decreasing values of MAC if probed against stable flames identified model. The results of the above validation are presented in Table

2, from which it is possible to confirm the truthfulness of those hypotheses.

Table 2: MAC Values for Cross-Validation of the Qualitative Analysis.

MAC		test PSAR		
		1.0	1.9	4.0
reference PSAR	4.0	0.0	0.67	1
	1.0	1.0	0.75	0.0

The validation step ends the whole proposed process for detecting evidence of the beginning of flame instability. Recalling what was mentioned in the introductory section, it is now possible to collect, from Eq. (10), the proper components of the discrete-time state transition matrix A , thus characterizing the dynamics of the system in the time domain, as it was initially proposed. Moreover, time-history of characteristic vector can be reconstructed from the identified system model and, as a consequence, one is able to infer how long flames with those features would take to be extinguished. The time-evolution of both measured and reconstructed characteristic vectors is shown in Figure 5, from which it can be asserted that unstable flames would last less than 20 seconds before total extinction.

It is important to point out that, in comparison to the previous work of Fleury *et al.* (2013), in which the white Gaussian noise represented the dynamics of flame propagation (in a state-space random walk model), the current research has been able to identify a second-order four degree-of-freedom model that describes the time evolution of the combustion process. Furthermore, data compression resulting from the application of modal identification, a feature that was not present in the previous work, tends to enhance the discrimination ability of the system, since redundancy is diminished.

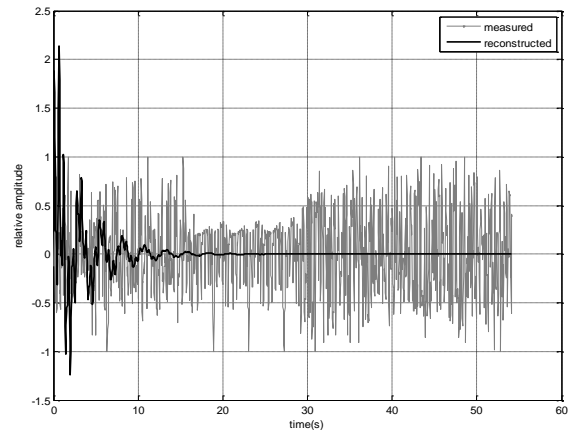


Figure 5: Comparative time-evolution of measured and reconstructed characteristic vectors for flames with $PSAR = 4.0$.

5. A CONTROL APPROACH

The identified four modes from ITDM/RANDOMDEC give rise to an experimental model. Here, frequencies and damping factors used in the experimental model are those described in Table 3.

Table 3: Identified Modes (Silva *et al.*, 2015).

Natural mode	Damped natural frequency f (Hz)	Damping factor ζ	Natural frequency ω_n (rad/s)
1	1.88	0.072	11.84
2	2.41	0.740	22.51
3	3.60	0.791	36.97
4	5.03	0.005	31.60

Thus, each mode can be represented as a second order system. Together, all four modes derive into an eighth degree dynamic system of the form:

$$\begin{aligned} \dot{\mathbf{x}} &= \mathbf{A}\mathbf{x} + \mathbf{B}\mathbf{u} \\ \mathbf{y} &= \mathbf{C}\mathbf{x} \end{aligned} \quad (19)$$

where $\mathbf{x} = [x_1 \dots x_8]^T$, $\mathbf{u} = [u_1 \dots u_4]^T$, $\mathbf{y} = [y_1 \dots y_8]^T$ and:

$$\mathbf{A} = \text{diag}[\mathbf{A}_i], \mathbf{A}_i = \begin{bmatrix} 0 & 1 \\ -\omega_{ni} & -2\zeta_i\omega_{ni} \end{bmatrix}, i = 1, \dots, 4$$

$$\mathbf{B} = \text{diag}[\mathbf{B}_i], \mathbf{B}_i = \begin{bmatrix} 0 \\ 1 \end{bmatrix}, i = 1, \dots, 4$$

For the sake of simplicity, let us consider that the output vector \mathbf{y} and the state vector \mathbf{x} have the same dimension. Of course, for other cases, one could design an observer to obtain the whole state. Thus, $\mathbf{C} = \mathbf{I}_{8 \times 8}$.

System (19) characterized above describes the dynamics of the flame, in respect of the modes derived from the images from the CCD camera. Each subsystem is a classic underdamped second order system, whose responses fade to zero in the absence of a permanent input signal. Recurring to the system of the flame, the absence of oscillation means that the flame had extinguished. Therefore, one way to maintain the flame is to excite it with an appropriate input so that all four modes never stabilize asymptotically to a position. The strategy is to maintain the system into an oscillatory movement, therefore assuring the flame characteristics for the time needed. This behavior can be obtained if an appropriate reference is defined and a simple LQR control is synthesized to follow this reference.

5.1. Reference definition

Reference will be defined in accordance to the desired behavior for system (19). A slight modification on system (19) would be enough to give it an oscillatory characteristic. Let us mirror the system (19) but modify matrix \mathbf{A} setting all damping factors $\zeta_i = 0$. That would make the subsystems to behave like undamped second order systems. Thus, consider the following reference system:

$$\dot{\mathbf{x}}_r = \mathbf{A}_r\mathbf{x}_r + \mathbf{B}_r\mathbf{u}_r \quad (20)$$

where $\mathbf{x}_r = [x_{r1} \dots x_{r8}]^T$, $\mathbf{u}_r = [u_{r1} \dots u_{r4}]^T$, $\mathbf{B}_r = \mathbf{B}$ and:

$$\mathbf{A}_r = \text{diag}[\mathbf{A}_{ri}], \mathbf{A}_{ri} = \begin{bmatrix} 0 & 1 \\ -\omega_{ni} & 0 \end{bmatrix}, \text{ for } i = 1, \dots, 4$$

In order to define completely the reference path, it is necessary to set up an initial condition for the reference system, $\mathbf{x}_0 = [0.5 \ 0 \ 0.5 \ 0 \ 0.5 \ 0 \ 0.5 \ 0]^T$ and define the input, for all time $t \geq 0$, $\mathbf{u}_r = [0 \ 0 \ 0 \ 0]^T$. These conditions could be interpreted, in an analogous mass-spring mechanical system, as an arbitrarily chosen initial position at 0.5 m , with initial velocity of the mass equal to zero, for each subsystem of (20). Moreover, the position of equilibrium of these mass-spring subsystems is also arbitrarily set to 1.0 m . As expected, the reference system responses are composed of a set of oscillatory movements shown in Figure 6 and Figure 7.

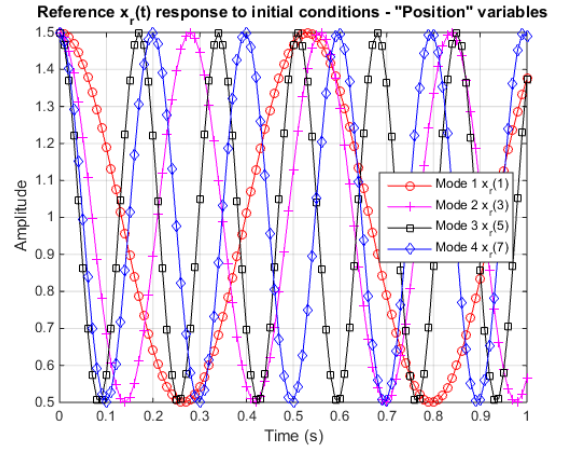


Figure 6: Reference $\mathbf{x}_r(\mathbf{t})$ Response to Initial Conditions for "Position" Variables

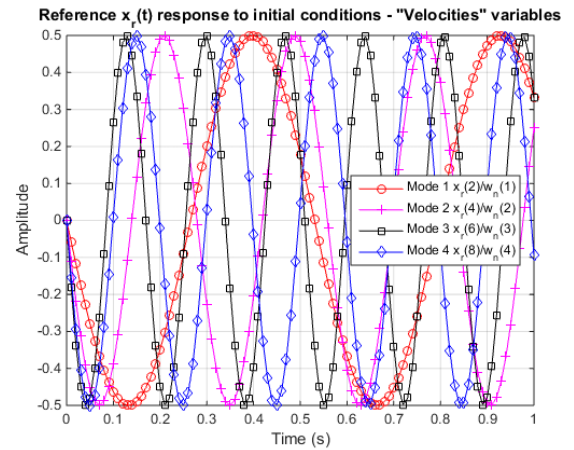


Figure 7: Reference $\mathbf{x}_r(\mathbf{t})$ Response to Initial Conditions for "Velocities" Variables

5.2. LQ Controller

Let us define the vector \mathbf{e} the error of the system:

$$\mathbf{e} = \mathbf{x} - \mathbf{x}_r \quad (21)$$

Then,

$$\begin{aligned} \dot{\mathbf{e}} &= \dot{\mathbf{x}} - \dot{\mathbf{x}}_r = \mathbf{A}\mathbf{x} + \mathbf{B}\mathbf{u} - \mathbf{A}_r\mathbf{x}_r - \mathbf{B}_r\mathbf{u}_r \\ \dot{\mathbf{e}} &= \mathbf{A}(\mathbf{e} + \mathbf{x}_r) + \mathbf{B}\mathbf{u} - \mathbf{A}_r\mathbf{x}_r - \mathbf{B}_r\mathbf{u}_r \\ \dot{\mathbf{e}} &= \mathbf{A}\mathbf{e} + (\mathbf{A} - \mathbf{A}_r)\mathbf{x}_r + \mathbf{B}\mathbf{u} - \mathbf{B}_r\mathbf{u}_r \end{aligned} \quad (22)$$

Now, let us define the augmented state variable vector $\bar{\mathbf{x}} = [\mathbf{e} \ \mathbf{x}_r]^T$ and the input vector $\bar{\mathbf{u}} = [\mathbf{u} \ \mathbf{u}_r]^T$ that will have to satisfy the following dynamic system:

$$\begin{aligned} \dot{\bar{\mathbf{x}}} &= \bar{\mathbf{A}}\bar{\mathbf{x}} + \bar{\mathbf{B}}\bar{\mathbf{u}} \\ \mathbf{y} &= \bar{\mathbf{C}}\bar{\mathbf{x}} \end{aligned} \quad (23)$$

where,

$$\bar{\mathbf{A}} = \begin{bmatrix} \mathbf{A} & \mathbf{A} - \mathbf{A}_r \\ \mathbf{0}_{8 \times 8} & \mathbf{A}_r \end{bmatrix}, \bar{\mathbf{B}} = \begin{bmatrix} \mathbf{B} & -\mathbf{B}_r \\ \mathbf{0}_{8 \times 4} & \mathbf{B}_r \end{bmatrix} \text{ and } \bar{\mathbf{C}} = \begin{bmatrix} \mathbf{C} & \mathbf{C}_r \end{bmatrix}$$

If the error $\mathbf{e}(\mathbf{t})$ goes to zero, it means that the system (19) is following the reference (20). To close the control loop and achieve zero error, a linear input $\bar{\mathbf{u}}(\mathbf{t})$ is defined for the system (23):

$$\begin{aligned} \bar{\mathbf{u}} = -\mathbf{K}\bar{\mathbf{x}} \Leftrightarrow \begin{bmatrix} \mathbf{u} \\ \mathbf{u}_r \end{bmatrix} &= \begin{bmatrix} -\mathbf{k}_e & -\mathbf{k}_r \\ -\mathbf{k}_e^r & -\mathbf{k}_r^r \end{bmatrix} \begin{bmatrix} \mathbf{e} \\ \mathbf{x}_r \end{bmatrix} \\ &= \begin{bmatrix} -\mathbf{k}\mathbf{e} - \mathbf{k}_r\mathbf{x}_r \\ -\mathbf{k}_e^r\mathbf{e} - \mathbf{k}_r^r\mathbf{x}_r \end{bmatrix} \end{aligned} \quad (24)$$

Gain matrix \mathbf{K} is determined through the LQR controller method. This method minimizes the performance index J :

$$J = \int_0^\infty \bar{\mathbf{x}}(t)^T (\mathbf{Q} + \mathbf{K}^T \mathbf{R} \mathbf{K}) \bar{\mathbf{x}}(t) dt, \quad (25)$$

where \mathbf{Q} is a positive semidefinite matrix and \mathbf{R} is a positive definite matrix and are chosen as follows:

$$\begin{aligned} \mathbf{Q} &= \begin{bmatrix} \mathbf{Q}' & \mathbf{0}_{8 \times 8} \\ \mathbf{0}_{8 \times 8} & \mathbf{0}_{8 \times 8} \end{bmatrix}, \\ \mathbf{Q}' &= \mathbf{I}_{8 \times 8} \cdot [1 \ 30 \ 1 \ 10^4 \ 1 \ 2 \times 10^4 \ 1 \ 10]^T \\ \mathbf{R} &= \mathbf{I}_{8 \times 8} \end{aligned} \quad (26)$$

One can find the gain matrix \mathbf{K} , through the solution algebraic of the Riccati equation that results from (25).

5.3. Simulation results

Simulation was performed considering that a flame is ongoing and the control is suddenly turned on to maintain it. The vector of initial conditions was arbitrarily chosen from positive realizations of Gaussian distributions with mean 1 and 0 respectively for “position” and “velocity”, and variance 1 for all state variables.

As it is observed from Figure 8 to Figure 11, the control action was able to make the system dynamics follow the desired reference within few seconds.

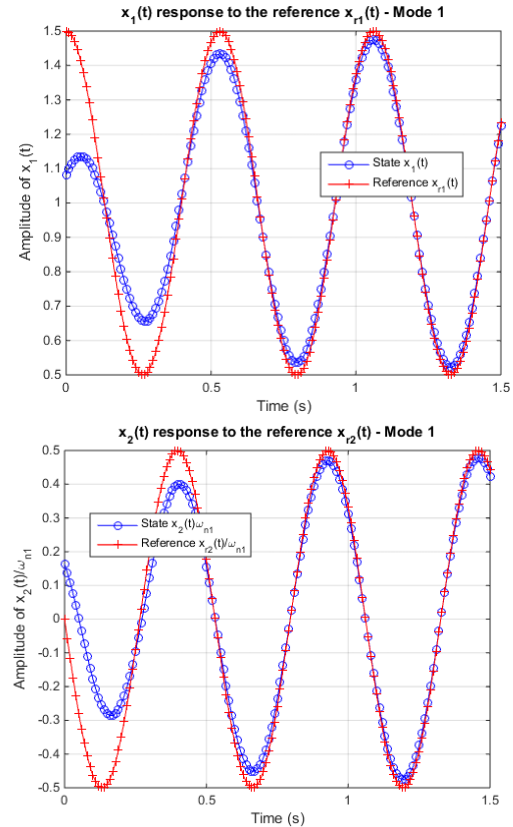


Figure 8: Mode 1 Response to Reference Tracking Control

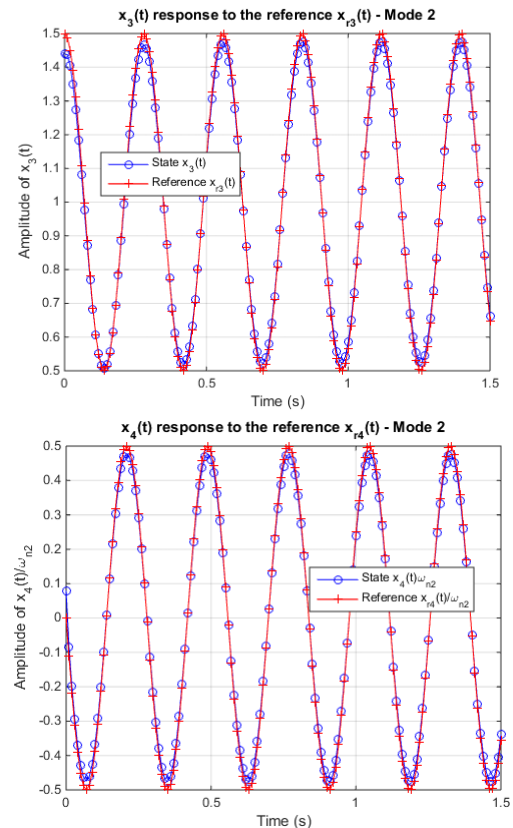


Figure 9: Mode 2 Response to Reference Tracking Control

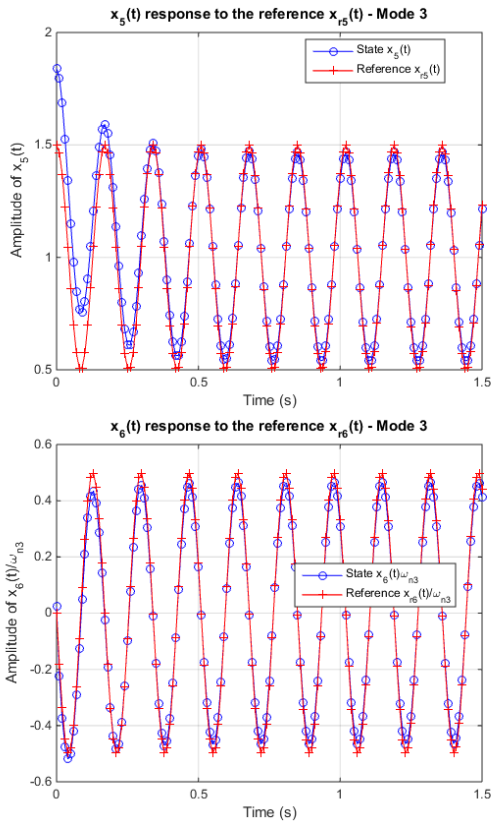


Figure 10: Mode 3 Response to Reference Tracking Control

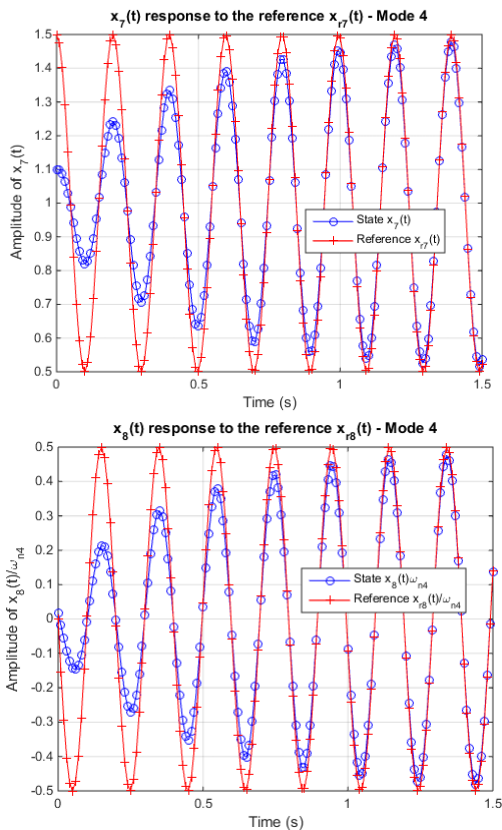


Figure 11: Mode 4 Response to Reference Tracking Control

6. CONCLUSIONS

This work has proposed a new approach to identify and control the dynamics of oil-flames in a prototype furnace. A time-domain method (ITDM) was employed in conjunction with the random decrement technique to identify an assumed four degree-of-freedom second order model of unstable flames from computer-vision processed grabbed images of CCD cameras. A Linear-Quadratic Controller was then designed based on the modal model identified for a *priori* known flame conditions, corroborated by qualitative and quantitative comparison with the outcomes of traditional spectral analysis of their reconstructed temporal signals.

The work must be considered a first incursion towards a complete control system able to assure clean combustion in oil furnaces. Achievement of a control system with attributes like this will require more sophisticated control techniques and, most important, an algorithm to correlate flame images to control actions. The choice for a cheap control technique (LQ) here is justified by the fact that the adaptive-predictive methods to be investigated are based on linear-quadratic approaches. The promising results achieved here using LQ design indicate a feasible way. Nevertheless, the topic control of oil furnaces is a fascinating one and authors intend to bring other subjects to discussion in future publications.

REFERENCES

- Bouziani, F., Landau, I. D., Bitmead, R. R., Voda-Besançon, A. (2005). An analytically tractable model for combustion instability. In Proceedings of the 44th IEEE conference on decision and control, and the European control conference 2005 (pp. 7398–7403). Seville, Spain.
- Cole, H. A. (1971). Failure Detection of a Space Shuttle Wing Flutter by Random Decrement. NASA, TMX-62.041.
- Ewins, D.J. Modal Testing: Theory, Practice and Application, 2nd ed. (2000). Hersfordshire, MSP.
- Fleury, A.T., Trigo, F.C., Martins, F.P.R. (2013). A new approach based on computer vision and non-linear Kalman filtering to monitor the nebulization quality of oil flames. Expert Systems with Applications, vol. 40(12), 4760-4769.
- Gonzalez, R.C., Woods, R.E. Digital Image Processing, 3rd ed. (1992). New York, Addison-Wesley.
- Grange, P., Clair, D., Baillet, L., Fogli, M. (2009). Brake squeal analysis by coupling spectral linearization and modal identification methods. Mechanical Systems and Signal Processing, vol. 23(8), 2575-2589.
- Ibrahim, S.R., Mikulcik, E.C. (1973). A time domain modal vibration test technique. The Shock and Vibration Bulletin, Vol.43, Part 4, 21-37.
- Ibrahim, S.R., Mikulcik, E.C. (1977). A Method for the Direct Identification of Vibration Parameters from the Free Response. The Shock and Vibration Bulletin, Vol. 47, Part 4, 183-198.
- Liu, T.Y., Chiang, W.L., Chen, C.W., Hsu, W.K., Lin, C.W., Chiou, D.J., Huang, P.C. (2012). Structural

system identification for vibration bridges using the Hilbert-Huang transform. *Journal of Vibration and Control*, vol. 18(13), p. 1939-1956.

- Moura, F.S., Aya, J.C.C., Fleury, A.T., Amato, M.B.P., Lima, R.G. (2010). Dynamic Imaging in Electrical Impedance Tomography of the Human Chest With Online Transition Matrix Identification. *IEEE Transactions on Biomedical Engineering*, vol. 57(2), p. 422-431.
- Pappa, R.S., Ibrahim, S.R. (1981). A Parametric Study of the Ibrahim Time Domain Modal Identification Algorithm. *The Shock and Vibration Bulletin*, Vol.51, Part 3, p. 43-72.
- Silva, R.P., Fleury, A.T., Martins, F.R.P., Pongeferreira, W.A.J., Trigo, F.C. (2015) Identification of the State-Space Dynamics of Oil Flames through Computer Vision and Modal Techniques. *Expert Systems with Applications*, v42, p. 2421-2428.
- Wang, S.Q., Zhang, Y.T., Feng, Y.X. (2010). Comparative Study of Output-based Modal Identification Methods Using Measured Signals from an Offshore Platform. *Proceedings of the ASME 29th International Conference on Ocean, Offshore and Arctic Engineering*, vol. 2, 561-567.
- Wu, W.H., Chen, C.C., Liao, J.A. (2012). A Multiple Random Decrement Method for Modal Parameter Identification of Stay Cables Based on Ambient Vibration Signals. *Advances in Structural Engineering*, vol. 15(6), p. 969-982.

AUTHORS BIOGRAPHY

Agenor de Toledo Fleury has a degree in mechanical engineering from ITA / Aeronautics Technological Institute (1973), a Master's degree (1978) and PhD in Mechanical Engineering from the University of São Paulo (1985). He is currently professor at FEI University and a part-time PhD professor at the Polytechnic School, University of Sao Paulo. He has led various projects with emphasis on Dynamics and Control Systems. His most recent projects address modeling and control of nonlinear systems, optimal control and estimation, in applications of Biomechanics, Robotics and Automotive Engineering.

Danilo de Santana Chui received the B. Eng. degree in mechanical engineering from University of São Paulo (USP), São Paulo, Brazil, in 2003, the M. Eng. degree in mechanical and control engineering from Tokyo Institute of Technology (TITech), Tokyo, Japan, in 2006 and is currently a PhD student at University of São Paulo. He is an Assistant Professor in the Department of Mechanical Engineering at Federal University of Amazonas (UFAM). His research interests include nonlinear control, stochastic control and control applications to combustion processes and vehicle technologies.

Flávio Celso Trigo was born in São Paulo, Brazil, in 1961. He graduated in Mechanical Engineering in 1985 and received a PhD in Mechanical Engineering at the Polytechnic College, USP in 2005. Since 2008, he works as a professor/researcher at the Department of

Mechanical Engineering, USP, Brazil. His main research interests include real-time parameter estimation and system identification through nonlinear techniques, flame dynamics modeling and controlling, simulation of offshore riser behavior, and sensor fusion for inertial guidance.

Flavius Portella Ribas Martins was born in São Paulo, Brazil, in 1956. He received BE degree in Naval Engineering from USP, 1979, and MSc in Naval Engineering and PhD degrees in Mechanical Engineering also from USP, in 1981 and 1999, respectively. Since July 2008, he has been with the University of São Paulo, São Paulo Brazil, as Assistant Professor at the Mechanical Engineering Department. His current research interests include theoretical mechanics, computer vision, and artificial intelligence. Dr Martins is a Fellow of the American Society of Mechanical Engineers.

DYNAMIC ANALYSIS AND 3D VISUALIZATION OF MULTIBODY SYSTEMS

Vjekoslav Damic^(a), Maida Cohodar^(b)

^(a) University of Dubrovnik, Cira Carica 4, Dubrovnik, Croatia,

^(b) University of Sarajevo, Faculty of Mechanical Engineering, Vilsonovo setaliste 9, Sarajevo, Bosnia and Herzegovina

^(a) vdamic@unidu.hr, ^(b) cohodar@mef.usa.ba

ABSTRACT

3D Visualisation is a powerful tool for dynamic analysis of multibody systems such as robots. The basic idea of the paper is to develop the models of multibody systems from two points of view: the dynamic and geometric. The dynamic model is based on bond graph technique and is developed using a suitable bond graphs modelling and simulation environment (BondSim). To develop 3D model in a virtual scene another program the BondSimVisual is used. It is based on VTK visualization pipeline technology. These two models interact by two-way inter process communication (IPC) based on the named pipes. Thus, two models appear as a single complex model running on the same or separate computers connected by a LAN. The attention of this paper is focused on development of visual 3D models of the multibody systems. The proposed approach is illustrated on example of a pendulum and industrial robot ABB IRB 1600.

Keywords: Multibody systems, 3D visualization, Bond Graph modelling, Inter process communications

1. INTRODUCTION

With increase of computer power, the processes of modelling and simulation become a powerful tool in dynamic analysis of engineering problems. Often it is not necessary to perform expensive experimental work with real system. The benefits of visualization are numerous. It enables representation of the system in a more familiar form. It can also help to recognize possible collisions between the bodies and thus enable better modelling of the problem.

These benefits are recognized by many software designers and they are included in many software packages for dynamic analysis, e.g. MATLAB/Simulink, Dymola, 20-SIM, etc. In MATLAB/Simulink, the bodies of multibody system can be represented as convex hull from body coordinate system locations or equivalent ellipsoid from mass properties. Also, bodies can be built by external graphical 3D model, developed in appropriate 3D CAD software packages, e.g. Solid Works, Catia etc. During simulations, animation of motion automatically starts allowing insight into system movements. Dynamic

model of PUMA560 with Robotics Toolbox for Matlab is given in (Corke 2011). A new robot modelling and simulation toolbox for Matlab devoted to robot control design is presented in (Dean-Leon Nair and Knoll 2012). KUKA control toolbox for motion control of KUKA robot manipulators is given in (Chinello Scheggi Morbid and Prattichizzo 2010).

The tool for translation of CAD models developed in CATIA to Modelica in order to get information about parts and joints and how they are related, is explained in (Elmqvist Mattsson and Chapuis 2007). The issue in design of a virtual reality robot implemented in Java 3D using a modified subsumption control architecture and the problems that may be appear with 3D platform are described in (Smith Egert Cuddihy and Walters 2006).

One of the first software packages which introduced a simulation based on CAD models and integrating the robotic cells and flexible manufacturing systems was GRASP (Graphical Robot Application Simulation Package), of BYG Systems ltd. The robot manufacturers develop their own software for off-line robot programming: ABB Robot Studio, Fanuc RoboGuide, Kuka KukaSim, Motoman MotoSim EG etc. Overview software and visualization technique applied in robotics is presented in (Zlajpah 2010).

This paper deals with modelling of multibody system from two points of view: the dynamical and geometric. The dynamical models are based on bond graph technique implemented in BondSim program. It supports systematic development of complex dynamic models. Using bond graphs the models are developed using effort/flow paradigm. To obtain the positional information the flows (velocities) are usually integrated. However, it is not easy to generate in this way a complex 3D geometric scene.

Thus, to represent a model of a mechanical system from 3D geometric point of view, a completely different approach is used and is implemented in a program BondSimVisual (developed by the first author). It is based on powerful VTK (Visualization Tool Kit) C++ library (VTK User's Guide 2010). Between these two programs an Inter Process Communication is established, which enables that on one side the dynamical model of the mechanical system drives the

corresponding bodies in a 3D virtual scene and in this way enables visualisation of the system motion.

On the other hand the visual (i.e. geometric) model can return positional information of interest to the dynamic model. Thus, e.g. in case of a collision of two bodies the point of contact and direction of the common normal could be of the interest. Thus, such information can be regularly collected during the simulation and sent back to the dynamic side for further processing. The dynamical process e.g. can restrict the further motion of the colliding bodies in the direction of the common normal and forces the motion only in the common tangential plane, or maybe the bodies reject.

The collision problem is one of problems where both positional and dynamical information are important. It is well known that the computer games typically use the dynamic models for the solution of the collisions as well.

The paper is organized as follows.

Because of its fundamental role we start with Inter Process Communication in Section 2. Next the approach used generate 3D visual models are given in the Section 3. In the Section 4 the method developed is applied to a relatively simple example of a pendulum hitting the ground. The pendulums are often used as the benchmarks for testing the formulations (Damic Cohodar and Damic 2013).

In Section 5, the attention is focused on a real industrial manipulator - ABB IRB 1600. Its dynamic model is developed using bond graphs by BondSim and 3D virtual model by BondSimVisual. Two-way communication is established during simulation between two models. Dynamic and visual model are verified by comparison of the simulation results with the ones obtained using Robot Studio (<http://new.abb.com/products/robotics/robotstudio;> (last approach: May, 09 2015)).

2. CONCEPT OF 3D VISUALIZATION BASED ON IPC

The basic idea is to develop two models of a multibody system – a dynamical and 3D visual, Fig.1. They are defined by two different applications running on the same or distant computers connected by a local net. Between them a two-way inter process communication (IPC) based on named pipe technology is used (Damic Cohodar and Damic 2014).

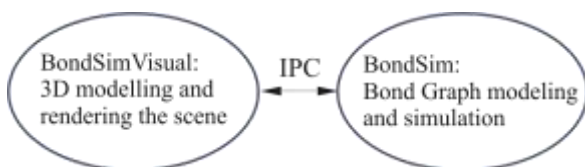


Figure 1: Inter Process Communication (IPC)

The dynamical model using BondSim regularly sends the angular or linear displacements data which are used in the visual space to transform positions of the objects in 3D virtual scene i.e. to rotate and/or translate the

body objects. The visual program responds by redrawing the scene.

On the other hand the 3D model can collect and send back some positional information. In the examples considered the coordinates of a point are picked and returned back. This is of course trivial information, which can be generated in bond graph model easily. It is used here to demonstrate that the both models and IPC work correctly.

The TCP/IP protocols are often used for the IPC. But, for the problems considered it was found that amount of data exchanged is very low for TCP/IP, really often in range of garbage. On other hand it is not permitted to gather data before transmitting it, which is a normal behaviour of TCP/IP; in that case the synchronism between two processes will be lost.

In spite of relatively small amount, the data are exchanged with a great frequency, e.g. every 50 ms or even more frequent. It was found that named pipes are ideally suited for this purpose. Fig. 2 shows the concept of named pipes used.

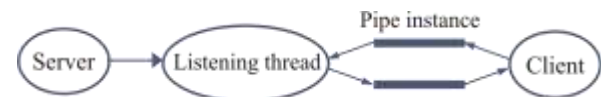


Figure 2: The configuration of named pipes IPC

The server (BondSimVisual) is responsible for creating the pipe with a specified name. It also creates a special processing thread, which enables that the program simultaneously with other tasks listens for the message from the Client. The server also asks the client (BondSim) to connect. When the client is successfully connected the two-way communications is established. Thus, most of IPC operation is on the server side. But, the client (BondSim) also has a part. To support IPC the client uses an IPC interface component. It serves to define signals which are transmitted to the server by IPC, and also which receive the data from the Server. It is also used to define the name of remote computer where the server (i.e. BondSimVisual) is running. If it is not defined the program assumes that the server is running on the same computer.

3. VISUALIZATION OF MULTIBODY SYSTEMS

Generating a virtual 3D scene in program BondSimVisual is as based on VTK (VTK User's Guide 2010).

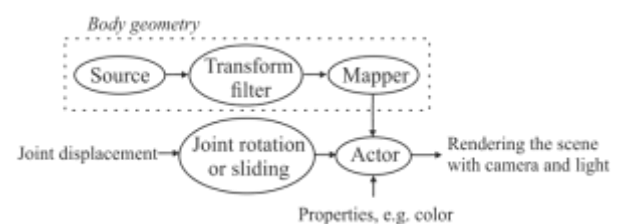
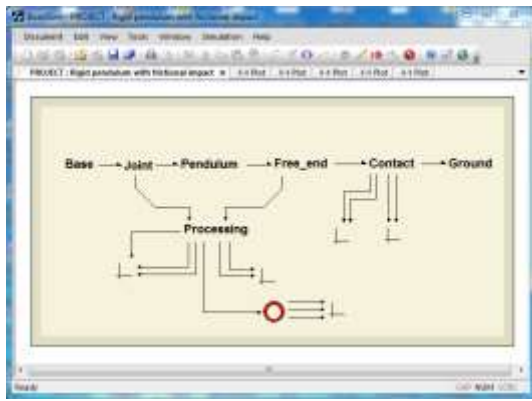
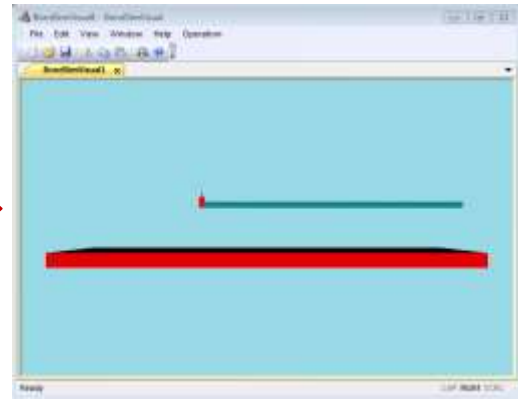


Figure 3: Body visualization pipeline



Dynamic model in bond graph settings, BondSim



3D visual model in BondSimVisual

Figure 4: Visualization of the pendulum

The central structure in VTK is the pipeline of data. The visual representation of a body in a 3D virtual scene with predefined camera and light is shown in Fig. 3. It uses concept of visualization pipelines.

The components in the first row in the figure define the geometry of the body. The *source* enables generation of the body in different forms. It could be primitives such as spheres, cylinders or cubes. But, also more complex forms such as poly-cylinders, or arbitrary modules. CAD models in the form of stl (stereo-lithography) files are supported as well. The *transform filter* is used to transform the body position with respect to a coordinate frame.

The *mapper* is a VTK component that receives data from the filters, or sources directly, and map them into the objects that can be rendered on the screen.

The *actor* is a physical representation of data as they appear in the scene. It accepts data from the mapper, which define the body, but allows also direct interface to the transform that represents the joint rotation or sliding. Also some other properties of the body, such as its colour, can be defined as well. The actors are directly connected to the rendering engine that draws the objects in the scene.

The geometric structure of a multibody system is defined by a script in textual form. It defines the coordinate frames, the bodies it is composed of, their interconnections, colour, etc. Based on this script the visualisation pipeline for the problem is generated and the bodies of the system under the study appear on the scene in its initial position.

4. VISUALIZATION OF A PENDULUM

The proposed approach for creating of visual model is explained on an example of well-known benchmark problem – rigid pendulum with frictional impact. Its dynamic model is developed in (Damic Cohodar and Damic 2014) using the bond graphs (Fig.4 left).

4.1. Bond Graph Model of Pendulum

Initially placed in a horizontal position, the rigid pendulum falls under action of the gravity and hits to the ground. The bond graph model of pendulum is shown in Fig. 4 (left) and consists of three physical components: the Base, Pendulum and Ground. The Base defines the pinned connections of the upper pendulum end. Component Pendulum is developed as a rigid body. Free_End defines the conditions on the body free. The component Contact represents the pendulum friction impact to the Ground.

Mass of pendulum is $m=1$ kg, lengths is $L=1$ m and circular cross area with diameter $D=0.02184$ m. Pendulum hits to the surface at an angle of $\varphi=80^\circ$.

4.2. Development of visual model using basic shapes (model V1)

The visual model can be composed from the basic shapes: cubes, cylinders, poly-prisms, etc. (Fig. 4 right). The coordinates for the pendulum and its components are shown in Fig. 5). They are transformed in the space (translated and rotated) and combined on such way to form the shape of multibody system components. Also, it is possible to create the shapes defined by the modules (defined by the faces, vertices and edges).

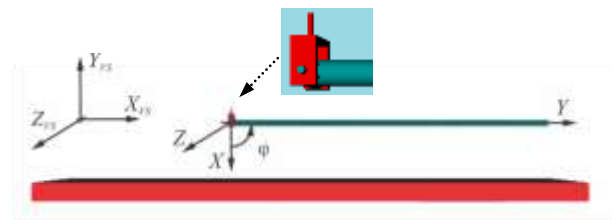


Figure 5: Visual model of the rigid pendulum

Script file of model (denoted V1) that evaluates falling rigid pendulum is given in Table 1. Its dynamic model is developed in coordinate frame whose orientation is shown in Fig. 5 (x -axis is directed down, y -axis to the right and z -axis is out of screen). Its orientation is different from orientation of default virtual screen coordinate frame (the system denoted by index VS in

Fig. 5). Hence, it is necessary to transform the vs frame to our coordinate frame by Euler angles (ZYZ) as given with the last part of the first instruction in the script file (Table 1). Pendulum is connected to the Base by the revolute joint, defined by instruction Joint (with argument in which the joint type and rotation axis are defined). Component Base is composed of three cubes and one cylinder that are set by the instruction “Set Base add...” with the necessary transformations.

Table 1: Script file to define visual model V1

```
!----- Impact_pendulum_V1 -----
Project Impact_Pendulum (euler -90.0 0.0 0.0)
  Joint 1 revolute Z
;
cube T0000170 40.000000 20.000000 4.160000 ;
cube T0000171 40.000000 20.000000 4.160000 ;
cube T0000172 5.000000 20.000000 21.680000 ;
cylinder T0000173 diameter 5.000000 resolution 16 length
20.000000;
set Base add T0000170 (shift x -28 y -10 z 10.84)
          T0000171 (shift x -28 y -10 z -15)
          T0000172 (shift x -28 y -10 z -10.84)
          T0000173 (shift x -28 euler 0 -90.0 0);
cube T0000174 50 1500 500;
Set Ground add T0000174 (shift x173.648 y-500);
Set Impact_Pendulum add Base
          Ground ;
Render Impact_Pendulum
  color 0.91 0 0;
cylinder T0000175 diameter 21.680000 resolution 16
length 1000.000000;
cylinder T0000176 diameter 24.000000 resolution 16
length 21.680000;
cylinder T0000177 diameter 6.000000 resolution 16 length
38.000000;
Set Pendulum add T0000175 (euler -90 -90.0 0)
          T0000176 (shift z-10.84)
          T0000177 (shift z-19);
Set Impact_Pendulum#1 add Pendulum ;
Render Impact_Pendulum#1
  color 0.0 0.6 0.6 ;
Probe Point1 Impact_Pendulum#1(shift y 1000) refer
Impact_Pendulum;
!----- End -----
```

The Ground is set using a simple cube in the appropriate position. The Impact_Pendulum is created consisting of the Base and Ground to which it hits. The model is drawn by instruction “Render”. Its colour is defined by RGB model (red-green-blue values from 0 to 1.0).

Next we define the Pendulum body consisting of three cylinders and added it to the system Impact_Pendulum at the Joint. It is drawn in a different colour.

4.3. Development of visual model using external 3D CAD models (model V2)

We may also develop the geometrical model using 3D CAD models of the Base, Pendulum and Ground, generated in CATIA, as shown in Fig. 6. It could be generated by some other 3D CAD tool (Solid Works,

Pro Engineer, etc.), Models are exported in stl format. In this case the script is very simple as given by table 2. The part names are used to find the stl files in the program the database, which define the parts.

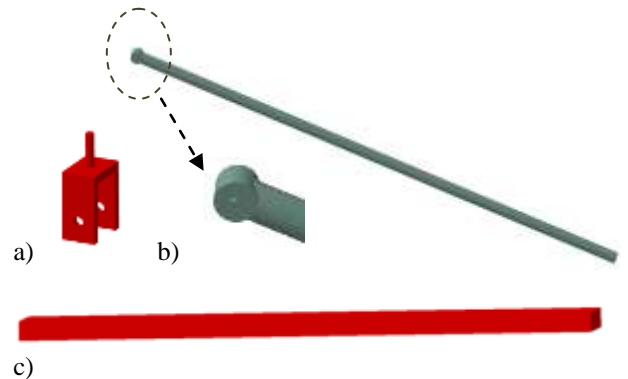
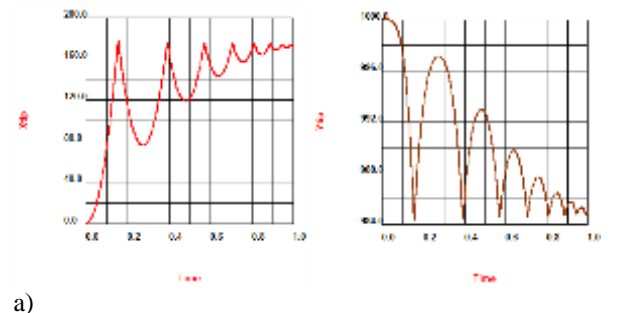


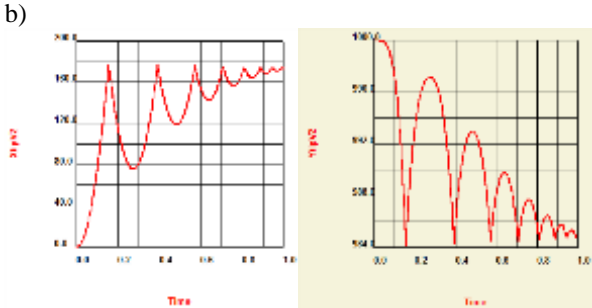
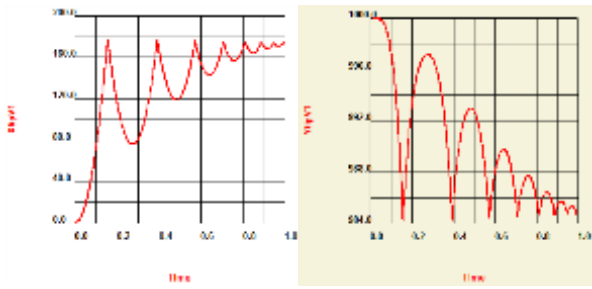
Figure 6: 3D CAD models: a) Base; b) Pendulum; c) Ground

Table 2: Script file for creating virtual model V2

```
!----- Impact_Pendulum_V2 -----
Robot Impact_Pendulum (euler -90.0 0.0 0.0)
  Joint 1 revolute Z
Part Ground;
Part Base;
Part Pendulum;
Set Impact_Pendulum add Base (shift x 12 y -10 euler 0 -
90 0)
          Ground (shift x 173.648 ) ;
Render Impact_Pendulum
  color 0.91 0 0;
Set Impact_Pendulum#1 add Pendulum ;
Render Impact_Pendulum#1
  color 0.0 0.6 0.6 ;
Probe Point1 Impact_Pendulum#1(shift y 1000) refer
Impact_Pendulum;
!----- End -----
```

Two simulations are carried out in order to verify two developed visual models. The last instruction in both script files is “Probe Point1 Impact_Pendulum#1(shift y 1000) refer to Impact_Pendulum;”. With this instruction the coordinates of the pendulum’s tip (the point located at distance of 1000 mm along Y-axis) are picked up from visual model and sent to dynamic side where they are graphically presented on display. In both simulations, the simulation period is 1s, the time step is 1e-5 s, and output interval is 1 ms.





c) Figure 7: Coordinate X_{tip} and Y_{tip} obtained from: a) dynamic model; b) V1; c) V2

Simulation results are presented in Fig. 7. Values of X- and Y-coordinates of tip pendulum obtained on dynamic side are presented in Fig. 7a. Value of X- and Y-coordinates, received from the visual model V1 are shown in Fig. 7b, and for the second visual model V2 in Fig. 7c. The dynamic model of the impact of the pendulum to the horizontal surface is described in detail in (Damic Cohodar and Damic 2013). The comparison of the two approaches for development of the visual model clearly shows that the second one based on 3D CAD models is much more comfortable and simpler to use for the bodies that have complex shapes. But, in the case of relatively simple shapes the first approach is very useful.

5. DYNAMIC AND VISUAL MODEL OF ABB IRB 1600

The robot manipulator ABB IRB 1600 is analysed as the second example. This manipulator is basically composed from seven bodies, Fig. 8. The first body is the base and it is fixed to the ground. The following six bodies are connected to each other by the revolute joints forming an open kinematic chain, as shown in Fig. 9.

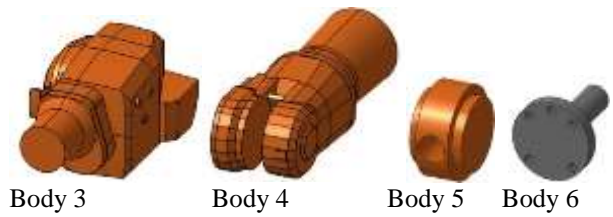
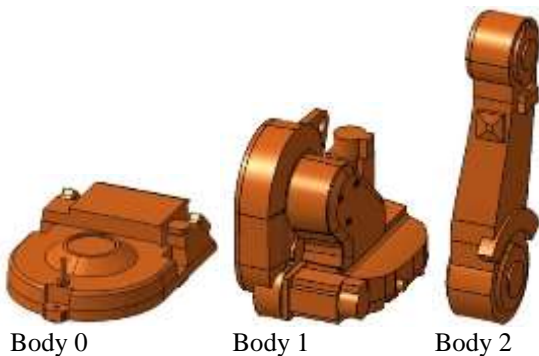


Figure 8: 3D CAD models of robot manipulator ABB IRB 1600

5.1. Direct kinematics of IRB 1600 robot manipulator

The direct kinematic model is evaluated following the Denavit-Hartenberg (DH) formulation and is given in (Cohodar, Begic and Cekic 2014). The coordinate frames are attached to the each body (Fig. 9). The corresponding DH parameters are given in Table 3.

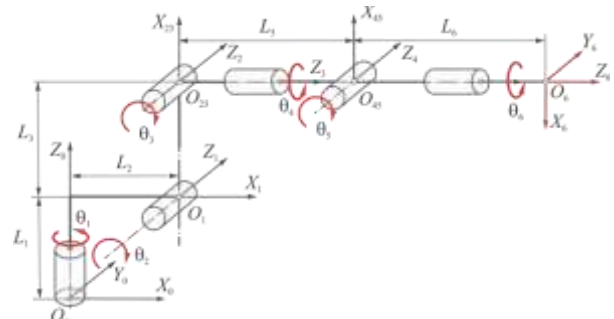


Figure 9: Kinematic scheme of robot manipulator IRB 1600

Table 3: DH parameters for ABB IRB 1600

Link	a_i	α_i	d_i	θ_i
1	L_2	$-\pi/2$	L_1	θ_1
2	L_4	0	0	$\theta_2 - \pi/2$
3	0	$-\pi/2$	0	θ_3
4	0	$\pi/2$	L_5	θ_4
5	0	$-\pi/2$	0	θ_5
6	0	0	L_6	$\theta_6 + \pi$

The matrices of homogenous transformations \mathbf{A}_i^{i-1} ($i=1,2,..6$) are defined for the neighbour frames according to:

$$\mathbf{A}_1^0 = \begin{bmatrix} c_1 & 0 & -s_1 & L_2 c_1 \\ s_1 & 0 & c_1 & L_2 s_1 \\ 0 & -1 & 0 & L_1 \\ 0 & 0 & 0 & 1 \end{bmatrix}, \mathbf{A}_2^1 = \begin{bmatrix} +s_2 & c_2 & 0 & L_4 s_2 \\ -c_2 & s_2 & 0 & -L_4 c_2 \\ 0 & 0 & 1 & 0 \\ 0 & 0 & 0 & 1 \end{bmatrix},$$

$$\mathbf{A}_3^2 = \begin{bmatrix} c_3 & 0 & -s_3 & 0 \\ s_3 & 0 & c_3 & 0 \\ 0 & -1 & 0 & 0 \\ 0 & 0 & 0 & 1 \end{bmatrix}, \mathbf{A}_4^3 = \begin{bmatrix} c_4 & 0 & s_4 & 0 \\ s_4 & 0 & -c_4 & 0 \\ 0 & 1 & 0 & L_5 \\ 0 & 0 & 0 & 1 \end{bmatrix}, \quad (1)$$

$$\mathbf{A}_5^4 = \begin{bmatrix} c_5 & 0 & -s_5 & 0 \\ s_5 & 0 & c_5 & 0 \\ 0 & -1 & 0 & 0 \\ 0 & 0 & 0 & 1 \end{bmatrix} \quad \mathbf{A}_6^5 = \begin{bmatrix} -c_6 & s_6 & 0 & 0 \\ -s_6 & -c_6 & 0 & 0 \\ 0 & 0 & 1 & L_6 \\ 0 & 0 & 0 & 1 \end{bmatrix}$$

The direct kinematics is obtained by product of matrices

\mathbf{A}_7^{i-1} ($i=1,2,..6$):

$$\mathbf{A}_6^0 = \mathbf{A}_1^0 \cdot \mathbf{A}_2^1 \cdot \mathbf{A}_3^2 \cdot \mathbf{A}_4^3 \cdot \mathbf{A}_5^4 \cdot \mathbf{A}_6^5 = \begin{bmatrix} r_{11} & r_{12} & r_{13} & p_X \\ r_{21} & r_{22} & r_{23} & p_Y \\ r_{31} & r_{32} & r_{33} & p_Z \\ 0 & 0 & 0 & 1 \end{bmatrix} \quad (2)$$

5.2. Dynamic model of IRB 1600 robot manipulator

Dynamic model of robot manipulator is developed following Newton-Euler formulation in this paper. It is developed by Bond Graphs using BondSim and its system level is shown in Fig. 10 left. Links are

considered as rigid bodies and represented by basic bond graph components of rigid body used from BondSim library. Similarly, joints are presented by bond graph components of revolute joint, also taken from BondSim library. More details about bond graph modelling of a rigid body and joints are given in (Damir and Montgomery 2003).

Unfortunately, we did not have the dynamics data of the robot; but just the geometrical parameters taken from ABB IRB 1600 manual. We know that mass of robot is 250 kg. Hence we imported 3D CAD models of robot bodies (Fig. 8) to CATIA and proportionally to the volumes of the links distribute the masses over the each link. Based on this, we obtained information about masses and moments of inertia.

The interface IPC component (in the form of a ring) sends information about the joint angles to the visual model and receive back X-, Y- and Z- coordinates of the manipulator tip.

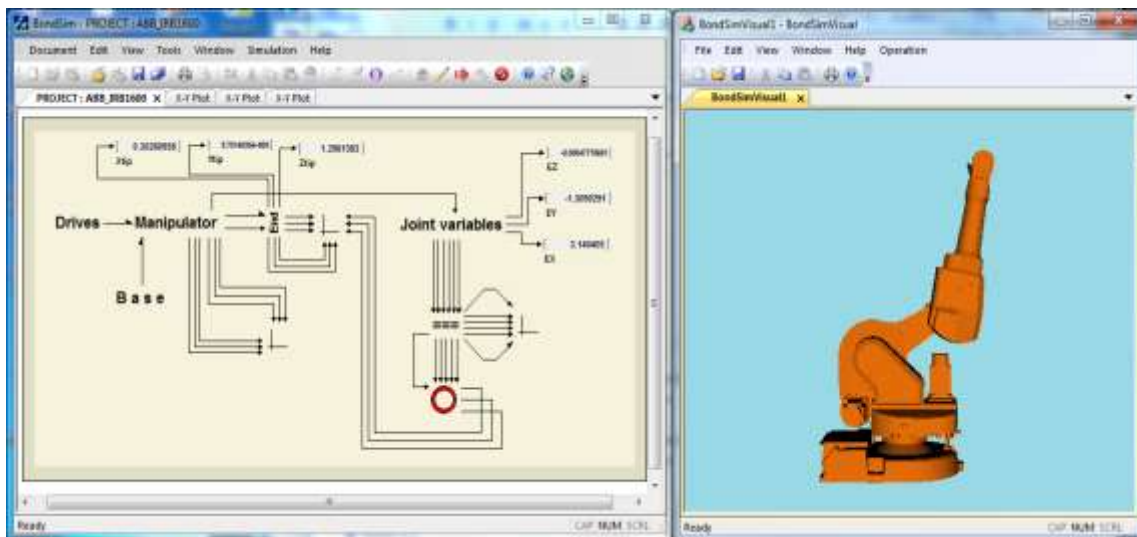


Figure 10: Dynamic and visual models of ABB IRB 1600 robot manipulator

5.3. Visual model of IRB 1600 robot manipulator

As we can see from Fig. 10, the robot links have complex shapes and to develop virtual model of robot we applied second approach from Section 4. 3D CAD models of robot links in stl-format are downloaded from ABB web site:

<http://new.abb.com/products/robotics/industrial-robots/irb-1600/irb-1600-cad>, last approach May, 07 2015 and used in the corresponding script file (Table 4).

Table 4: Script file for creating visual model of ABB IRB 1600

```
!----- ABB IRB1600_12 -----
Robot ABB_IRB1600_12 (euler -90.0 -90.0 90.0)
  Joint 1 revolute Z
  Joint 2 (shift x 150 z 486.5 ) revolute y
  Joint 3 (shift z 475) revolute y
```

```
Joint 4 ( shift x 600 ) revolute x
Joint 5 revolute y
Joint 6 revolute x
initial (0.0 0.0 0.0 0.0 0.0 0.0)
maximum ( 180.0 136 55.0 200.0 115.0 400.0)
;
Part IRB1600_X-120_m2004_rev0_01-1_Body0;
Part IRB1600_X-120_m2004_rev0_01-7_Body1;
Part IRB1600_X-120_m2004_rev0_01-4_Body2;
Part IRB1600_X-120_m2004_rev0_01-5_Body3;
Part IRB1600_X-120_m2004_rev0_01-3_Body4;
Part IRB1600_X-120_m2004_rev0_01-2_Body5;
Part IRB1600_X-120_m2004_rev0_01-6_Body6;
Set ABB_IRB1600_12 add IRB1600_X-
120_m2004_rev0_01-1_Body0 ;
Render ABB_IRB1600_12
color 0.89 0.423 0.039;
Set ABB_IRB1600_12#1 add IRB1600_X-
120_m2004_rev0_01-7_Body1 ;
```

```

Render ABB_IRB1600_12#1
  color 0.0 0.6 0.6 ;
Set ABB_IRB1600_12#2 add IRB1600_X-
120_m2004_rev0_01-4_Body2 (shift x -150 z -486.5) ;
Render ABB_IRB1600_12#2
  color 0.0 0.2 0.8 ;
Set ABB_IRB1600_12#3 add IRB1600_X-
120_m2004_rev0_01-5_Body3 (shift x -150 z -961.5) ;
Render ABB_IRB1600_12#3
  color 0.89 0.423 0.039 ;
Set ABB_IRB1600_12#4 add IRB1600_X-
120_m2004_rev0_01-3_Body4 (shift x -750 z -961.5) ;
Render ABB_IRB1600_12#4
  color 0.1 0.1 1.0 ;
Set ABB_IRB1600_12#5 add IRB1600_X-
120_m2004_rev0_01-2_Body5 (shift x -750 z -961.5) ;
Render ABB_IRB1600_12#5
  color 1.1 1.1 1.1 ;
Set ABB_IRB1600_12#6 add IRB1600_X-
120_m2004_rev0_01-6_Body6 (shift x -750 z -961.5) ;
Render ABB_IRB1600_12#6
  color 0.1 0.1 0.1 ;
Probe Point1 ABB_IRB1600_12#6( shift x 65) refer
ABB_IRB1600_12;
!----- End -----

```

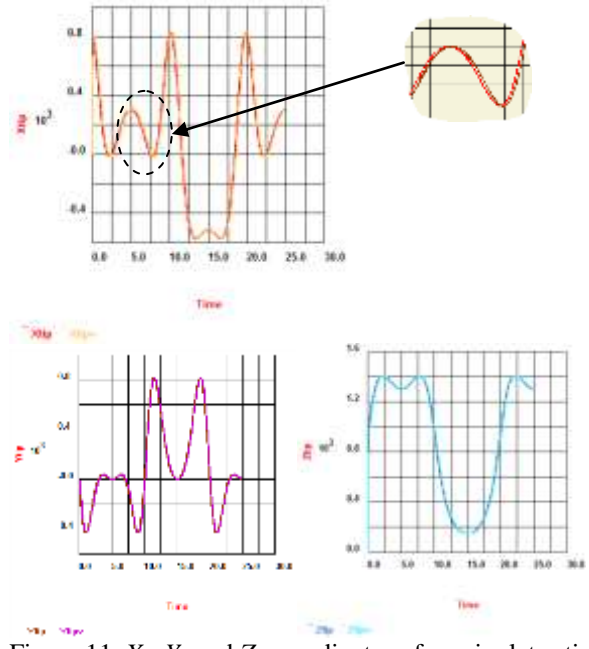


Figure 11: X-, Y- and Z- coordinates of manipulator tip

The simulation interval was set to 25 s. The joints are driven with angular velocities in [rad/s] as follows:

$$\omega_i = -a_i \frac{\pi^2}{10} \cdot \cos\left(\frac{\pi}{10} t\right), (i = 1, 2, \dots, 6), \quad (3)$$

where $a_1=a_4=a_6=1$, $a_2=1/3$, $a_3=2/9$ and $a_5=11.5/18$.

Fig. 11 shows comparison of X-, Y- and Z- coordinates of manipulator tip in the global frame (denoted by index 0 in Fig. 9), which are obtained from the dynamic model and that received from the visual model of the robot manipulator. We can see very good agreement. Also, we can notice that received coordinates from virtual model are shifted in time. This is time required for transfer of necessary information and synchronisation of the motion of geometric and dynamic models.

In order to verify developed dynamic model we compared the values of X-, Y- and Z- coordinates of the manipulator tip from the dynamic model) with that of the exact analytical solution (p_x , p_y and p_z from Eq. 2). Fig. 12a shows that these differences are in order of $1e-6$ m.

Finally, we check our results with the one obtained with RobotStudio (ABB software for off-line robot programming). In workspace of RobotStudio we inserted robot IRB 1600 (1.2), moved the links to set up values of joint angles achieved at the end of the simulation ($\theta_1=\theta_4=\theta_6=-180^\circ$, $\theta_2=-60^\circ$, $\theta_3=-40^\circ$ and $\theta_5=-115^\circ$) and read obtained values of X-, Y- and Z-coordinates and three Euler angles from Virtual Flex Pendant (Fig.12b). These values, read from Virtual Flex Pendant of Robot Studio are in the agreement with the values obtained by the dynamic model (values shown on display components in Fig. 10 left).

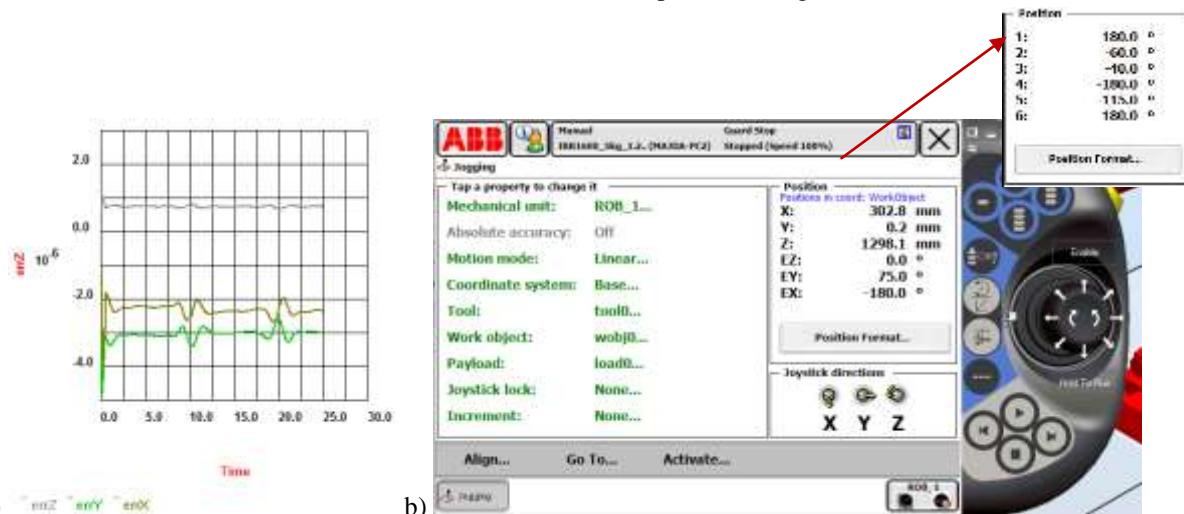


Figure 12: a) Deviation of obtained coordinates by simulations from the analytical solution; b) Position and orientation of end-effector

6. CONCLUSION

Basic idea of the paper is to create two models – dynamic and visual ones using two separate software packages: BondSim and BondSimVisual. Between them there is two-way communications, based on named pipe technology. The paper describes two approaches to developing the virtual models.

One is based on the use of basic shapes, as well as creating some special shapes. Second way uses 3D CAD model developed in appropriate 3D CAD models as Solid Works, Catia etc, that are exported from these software packages in form of stl-file.

Script file is more a simpler in the second case. Proposed approaches are applied to an example of falling pendulum and the motion of industrial manipulator ABB IRB 1600.

ACKNOWLEDGMENTS

This paper is realized in framework of project supported by Federal ministry of education of Bosnia and Herzegovina.

REFERENCES

- Chinello F, Scheggi S, Morbidi F, Prattichizzo D, 2010. The KUKA Control Toolbox: Motion control of KUKA robot manipulators with MATLAB. Robotics and Automation Magazine (ICRA). IEEE International Conference, pp.4603:4608, May 3-7.
- Cohodar M, Begic D, Cekic A, 2014. Machining systems and industrial robots. Sarajevo: Faculty of Mechanical Engineering.
- Corke P, 2011. Robotics, Vision and Control, fundamentals algorithms in Matlab. Springer.
- Damic V, Montgomery J, 2003. Mechatronics by Bond Graphs: An Object-Oriented Approach to Modelling. Berlin-Heidelberg: Springer-Verlag.
- Damic V, Cohodar M, Damic D, 2013. Bond Graph Formulation of Impact with Friction in Multibody Systems, Proceedings of the IASTED (MIC 2013), Acta Press, 794-085, pp. 298:302, February 11-15, Innsbruck, Austria.
- Damic V, Cohodar, M, Damic D, 2014. Multibody Systems Dynamical Modeling and Visualization based on IPC technique, The proceedings of the 2014 Int. Con. on Bond Graph Modeling and Simulation – ICBGM'2014, Simulation Series, The Society of Modeling & Simulation, Vol.46, No.8, pp. 773:778, July 6-10, Monterey, USA.
- Dean-Leon E, Nair S, Knoll A, 2012. User Friendly Matlab-Toolbox for Symbolic Robot Dynamic Modeling used for Control Design. Proceedings of the 2012 IEEE International Conference on Robotics and Biomimetics, December 11-14, Guangzhou, China.
- Elmqvist H, Mattsson S.E, Chapuis C, 2007. Redundancies in Multibody Systems and Automatic Coupling of Catia and Modelica, Proceeding 7th Modelica Conference, pp. 551:560, Sep. 20-22, Como, Italy.
- Karnopp D. C, Margolis D. L, Rosenberg R. C, 2006. System Dynamics: Modeling and Simulation of Mechatronic Systems (4th ed.). Hoboken, NJ: John Wiley & Sons.
- Smith N, Egert C, Cuddihy E, Walters D, 2006. Implementing Virtual Robots in Java3D Using a Sdsumption Architecture, Proceedings from the Association for the Advancement of Computing in Education.
- VTK User's Guide, Install, Use and Extend The Visualization Toolkit, Kitware, Inc., 11th ed., 2010.
- Zlajpah, L, 2010. Robot Simulation for Control Design, Robot Manipulators Trends and Development, Agustin Jimenez and Basil M Al Hadithi (Ed.), ISBN: 978-953-307-073-5, InTech, DOI: 10.5772/9206. Available from: <http://www.intechopen.com/books/robot-manipulators-trends-and-development/robot-simulation-for-control-design>
<http://new.abb.com/products/robotics/industrial-robots/irb-1600/irb-1600-cad>
[http://new.abb.com/products/robotics/robotstudio:](http://new.abb.com/products/robotics/robotstudio;) (approach date: May, 09 2015)

FRACTIONAL ORDER $PI^\lambda D^\mu$ CONTROLLER: APPLIED TO CONTROL A MANIPULATOR ROBOT WRIST

ZENNIR Youcef ^(a), MAKHBOUCHE Adel ^(b)

^(a,b) Automatic Laboratory of Skikda, Route El-Hadeaik, BP26. 21000 Skikda, Algeria

^(a) youcef.zennir@univ-skikda.dz, ^(b) adel.makbouche@univ-skikda.dz

ABSTRACT

The work presented in this paper focuses on the use of multi-controller approach to control a robot wrist (STÄUBLI robot RX 90). A description and a nonlinear Mathematical model of process have been presented along with the local parametric models around operating points. Due to the advantage of fractional order PID control compared to conventional PID, a Fractional order PID controller has been developed around each selected operating points for each local parametric models with the Oustaloup recursive approximation method (ORA) method are presented. at the end we present the results obtained in the different simulations with 3D simulation robot model developed in CAO solid Works software and some perspectives for future work.

Keywords: Modeling, Local Control, Multi-controller control, Fractional PID controller, Approximation Oustaloup method.

1. INTRODUCTION

Invariant linear model for a physical process can only be an approximation. Indeed, a physical process generally has non-linearities (Slotine 1991) that are not taken into account in the modeling process. For some operating points of the physical process a local linear model can be determined. Two ways can be used to derive these linear models the first is based on the priori knowledge of the process and the second using identification. We may then seek to enslave the whole process in operational space using the local information (Balakrishnan 1994), (Chebassier, 1999). The objectives of this work are to develop a control structure in which control law is deduced from a set of controllers that are working together. The controllers parameters are deduced from the local models of the process. The purpose of the multi-controller command (Balakrishnan 1997) is to control the output of any process in space operation using

controls developed by different local controllers. The diagram block of the multi-controllers control approach is represented as follows:

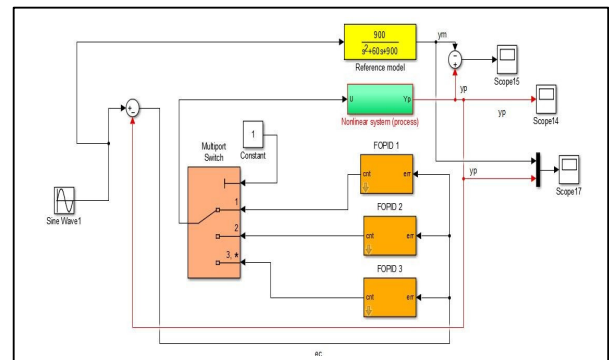


Figure 1: Multi-controller structure approach.

The multi-controller command is used to specify:

- The controller's structures.
- The switching type (Pagès 2000; Duchamp 1998).

Different solutions are proposed such as:

- Fractional order PID controllers (Bensafia 2011).
- Digital RST controller and Adaptive controllers (Karimi 1998) (Toscano 1997).
- Frank or fuzzy switching (Pagès 2000; Foulloy 1998).
- Direct or indirect approach to collaboration control law (Pagès 2000; Foulloy 1998).

In our work we have choose the use of an indirect approach based on local fractional order PID controllers and frank switching for robot wrist control.

2. PROCESS MODELING

The geometric series structure model of STÄUBLI Robot Rx-90 is give by the figure 2 (Khalil 2009):

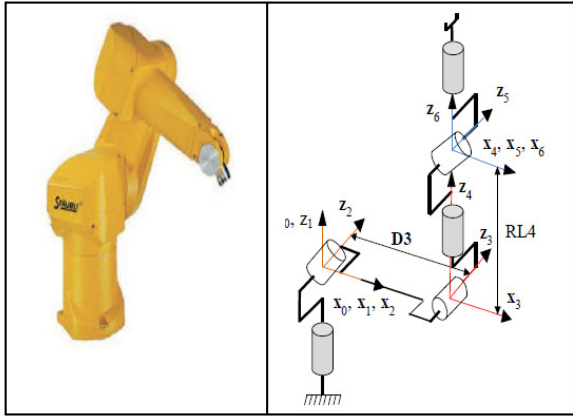


Figure 2: RX-90 Robot model.

This robot has coupling between axis 5 and 6. The actuators are brushless motors and the engine control uses the rotor position to magnetic flux rotate to achieve desired torque value and generally this motor as a DC motor behave (Sabatier 2010). Our process corresponds to a robot wrist (axis 6) can be represented by the following figure:

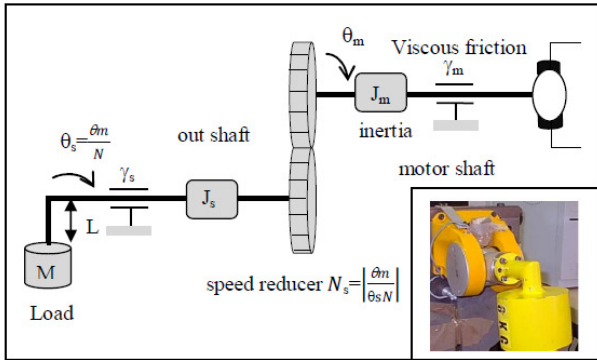


Figure 3: Process model.

Mathematic dynamic process model is given by the following equations (ZENNIR 2013):

$$\Gamma_m - \Gamma_s = \left(J_m + \frac{J_s + M \cdot L^2}{N^2} \right) \cdot \ddot{\theta}_m + \left(\gamma_m + \frac{\gamma_s}{N^2} \right) \cdot \dot{\theta}_m \quad (1)$$

With:

$$J_t = \left(J_m + \frac{J_s + M \cdot L^2}{N^2} \right) \quad (2)$$

Where:

J_m : inertia moment applied in the motor shaft.
 J_s : inertia moment applied in the output shaft (output shaft with mass).

$$\gamma_t = \gamma_m + \frac{\gamma_s}{N^2} \quad (3)$$

γ_m : Viscous friction applied to the motor shaft.

γ_s : Viscous friction applied to the output shaft.

The motor torque is given by:

$$\Gamma_m = K_e \cdot u(t) \quad (4)$$

Where: K_e is the torque constant and $u(t)$ control voltage.

Then the nonlinear model is given by:

$$X_1 = \theta_m(t); X_2 = \dot{\theta}_m(t) \quad ; \quad X = \begin{pmatrix} X_1 \\ X_2 \end{pmatrix} \quad (5)$$

$$\dot{X} = \begin{bmatrix} 0 & 1 \\ \frac{M \cdot g \cdot L}{N \cdot J_t} & -\frac{\gamma_t}{J_t} \end{bmatrix} \cdot \begin{bmatrix} \sin\left(\frac{X_1}{N}\right) \\ X_2 \end{bmatrix} + \begin{bmatrix} 0 \\ \frac{K_e}{J_t} \end{bmatrix} \cdot u(t) \quad (6)$$

$$Y = \theta_s(t) = \begin{bmatrix} -\frac{1}{N} & 0 \end{bmatrix} \cdot X \quad (7)$$

Which is the state space representation for the nonlinear model? To find the structure of local parametric models, we applied the tangent linearization and hence the linear local model is as follows (zennir 2013):

$$G(p) = \frac{-K_p}{p^2 + a_{p1} \cdot p + a_{p2}} \quad (8)$$

Where:

$$K_p = \frac{K_e}{N \cdot J_t}, a_{p1} = \frac{\gamma_t}{J_t} \text{ and } a_{p2} = \frac{M \cdot g \cdot L}{N^2 \cdot J_t} \cdot \cos\left(\frac{X_{10}}{N}\right) \quad (9)$$

After identification of the linear local model near each operating point (zennir 2013). The corresponding continuous linear model is as follows:

- operating points, $\theta_{s0}=0$:

$$G(p) = \frac{-111.5}{p^2 + 11.25 \cdot p + 79.14} \quad (10)$$

- operating points, $\theta_{s0}=\pi/3$ and $\theta_{s0}=2\pi/3$ respectively:

$$G(p) = \frac{-111.5}{p^2 + 11.25 \cdot p + 39.57} ; \quad G(p) = \frac{-111.5}{p^2 + 11.25 \cdot p - 39.57} \quad (11)$$

3. LOCAL CONTROLLERS STRUCTURES

The structure of the local controllers is of type Fractional $PI^\lambda D^\mu$. The applications of the fractional calculus takes the order of integrals and derivatives have been defined in literatures, such as control theory (Yuquan, 2011), (Bagley 1991), (Makroglou 1994), and electro-analytical chemistry (Oldham 1976), (Goto 1975). In control theory, the general conclusion about fractional control system is that it could enlarge the stability region (Podlubny 1994) moreover it gives performance at least as good as its integer counterpart. In the other hand another important advantage is that fractional integrals or derivatives are hereditary functional while the ordinary ones are point functional. Here we should mention that for Fractional order PID controllers, many contributions and studies are presented in the past years

particularly in the tuning rules (Luo 2009), (Xue 2006), approximation and stability conditions (Sabatier, 2010). In generally Fractional-order calculus is an area of mathematics that deals with derivatives and integrals from non-integer orders. In other words, it is a generalization of the traditional calculus that leads to similar concepts and tools, but with a much wider applicability. In recent years, according to the advances in the field of fractional calculus, there had been a great interest to develop a new generation of PID controllers, which is commonly known as the Fractional-order PID (FOPID) or $PI^\lambda D^\mu$ controller. The transfer function of FOPID controller, which was initially proposed by Podlubny (Vinagre 1997), is given by:

$$G_c(p) = \frac{U(p)}{E(p)} = K_p + K_I \frac{1}{p^\lambda} + K_D p^\mu, (\lambda, \mu > 0) \quad (12)$$

Where $K_p, K_I, K_D \in \mathbb{R}$ and $\lambda, \mu \in \mathbb{R}^+$ are the tuning parameters and the controller design problem is to determine the suitable value of these unknown parameters such that a predetermined set of control objectives is met (Vinagre 1997). Note that in (12) the fractional Laplace variable “p” powers are commonly interpreted in the time domain using either the Grunwald-Letnikov, Riemann-Liouville or the Caputo definition (Bettou, 2011). It should be noted that any conventional PID controller is a particular case of the FOPID controller (12) with $\lambda=1$ and $\mu=1$. Assuming $\lambda=1$ and $\mu=0$, or $\lambda=0$ and $\mu=1$ respectively corresponds conventional PI or PD controllers are the special cases of the fractional $PI^\lambda D^\mu$ controller given by (12). Functional diagram of local FOPID controller is represented by the following figure:

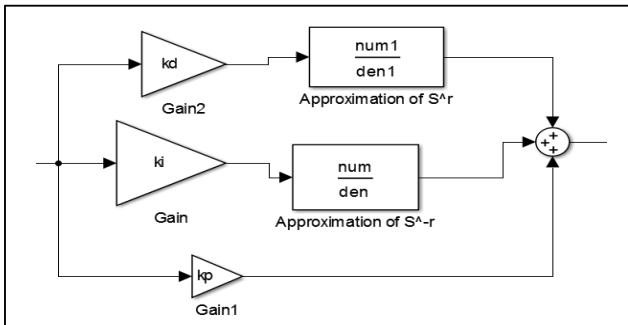


Figure 4: Structure of FOPID local controller.

Many methods in literature have been proposed to FOPID approximation (Vinagre 1997). In this step of our work we used the Oustaloup recursive approximation method (ORA) (Oustaloup 1995), (Djouambi 2007, Djouambi 2006). With this FOPID we have using the approximation of Oustaloup. This method is based on the approximation of a function of the form:

$$H(p) = p^\mu, \mu \in \mathbb{R}^+ \quad (13)$$

By a following rational function:

$$\hat{H}(p) = C \prod_{k=-N}^N \frac{1 + \frac{p}{w_k}}{1 + \frac{p}{\hat{w}_k}} \quad (14)$$

With: $\hat{w}_0 = \alpha^{-0.5} w_u; w_0 = \alpha^{0.5} w_u;$

$$\frac{\hat{w}_{k+1}}{\hat{w}_k} = \frac{w_{k+1}}{w_k} = \alpha \eta > 1 \quad (15)$$

$$\frac{\hat{w}_{k+1}}{\hat{w}_k} = \eta > 0; \frac{w_k}{\hat{w}_k} = \alpha > 0; N = \frac{\log(\frac{w_N}{w_0})}{\log(\alpha \eta)}; \quad (16)$$

$$\mu = \frac{\log \alpha}{\log(\alpha \eta)} \quad (17)$$

With w_u being the unit gain frequency and the central frequency of a band of frequencies geometrically distributed around it. That is, $w_u = \sqrt{w_h w_l}$, where w_h, w_l are the high and the low transitional frequencies. The parameters used in the Oustaloup approximation are:

- $G(p)$: Transfer function of local model of process.
- $N=5$: Approximation order.
- $r_1=-0.2$ & $r_2=0.2$: Integration & derivative order respectively.
- $w_l=10^{-2}$; low transitional frequency
- $w_h=10^3$; high transitional frequency
- $w_u=10$; Cutoff frequency

The transfer function of reference model is given by the following function:

$$Y_m(p) = \frac{\gamma^2}{(p+\gamma)^2} \cdot R(p) = G_m(p) \cdot R(p) \quad (18)$$

With :

$$G_m(p) = \frac{\gamma^2}{p^2 + \lambda_1 \cdot p + \lambda_0} \quad (19)$$

With: $R(p)$ is the set of the loop closes.

4. SIMULATION

The synthesis of the controllers is continuous. The simulation is done in continuous time around the following operating points $\theta_{s0}=0\text{rad}$, $\theta_{s0}=\pi/3\text{rad}$ and $\theta_{s0}=2\pi/3\text{rad}$ chosen with two stable position and unstable. The parameter values of the reference model λ_0 and λ_1 are:

$$\gamma = 30; \lambda_0 = 900; \lambda_1 = 60 \quad (20)$$

The PID controllers parameters determined with $\lambda=1$ and $\mu=1$ (Traditional PID) around the operating points are:

TABLE 1: PARAMETERS OF THE LOCAL CONTROLLER

parameters	K_p	K_i	K_d
Controller ($\theta_s=0$)	-2	-5	-0.7
Controller ($\theta_s=\pi/3$)	-2	-0.4	-0.4
Controller ($\theta_s=2\pi/3$)	-3	0.1	-0.4

Two simulations have been performed for each operating point in order to verify the role of the integrator, the stability of the closed loop and the proper functioning of the controllers around the operating points. The block diagram of simulation for each operating points is illustrated by the following figure:

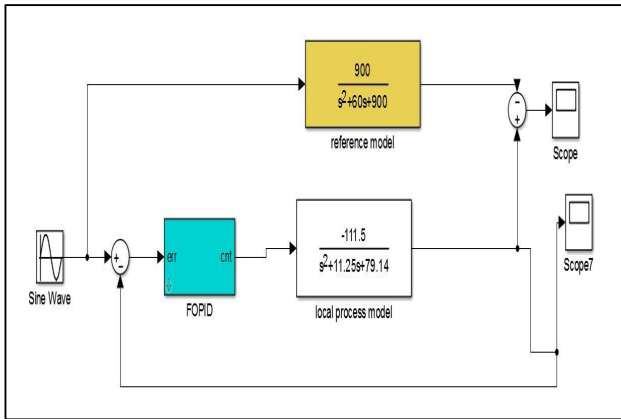


Figure 5: Closed loop control around operating point.

- The simulation around the operating point $\theta_{s0}=0$ rad
With controller parameters around $\theta_{s0}=0$ rad and reference signal $r(t)$ is equal to:

$$r(t) = 0.1 \cdot \sin(5 \cdot t) \quad (21)$$

The simulation results are illustrated in the followings figures:

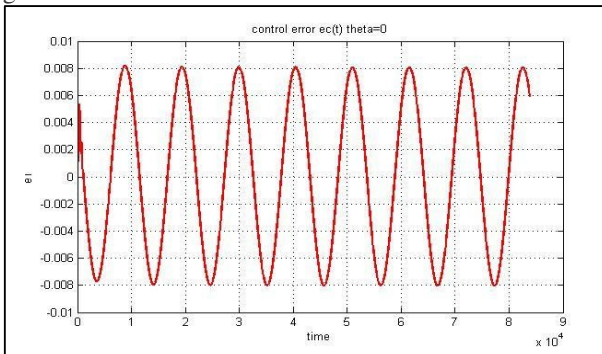


Figure 6.a: Control error $ec(t)$.

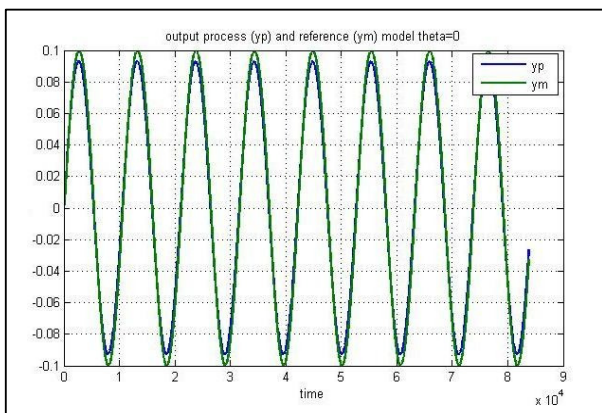


Figure 6.b: Output of the model and the reference model.

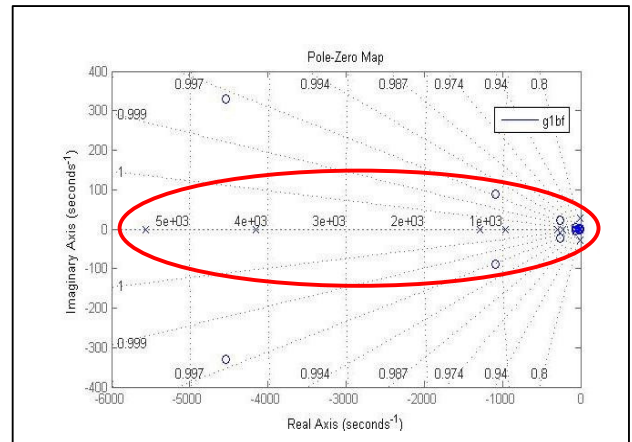


Figure 6.c: Pole Zero map for closed loop.

- Approximation FOPID Transfer function around $\theta_{s0}=0$ rad

$$C1 = \frac{-6.5059 (s^2 + 0.004757s + 5.66e-06) (s^2 + 0.02047s + 0.0001048) (s^2 + 0.08798s + 0.001937) (s^2 + 0.3773s + 0.03564) (s^2 + 1.612s + 0.6516) (s^2 + 6.864s + 11.82) (s^2 + 29.09s + 212.6) (s^2 + 122.7s + 3789) (s^2 + 516.3s + 6.709e04) (s^2 + 2168s + 1.183e06) (s^2 + 9080s + 2.072e07)}{(s+5565) (s+4151) (s+1286) (s+959) (s+297) (s+221.5) (s+68.61) (s+51.18) (s+15.85) (s+11.82) (s+3.661) (s+2.731) (s+0.8458) (s+0.631) (s+0.1954) (s+0.1458) (s+0.04514) (s+0.03367) (s+0.01043) (s+0.007779) (s+0.002409) (s+0.001797)}$$

- The simulation around the operating point $\theta_{s0}=\pi/3$ rad

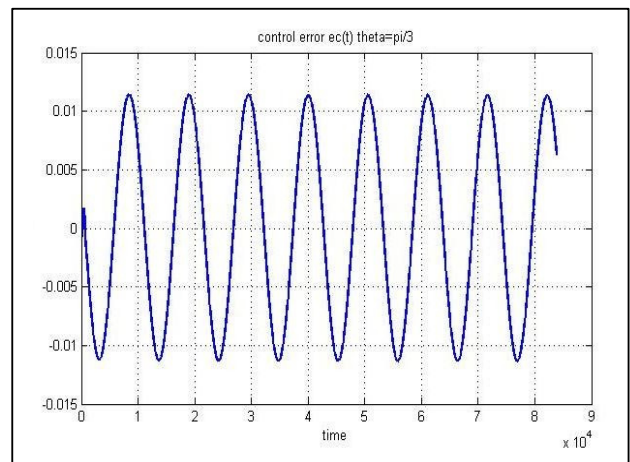


Figure 7.a: Control error $ec(t)$.

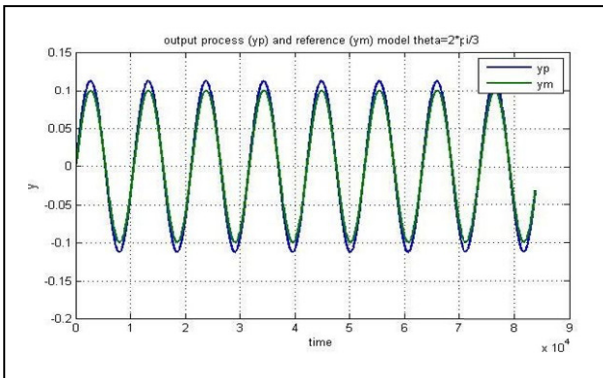


Figure 7.b: Output of the model and the reference model.

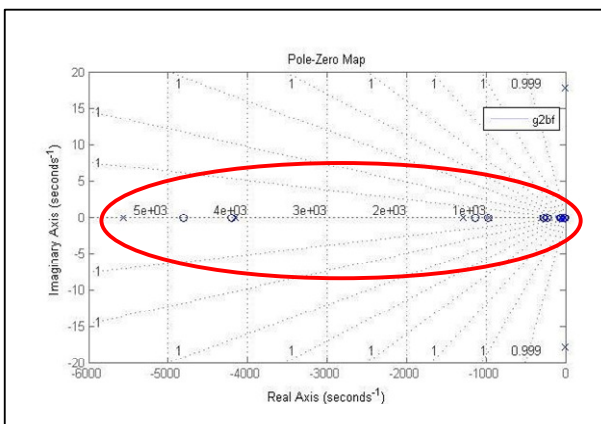


Figure 7.c: Pole Zero map for closed loop.

- Approximation FOPID Transfer function around $\theta_{s_0}=\pi/3$ rad

$$C2 = \frac{-4.0846 (s+4803) (s+4201) (s+1141) (s+975.4) (s+269.4) (s+226.6) (s+63.39) (s+52.72) (s+14.88) (s+12.29) (s+3.484) (s+2.87) (s+0.8138) (s+0.672) (s+0.1897) (s+0.1577) (s+0.04413) (s+0.03712) (s+0.01025) (s+0.008762) (s+0.00238) (s+0.002082)}{(s+5565) (s+4151) (s+1286) (s+959) (s+297) (s+221.5) (s+68.61) (s+51.18) (s+15.85) (s+11.82) (s+3.661) (s+2.731) (s+0.8458) (s+0.631) (s+0.1954) (s+0.1458) (s+0.04514) (s+0.03367) (s+0.01043) (s+0.007779) (s+0.002409) (s+0.001797)}$$

- The simulation around the operating point $\theta_{s_0}=2*\pi/3$ rad

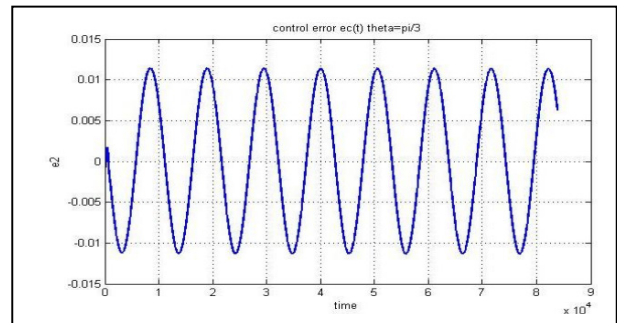


Figure 8.a: Control error $e_c(t)$.

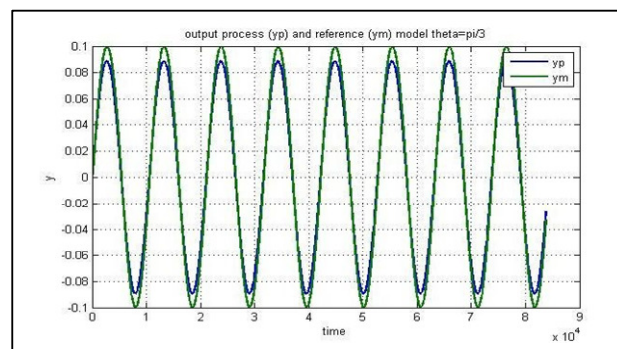


Figure 8.b: Output of the model and the reference model.

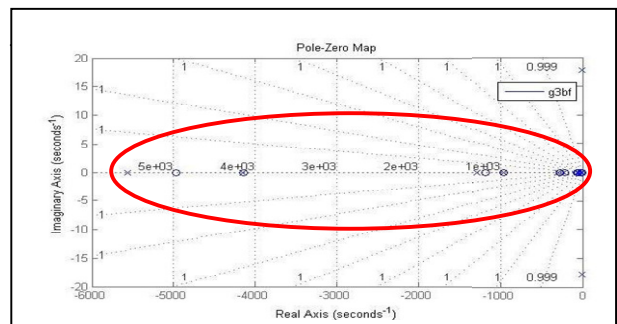


Figure 8.c: Pole Zero map for closed loop.

- Approximation FOPID Transfer function around $\theta_{s_0}=2*\pi/3$ rad

$$C3 = \frac{-4.9848 (s+4964) (s+4143) (s+1177) (s+956.2) (s+276.8) (s+220.7) (s+64.91) (s+50.91) (s+15.18) (s+11.74) (s+3.541) (s+2.705) (s+0.8244) (s+0.6228) (s+0.1916) (s+0.1432) (s+0.04448) (s+0.03286) (s+0.01031) (s+0.007516) (s+0.00239) (s+0.001701)}{(s+5565) (s+4151) (s+1286) (s+959) (s+297) (s+221.5) (s+68.61) (s+51.18) (s+15.85) (s+11.82) (s+3.661) (s+2.731) (s+0.8458) (s+0.631) (s+0.1954) (s+0.1458) (s+0.04514) (s+0.03367) (s+0.01043) (s+0.007779) (s+0.002409) (s+0.001797)}$$

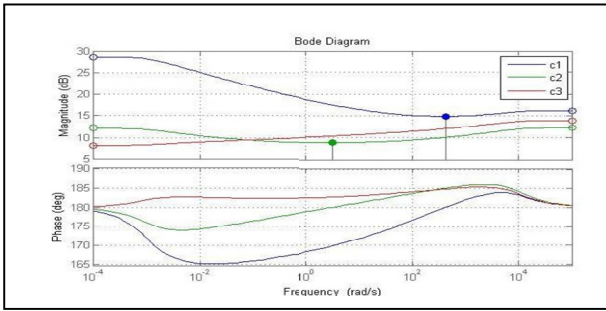


Figure 9: Frequency response of each local FOPID control.

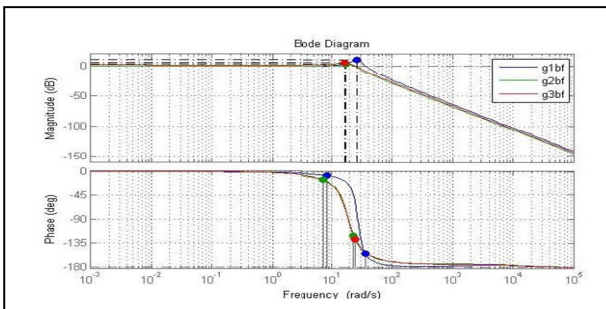


Figure 10: Frequency response of each closed local model.

3D simulation of the robot is constructed in Malab-Simulink with SimMechanics block library. The System (robot) is represented by the following blocks: the body, joints, constraints, and force. The SimMechanics block library provided us the tools to formulate and solve motion equations of complete mechanical system. We used a bridge between solidworks_matlab with same adaptations (SimMechanics 2 2007), (MATLAB 2010) to operate the robot model that we designed with solidworks. The Simulink modeling then appears (figure 11, figure 12 and figure 13) :

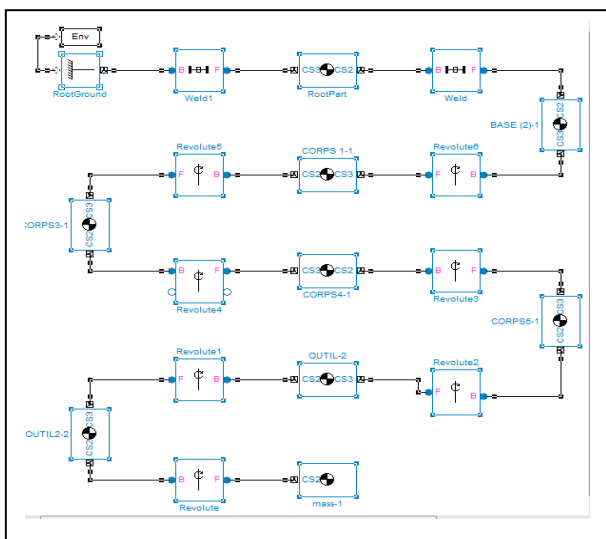


Figure 11: Block diagram of robot Rx-90 model.

To simplify the simulation we have block all robot joints except the terminal element and after we applied a simple control signal. A block diagram of the robot with the actuator and the sensor is illustrated in the following figure:

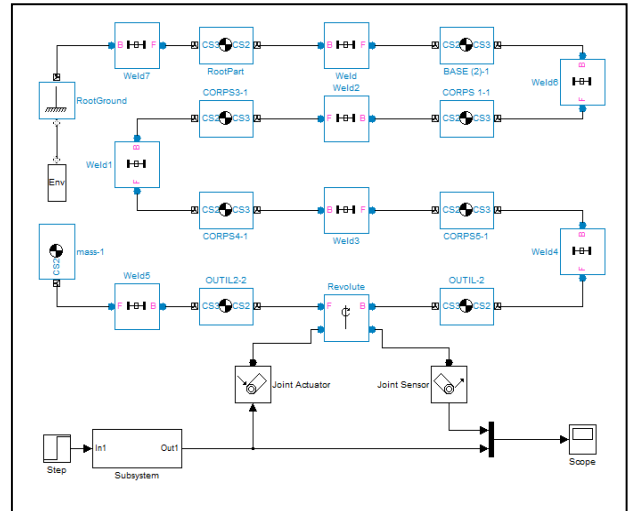


Figure 12: Control diagram block

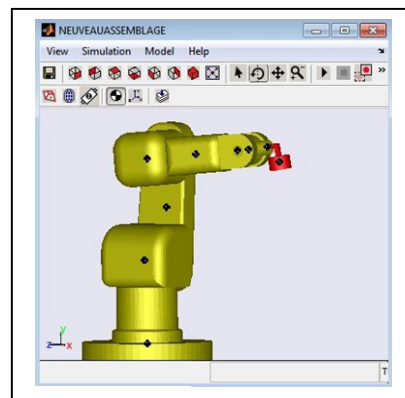


Figure 13: CAO (with Solid Works) 3D robot model.

With the obtained results we can observe that:

- All poles and zeros in the left of complex plan (figure 6.c, figure 7.c and figure 8.c) .
- Each local system is stable (figure.6.c, figure.7.c and figure.8.c) and error control given by closed loop system around $\theta_{s0}=0$ is very small compared other local linear model (figure.6.a, figure.7.a, figure.8.a).
- The closed output loop of the local system around $\theta_{s0}=0$ has the same curve although the reference output model compared other local system (figure.6.b, figure.7.b, figure.8.b).
- The local controller around $\theta_{s0}=0$ is more robust compared with other local controller figure.9 and more stable figure 10.

- In the figure.11, figure 12 and figure 13 we have developed RX90 Robot CAO Solid works software for simulation with Matla-Simulink.
- We can observed too the order of local controller after approximation its high for realization

5. CONCLUSION

In this work, we have presented the modeling of nonlinear process (Wrist of Rx-90 Stäubli Robot). After that the local linear model near each considered operating points has been developed. We have described FOPID controller principal with Oustaloup Recursive Approximation method (ORA).

Based in Simulation results we noted that the application of CRON structure control is very interesting in this case of system but we need more optimal approximation for order minimization and chose of FOPID parameters. The results obtained allow concluding that the local controllers give good results around the operating points. But the results are local. Therefore, we must seek a collaborative approach these local control laws to obtain good results in all operating space.

Finally we will study at the future work another interesting approximation Fractional-order controller method of Charef (singularity function method) (Djouambi 2007) and frank switching with the indirect approach (collaboration between controller), then the same category with other type of controller as example Digital Fractional -order PID controller or RST controller.

REFERENCES

- Balakrishnan J. and Narendra S. 1994. Improving Transient Response of Adaptive Control Systems Using Multiple Models and Switching. *IEEE Trans. on Automatic Control*, Vol. 39, n°9, Septembre 1994, pp. 1861-1866.
- Balakrishnan J. and Narendra S. 1997. Adaptive Control using Multiple Models. *IEEE Trans. on Automatic Control*, Vol. 42, n°2, Février 1997, pp. 171-187.
- Chebassier J.1999. Méthadologies pour la conception d'un système de commande par ordinateur. Thèse Laboratoire d'Automatique de grenoble (INPG) , 1999.
- Duchamp J-M. 1998. Commutation Floue de lois de Commande applique à la Robotique. Rapport de DEA , LAMII /CESALP.
- Slotine JJE. 1991. *Applied Nonlinear Control*. Prentice-Hall International, ISBN: 0-13-040049.
- Karimi A. and Landau I-D. 1998. Robust Adaptive Control of a Flexible Transmission System Using Multiple Models. Laboratoire d'Automatique de Grenoble (CNRS-INPG-UJF). *Design-CSD*, 1998.
- Pagès O., Mouille P. and Caron B. 2000. Two approaches of the multi-model control. Real time Implementation for a wrist of a Robot. *Mechatronics 2000*, 1st IFAC Conference on mechatronic systems, Darmstadt, Allemagne, Septembre, 2000.
- Pagès O., Mouille P. and Caron B. 2000. Multi-Model Control by Applying a Symbolic Fuzzy Switcher. *Control Systems Design-CSD 2000*, IFAC Conference, Bratislava, République Slovaque, Juin, 2000.
- Toscano R., Martin-Calle D. and Passerieu P. 1997. Adaptation paramétrique floue d'une commande au premier ordre en fonction du point d'équilibre courant. *Laboratoire d'Automatique E.N.I St ETIENNE LFA'97 -Lyon-décembre*, pp.3-10.
- Foulloy L. and Ramdani M. 1998. *Logique Floue Exercices corrigés et exemples d'applications*. cEpaduEs-EDITIONS, juillet, 1998.
- Bensafia Y. and Ladaci, S. 2011. Adaptive Control with Fractional Order Reference Model. *IJ-STA*, Vol 5, N° 2, pp.1614-1623.
- Djouambi, A. Charef, A. Bensaçon, A.V. 2007. Optimal approximation, simulation and analog realization of the fundamental fractional order transfer function". *International Journal Applied Math.Comput.Sci.*, vol. 17, N° 4, pp.455-462.
- Djouambi, A. Charaf, A. Bensaçon, A.V. 2006. Approximation and synthesis of non integer order systems. 2nd IFAC workshop on Fractional Differentiation and its Applications, FDA'06, Porto, Portugal,july 19-21, p.4.
- Vinagre, B.M. Podlubny, I. Hernandez, A. Feliu, V. 1997. Some approximations of fractional order operations. Partially supported by FEDER Research Grant IFD97-0755-C02-01 AND BY VEGA Research Grant 1/7098/20.
- Yuquan, W. 2011. Fractional Order PID design for Nonlinear Motion Control Based on adept 550 Robot." . *Proceedings of The 2011 IAJC-ASEE International Conference*. ISBN 978-1-60643-379-9, p. 165.
- Bagley, R.L. Calico, R.A. 1991. Fractional Order State Equations for the Control of Viscoelastically Damped Structures, *J.Guidance*, vol. 14, no. 5 pp.304-311.
- Makroglou A., Miller R.K. Skkar, S. 1994. Computational Results for a Feedback Control for a Rotating Viscoelastic Beam, *J of Guidance, Control and Dynamics*, vol. 17, no. 1, pp. 84-90.
- Oldham, K.B. 1976. A Signal Independent Electro-analytical Method, *Anal. Chem.*, vol.72 pp.371-378.
- Goto M. and Ishii D. 1975. Semi-differential Electro-analysis, *J. Electro anal. Chem. and Interfacial Electrochemical.*, vol.61, pp.361-365.
- Podlubny, I. 1994. Fractional-Order Systems and Fractional-Order Controllers, *Inst. Exp. Phys., Slovak Acad. Sci.*, Vol.4, No.2, pp.28-34.
- Luo, Y. Chen Y.Q. 2009. Fractional-order [proportional derivative] controller for robust motion control: Tuning procedure and validation. *American Control Conference, ACC '09*. pp.1412-1417.
- Xue D. Zhao C. Chen Y.Q. 2006. A Modified Approximation Method of Fractional Order System. *Mechatronics and Automation, Proceedings of the 2006 IEEE International Conference*, pp.1043-1048.

- Sabatier J. Moze M. Farges C. 2010. LMI stability conditions for fractional order systems, *Computers & Mathematics with Applications*, Volume 59, Issue 5, Fractional Differentiation and Its Applications, March 2010, Pages 1594-1609, ISSN 0898-1221.
- Zennir, Y. Mouille, P.2013. Multi-controllers approach applied to a wrist of a robot. 25th European Modeling and Simulation Symposium (EMSS'2013),p.6.
- Khalil, W. Lemoine, P. Gautier, M. Erginer, O. 2006. Identification expérimentale des paramètres inertiels de la charge d'un robot Stäubli RX 90. Conférence Internationale Francophone d'Automatique - CIFA'06, Bordeaux, France, 19 Feb 2009, p6.
- Oustaloup. A. 1995. La dérivation non entière: théorie, synthèse et applications. Hermes. Paris, 1995.
- Bettou, K. 2011. Analyse et réalisation de correcteurs analogiques d'ordre fractionnaire. Mémoire de thèse, Université de Constantine, p.111.
- SimMechanics 2 User's Guide MATLAB & SIMULIK, The MathWorks, September 2007 Online only Revised for Version 2.7 (Release 2007b)
- MATLAB® Creating Graphical User Interfaces, September 2010 Online Only Revised for MATLAB 7.11 (Release 2010b)

OBSTACLE AVOIDING STRATEGY OF A RECONFIGURABLE REDUNDANT SPACE ROBOT

Vijay Kumar Dalla^(a), Pushparaj Mani Pathak^(b),

^{(a),(b)} Mechanical and Industrial Engineering Department
Indian Institute of Technology, Roorkee
Roorkee-247667, India

^(a)vijaydalla@gmail.com, ^(b)pushpfme@iitr.ac.in

ABSTRACT

This paper presents a strategy for collision-free robot tip trajectory in space works. Obstacles present in the workspace may collide with a space robotic system engaged in on-orbital servicing missions. The resultant collision may damage to the manipulator which ultimately leads to the space mission failure. When a space robot needs to perform in a limited volume with obstacles present, the robot must possess some unique capability to reach around obstacles during maneuvering. The redundant robot can perform various tasks in a limited workspace with obstacles. Hence, for this, a 6DOF space robot has been proposed for manipulation in the workspace with two static obstacles. Collision avoidance is based on reconfiguration approach where the joints are made active/passive to facilitate collision-free tip trajectory. Before reconfiguration, collision detection has been proposed to be done. The bond graph technique has been used for the dynamic model of the system and to formulate system equations.

Keywords: redundant space robot, collision avoidance, trajectory planning, bond graph modeling.

1. INTRODUCTION

Redundant manipulator (Agrawal 1994; Sutar et al. 2015) refers to a kind of robot which possesses additional degree of freedom than required to perform the desired tasks. Among various task execution capabilities (Sardana et al. 2013) of a redundant robot, obstacle avoidance characteristics have its own significant because if the robot collides with the obstacles, both the robot and the obstacles may get damages. The collision free trajectory has two folds: robot tip motion planning known as main task and the robot link collision avoidance known as sub-task. The tip motion planning is needed when the obstacles are located in the workspace. The dynamic motion planning of the space robot is itself a complex task due to its floating base and has been paying considerable attention during the last years (Pathak et al. 2006; Saha 1996; Shah et al. 2013). Obstacle avoidance (Dasgupta et al. 2009; Singla et al. 2010) is a further additional difficulty.

Most of the previous researches have only focused on industrial and mobile manipulators. Some of them are discussed here as: Usually, strategies of collision free trajectory are based on Artificial Potential Field (Csiszar et al. 2012) by imposing repulsive and attractive forces, where the sources are the obstacles and the target, respectively. In which, the robot is repulsed away from the obstacles (static and dynamic) and is attracted to the target position. This method is simple and has elegant mathematics. Some inherent weaknesses are studied by (Koren and Borenstein 1999). (Bjerkeng et al. 2011) discussed a novel approach for collision-free tip motion for industrial manipulators based on the weighted pseudo inverse kinematic redundancy resolution technique (Whitney 1969). To use the pseudo inverse control approach is a big challenge due to the requirement of a well behaved task parameterization. The inherent limitations of the weighted pseudo inverse are discussed in (Klein et al. 1983). A nonholonomic mobile robot was presented for trajectory tracking with obstacle avoidance based on an analytical method (Korayem et al. 2014). The limitation of this method is that the generated path solution was parameterized to a limited fixed-order polynomial.

Most of the earlier works on collision avoidance are based on an optimization approaches. These approaches have their inherent limitations such as one does not have any information about the manipulator configuration after collision-avoidance. In a work (Shari and Troch 1996), based on reconfiguration approach, one can know the final configuration, i.e., configuration after obstacles avoidance which can be influenced by further requirements such as joint limit, singularity avoidance, etc. For behavior based control strategy, a fuzzy method has been developed for obstacle avoidance of multi-link manipulator (Dassanayake et al. 1999). Using this method, there is no need to evaluate inverse kinematics.

Still, a few literatures discuss about collision free trajectories in space. A practical 3-D seven DOF redundant manipulator was taken for collision-free trajectory planning (Mu et al. 2014) based on pseudo-distance. The natures of obstacles were both static and

dynamics. To plan a 3-D trajectory planning with collision avoidance, gradient projection was presented. This method provides high computation efficiency and good real time due to avoidance of complex computation of Euclidean distance. These aforementioned literatures motivated us to utilize unconventional features of the redundant space robot for collision-free trajectory planning.

In our work, 6 DOF space robot has been proposed for safe trajectory tracking with static environments. The static environments include two obstacles in the workspace. This work is based on reconfiguration approach. Among 6 joints only two joints are supposed to be actuated at a time, whereas others are kept passive. However, every joint can be actuated but some of them will not for the kinematic control purpose. When a link comes close to the obstacles, the joint of the respective/influencing link is made passive and in between other passive is released to be actuated and then the manipulator is reconfigured. In this way, by exploiting redundancy, a collision-free trajectory can be achieved. It is worth mentioning that each joint is controlled independently by using Proportional-Derivative controller. The end-effector trajectory tracking is taken care by using Proportional-Integral-Derivative controller.

This paper is organized in 6 sections. Section 2 presents a physical model of 6 DOF planar space robots. Section 3 discusses about recognition of obstacles present in the workspace. Section 4 deals the simulation and the animation results. Finally, section 6 presents conclusions.

2. MODEL OF 6DOF PLANAR SPACE ROBOTIC SYSTEM

This section discusses about the entire procedure of development of a dynamic model of 6 DOF planar space robot. Modeling of the 6DOF planar space robot involves translational and rotational dynamics of the links. The basis of modeling depends upon assumptions that the robot base and all the links are rigid body. Also, the joints are assumed to be revolute joints and the robot has a single arm and it is an open kinematic chain. Figure 1 represents a schematic sketch of the 6 DOF planar space robot. In this Figure, $\{A\}$ is the inertial or absolute frame and $\{V\}$ is the vehicle frame located at the center of mass (CM) of the space robot. A frame $\{0\}$ is located on space robot base at the root of the manipulator of space robot. Frame $\{1\}$ is also located at the root of manipulator at the first joint. Frames $\{2\}$ to $\{6\}$ are attached at the joints 2 to 6 of the manipulator, respectively. Frame $\{7\}$ is located at the tip of the manipulator or at the end effector of the space robot. Let, r is the distance between the vehicle frame and the root of the robot frame. Let, l_1 to l_6 are the length of the links 1 to 6 of the manipulator, respectively.

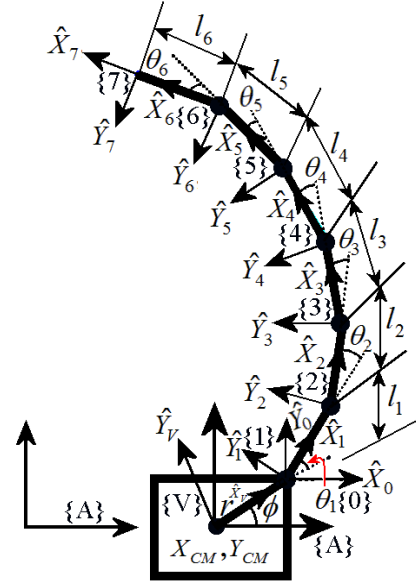


Figure 1. Schematic Sketch of 6DOF Planar Space Robot System

Let ϕ represents the rotation of the frame $\{V\}$ with respect to the frame $\{A\}$. Let θ_1 to θ_6 show 1st to 6th joint angles of the manipulator, respectively. Let X_{CM} , and Y_{CM} denote the center of mass (CM) of the robot base with respect to the absolute frame $\{A\}$. Kinematic relations are expressed in terms of the tip position and orientation as:

$$X_{tip} = X_{CM} + r c(\phi) + l_1 c(\theta_{\phi 1}) + l_2 c(\theta_{\phi 12}) + l_3 c(\theta_{\phi 123}) + l_4 c(\theta_{\phi 1234}) + l_5 c(\theta_{\phi 12345}) + l_6 c(\theta_{\phi 123456}) \quad (1)$$

$$Y_{tip} = Y_{CM} + r s(\phi) + l_1 s(\theta_{\phi 1}) + l_2 s(\theta_{\phi 12}) + l_3 s(\theta_{\phi 123}) + l_4 s(\theta_{\phi 1234}) + l_5 s(\theta_{\phi 12345}) + l_6 s(\theta_{\phi 123456}) \quad (2)$$

$$\theta_{\phi 1} = \phi + \theta_1, \theta_{\phi 12} = \theta_{\phi 1} + \theta_2, \theta_{\phi 123} = \theta_{\phi 12} + \theta_3$$

Where, $\theta_{\phi 1234} = \theta_{\phi 123} + \theta_4, \theta_{\phi 12345} = \theta_{\phi 1234} + \theta_5,$

$$\theta_{\phi 123456} = \theta_{\phi 12345} + \theta_6.$$

$$\theta_{tip} = \theta_{\phi 123456} = \phi + \theta_1 + \theta_2 + \theta_3 + \theta_4 + \theta_5 + \theta_6 \quad (3)$$

Here, $s(\)$ and $c(\)$ represent $\sin(\)$ and $\cos(\)$, respectively. The tip translational and the angular velocities can be evaluated with help of Equations 1, 2 and 3 as,

$$\dot{X}_{tip} = \dot{X}_{CM} - r \dot{\phi} s(\phi) - l_1 (\dot{\theta}_{\phi 1}) s(\theta_{\phi 1}) - l_2 (\dot{\theta}_{\phi 12}) s(\theta_{\phi 12}) - l_3 (\dot{\theta}_{\phi 123}) s(\theta_{\phi 123}) - l_4 (\dot{\theta}_{\phi 1234}) s(\theta_{\phi 1234}) - l_5 (\dot{\theta}_{\phi 12345}) s(\theta_{\phi 12345}) - l_6 (\dot{\theta}_{\phi 123456}) s(\theta_{\phi 123456}) \quad (4)$$

$$\begin{aligned} \dot{Y}_{tip} = & \dot{X}_{CM} + r\dot{\phi}c(\phi) + l_1(\dot{\theta}_{\phi 1})c(\theta_{\phi 1}) + l_2(\dot{\theta}_{\phi 12})c(\theta_{\phi 2}) \\ & + l_3(\dot{\theta}_{\phi 123})c(\theta_{\phi 123}) + l_4(\dot{\theta}_{\phi 1234})c(\theta_{\phi 1234}) \\ & + l_5(\dot{\theta}_{\phi 12345})c(\theta_{\phi 12345}) + l_6(\dot{\theta}_{\phi 123456})c(\theta_{\phi 123456}) \end{aligned} \quad (5)$$

$$\dot{\theta}_{tip} = \dot{\theta}_{\phi 123456} = \dot{\phi} + \dot{\theta}_1 + \dot{\theta}_2 + \dot{\theta}_3 + \dot{\theta}_4 + \dot{\theta}_5 + \dot{\theta}_6 \quad (6)$$

Since we will not actuate all joints simultaneously for the kinematic control purpose, the robot needs to be reconfigured. Suppose, initially joints 1 and 4 are active and the rest are passive joints. Figure 2 consists of the original configuration of 6DOF robot and the reconfigured robot. In this case, where, joint 1 and joint 4 are actuated, the kinematic relations for the tip displacements $X_{tip}^{\#}$ and $Y_{tip}^{\#}$ in X and Y directions can be derived as,

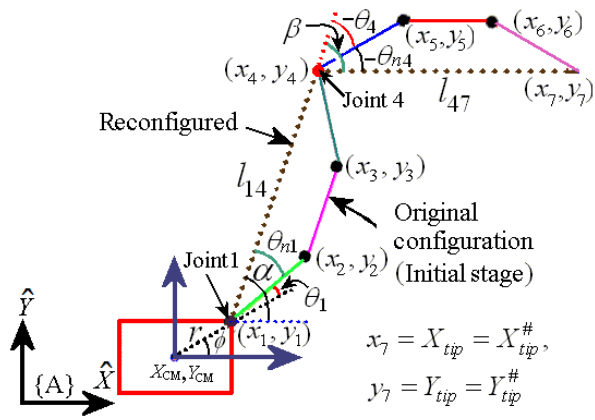


Figure 2. Schematic Sketch of the Original Configuration of 6DOF Robot and the Reconfigured Robot

$$X_{tip}^{\#} = X_{CM} + rc(\phi) + l_{14}c(\alpha) + l_{47}c(\beta) \quad (7)$$

$$Y_{tip}^{\#} = Y_{CM} + rs(\phi) + l_{14}s(\alpha) + l_{47}s(\beta) \quad (8)$$

$$\text{Where, } \begin{aligned} \alpha &= \phi + \theta_1 + \theta_{n1} = \phi + \theta_{1n1}, \\ \beta &= \alpha - \theta_4 - \theta_{n4} = \alpha - \theta_{4n4}. \end{aligned} \quad (9)$$

Here, θ_{n1} and θ_{n4} are unknown, hence, α and β become unknown.

$$l_{14} = \sqrt{(x_4 - x_1)^2 + (y_4 - y_1)^2}, \quad (10)$$

$$l_{47} = \sqrt{(x_7 - x_4)^2 + (y_7 - y_4)^2}$$

The variables used in the Equation 10 can be evaluated from the original configuration (Fig. 2) as,

$$x_1 = X_{CM} + rc(\phi) \quad (11)$$

$$y_1 = Y_{CM} + rs(\phi) \quad (12)$$

$$x_4 = X_{CM} + rc(\phi) + l_1c(\theta_{\phi 1}) + l_2c(\theta_{\phi 12}) + l_3c(\theta_{\phi 123}) \quad (13)$$

$$y_4 = Y_{CM} + rs(\phi) + l_1s(\theta_{\phi 1}) + l_2s(\theta_{\phi 12}) + l_3s(\theta_{\phi 123}) \quad (14)$$

$x_7 = X_{tip}$, $y_7 = Y_{tip}$ where, X_{tip} and Y_{tip} are evaluated from Equations 1 and 2.

Now, the unknown joint variables α and β of Equations 7 and 8, need to be calculated.

For reconfigured robot, x_4 and y_4 of Equations 13 and 14 can also be expressed as,

$$x_4 = X_{CM} + rc(\phi) + l_{14}c(\alpha) \quad (15)$$

$$y_4 = Y_{CM} + rs(\phi) + l_{14}s(\alpha) \quad (16)$$

By equating Equation 13 with 15 and 14 with 16 and simplifying them, α is calculated as,

$$\alpha = \tan^{-1}[(l_1s(\theta_{\phi 1}) + l_2s(\theta_{\phi 12}) + l_3s(\theta_{\phi 123})) / (l_1c(\theta_{\phi 1}) + l_2c(\theta_{\phi 12}) + l_3c(\theta_{\phi 123}))] \quad (17)$$

Similarly, β can be found by equating and simplifying the tips of 6DOF robot (original robot) and reconfigured robot (Fig. 2), i.e., Equation (7) with (1) and (8) with (2).

$$\begin{aligned} \beta = \tan^{-1}[\{l_1s(\theta_{\phi 1}) + l_2s(\theta_{\phi 12}) + l_3s(\theta_{\phi 123}) \\ + l_4s(\theta_{\phi 1234}) + l_5s(\theta_{\phi 12345}) + l_6s(\theta_{\phi 123456}) \\ - l_{14}s(\alpha)\} / \{l_1c(\theta_{\phi 1}) + l_2c(\theta_{\phi 12}) + l_3c(\theta_{\phi 123}) \\ + l_4c(\theta_{\phi 1234}) + l_5c(\theta_{\phi 12345}) + l_6c(\theta_{\phi 123456}) \\ - l_{14}c(\alpha)\}] \end{aligned} \quad (18)$$

The tip velocity can be found by differentiating Equations 7 and 8 as,

$$\dot{X}_{tip}^{\#} = \dot{X}_{CM} - r(\dot{\phi})s(\phi) - l_{14}(\dot{\alpha})s(\alpha) - l_{47}(\dot{\beta})s(\beta) \quad (19)$$

$$\dot{Y}_{tip}^{\#} = \dot{Y}_{CM} + r(\dot{\phi})c(\phi) + l_{14}(\dot{\alpha})c(\alpha) + l_{47}(\dot{\beta})c(\beta) \quad (20)$$

Equations 19 and 20 help in evaluating transformer moduli (Table 1) for drawing bond graph model of the reconfigured space robot as shown in Figure 3. In Figure 3, I elements are used to model translational and rotational inertia of the space robot system. The R element represents the damping present at joints. The inertial element in the controller (Figure 4) is differentially causalled which is removed by adding a Soft Pad. The dynamic consequence of the Soft Pad

$$\begin{aligned} \begin{bmatrix} \dot{X}_{tip}^{\#} \\ \dot{Y}_{tip}^{\#} \end{bmatrix} &= \begin{bmatrix} \dot{X}_{CM} - r\dot{\phi}s\phi \\ \dot{Y}_{CM} + r\dot{\phi}c\phi \end{bmatrix} + \\ &\begin{bmatrix} -l_{14}s(\alpha) - l_{47}s(\beta) & -l_{47}s(\beta) \\ l_{14}c(\alpha) + l_{47}c(\beta) & l_{47}c(\beta) \end{bmatrix} \begin{bmatrix} \dot{\alpha} \\ \dot{\beta} \end{bmatrix} \\ &+ \begin{bmatrix} -l_{14}s(\alpha) - l_{47}s(\beta) \\ l_{14}c(\alpha) + l_{47}c(\beta) \end{bmatrix} \begin{bmatrix} \dot{\phi} \end{bmatrix} \end{aligned} \quad (24)$$

The above Equation 24 can be rewritten in compact form as,

$$\begin{bmatrix} \dot{X}_{tip} \\ \dot{Y}_{tip} \end{bmatrix} = \begin{bmatrix} \dot{X}_{CM} + \dot{\phi}\mu_2 \\ \dot{Y}_{CM} + \dot{\phi}\mu_1 \end{bmatrix} + \begin{bmatrix} K_3 & K_1 \\ K_4 & K_2 \end{bmatrix} \begin{bmatrix} \dot{\alpha} \\ \dot{\beta} \end{bmatrix} + \begin{bmatrix} K_5 \\ K_6 \end{bmatrix} \begin{bmatrix} \dot{\phi} \end{bmatrix} \quad (25)$$

Where, gains K_1, K_2, K_3, K_4, K_5 and K_6 are used for the Jacobian of the space robot.

2.2. PD Controllers

PD controllers are used herein at each joint to control the joint motion, i.e., to make joints active and passive. As shown in Figure 3, initially joints 1 and 4 are made active while others are kept passive. The actuated (active) joints are regulated by the PID controllers. Redundancy of the proposed robot system facilitates to choose joint as active/passive as per requirement. To control joint motion, PD control is used as shown in Fig. 4. The control law for the actuator at the joint is given as,

$$\tau = K_p(\theta_d - \theta_a) - K_d\dot{\theta}_a \quad (26)$$

Where, τ is the joint torque, θ_d is the desired position of

joint and θ_a is the actual position of joint, $\dot{\theta}_a$ is the actual joint angular velocity. K_p and K_d are the proportional and the derivative gain parameters, respectively.

2.3. PID Controllers

PID controllers are used herewith in X and Y tip of the space robot as shown in figure 4. The aim of using it is to compare the actual velocity signal to the reference velocity signal and to correct it in case of error presence. The corrected signals are then sent to the each actuated joint of the manipulator through the Jacobian. Hence, one can get a close trajectory tracking during the task. The PID controllers are represented in the form of signal block diagrams in figure 4. In these block diagrams, K_p , K_i and K_d represent proportional gain, integral gain and derivative gain, respectively. \dot{X}_{tip} and \dot{Y}_{tip} are the actual velocity signals and \dot{X}_{ref} and \dot{Y}_{ref} are the reference velocity signals in X and Y directions, respectively. δx and δy are the trajectory error in X and Y directions, respectively.

3. RECOGNITION OF OBSTACLES

The obstacles present in the workspace are recognized by providing a barrier encircling the obstacles as shown in Figure 5. Assuming that obstacle 1 has a hexagonal shape and obstacle 2 is of a square shaped. The mathematical expression for obstacle detection (Mu et al. 2014; Shari and Troch 1996) can be given as,

$$d_{iLO} = f(x_i, y_i) \quad (27)$$

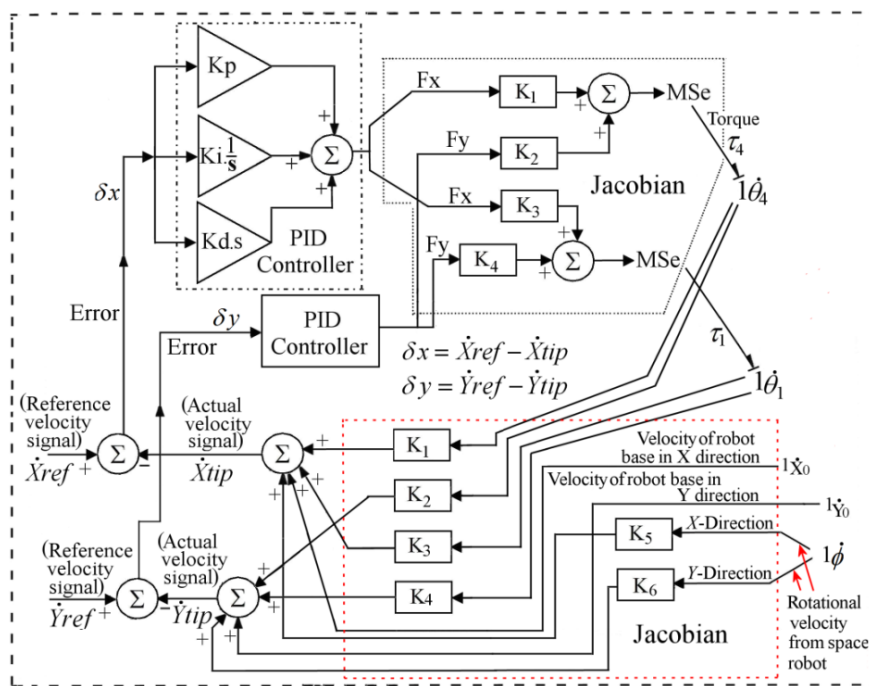


Figure 4. Jacobian and PID Controllers Interfacing with Space Robot System.

Where, d_{iLO} denotes the pseudo-distance between the manipulator link and i number of the obstacles.

$$\text{and, } f(x_i, y_i) = (x_i - x_{ci})^2 + (y_i - y_{ci})^2 - a_i^2 \quad (28)$$

The co-ordinates, x_i and y_i represent the tip position near the obstacles. The co-ordinates x_{ci} and y_{ci} are the centre of mass coordinates of the obstacles's barrier and a_i is the radius of the barrier.

- If, $d_{iLO} > 0$, there is no collision
 $= 0$, there is possibility of collision
 < 0 , there is possibility of serious collision.

To avoid obstacles, we need to maintain $d_{iLO} > 0$. This condition can be satisfied completely by arresting the tip motions when it comes close to the obstacles. This can be done through locking the respective or influencing joint variable. Then, one of the passive joints needs to be made active simultaneously and hence the robot needs to be reconfigured to continue the desired motion planning. Now the question may arise that at what positive value of the pseudo-distance, the robot need to be reconfigured. This should be done at a minimum positive value of the pseudo-distance. However, it's as much as positive value can provide safest motion planning.

This concept can be extended for the proposed robot system as follows:

Stage I: This stage is schematically represented in Figure 5. The circumstance when both the obstacles collide with the manipulator is shown in this figure. Let's divide the whole manipulator into two sections for simplicity as shown in figure 5. In the first section of the manipulator only joint 1 is active and in the second section, only joint 4 is active. At this stage, let we get $d_{1LO} < 0$ for obstacle 1 and $d_{2LO} < 0$ for obstacle 2 in section 1 and 2 of the manipulator, respectively. These mean that the robot system suffers a serious collision from both the obstacles.

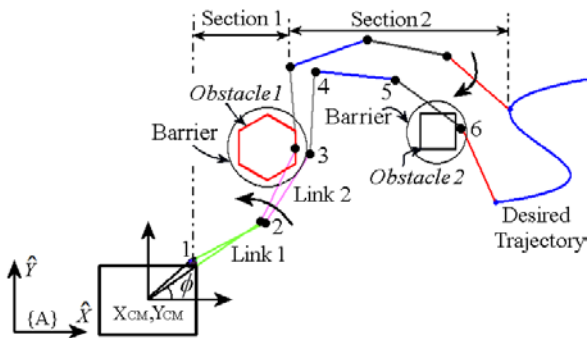


Figure 5: Stage I

Let us now assume that the space robot system avoids both the obstacles one by one.

Stage II: This stage is schematically represented in Figure 6. This figure shows the circumstance (assuming) when the robot avoids obstacle 1 but unable to avoid obstacle 2. Let us now discuss the occurrence of this situation. Suppose link 2 tip comes close to the obstacle 1 during the task. If it continues, first section of the manipulator will collide to the obstacle 1. To avoid this collision, let joint 1 is made passive during manipulation at minimum positive value of d_{1LO} ensuring safe margin between the barrier and the surrounding links. This act will restrict motion of its influencing link tip, i.e., tip of link 2 as joints 2 and 3 are already passive. At this moment, however, the first section of the manipulator will not collide to the obstacle 1 but the robot tip will not trace the designated path due to lacking of the necessary and required two active joints.

To avoid this problem let joint 6 is made active. Hence, joints 4 and 6 are now active. A selection of which joint to be actuated while manipulation depends upon instant manipulator's configuration ensuring collision free-trajectory. By doing this, condition, i.e., $d_{1LO} > 0$ will be satisfied. But it does not guarantee about the avoidance of manipulator from the obstacle 2. This means that $d_{2LO} < 0$. At this stage, only one condition is satisfied while the other is not satisfied. For, a collision-free trajectory both conditions must be fully satisfied. This will be addressed in stage III.

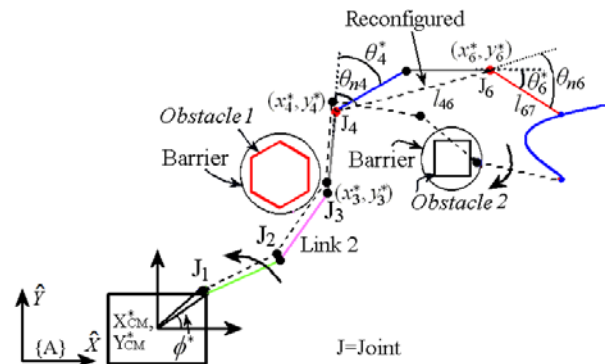


Figure 6: Stage II

The tip displacement expressions can be given as,

$$X_{tip}^* = X_{CM}^* + rc(\phi^*) + l_1 c(\theta_{(\phi_1)}^*) + l_2 c(\theta_{(\phi_{12})}^*) + l_3 c(\theta_{(\phi_{123})}^*) + l_{46} c(\alpha^*) + l_{67} c(\beta^*) \quad (29)$$

$$Y_{tip}^* = Y_{CM}^* + rs(\phi^*) + l_1 s(\theta_{(\phi_1)}^*) + l_2 s(\theta_{(\phi_{12})}^*) + l_3 s(\theta_{(\phi_{123})}^*) + l_{46} s(\alpha^*) + l_{67} s(\beta^*) \quad (30)$$

$$\alpha^* = \theta_{\phi_{123}}^* - \theta_{n4}^*, \beta^* = \alpha^* - \theta_{n6}^*$$

$$\text{Where, } l_{46} = \sqrt{(x_6^* - x_4^*)^2 + (y_6^* - y_4^*)^2}, \quad (31)$$

$$l_{67} = \sqrt{(x_7^* - x_6^*)^2 + (y_7^* - y_6^*)^2}$$

It is notable that the superscript “*” with variables denotes the parameter’s values at $d_{1LO} > 0$ and $t = 9s$, are known by the sensors used in model as shown in Figure 3. The joint variables α^* and β^* of the reconfigured robot can be evaluated in the same way as Equations 15 to 18.

Stage III: This stage is schematically represented in Figure 7. The circumstance when the manipulator could avoid both the obstacles is shown in this figure. Now to satisfy both the conditions as discussed in stage II, let joint 4 is made passive and joint 1 is again resumed which was locked in stage II. Hence, joints 1 and 6 are now active. Now problem may arise by selecting the joint 1 again as active (which was active in stage I and then made passive in stage II) if it causes collision of the manipulator’s first section with the obstacle 1. To resolve this problem, one must always be assure that $d_{1LO} > 0$ and motion of the manipulator’s first section must be away from that obstacle. If not then one must select other joint as active imparting complete collision-free trajectory.

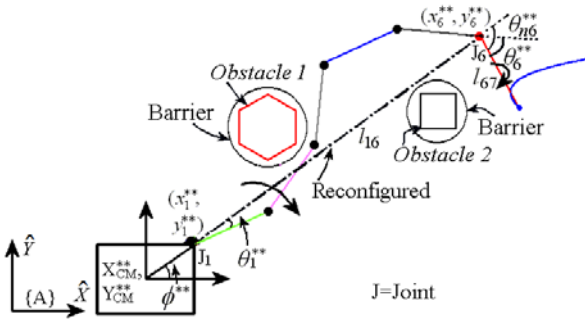


Figure 7: Stage III

The tip displacement expressions can be given as,

$$X_{tip}^{**} = X_{CM}^{**} + rc(\phi^{**}) + l_{16}c(\alpha^{**}) + l_{67}c(\beta^{**}) \quad (32)$$

$$Y_{tip}^{**} = Y_{CM}^{**} + rs(\phi^{**}) + l_{16}s(\alpha^{**}) + l_{67}s(\beta^{**}) \quad (33)$$

$$\alpha^{**} = \phi^{**} - \theta_1^{**}, \beta^{**} = \alpha^* - \theta_{n6}^{**},$$

$$\text{Where, } l_{16} = \sqrt{(x_6^{**} - x_1^{**})^2 + (y_6^{**} - y_1^{**})^2}, \quad (34)$$

$$l_{67} = \sqrt{(x_7^{**} - x_6^{**})^2 + (y_7^{**} - y_6^{**})^2}.$$

α^{**} and β^{**} of equations 32 and 33 can be found in the similar way as equations 15 to 18. Here, variables with superscript “**” are their values at $d_{1LO}, d_{2LO} > 0$ and $t = 17.5 s$.

The Jacobian for stages I and II, can be evaluated in the same fashion as mentioned in section 3 and bond graph model can be drawn for the same.

How to choose which joint to be actuated can be decided by adopting optimization criterion such as energy optimum, smooth trajectory, etc. It is also worth mentioning that the obstacle avoidance as discussed above can be performed in a single attempt too. However, it is presented in three stages for better understanding and simplicity.

4. SIMULATION AND ANIMATION RESULTS

The proposed collision-free avoidance strategy has been considered to be validated through simulation and animation results. The bond graph model of the system equation has been implemented by the Symbol Shakti software (Mukherjee A. 2006). The simulation is carried out for 60 seconds. The input parameters used for simulation study are shown in Table 2.

Table 2: Input Parameters and their Value

Robot Base and Link Parameters		
Space Robot Base Mass (M_v)(kg)	200	
Rotary Inertia of Base (I_v)(kg m ²)	40	
Location of Base of Arm from Vehicle CM (r)(m)	0.5	
Length of each Link	0.5	
Mass of each Link with Actuator (kg)	1	
Rotary Inertia of each Link (kg m ²)	0.5	
Pad Parameters		
Stiffness of Spring (K_s) (Nm/rad)	5×10^4	
Stiffness of Spring (K_h)(Nm/rad)	3×10^4	
Damping Resistance (R_d)(Nms/rad)	1×10^4	
PID Gain Parameters		PD Gain Parameters
Proportional Gain (K_p)	3000	5×10^4
Integrative Gain (K_i)	2500	-
Derivative Gain (K_d)	2000	5×10^4
Reference Trajectory: Control Points (m)		
$p_{x0}=2.892, p_{y0} = 1.115, p_{x1}=1.572, p_{y1}=0.8822,$		
$p_{x2}=3.655, p_{y2} = 0.54, p_{x3}= 2.35, p_{y3}= 0.3674.$		
Obstacle Parameters		
	Obstacle 1	Obstacle 2
Length of side (m)	0.2	0.15
CM Coordinates from Absolute Frame{A} (m)	$x_{c1} = 0.90$ $y_{c1} = 0.72$	$x_{c2} = 2.0$ $y_{c2} = 0.15$
Radius of barrier (m)	$a_1 = 0.24$	$a_2 = 0.21$

Initial configuration of the space manipulator is given by the following joint coordinates in all cases:

$$\theta = [0 \ 10^\circ \ 30^\circ \ 30^\circ \ -30^\circ \ -30^\circ \ -30^\circ]$$

As a reference tip trajectory input, a B-spline curve of “S” shaped tip trajectory is taken. Let a B-spline curve with four control points (polynomial’s third degree) is constructed for tip trajectory tracking. The reference tip displacement and velocity equations are as,

$$X_{tip} = p_{x0}(1-t/t_f)^3 + 3p_{x1}(t/t_f)(1-t/t_f)^2 + 3p_{x2}(t/t_f)^2(1-t/t_f) + p_{x3}(t/t_f)^3 \quad (35)$$

$$Y_{ip} = p_{y0}(1-t/t_f)^3 + 3p_{y1}(t/t_f)(1-t/t_f)^2 + 3p_{y2}(t/t_f)^2(1-t/t_f) + p_{y3}(t/t_f)^3 \quad (36)$$

$$\dot{X}_{ip} = [-3p_{x0}(1-t/t_f)^2 - 6p_{x1}(t/t_f)(1-t/t_f) + 3p_{x1}(1-t/t_f)^2 - 3p_{x2}(t/t_f)^2 + 6p_{x2}(t/t_f)(1-t/t_f) + 3p_{x3}(t/t_f)^2] / t_f \quad (37)$$

$$\dot{Y}_{ip} = [-3p_{y0}(1-t/t_f)^2 - 6p_{y1}(t/t_f)(1-t/t_f) + 3p_{y1}(1-t/t_f)^2 - 3p_{y2}(t/t_f)^2 + 6p_{y2}(t/t_f)(1-t/t_f) + 3p_{y3}(t/t_f)^2] / t_f \quad (38)$$

Where, $(p_{x0}, p_{y0}) \dots (p_{x3}, p_{y3})$ are four control points of B-spline curve corresponding to X and Y directions and t is time and t_f is final travel time.

Let us now discuss the simulation and the animation results.

4.1. Collision Recognition

To detect collisions, pseudo-distance (Mu et al. 2014) criterion has been used. Figure 8 shows the pseudo-distance between the manipulator and the obstacles during the task. Figure 8 (a) depicts the pseudo-distance for traditional trajectory planning (stage I). From this figure, one can observe that the pseudo-distance, $d_{1LO} < 0$ between the time interval of 12.6s and 17.1s. This is the period when the manipulator collides critically with the obstacle 1. Also, the pseudo-distance, $d_{2LO} < 0$ after $t = 58.7s$. This means that the whole manipulator suffers a serious collision with the obstacle 2 after $t = 58.7s$. Figure 8(b) exhibits the pseudo-distance for partial collision-free trajectory. From this figure, it is seen that the pseudo-distance, $d_{1LO} > 0$ throughout the manipulation. This means that the first section of the manipulator is now able to save itself from the obstacle 1. It is also seen that the pseudo-distance, $d_{2LO} < 0$ between the time interval of 25.7s and 54s which illustrates the serious collision of the manipulator's second section as discussed with the obstacle 2. Hence, from this figure one gets to know that the manipulator could avoid the obstacle 1 but not the obstacle 2. Figure 8(c) shows the pseudo-distance for complete collision-free trajectory. From this figure, it is seen that the pseudo-distance, d_{1LO} and $d_{2LO} > 0$ throughout the manipulation. This means that the whole manipulator now completely avoids both the obstacles and provides complete collision-free trajectory.

4.2. Trajectory Planning

This sub-section deals about the simulation results of trajectory tracking planning in the presence of the obstacles in the workspace for all three stages as discussed.

Figure 9 shows the reference and the actual tip trajectory in the presence of the two obstacles in the workspace. Figure 9(a) depicts the tip trajectory when both the obstacles collide with the whole manipulator (stage I as discussed). This stage is expressed as

traditional trajectory planning in (Mu et al. 2014). From figure 9 (a), it is observed that the tip closely follows the designated path. In this figure, 1,4A denotes that joints 1 and 4 are active joints. Figure 9(b) represents the tip trajectory when the manipulator avoids obstacle 1 but collides with obstacle 2 (stage II). This stage can be expressed as partial collision-free trajectory. From figure 9(b), it is seen that the robot closely track about half of the designated path but does not the rest half. This trajectory error occurs due to not to be sufficient torque generation by the active joints 4 and 6. This trajectory tracking is the resultant of the circumstance when the active joint 1 is made passive and the passive joint 6 is made active during manipulation. The joint 1 is made active to avoid collision to its influencing link and joint 6 is made active to keep continue the desired motion. Hence, joints 4 and 6 are now active which are denoted by 4,6A in figure 9(b). From this figure, close trajectory tracking is observed. Figure 9(c) shows the tip trajectory when the whole manipulator avoids both the obstacles completely (stage III). This stage can be expressed as complete collision-free trajectory. From this figure, one can see that the robot closely trace the given reference input. In this figure, other than 1,4A, 4,6A represents that joints 4 and 6 are now active and 1,6A represents that joints 1 and 6 are then now active.

4.3. Joint Rotation

This sub-section gives information about which joint is whether actuated or not during the task. Figure 10 shows the joint rotation with respect to time. Figure 10(a), (b) and (c) represents the joint rotation for the three stages I, II and III, respectively, as discussed in sub-section 4.2. Figure 10(a) illustrates that only joints 1 and 4 are active, whereas others are passive. Figure 10(b) exhibits that joints 1 and 6 are made passive and active, respectively, at $t = 9s$ during the task. From figure 10(c), it is seen that joint 4 is made passive and instead of it, joint 1 is again made active at $t = 17.5s$ during the task. The reason behind making active/passive to which joint and at what circumstances is well addressed in sub-section 4.2.

4.4. Animated View of Trajectory Planning

This sub-section discusses about the animation results. Animation is the other way of validation of the proposed work in addition to the simulation. Figure 11 shows the animated view of the trajectory planning as discussed in sub-section 4.2. Figure 11(a), (b) and (c) represents the animation results for the three stages I, II and III, respectively, as discussed in sub-section 4.2. From figure 11(a), it is seen that trajectory tracking is successfully accomplished but both the static obstacles collide with the space manipulator. From figure 11 (b), one can see that the manipulator is able to avoid obstacle 1 but at the same time it collides with the obstacle 2. From figure 11(c), it is illustrated that the manipulator is now able to avoid both the static obstacles during its tip trajectory.

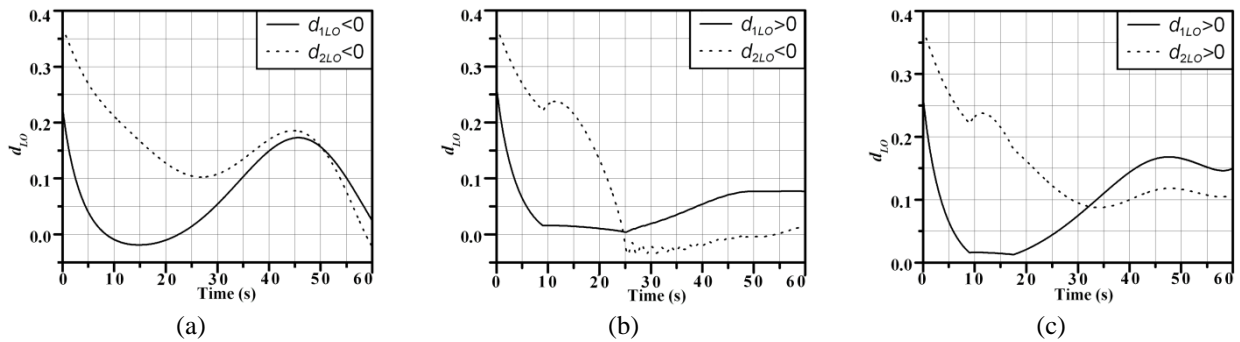


Figure 8: The pseudo-distance between the manipulator and the obstacles, (a) stage I (b) stage II and (c) stage III.

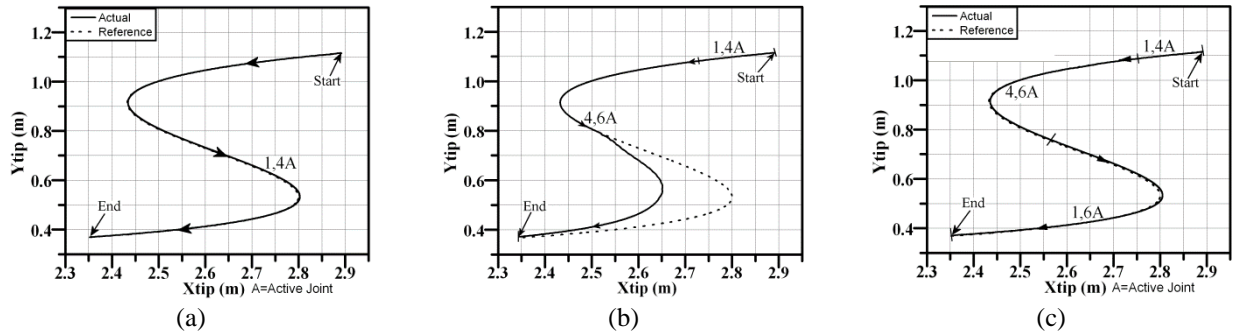


Figure 9: The tip trajectory tracking of the 6 links space robot system, (a) stage I (b) stage II and (c) stage III.

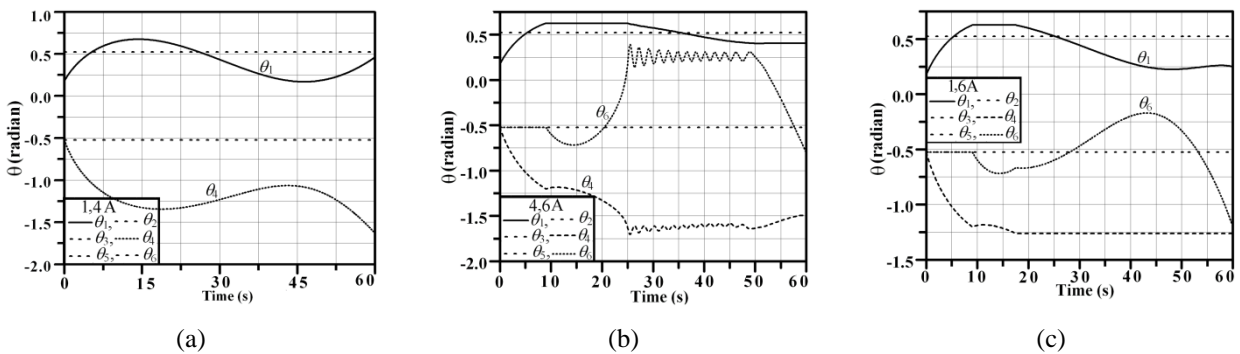


Figure 10: The joint rotation of the 6 links space robot system, (a) stage I (b) stage II and (c) stage III.

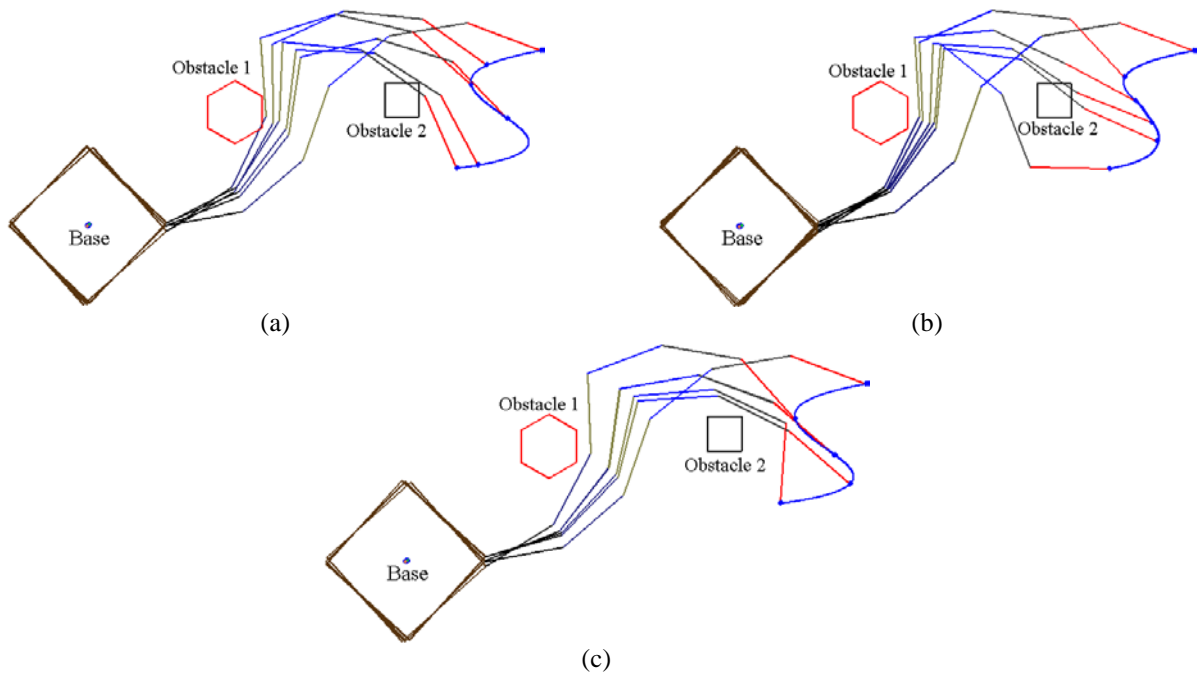


Figure 11: Animated view of collision-free trajectory of the 6 links space robot, (a) stage I (b) stage II and (c) stage III.

5. CONCLUSION

Based on the reconfiguration approach, we proposed 6DOF space manipulator for obstacle avoidance during trajectory tracking in the presence of the two obstacles in the workspace. For the kinematic control purpose, only two joints are made active at a time during the task. Reconfigurations have been done after detection of the obstacles in the workspace based on the pseudo-distance criterion. Each joint is controlled by employing the PD controller, whereas for tip motion control, PID controllers have been used. The simulation and the animation results validated the successful execution of the proposed approach for collision-free trajectory planning. This work will be extended for dynamic obstacles in the workspace. Also, a practical 3-D collision-free trajectory planning will be done.

REFERENCES

- Agrawal O P and Xu Y, 1994. On the global optimum path planning for redundant space manipulators. *IEEE Transactions on Systems, Man and Cybernetics* 24(9): 1306-1316.
- Bjerkeng M, Transteth A A, Pettersen K Y, Kyrkjebø E and Fjerdingen S A, 2011. Active Camera Control with Obstacle Avoidance for Remote Operations with Industrial Manipulators: Implementation and Experimental Results. *IEEE/RSJ International Conference on Intelligent Robots and Systems (IROS)*, September 25-30, San Francisco, CA, USA.
- Csiszar A, Drust M, Dietz T, Verl A and Brisan C, 2012. Dynamic and interactive path planning and collision avoidance for an industrial robot using artificial potential field based method. *Mechatronics*. Springer Berlin Heidelberg, 413-421.
- Dassanayake P, Watanabe K and Izumi K, 1999. Fuzzy Behavior-Based Control for a Task of Three- Link Manipulator. *Proceedings of the 1999 IEEE International Conference on Systems, Man and Cyber, II-776-781*, 12-15 October, Tokyo, Japan.
- Klein C A and Huang C H, 1983. Review of pseudoinverse control for use with kinematically redundant manipulators. *Systems, Man and Cybernetics, IEEE Transactions* 13(3): 245-250.
- Korayem M H, Nazemizadeh M and Rahimi H N, 2014. Dynamic optimal payload path planning of mobile manipulators among moving obstacles. *Advanced Robotics* 28.20: 1389-1402.
- Koren Y, Borenstein J, 1999. Potential Field Methods and their Inherent Limitations for Mobile Robot Navigation. *Proceedings of the IEEE International Conference on Robotics and Automation*, 1398-1404, April 9-11, Sacramento, California.
- Kumar A, Pathak P M, and Sukavanam N, 2011. Reduced model based control of two link flexible space robot. *Intelligent Control and Automation*, 2.02: 112.
- Kumar V. and Pathak PM. 2013. A Stable Docking Operation by a Group of Space Robots. *Proceedings of the 1st International and 16th National Conference on Machines and Mechanisms (iNaCoMM2013)*, IIT Roorkee, India, Dec. 18-20.
- Mu Z, Xu W, Gao X, Xue L and Li C, 2014. Obstacles Modeling and Collision Detection of Space Robots for Performing On-Orbit Services. *The 4th IEEE Conference on International Information Science and Technology (ICIST)*, 2014, 2014.
- Mukherjee A, Karmarkar R and Samantray A K, 2006. *Bond Graph in Modeling, Simulation and Fault Identification*. New Delhi, I. K. International Publishing House Private. Limited.
- Pathak P M, Mukherjee A and Dasgupta A, 2006. Attitude control of a free-flying space robot using a novel torque generation device. *Simulation*, 82.10: 661-677.
- Pathak P M, Mukherjee A and Dasgupta A, 2006. Impedance control of space robot. *International Journal of Modelling and Simulation*, 26.4: 316.
- R Merzouki, Samantray A K, Pathak P M and Bouamam B O, 2013. *Intelligent Mechatronic Systems: Modelling, Control and Diagnosis*, Springer 2013.
- Saha S K. 1996. A unified approach to space robot kinematics. *Robotics and Automation, IEEE Transactions on* 12.3: 401-405.
- Sardana L, Sutar M K and Pathak P M, 2013. A geometric approach for inverse kinematics of a 4-link redundant in-vivo robot for biopsy. *Robotics and Autonomous Systems* 61.12: 1306-1313.
- Shahri R N and Troch I, 1996. Collision-avoidance for redundant robots through control of the self-motion of the manipulator. *Journal of Intelligent and Robotic Systems*, 16.2: 123-149.
- Singla E, Trinathi S, Rakesh V, Dasgupta B. 2010. Dimensional synthesis of kinematically redundant serial manipulators for cluttered environments. *Robotics and Autonomous Systems*, 58.5: 585-595.
- Sutar M K, Pathak P M, Mehta N K, Sharma, A K and Gupta V K, 2014. Inverse kinematics and control of 4-degree-of-freedom wire-actuated in vivo robot. *Proceedings of the Institution of Mechanical Engineers, Part I: Journal of Systems and Control Engineering*, 229: 77-91.
- Whitney D E, 1969. Resolved motion rate control of manipulators and human prostheses. *IEEE Transactions on Man-Machine Systems*, MMS, 10(2), 47-53.

Vijay Kumar Dalla is a Ph.D. student at Robotics and Control Lab in the Department of Mechanical and Industrial Engineering, IIT Roorkee, India. He did Master of Technology (M.Tech.) from IIT Bombay in 2008. He did Bachelor of Engineering (B.E.) in Mechanical Engineering from Government Engineering College, Bilaspur, Chhattisgarh, India in 2006. His research area is a space robotics.

Pushparaj Mani Pathak received the B. Tech. degree in 1988 from NIT, Calicut, India and M. Tech. degree in 1998 from IIT, Kanpur, India both in Mechanical Engineering. He received Ph. D. degree in 2005 from IIT, Kharagpur, India. Currently he is an Associate Professor in the Department of Mechanical and Industrial Engineering, Indian Institute of Technology, Roorkee, India. His areas of interest are space robotics, walking robots, and dynamics and control.

LINEAR STABILITY ANALYSIS FOR SEVERE SLUGGING: SENSITIVITY TO VOID FRACTION CORRELATIONS

G. R. Azevedo¹, J. L. Baliño², K. P. Burr³

^{1,2}Departamento de Engenharia Mecânica, Escola Politécnica, Universidade de São Paulo, São Paulo, Brazil

³Centro de Engenharia, Modelagem e Ciências Sociais Aplicadas, Universidade Federal do ABC, Santo André, Brazil

¹gazevedo00@gmail.com, ²jlbaliño@usp.br, ³karl.burr@ufabc.edu.br

ABSTRACT

In this paper a numerical linear stability analysis is performed to a mathematical model for the two-phase flow in a pipeline-riser system. Void fraction is a key variable, as it influences the mixture properties and slip between the phases. In the model, it is assumed that an algebraic relationship exists between the void fraction and the state variables. This general representation allows to use empirical or drift flux based correlations. For a correct prediction of the stability behavior of a pipeline-riser flow, preventing the occurrence of severe slugging, it is important to assess the sensitivity of the system response to different void fraction correlations. Three void fraction correlations are implemented: Bendiksen (1984), Chexal *et al.* (1997) and Bhagwat and Ghajar (2014). The resulting stability maps and state variables profiles for vertical risers are compared for the different correlations. Results show that the different correlations give similar stability maps, with very small differences in the near horizontal branch (low gas superficial velocities) of the stability boundary and slight differences in the near vertical branch (low liquid superficial velocities). The different void fraction correlations show the right experimental trend by increasing the unstable region as the equivalent buffer length in the pipeline is increased.

Keywords: severe slugging, pipeline-riser system, air-water flow, linear stability theory, petroleum production technology

1. INTRODUCTION

Severe slugging may appear in offshore oil production systems for low gas and liquid flow rates when a section with downward inclination angle (pipeline) is followed by another section with an upward inclination (riser). This phenomenon, characterized by the formation and cyclical production of long liquid slugs and fast gas blow-down, may have a period of hours, causing higher average pressures, instantaneous flow rates and oscillations at the reservoir. These operational conditions may lead to the oil production shutdown. The steps leading to the process of severe slugging formation can be seen in Taitel (1986).

Many studies for severe slugging in air-water systems were made, specially for vertical riser with one-dimensional and isothermal flow and a mixture momentum equation in which only the gravitational term is relevant (Taitel *et al.*, 1990; Sarica and Shoham, 1991). In all

these models, inertial effects and propagation of pressure waves were neglected, resulting in the no-pressure-wave (NPW) approximation (Masella *et al.*, 1998). As a result of this approximation, pressure changes are felt instantaneously at any point in the riser. Besides, a stratified flow pattern was assumed at the pipeline and variations of void fraction were neglected. The void fraction at the pipeline was obtained from a momentum balance in the gas and liquid phases, resulting in an algebraic relation between the mean variables (Taitel and Dukler, 1976).

In Baliño *et al.* (2010) a model including friction term and riser variable inclination was presented, while in Baliño (2012, 2014) the model was improved by taking into account inertial effects using the rigid water-hammer approximation.

A pipeline-riser system is designed to operate at steady state. However, it is possible that this condition does not exist. The stability of a pipeline-riser flow depends on the set of parameters that defines the operational state. It is common to represent the stability in a map with liquid and gas reference superficial velocities in the axes, leaving the rest of the parameters fixed. The stability curve is defined as the relationship between the superficial velocities at the stability boundary between the regions where the stationary state is stable or unstable.

Many stability criteria were developed based on simplified models for vertical risers ((Bøe, 1981; Taitel, 1986; Pots *et al.*, 1987; Jansen *et al.*, 1996). Although these stability criteria are useful for a first estimation of the unstable region (they are even used in commercial steady-state computer codes), a common drawback is that they were not derived from complete dynamic system models, but from ad-hoc conditions in which many physical effects were disregarded; consequently, their applicability is quite limited.

The stability curve for any pipeline riser system can be obtained numerically. The stationary solution for a given point in the system parameter space is given as initial condition for the numerical simulation; if the numerical solution does not go away from the initial condition with time, the stationary solution is stable and it is the system steady state. If the numerical solution goes away with time, the stationary state is unstable, there is no steady state and an intermittent solution develops with time. By changing the point and repeating this process, the stability map can be built. For unstable flow, the analysis of the oscillatory solution leads to the determination of the flow regime map, showing the regions correspond-

ing to the different types of intermittency.

As a numerically cost efficient alternative to temporal simulations, the linear stability theory is a powerful technique to identify the stable and unstable regions. To perform the linear stability analysis of a dynamic system, a model characterized by a set of governing equations is needed. Then, the stationary state is obtained by setting to zero the time derivatives. The governing equations are linearized with respect to the stationary solution. These linearized equations determine how infinitesimal perturbations of the stationary solution evolve with time. The growth rate of the perturbations is given by the real part of the eigenvalues of the spectrum associated with the linearized equations. If all eigenvalues have negative real part, then the stationary solution is stable, but if at least one eigenvalue has positive real part, the stationary solution is unstable.

In [Zakarian \(2000\)](#), the linear stability theory was applied for a pipeline-riser system with a vertical riser using the NPW model and considering only two nodes. All dependent variables were considered to vary linearly in space. Then, gas and liquid mass conservation equations and a mixture linear momentum conservation equation were integrated in space. To close the model, an algebraic drift-flux relation was considered resulting in a system of differential-algebraic equations. For a vertical riser, an equation for the flow instability evolution was presented. The stability maps obtained showed a good qualitative agreement with the experimental results reported in the literature.

In [Azevedo et al. \(2015\)](#), a linear stability analysis was made for the model developed in [Baliño et al. \(2010\)](#), considering an arbitrary discretization and including severe slugging mitigation devices such as increase in separation pressure, choke valve at the top of the riser and gas injection at the bottom of the riser. Results were compared with experimental and numerical results reported in the literature with excellent agreement. The results also showed a better agreement with experimental results and with the stability curves obtained through numerical time simulations when the nodalization is increased from the simplest two-node description made in [Zakarian \(2000\)](#).

The void fraction averaged on the flow passage area is a key variable in the behavior of multiphase systems, as it affects virtually all the mixture variables and transport processes. The determination of the void fraction is usually made through correlations in which it is assumed that the void fraction depends algebraically on the process variables. Moreover, many void fraction correlations are framed in the drift flux model ([Zuber and Findlay, 1965](#); [Wallis, 1969](#)), in which attention is focused on the relative motion rather than on the motion of the individual phases.

As many multiphase models and commercial computer codes are based on the void fraction behavior, it is important to study the sensitivity of the system response to the drift flux correlation. In this paper, the influence of different drift flux correlations on the stability of a mul-

tiphase model is studied. Three correlations are studied: [Bendiksen \(1984\)](#), [Chexal et al. \(1997\)](#) and [Bhagwat and Ghajar \(2014\)](#).

A comparison is made for the stationary state and for the stability maps. The results obtained show that the drift flux correlation alters the stationary state and influences the stability maps for the boundaries corresponding to higher gas superficial velocities.

2. MODEL

The model equations are based on [Baliño et al. \(2010\)](#). It considers one-dimensional flow in both pipeline and riser subsystems. The liquid phase is assumed incompressible, while the gas phase is considered as an ideal gas. The two-phase flow is in isothermal condition and the flow pattern, in the pipeline, is assumed as a stratified flow. At the separator, a constant pressure is assumed. In this paper, no additional severe slugging mitigation devices are considered.

2.1 Pipeline

As stated in [Baliño et al. \(2010\)](#), the pipeline can be either in a condition of liquid accumulation or in a condition of continuous gas penetration (see Fig. 1). As the stationary state exists only for the condition of continuous gas penetration ($x = 0$), the equations for the pipeline subsystem can be written as:

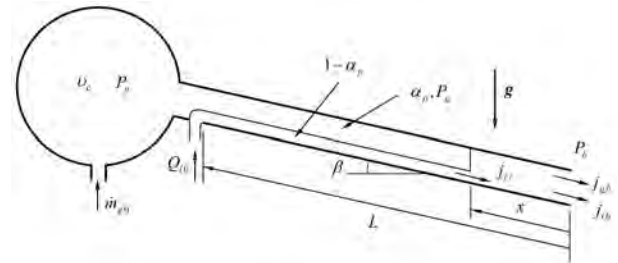


Figure 1: Definition of variables at the pipeline (from [Baliño et al. \(2010\)](#)).

$$j_{lb} = j_{l0} \quad (1)$$

$$\frac{dP_b}{dt} = \frac{-P_b j_{gb} + \frac{T_g}{T_0} P_0 j_{g0}}{L \alpha_p + L_e} \quad (2)$$

where j_{lb} and j_{gb} are, respectively, the superficial velocities for the liquid and gas at the bottom of the riser, L is the pipeline length, P_b and P_g are, respectively, the pressure at the bottom of the riser and the gas pressure ($P_b = P_g$), T_g is the gas temperature, t is time and α_p and β are respectively the pipeline void fraction and inclination angle (positive when downwards). The superficial velocities at a reference condition for gas and liquid, respectively j_{g0} and j_{l0} , used to represent the stability maps, are defined as:

$$j_{g0} = \frac{R_g T_0 \dot{m}_{g0}}{P_0 A} \quad (3)$$

$$j_{l0} = \frac{Q_{l0}}{A} \quad (4)$$

where \dot{m}_{g0} is the gas mass flow rate injected in the pipeline, R_g is the gas constant and Q_{l0} is the liquid volumetric flow injected in the pipeline. The reference condition is defined for pressure $P_0 = 1.013 \times 10^5 Pa$ and temperature $T_0 = 293 K$.

The existence of a buffer vessel with volume v_e is considered in order to simulate an equivalent pipeline length $L_e = \frac{v_e}{A}$, where A is the flow passage area ($A = \frac{1}{4} \pi D^2$, where D is the inner diameter).

As stated before, variations in the pipeline void fraction α_p are neglected during the transient; this assumption is justified, as in [Baliño \(2012, 2014\)](#) it was shown that void fraction variations in the pipeline are very small. The value used in the transients is determined from an algebraic relationship evaluated for the stationary state ([Taitel and Dukler, 1976](#)).

2.2 Riser

Based on Fig. 2, the conservation equations for the riser can be written as:

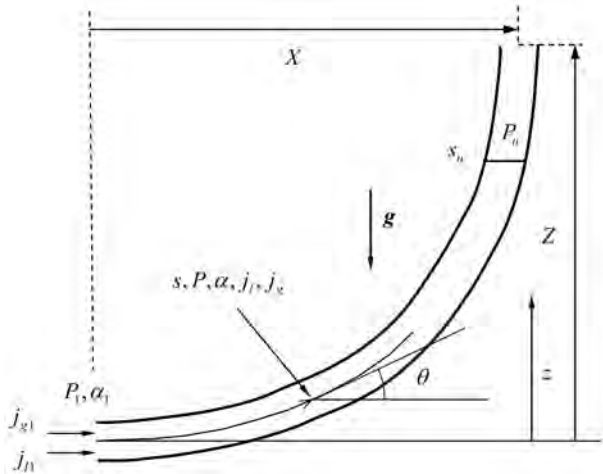


Figure 2: Definition of variables at the riser (from [Baliño et al. \(2010\)](#)).

$$-\frac{\partial \alpha}{\partial t} + \frac{\partial j_l}{\partial s} = 0 \quad (5)$$

$$\frac{\partial}{\partial t} (P \alpha) + \frac{\partial}{\partial s} (P j_g) = 0 \quad (6)$$

A mixture momentum equation is considered, where the inertial terms are neglected:

$$\frac{\partial P}{\partial s} + \rho_m \left(g \sin \theta + 2 \frac{f_m}{D} j |j| \right) = 0 \quad (7)$$

The following relations can be written:

$$\rho_m = \rho_l (1 - \alpha) + \frac{P}{R_g T_g} \alpha \quad (8)$$

$$f_m = f \left(Re_m, \frac{\epsilon}{D} \right) \quad (9)$$

$$Re_m = \frac{\rho_m D |j|}{\mu_m} \quad (10)$$

$$j = j_l + j_g \quad (11)$$

$$\mu_m = \mu_l (1 - \alpha) + \mu_g \alpha \quad (12)$$

where g is the gravity acceleration constant, j_g , j_l and j are respectively the gas, liquid and total superficial velocities, P is the pressure, s is the position along the riser, α is the void fraction, μ_g , μ_l and μ_m are respectively the gas, liquid and mixture dynamic viscosities, ρ_l and ρ_m are respectively the liquid and mixture density and θ is the local inclination angle of the riser. The Fanning friction factor f_m depends on the Reynolds number Re_m and the relative roughness ϵ/D , (where ϵ is the pipe roughness) and is calculated from [Chen \(1979\)](#) using a homogeneous mixture two-phase model.

It will be assumed that there is an algebraic relation between the void fraction and the local flow conditions:

$$\alpha = \alpha(j_g, j_l, P, \theta) \quad (13)$$

Equation (13) allows for using many empirical void fraction correlations, as well as correlations based on the drift flux model:

$$\alpha = \frac{j_g}{C_d j + U_d} \quad (14)$$

It will be assumed that the drift parameters C_d (distribution parameter) and U_d (drift velocity) depend at most on the local flow conditions and inclination angle $\theta = \theta(s)$, this is, $C_d = C_d(\alpha, j_g, j_l, P, \theta)$ and $U_d = U_d(\alpha, j_g, j_l, P, \theta)$.

2.3 Continuity between the subsystems

Assuming the same flow passage area for the pipeline and riser, the pressure and superficial velocities at the bottom of the riser are continuous:

$$P(0, t) = P_1(t) = P_b(t) \quad (15)$$

$$j_l(0, t) = j_{l1}(t) = j_{lb}(t) \quad (16)$$

$$j_g(0, t) = j_{g1}(t) = j_{gb}(t) \quad (17)$$

Pressure at the top of the riser (position s_t) satisfies:

$$P(s_t, t) = P_s \quad (18)$$

3. STATIONARY STATE

The stationary state is used as the initial condition for the transient simulations and also as the base solution for the linear stability analysis. The stationary state can be obtained by setting to zero the time derivatives in the dynamic equations. Variables at stationary state are denoted with superscript \sim .

3.1 Pipeline

For the pipeline, Eq. (1) and (2) give:

$$\tilde{j}_{lb} = j_{l0} \quad (19)$$

$$\tilde{j}_{gb} = \frac{T_g P_0}{T_0 \tilde{P}_b} j_{g0} \quad (20)$$

3.2 Riser

For the riser, Eq. (5) and (6) and the coupling conditions (Eq. (15) and (16)), give:

$$\tilde{j}_l = j_{l0} \quad (21)$$

$$\tilde{j}_g = \frac{T_g}{T_0} \frac{P_0}{\tilde{P}} j_{g0} \quad (22)$$

The void fraction in the riser can be calculated from Eq. (13) or from Eq.(14) as:

$$\tilde{\alpha} = \frac{j_{g0}}{\tilde{C}_d j_{g0} + (j_{l0} + \tilde{U}_d) \frac{T_0}{T_g} \frac{\tilde{P}}{P_0}} \quad (23)$$

The pressure distribution can be calculated by numerically integrating Eq. (7), as all terms are functions of pressure; and as $\tilde{j} > 0$, the stationary pressure satisfies:

$$\frac{\partial \tilde{P}}{\partial s} = -\tilde{\rho}_m \left(g \sin \theta + 2 \frac{\tilde{f}_m}{D} \tilde{j}^2 \right) \quad (24)$$

4. PERTURBATION EQUATIONS

4.1 Pipeline

Variables involved in the pipeline dynamics are written in terms of a stationary and a perturbation contribution:

$$j_{lb}(t) = \tilde{j}_{lb} + \hat{j}_{lb}(t) \quad (25)$$

$$j_{gb}(t) = \tilde{j}_{gb} + \hat{j}_{gb}(t) \quad (26)$$

$$P_b(t) = \tilde{P}_b + \hat{P}_b(t) \quad (27)$$

Taking into account Eq. (19) and (20), the pipeline perturbation equations result:

$$\hat{j}_{lb} = 0 \quad (28)$$

$$\frac{d\hat{P}_b}{dt} + C_{gb} \hat{j}_{gb} + C_{pb} \hat{P}_b = 0 \quad (29)$$

where:

$$C_{gb} = \frac{\tilde{P}_b}{L\alpha_p + L_e} \quad (30)$$

$$C_{pb} = \frac{j_{g0}}{L\alpha_p + L_e} \frac{T_g}{T_0} \frac{P_0}{\tilde{P}_b} \quad (31)$$

4.2 Riser

As there is an algebraic relation between void fraction and the rest of the variables, given by Eq. (13), the void fraction can be eliminated, decreasing the system order. After some algebra, the dynamic equations (5) to (7) can be written as:

$$\{A(\{v\})\} + \underline{B} \left\{ \frac{\partial v}{\partial t} \right\} + \underline{C} \left\{ \frac{\partial v}{\partial s} \right\} = 0 \quad (32)$$

where:

$$\{v\} = \left\{ \begin{array}{c} j_g \\ j_l \\ P \end{array} \right\} \quad (33)$$

$$\{A\} = \left\{ \begin{array}{c} 0 \\ 0 \\ A_3 \end{array} \right\} \quad (34)$$

$$A_3 = \rho_m \left(g \sin \theta + 2 \frac{f j^2}{D} \right) \quad (35)$$

$$\underline{B} = \left\{ \begin{array}{ccc} B_{11} & B_{12} & B_{13} \\ 0 & 0 & B_{23} \\ 0 & 0 & 0 \end{array} \right\} \quad (36)$$

$$B_{11} = -\frac{\partial \alpha}{\partial j_g} \quad (37)$$

$$B_{12} = -\frac{\partial \alpha}{\partial j_l} \quad (38)$$

$$B_{13} = -\frac{\partial \alpha}{\partial P} \quad (39)$$

$$B_{23} = \alpha \quad (40)$$

$$\underline{C} = \left\{ \begin{array}{ccc} 0 & C_{12} & 0 \\ C_{21} & C_{22} & C_{23} \\ 0 & 0 & C_{33} \end{array} \right\} \quad (41)$$

$$C_{12} = 1 \quad (42)$$

$$C_{21} = C_{22} = P \quad (43)$$

$$C_{23} = j_g \quad (44)$$

$$C_{33} = 1 \quad (45)$$

As usual, variables involved in the riser dynamics are written in terms of a stationary and a perturbation contribution (superscript $\hat{}$):

$$j_g = \tilde{j}_g(s) + \hat{j}_g(s, t) \quad (46)$$

$$j_l = \tilde{j}_l(s) + \hat{j}_l(s, t) \quad (47)$$

$$P = \tilde{P}(s) + \hat{P}(s, t) \quad (48)$$

After some algebra, the differential equations for the perturbations can be written as:

$$\tilde{A} \{\hat{v}\} + \tilde{B} \left\{ \frac{\partial \hat{v}}{\partial t} \right\} + \tilde{C} \left\{ \frac{\partial \hat{v}}{\partial s} \right\} = 0 \quad (49)$$

where:

$$\{\hat{v}\} = \left\{ \begin{array}{c} \hat{j}_g \\ \hat{j}_l \\ \hat{P} \end{array} \right\} \quad (50)$$

$$\tilde{A}_{ij} = \left(\frac{\partial A_i}{\partial v_j} + \sum_k \frac{\partial C_{ik}}{\partial v_j} \frac{\partial v_k}{\partial s} \right) \sim \quad (51)$$

$$\underline{A} = \begin{Bmatrix} 0 & 0 & 0 \\ A_{21} & 0 & A_{23} \\ A_{31} & A_{32} & A_{33} \end{Bmatrix} \quad (52)$$

$$A_{21} = \frac{\partial \tilde{P}}{\partial s} \quad (53)$$

$$A_{23} = \frac{\partial \tilde{j}_g}{\partial s} \quad (54)$$

$$A_{31} = -\frac{1}{\tilde{\rho}_m} \frac{\partial \tilde{\rho}_m}{\partial \tilde{j}_g} \frac{\partial \tilde{P}}{\partial s} + \frac{2}{D} \tilde{\rho}_m \frac{\partial}{\partial \tilde{j}_g} (\tilde{f}_m \tilde{j}^2) \quad (55)$$

$$A_{32} = -\frac{1}{\tilde{\rho}_m} \frac{\partial \tilde{\rho}_m}{\partial \tilde{j}_l} \frac{\partial \tilde{P}}{\partial s} + \frac{2}{D} \tilde{\rho}_m \frac{\partial}{\partial \tilde{j}_l} (\tilde{f}_m \tilde{j}^2) \quad (56)$$

$$A_{33} = -\frac{1}{\tilde{\rho}_m} \frac{\partial \tilde{\rho}_m}{\partial \tilde{P}} \frac{\partial \tilde{P}}{\partial s} + \frac{2}{D} \tilde{\rho}_m \tilde{j}^2 \frac{\partial \tilde{f}_m}{\partial \tilde{P}} \quad (57)$$

$$\tilde{B}_{ij} = (B_{ij}) \sim \quad (58)$$

$$\tilde{C}_{ij} = (C_{ij}) \sim \quad (59)$$

The superscript \sim indicates an evaluation at the stationary condition.

5. DISCRETIZED PERTURBATION EQUATIONS AND STABILITY ANALYSIS

5.1 Discretized perturbation equations

The riser length is discretized in N nodes and Eq. (49) is integrated in the interval $s_i \leq s \leq s_{i+1}$. Representative values for any function ϕ within the integration interval are calculated as:

$$\phi(\tilde{v}) = \phi_{i+1/2} \simeq \frac{1}{2} [\phi(\tilde{v}_i) + \phi(\tilde{v}_{i+1})] \quad (60)$$

Representative values of the perturbed variables, as well as space and time derivatives are calculated as:

$$\hat{v}_{i+1/2} \simeq \frac{1}{2} (\hat{v}_i + \hat{v}_{i+1}) \quad (61)$$

$$\left(\frac{\partial \hat{v}}{\partial s} \right) = \left(\frac{\partial \hat{v}}{\partial s} \right)_{i+1/2} \simeq \frac{\hat{v}_{i+1} - \hat{v}_i}{\Delta s_i} \quad (62)$$

$$\left(\frac{\partial \hat{v}}{\partial t} \right) = \left(\frac{\partial \hat{v}}{\partial t} \right)_{i+1/2} \simeq \frac{1}{2} \left(\frac{d\hat{v}_i}{dt} + \frac{d\hat{v}_{i+1}}{dt} \right) \quad (63)$$

where $\Delta s_i = s_{i+1} - s_i$. The following set of equations is obtained:

$$\underline{G} \left\{ \frac{d\hat{v}}{dt} \right\} + \underline{H} \{\hat{v}\} = 0 \quad (64)$$

$$\underline{G} = \begin{bmatrix} G_{11} & G_{12} & G_{13} \\ 0 & 0 & G_{23} \\ 0 & 0 & 0 \end{bmatrix} \quad (65)$$

$$\underline{H} = \begin{bmatrix} 0 & H_{12} & 0 \\ H_{21} & H_{22} & H_{23} \\ H_{31} & H_{32} & H_{33} \end{bmatrix} \quad (66)$$

In Eq. (64), \underline{G} and \underline{H} are rectangular sparse matrices with dimension $3N - 3 \times 3N$, while \hat{v} is the vector of nodal values of the perturbed variables ($3N$ components), defined as:

$$\{\hat{v}\}_j = \begin{cases} \hat{j}_{gj} & \text{for } 1 \leq j \leq N \\ \hat{j}_{lj-N} & \text{for } N+1 \leq j \leq 2N \\ \hat{P}_{j-2N} & \text{for } 2N+1 \leq j \leq 3N \end{cases} \quad (67)$$

The sub-matrices defined in Eq. (65) and (66) are rectangular sparse matrices with dimension $(N-1) \times N$, with the following non-zero elements:

$$\{G_{11}\}_{i,i} = \{G_{11}\}_{i,i+1} = \frac{1}{2} \{B_{11}\}_{i+1/2} \quad (68)$$

$$\{G_{12}\}_{i,i} = \{G_{12}\}_{i,i+1} = \frac{1}{2} \{B_{12}\}_{i+1/2} \quad (69)$$

$$\{G_{13}\}_{i,i} = \{G_{13}\}_{i,i+1} = \frac{1}{2} \{B_{13}\}_{i+1/2} \quad (70)$$

$$\{G_{23}\}_{i,i} = \{G_{23}\}_{i,i+1} = \frac{1}{2} \{B_{23}\}_{i+1/2} \quad (71)$$

$$\{H_{12}\}_{i,i} = -\{H_{12}\}_{i,i+1} = -\frac{\{C_{12}\}_{i+1/2}}{\Delta s_i} \quad (72)$$

$$\{H_{21}\}_{i,i} = \frac{1}{2} \{A_{21}\}_{i+1/2} - \frac{\{C_{21}\}_{i+1/2}}{\Delta s_i} \quad (73)$$

$$\{H_{21}\}_{i,i+1} = \frac{1}{2} \{A_{21}\}_{i+1/2} + \frac{\{C_{21}\}_{i+1/2}}{\Delta s_i} \quad (74)$$

$$\{H_{22}\}_{i,i} = -\{H_{22}\}_{i,i+1} = \frac{\{C_{22}\}_{i+1/2}}{\Delta s_i} \quad (75)$$

$$\{H_{23}\}_{i,i} = \frac{1}{2} \{A_{23}\}_{i+1/2} - \frac{\{C_{23}\}_{i+1/2}}{\Delta s_i} \quad (76)$$

$$\{H_{23}\}_{i,i+1} = \frac{1}{2} \{A_{23}\}_{i+1/2} + \frac{\{C_{23}\}_{i+1/2}}{\Delta s_i} \quad (77)$$

$$\{H_{31}\}_{i,i} = \{H_{31}\}_{i,i+1} = \frac{1}{2} \{A_{31}\}_{i+1/2} \quad (78)$$

$$\{H_{32}\}_{i,i} = \{H_{32}\}_{i,i+1} = \frac{1}{2} \{A_{32}\}_{i+1/2} \quad (79)$$

$$\{H_{33}\}_{i,i} = \frac{1}{2} \{A_{33}\}_{i+1/2} - \frac{\{C_{33}\}_{i+1/2}}{\Delta s_i} \quad (80)$$

$$\{H_{33}\}_{i,i+1} = \frac{1}{2} \{A_{33}\}_{i+1/2} + \frac{\{C_{33}\}_{i+1/2}}{\Delta s_i} \quad (81)$$

To close the system of equations, it is necessary to load three additional lines, corresponding to the boundary conditions. Considering Section 2.3 and Eq. (28) and (29) it results:

$$\hat{j}_{l1} = 0 \quad (82)$$

$$\frac{d\hat{P}_1}{dt} + C_{g1}\hat{j}_{g1} + C_{p1}\hat{P}_1 = 0 \quad (83)$$

where:

$$C_{g1} = \frac{\tilde{P}_1}{L\alpha_p + L_e} \quad (84)$$

$$C_{p1} = \frac{j_{g0}}{L\alpha_p + L_e} \frac{T_g}{T_0} \frac{P_0}{\tilde{P}_1} \quad (85)$$

Considering a constant pressure separator at top of the riser and from Eq. (18), it gives:

$$\hat{P}_N = 0 \quad (86)$$

It results:

$$\underline{G}^* \left\{ \frac{d\hat{v}}{dt} \right\} + \underline{H}^* \{\hat{v}\} = 0 \quad (87)$$

where the square matrices \underline{G}^* and \underline{H}^* (dimension $3N \times 3N$) are defined as the matrices \underline{G} and \underline{H} augmented with the boundary conditions.

5.2 Stability Analysis

Considering Eq. (87), the following transformation can be written:

$$\{\hat{v}\} = \{\hat{r}\} \exp(\lambda t) \quad (88)$$

where λ is an eigenvalue and $\{\hat{r}\}$ is an eigenvector. From Eq. (87) and (88):

$$(\lambda \underline{G}^* + \underline{H}^*) \{\hat{r}\} = 0 \quad (89)$$

The transformation from Eq. (88) reduced Eq. (87) to a generalized eigenvalue/vector problem. Equation (89) has no trivial solution only when λ satisfies the characteristic polynomial:

$$\det(\lambda \underline{G}^* + \underline{H}^*) = 0 \quad (90)$$

The stability of the stationary state can be decided according to the solution of characteristic polynomial.

5.3 Numerical implementation

For a set of flow, geometry and simulation parameters, the system of equations corresponding to the stationary state were solved and the matrices \underline{G}^* and \underline{H}^* were assembled.

The numerical procedure was implemented using the software MATLAB (Magrab *et al.*, 2005). The subroutine EIGS, which is the ARPACK implementation for Matlab, was used. ARPACK (Lehoucq *et al.*, 1997) is a set of routines, initially developed to solve large scale eigenvalue problems; it is based on an variation of the Arnoldi process called the Implicitly Restarted

Arnoldi/Lanczos Method (IRAM). ARPACK routines are capable of solving large scale symmetric, nonsymmetric, and generalized eigen-problems. They were designed to compute a subset of eigenvalues with user specified features such as those of largest real part or largest magnitude. For every request, a set of numerically accurate eigenvalues and eigenvectors is available.

In Burr *et al.* (2013) a fixed grid was considered in the plane of superficial velocities, determining the stability for each grid point. In the present work, a routine was implemented to track the stability curve, starting from a point located in the upper branch (low gas superficial velocity and high liquid superficial velocity) and using the bisection method to determine, with the required precision, the neutral stability condition.

6. VOID FRACTION CORRELATIONS

6.1 Bendiksen (1984)

Bendiksen (1984) made experiments in straight tubes with inclination angles between -30° and 90° using air and water in order to measure the velocity of long bubbles. The resulting drift flux correlation is:

$$C_d = \begin{cases} 1.05 + 0.15 \sin \theta & \text{for } Fr_j < 3.5 \\ 1.2 & \text{for } Fr_j \geq 3.5 \end{cases} \quad (91)$$

$$U_d = \begin{cases} \sqrt{gD} (0.35 \sin \theta + 0.54 \cos \theta) & \text{for } Fr_j < 3.5 \\ 0.35 \sqrt{gD} \sin \theta & \text{for } Fr_j \geq 3.5 \end{cases} \quad (92)$$

where the Froude number Fr_j is defined as:

$$Fr_j = \frac{j}{\sqrt{gD}} \quad (93)$$

Bendiksen's correlation was used in previous contributions (Baliño *et al.*, 2010; Azevedo *et al.*, 2015) because of its simplicity (void fraction is explicit and drift parameters are independent of state variables). The main disadvantage is that the database used is only for low pressure air-water flow and for a restricted flow pattern.

6.2 Chexal *et al.* (1997)

Chexal-Lellouche's correlation (Chexal *et al.*, 1997) covers a full range of conditions and flow orientations, as well as different fluid types (steam-water, air-water and refrigerants), making it suitable for high-pressure systems like the ones in nuclear systems and possibly in petroleum systems; for this reason, it was implemented in codes for large system thermal-hydraulic analysis. The drift parameters satisfy continuity and have finite first derivatives and restrict the resulting void fraction to be in the range from zero to one. Moreover, the drift parameters satisfy limiting conditions for critical and zero pressure, as well as for zero and unity void fraction. Void fraction has to be determined iteratively, as the drift parameters are dependent on the state variables. The resulting drift flux correlation is, for co-current upward air-water flows:

$$C_d = \frac{L}{K_0 + (1 - K_0) \alpha^r} \quad (94)$$

where:

$$L = F_r L_v + (1 - F_r) L_h \quad (95)$$

$$F_r = \left(\frac{\theta}{90^\circ} \right)^{0.2} \quad (96)$$

$$L_v = \min(1.15\alpha^{0.45}, 1) \quad (97)$$

$$L_h = \min(1.125\alpha^{0.6}, 1) \left[1 + \alpha^{0.05} (1 - \alpha)^2 \right] \quad (98)$$

$$K_0 = B_1 + (1 - B_1) \left(\frac{\rho_g}{\rho_l} \right)^{0.25} \quad (99)$$

$$r = \frac{1 + 1.57 \left(\frac{\rho_g}{\rho_l} \right)}{1 - B_1} \quad (100)$$

$$B_1 = F_r B_{1v} + (1 - F_r) B_{1h} \quad (101)$$

$$B_{1(v,h)} = \min(0.8, A_{1(v,h)}) \quad (102)$$

$$A_{1(v,h)} = \frac{1}{1 + \exp(-Re_{v,h}/60000)} \quad (103)$$

$$Re_v = \begin{cases} Re_g & \text{for } Re_g > Re_l \\ Re_l & \text{for } Re_g < Re_l \end{cases} \quad (104)$$

$$Re_h = \begin{cases} |Re_g| & \text{for } |Re_g| > |Re_l| \\ |Re_l| & \text{for } |Re_g| < |Re_l| \end{cases} \quad (105)$$

$$U_d = 1.41 \left[\frac{(\rho_l - \rho_g) \sigma g}{\rho_l^2} \right]^{0.25} C_1 C_2 C_3 C_4 \quad (106)$$

where σ is the surface tension and:

$$C_1 = (1 - \alpha)^{B_1} \quad (107)$$

$$\text{For } (\rho_l/\rho_g) \leq 18 : C_2 = 0.4757 \left[\ln \left(\frac{\rho_l}{\rho_g} \right) \right]^{0.7} \quad (108)$$

$$\text{For } (\rho_f/\rho_g) > 18 : \begin{cases} \text{if } C_5 \geq 1, & C_2 = 1 \\ \text{if } C_5 < 1, & C_2 = 1 - \exp \left(\frac{-C_5}{1 - C_5} \right) \end{cases} \quad (109)$$

$$C_5 = \sqrt{\frac{150}{(\rho_l/\rho_g)}} \quad (110)$$

$$C_3 = F_r C_{3v} + (1 - F_r) C_{3h} \quad (111)$$

$$C_{3v} = \max[0.5, 2 \exp(-Re_l/300000)] \quad (112)$$

$$C_{3h} = \max(0.125, 0.5 \exp(-Re_l/300000)) \quad (113)$$

$$C_4 = \begin{cases} 1 & \text{for } C_7 \geq 1 \\ \frac{1}{1 - \exp \left(\frac{C_7}{1 - C_7} \right)} & \text{for } C_7 < 1 \end{cases} \quad (114)$$

$$C_7 = \left(\frac{0.09144 m}{D} \right)^{0.6} \quad (115)$$

6.3 Bhagwat and Ghajar (2014)

Bhagwat and Ghajar (2014) recently presented new equations for the drift parameters applicable to gas-liquid flows in a wide range of fluid combinations, thermodynamic states and pipe diameters, correlating 8255 data points from 60 different sources. For low pressures and air-water flows, this correlation is applicable to different flow patterns and gives similar results as Bendiksen's correlation. The correlation is also implicit in void fraction.

$$C_d = \frac{2 - (\rho_g/\rho_l)^2}{1 + (Re_{tp}/1000)^2} + \frac{\left[\frac{1 + (\rho_g/\rho_l)^2 \cos \theta}{1 + \cos \theta} \right]^{\frac{1}{5}(1-\alpha)}}{1 + (1000/Re_{tp})^2} + C_{d,1} \quad (116)$$

where:

$$C_{d,1} = 0.2 \left(1 - \sqrt{\frac{\rho_g}{\rho_l}} \right) \left[(2.6 - \beta)^{0.15} - \sqrt{f_{tp}} \right] (1 - x)^{1.5} \quad (117)$$

$$\frac{1}{\sqrt{f_{tp}}} = -4 \log_{10} \left(\frac{\epsilon/D_h}{3.7} + \frac{1.256}{Re_{tp} \sqrt{f_{tp}}} \right) \quad (118)$$

$$Re_{tp} = \frac{\rho_l j D}{\mu_l} \quad (119)$$

$$x = \frac{\rho_g j_g}{\rho_g j_g + \rho_l j_l} \quad (120)$$

$$\beta = \frac{j_g}{j_g + j_l} \quad (121)$$

$$U_d = (0.35 \sin \theta + 0.45 \cos \theta) \times \sqrt{\frac{g D (\rho_l - \rho_g)}{\rho_l}} (1 - \alpha)^{0.5} C_2 C_3 C_4 \quad (122)$$

where:

$$C_2 = \begin{cases} \left(\frac{0.434}{\log_{10} \mu_l^*} \right)^{0.15} & \text{for } \mu_l^* > 10 \\ 1 & \text{for } \mu_l^* \leq 10 \end{cases} \quad (123)$$

$$\mu_l^* = \mu_l / (0.001 Pa s) \quad (124)$$

$$C_3 = \begin{cases} (La/0.025)^{0.9} & \text{for } La < 0.025 \\ 1 & \text{for } La \geq 0.025 \end{cases} \quad (125)$$

$$C_4 = \begin{cases} -1 & \text{for } (-50^\circ \leq \theta < 0^\circ \text{ and } Fr_{sg} \leq 0.1) \\ 1 & \text{otherwise} \end{cases} \quad (126)$$

where Fr_{sg} and La are respectively the Froude and Laplace numbers, defined as:

$$Fr_{sg} = \sqrt{\frac{\rho_g}{\rho_l - \rho_g}} \frac{j_g}{\sqrt{g D} \cos \theta} \quad (127)$$

$$La = \frac{\sqrt{\frac{\sigma}{g(\rho_l - \rho_g)}}}{D} \quad (128)$$

7. RESULTS

Comparative results are shown for the stability maps and the stationary distributions of the state variables for the system conditions from Taitel *et al.* (1990) (see Table 1), corresponding to a vertical riser connected to a separator.

Table 1: Parameters for vertical riser (Taitel *et al.*, 1990).

Definition	Parameter	Value	Unit
Liquid viscosity	μ_l	1×10^{-3}	$kg/(m \cdot s)$
Gas viscosity	μ_g	1.8×10^{-5}	$kg/(m \cdot s)$
Liquid density	ρ_l	1000	kg/m^3
Gas constant	R_g	287	$m^2/(s^2 \cdot K)$
Temperature	T_g	293	K
Pipeline length	L	9.1	m
Buffer length	L_e	1.69, 5.1, 10	m
Pipeline diameter	D	2.54×10^{-2}	m
Pipeline-riser roughness	ϵ	1.5×10^{-6}	m
Pipeline inclination	β	5	degree
Riser height	Z	3	m
Separator pressure	P_s	1.03×10^5	Pa

In Azevedo *et al.* (2015) discretization and eigenvalues well-posedness studies were made, resulting that $N = 50$ is a satisfactory nodalization.

Figure 3 shows the stability map for a buffer length $L_e = 1.69 m$ calculated with the linear stability theory, for the different void fraction correlations. It can be observed that the three correlations predict similar stability maps. The differences for the near horizontal branch with low gas superficial velocities are small, because the predicted void fractions are very small for this flow range. For the nearly vertical branch with low liquid superficial velocities, there are slight differences in the predicted stability boundaries.

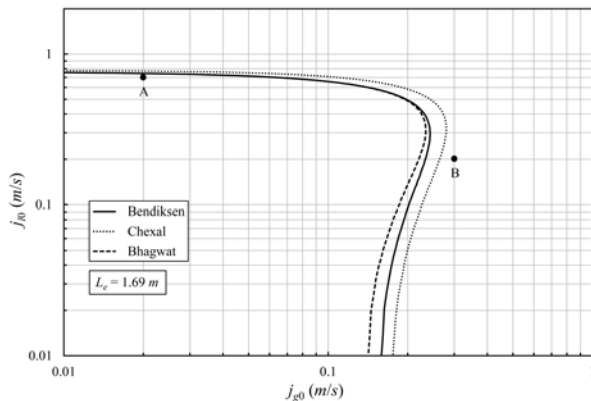


Figure 3: Stability maps for $L_e = 1.69 m$.

To elucidate the behavior of the different correlations, two operating points were chosen in Fig. 3: point A, corresponding to $j_{g0} = 0.02 m/s$, $j_{l0} = 0.7 m/s$, is located closed to the low gas superficial velocity branch, while point B, corresponding to $j_{g0} = 0.3 m/s$, $j_{l0} = 0.2 m/s$, is located closed to the high gas superficial velocity branch. Notice that point A is located within the unstable region for any void fraction correlation, so the model predicts that there is no steady state for this configuration; on the other hand, point B is in the stable region.

Figures 4, 5 and 6 show respectively the stationary state profiles in the riser for void fraction, gas superficial velocity and pressure for point A. It can be observed that the void fractions are very low and that Bendiksen's and Bhagwat's correlations give very similar results, while Chexal's correlation gives little higher values. According to the stationary conditions (Eqs. (22) and (23)) as the void fraction is higher, pressure is lower and gas superficial velocity is higher.

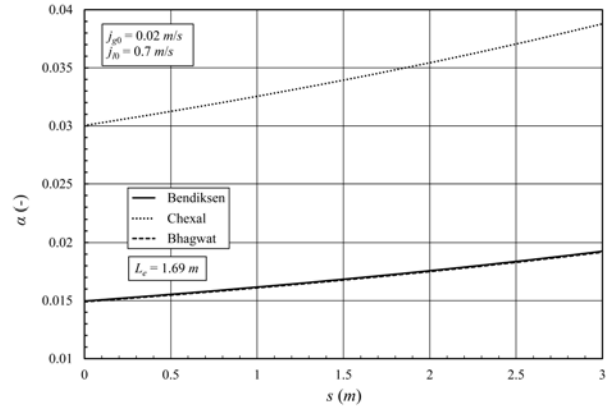


Figure 4: Void fraction profile for $L_e = 1.69 m$ (point A).

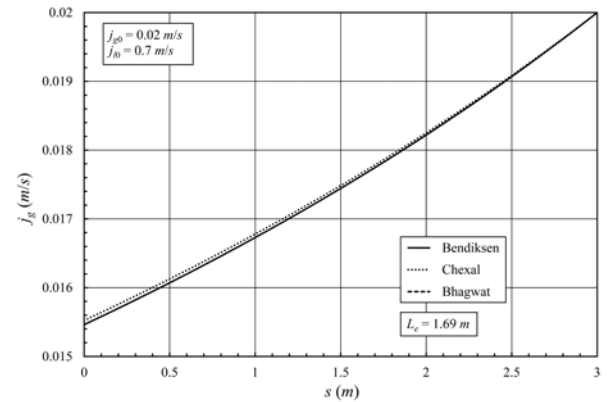


Figure 5: Gas superficial velocity profile for $L_e = 1.69 m$ (point A).

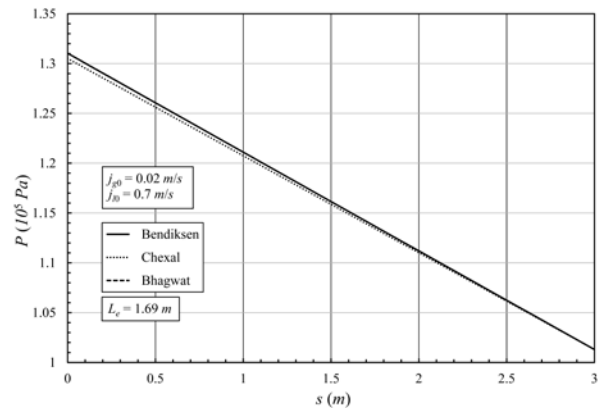


Figure 6: Pressure profile for $L_e = 1.69 m$ (point A).

Figures 7, 8 and 9 show respectively the stationary

state profiles in the riser for point B. Void fractions are higher; the highest values are predicted by Bhagwat's correlation, followed by Chexal's and Bendiksen's correlations.

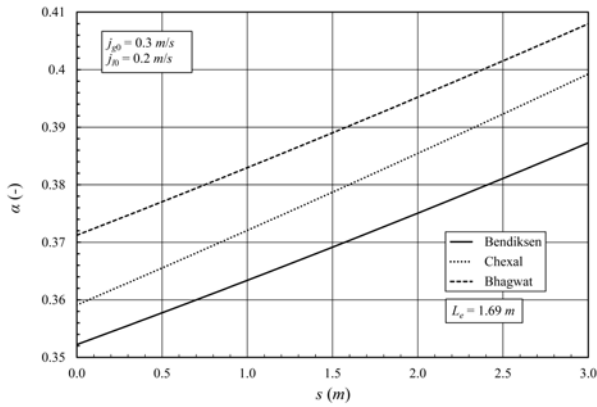


Figure 7: Void fraction profile for $L_e = 1.69 m$ (point B).

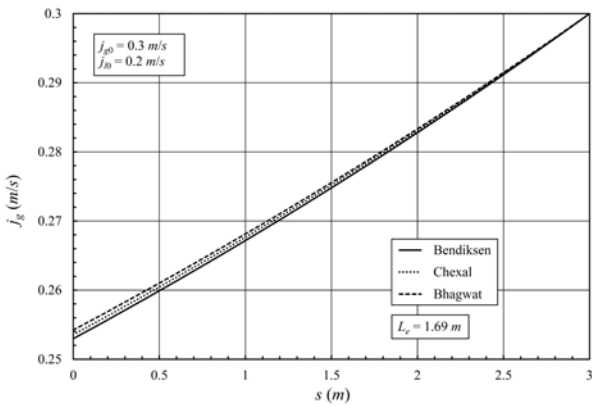


Figure 8: Gas superficial velocity profile for $L_e = 1.69 m$ (point B).

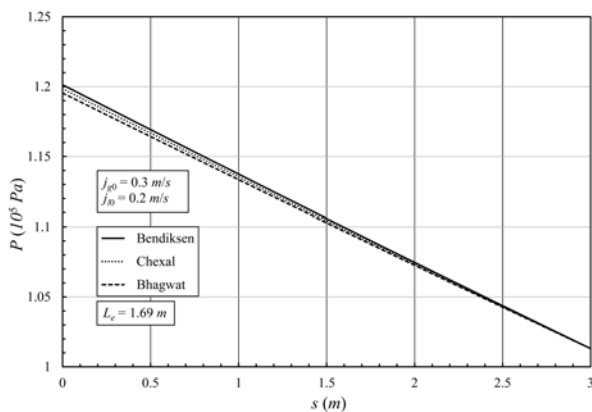


Figure 9: Pressure profile for $L_e = 1.69 m$ (point B).

Finally, Fig. 10 shows the stability map for a buffer length $L_e = 5.1 m$ calculated with the linear stability theory, for the different void fraction correlations. It can be observed that the three correlations predict similar stability maps and also an increase in the unstable region for

higher buffer lengths, which is in agreement with the experimental trends.

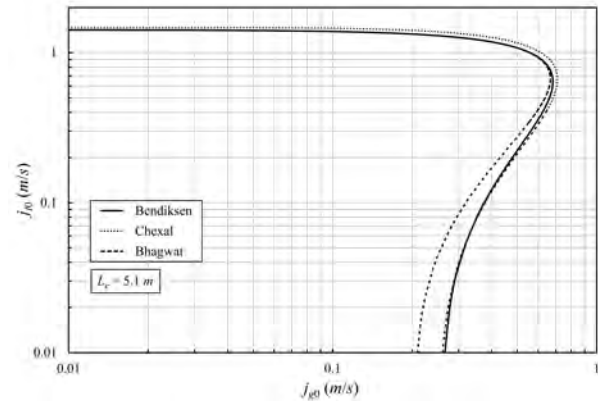


Figure 10: Stability maps for $L_e = 5.1 m$.

8. CONCLUSIONS

The stability analysis using the linear stability theory was proven to be a very efficient tool to predict the influence of different operating conditions on the occurrence of severe slugging. In particular, three different void fraction correlations were implemented and their influence was assessed. It was found that there is a very small influence on the near horizontal branch of the stability boundary and a slight influence in the near vertical branch. Moreover, the different correlations exhibit the right trend, increasing the unstable region as the buffer equivalent length is increased. Although the correlations give slightly different values of void fraction, the calculations show that the methodology is robust when different correlations are considered.

It would be desirable to extend this methodology for more complex geometries like the ones in hilly terrain flows. For doing this, it is necessary to count with reliable void fraction correlations valid for different pipe inclinations, flow directions and fluid conditions.

As severe slugging is an important issue in the design of offshore petroleum systems, the necessity of including a stability analysis derived from the dynamic models in computer simulation codes is evident; for the case of stationary simulation codes the necessity is even more important, as the dynamic simulation is not available and the stationary solution may not physically exist. If the objective is only deciding about the system stability, the stability module would be an useful tool in dynamic simulation codes as well, as computational cost is much less compared to simulations in the time domain.

ACKNOWLEDGEMENTS

This work was supported by Petr leo Brasileiro S. A. (Petrobras). The authors wish to thank *Conselho Nacional de Desenvolvimento Cient fico e Tecnol gico* (CNPq, Brazil) and *Ag ncia Nacional de Petr leo*, (ANP, Brazil).

REFERENCES

- Azevedo, G.R., Baliño, J.L. and Burr, K.P., 2015. "Linear stability analysis for severe slugging in air-water systems considering different mitigation mechanisms". *International Journal of Multiphase Flow*, Vol. 73, pp. 238–250.
- Baliño, J.L., 2012. "Modeling and simulation of severe slugging in air-water systems including inertial effects". In *The 6th. International Conference on Integrated Modeling and Analysis in Applied Control and Automation (IMAACA 2012)*. Wien, Austria, p. 10.
- Baliño, J.L., 2014. "Modeling and simulation of severe slugging in air-water systems including inertial effects". *Journal of Computational Science*, Vol. 5, pp. 482–495.
- Baliño, J.L., Burr, K.P. and Nemoto, R.H., 2010. "Modeling and simulation of severe slugging in air-water pipeline-riser systems". *International Journal of Multiphase Flow*, Vol. 36, pp. 643–660.
- Bendiksen, K.H., 1984. "An experimental investigation of the motion of long bubbles in inclined tubes". *International Journal of Multiphase Flow*, Vol. 10, No. 4, pp. 467–483.
- Bhagwat, S.M. and Ghajar, A.J., 2014. "A flow pattern independent drift flux model based void fraction correlation for a wide range of gas-liquid two phase flow". *International Journal of Multiphase Flow*, Vol. 59, pp. 186–205.
- Bøe, A., 1981. *Severe slugging characteristics. Part I: Flow regime for severe slugging. Part II: Point model simulation study*. Trondheim, Norway.
- Burr, K.P., Baliño, J.L. and Azevedo, G.R., 2013. "Discretization effects on the linear numerical stability analysis of two-phase flows in pipeline-riser systems". In *Proceedings do XXII International Congress of Mechanical Engineering (COBEM 2013)*. Ribeirão Preto, SP, Brazil, p. 12.
- Chen, N.H., 1979. "An explicit equation for friction factor in pipe". *Ind. Engng. Chem. Fundam.*, Vol. 18, pp. 296–297.
- Chexal, B., Merilo, M., Maulbetsch, J., Horowitz, J., Harrison, J., Westacott, J., Peterson, C., Kastner, W. and Schmidt, H., 1997. *Void Fraction Technology for Design and Analysis*. EPRI, Palo Alto, California, USA.
- Jansen, F.E., Shohan, O. and Taitel, Y., 1996. "The elimination of severe slugging - experiments and modeling". *International Journal of Multiphase Flow*, Vol. 22, No. 6, pp. 1055–1072.
- Lehoucq, R.B., Sorensen, D.C. and Yang, C., 1997. *ARPACK User's Guide: Solution of Large Scale Eigenvalue Problems with Implicit Restarted Arnoldi Methods*. <http://www.caam.rice.edu/software/ARPACK/>.
- Magrab, E.B., Azarm, S., Belachandran, B., Duncan, J.H., Herold, K.H. and Walsh, G.C., 2005. *An Engineer's Guide to MATLAB*. Pearson Prentice Hall.
- Masella, J.M., Tran, Q.H., Ferre, D. and Pauchon, C., 1998. "Transient simulation of two-phase flows in pipes". *International Journal of Multiphase Flow*, Vol. 24, pp. 739–755.
- Pots, B.F.M., Bromilow, I.G. and Konijn, M.J.W.F., 1987. "Severe slug flow in offshore flowline riser systems". *SPE Production Engineering*, pp. 319–324.
- Sarica, C. and Shoham, O., 1991. "A simplified transient model for pipeline-riser systems". *Chemical Engineering Science*, Vol. 46, No. 9, pp. 2167–2179.
- Taitel, Y., 1986. "Stability of severe slugging". *International Journal of Multiphase Flow*, Vol. 12, No. 2, pp. 203–217.
- Taitel, Y. and Dukler, A.E., 1976. "A model for predicting flow regime transitions in horizontal and near horizontal gas-liquid flow". *AIChE Journal*, Vol. 22, No. 1, pp. 47–55.
- Taitel, Y., Vierkand, S., Shoham, O. and Brill, J.P., 1990. "Severe slugging in a riser system: experiments and modeling". *International Journal of Multiphase Flow*, Vol. 16, No. 1, pp. 57–68.
- Wallis, G.B., 1969. *One-dimensional Two-phase Flow*. McGraw-Hill Book Company, New York.
- Zakarian, E., 2000. "Analysis of two-phase flow instabilities in pipe-riser systems". In *2000 ASME Pressure Vessel and Piping Conference*. ASME, Seattle, Washington, USA, pp. 1–9.
- Zuber, N. and Findlay, J., 1965. "Average volumetric concentration in two-phase flow system". *Journal of Heat Transfer*, Vol. 87, p. 453.

AUTHOR BIOGRAPHIES

Gabriel Romualdo de Azevedo was born in Joinville, Brazil, in 1986. He graduated in Mechanical Engineering from Polytechnic School, University of São Paulo (2010). He worked for JKK Consulting (2011-2013) in São Paulo, Brazil. Since 2013, he is a PhD student at University of São Paulo. His research interests are fluid dynamics, multiphase flow and hydrodynamic instabilities.

Jorge Luis Baliño was born in Buenos Aires, Argentina in 1959. He graduated in Nuclear Engineering (1983) and made PhD in Nuclear Engineering (1991) from *Instituto Balseiro*, Argentina. He worked for Techint S.A. (1983-1984), *Centro Atómico Bariloche* and *Instituto Balseiro* (1985-2000) in Argentina, *Instituto de Pesquisas Energéticas e Nucleares* (2001-2003) in São Paulo, Brazil. Since 2004 he is Professor at *Universidade de São Paulo*. His research interests are fluid dynamics, heat transfer and multiphase flow.

Karl Peter Burr was born in São Paulo, Brasil in 1964. Received his Bachelor of Science (1988) and his Master of Science (1993) in Ocean Engineering from University of São Paulo, and his PhD (2001) in Ocean engineering from Massachusetts Institute of Technology. He was a post-doctoral fellow at the MIT Ocean Engineering department (2001-2003) and at the Mechanical Engineering Department of *Escola Politécnica* at University of São Paulo (2004-2007). Since 2008 he is Professor at Federal University of ABC. His research interest are hydrodynamic stability, water waves, aerodynamics and multiphase flows.

Experimentally Validated Bond Graph Model of a Brazed-Plate Heat Exchanger (BPHE).

M.Turki, M. Kebdani^(a), G. Dauphin-Tanguy^(a), A. Dazin^(b), P. Dupont^(c)

^(a) Ecole Centrale de Lille/ CRISAL UMR CNRS 9189, CS 20048, 59651 Villeneuve d'Ascq. France.

^(b) Arts et Métiers Paris Tech/ LML UMR CNRS 8107, Boulevard Louis XIV, 59000 Lille. France.

^(c) Ecole Centrale de Lille/LML UMR CNRS 8107, CS 20048, 59651 Villeneuve d'Ascq. France.

^(a) mohamed.kebdani@ec-lille.fr, ^(a) marwa.turki@ec-lille.fr, ^(a) genevieve.dauphin-tanguy@ec-lille.fr,

^(b) antoine.dazin@ensam.eu, ^(c) patrick.dupont@ec-lille.fr.

ABSTRACT

The paper deals with the Bond Graph (BG) modeling and the model validation of a brazed-plate heat exchanger. This device is an important part of a mechanically pumped cooling loop. A thermo hydraulic BG model is developed and compared with experimental data. Optimization is performed to determine the best value of the convection heat exchange coefficients to be fixed in the model.

Keyword: Fluid loop, heat exchanger, bond graph, dynamic, single phase flow.

1. INTRODUCTION

Power components dissipate heat flows which represent a significant source of heat. If it is not processed properly, these results in problems that leads to a complete dysfunction of the component. Several solutions have been proposed to prevent the damage of embedded devices and ensure their proper functioning.

Based on these solutions, the choice of the enterprises has been oriented towards mechanically pumped cooling loops that are undoubtedly the most efficient in terms of heat transfer (Kebdani, Dauphin-Tanguy, Dazin, and Dupont 2015). Indeed, in addition to their architectural flexibility, they guarantee appropriate cooling in suitable operational conditions. It is a very important property especially when we know that the continuous cycling of the temperature has a negative impact on the electronic components' life.

The **figure 1** shows up the considered cooling loop. It is composed of a pump, a pressure regulator, an evaporator, a condenser and pipes.

Various heat exchanger technologies exist; the choice depends on the nature of intended use. For example, for

space activities, one can use a radiator; for land-based activities (automotive, rail...) an air exchanger with air cross-flow may be adequate.

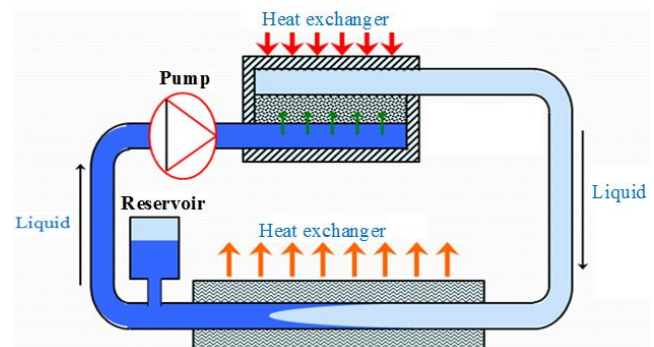


Figure 1: Design of the cooling loop

A single-phase fluid loop is a heat transfer circuit. It is generally a closed loop, wherein a fluid is initially in the liquid state. The fluid is heated to store thermal flux from a heat source, and is then transferred to a heat sink where the hot fluid is cooled and even sub cooled releasing heat to a cold source. Such fluidic loops have high cooling efficiency.

For our purpose, we have chosen to work with the condenser SWEP of reference: "B5Tx6" (*Fig.2*).

The BPHEs have been used for the first time in the 1930s. They were mostly integrated as mono-phasic (liquid-to-liquid) exchangers in the food industry (Sarraf, Launay, and Tadrist 2006) and in the heat pumps (Cremaschi, Barve, and Wu X 2012) thanks to their multiple benefits listed below:

- Optimized effective exchange surface.
- Rational distribution of the flow in the channels.
- Good adaptability.
- High compacity.

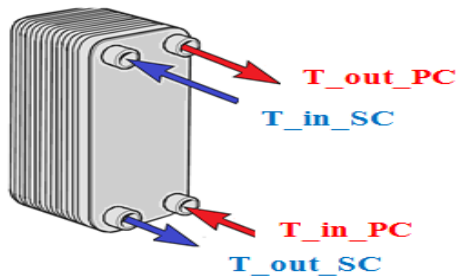


Figure 2: Design of the condenser

Also, the corrugated structure of the thermal plates and chevrons promote turbulent flow (Focke, Zachariades, and Olivier 1985). This leads to high heat transfer efficiency and consequently better performance of the whole installation.

This paper is organized into five sections; the first section is a presentation of our work's overall context and focuses on what has already been done in the BG condenser modeling. The second part deals with the BG model proposed by introducing various assumptions taken into account and the equations put in. The third section is dedicated to the experimental set-up and the various tests performed. The fourth section illustrates an optimization of the heat transfer coefficient. The last part concerns the validation of the proposed model with experimental results

State of the art

The evaluation of such exchanger's performance is not easy as it needs the development of specific experimental methods, especially for prediction of the exchange coefficient and pressure drops. In this context, various authors conducted studies of instrumentation and visualization:

□ Among the works related to this type of heat exchangers, there have been attempts based on the observation of two-phase water-air flows (Vlasogiannis, Karagianni, Argyropoulos, and Bontozoglou 2002, Volker and Kabelac 2010) for a plate heat exchanger formed of a single channel constituted with a transparent plate. Consequently a flow pattern map is performed.

□ More recently (Freund and Kabelac 2010) have developed an experimental technique based on infrared visualization, to characterize the spatial distribution of the convective heat exchange coefficient for a single-phase flow (water).

□ (Rong, Kawaji, and Burgers 1995) declare that it is possible to estimate theoretically the performance of a BPHE operating in single phase with water as refrigerant fluid. The final results of their work show that it would be appropriate to utilize correlations of pressure drop and heat transfer that take into account corrugation chevron angles.

□ Performance of plate heat exchangers under single phase operations are extensively inspected since the 1980s (Cooper, and Usher 1983, Raju and Bansal 1983, Focke, Zachariades, and Olivier 1985, Shah and Focke 1988, Bansal and Muller-Steinhagen 1993).

According to these authors, these theoretical works provide a reliable basis that ensures an efficient sizing of the exchanger.

□ (Ould Bouamama, Thoma, and Cassar 1997) proposes a model, based on BG methodology, of a simple tubular condenser. The mathematical formulation of the problem is clearly described and used to generate a BG intending to predict the dynamic behavior of the condenser operating under two-phase conditions.

In our knowledge, there are no other attempts in the published literature which aim to model BPHEs by referring to the BG approach.

The main purpose of this paper is to propose a validated thermo hydraulic BG model of a chevron type BPHE, operating under single-phase conditions, where the dynamic regime is considered. Simulation results are validated using the test rig developed by the French enterprise Atmosstat.

Moreover, according to the research mentioned above, the correlations of the heat exchange are strongly related to experimental conditions in which they were developed. This means that for our case it would be legitimate to pick up the most suitable correlation and, thereafter, perform an optimization study in order to minimize the difference between experimental results and those provided by the model.

Given the nature of the device which involves several physical domains (thermal, hydraulic, electric ...), the bond graph methodology appeared as an appropriate modeling tool.

2. BOND GRAPH MODEL OF THE CONDENSER

The thermal fluid processes involve two phenomena: convection, describing the heat transfer between the fluid in motion and walls, and heat conduction, representing the thermal power transmitted due to a temperature difference.

Furthermore, the friction effect in the fluid in movement contributes to the heating of the fluid, especially in case of complicated geometries. Then, it would be wise to analyze the thermo hydraulic coupling for a better modeling of the brazed-plate heat exchanger. This is the purpose of the present section.

2.1. Generalized variables used.

- **Hydraulic part:** Pressure P'' and mass flow rate m'' for which the product is not a power. The developed model is a "pseudo bond graph".

- **Thermal part:** for a fluid in motion the entropy balance is not conservative, which justifies the necessity to choose the heat balance instead.

2.2. Coupled Bond Graph of the condenser

The condenser is mainly composed of a (hot) primary circuit (PC) and a (cold) secondary circuit (SC) separated by brazed-plates as shown **Fig.3**.

Assumptions

1. The internal geometry of the brazed-plate condenser is too complicated to be precisely modeled. Thus we simply consider that such exchanger has a simple rectangular section ($e * e$) without any corrugations.

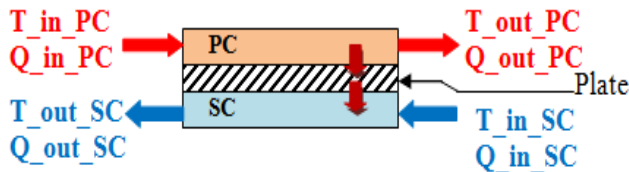


Figure 3: longitudinal cup of the condenser

2. The upstream pressure variation is known and modeled as MS_e: effort source **Fig.4**.
3. The device is not correctly isolated from the ambient, which is modeled as a MS_e.
4. The flow is supposed to be constantly monophasic.
5. Working fluid and secondary fluid are pure water.
6. Each part of the condenser (PC and SC) is modeled as a unique volume where the phenomena are supposed to be homogeneous.

The figure 4 shows up the bond graph model of the condenser.

2.3. RC-elements

The hydraulic power transfer is represented **Fig.4** by blue half arrows, while the thermal part appears in orange half arrows. The coupling element **RC** represents both the pressure losses generated by walls friction (R part) and the thermal energy storage phenomenon in the exchanger (thermal capacitance effect). The equations describing these phenomena are:

Hydraulic part:

For this part, two kinds of pressure losses are taken into account in the dynamic model:

- **Linear pressure drop:**

$$\Delta P_1 = \frac{1}{2} * \rho * v^2 * f * \frac{l}{e} \quad (1)$$

where the Darcy coefficient « f » depends on the flow regime as shown in table.1.

Table 1: Darcy coefficient as a function of the flow regime.

Re < 2100 Laminar regime	$f = \frac{64}{Re}$
2100 < Re < 3000 Transient regime	$f = \frac{0.316}{Re^{0.25}}$
Re > 3000 Turbulent regime	$f = \frac{1}{(1.81 \lg Re - 1.5)^2}$

The Reynolds number $Re = \frac{\rho * v * e}{\mu}$ is a function of the flow

velocity/

$$v = \frac{\dot{m}}{\rho * e * e}$$

- **Singular pressure losses due to two elbows:**

$$\Delta P_2 = 2 * [\frac{1}{2} * \rho * v^2 * \zeta] \quad (2)$$

For an elbow with sharp angle “90°” one can take $\zeta = 1.3$.

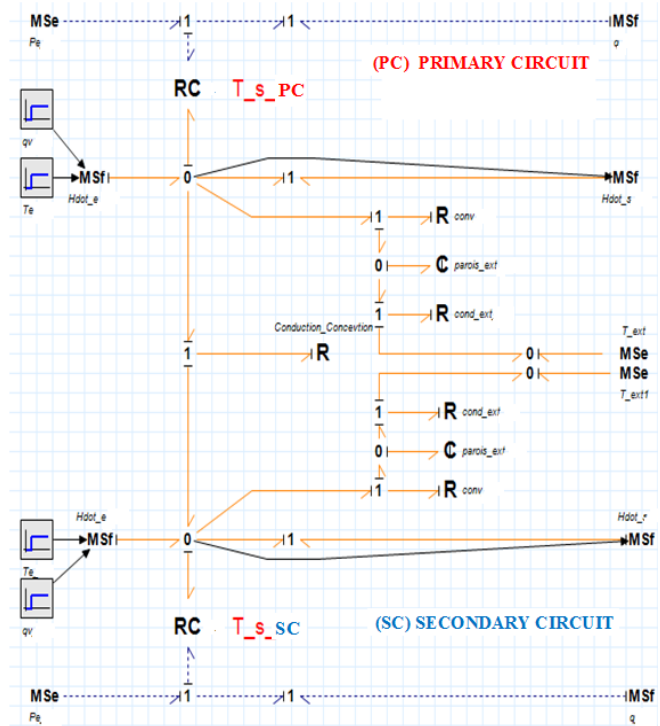


Figure 4: Pseudo Bond Graph model of the condenser.

Thermal part

- The heat flow due to the total pressure losses lead to

$$\dot{Q} = (\Delta P_1 + \Delta P_2) * \frac{\dot{m}}{\rho} \quad (3)$$

- Temperature in each part of the condenser is given by

$$T = \frac{H_{cond}}{m_0 * C_p} \quad (4)$$

with

$$H_{cond} = \int ((\dot{H}_e - \dot{H}_s) + \dot{Q}) dt + H_0 \quad (5)$$

With initial enthalpy: $H_0 = m_0 * C_p * T_0$

And initial mass $m_0 = \rho_{liq} * V_{cond}$

2.4. R- elements

The two elements R: conv deal with the heat exchange by convection between each working fluid and the brazed-plate that separate the two fluids.

The corresponding heat flow is:

$$\dot{Q}_{conv} = h \times S \times \Delta T \quad (6)$$

The two elements R: cond_ext represent the heat transfer by conduction within the wall of the condenser to the ambient.

The corresponding heat flow is:

$$\dot{Q}_{cond} = K_{equiv} \times S \times \Delta T \quad (7)$$

The problem is now to experimentally determine the values of the convection coefficients h_{PC} and h_{SC} .

$$K_{equiv} = \frac{1}{\frac{1}{h_{cond}} + \frac{1}{h_{CP}} + \frac{1}{h_{CS}}} \quad (8)$$

3. Experimental set-up

The set-up presented in Fig.5 has been designed by the French company Atmosat. It is composed of all the devices of the cooling loop.

The test bench was equipped with pressure, temperature, and flow rate sensors. All the experiments have been realized in single-phase state of the fluids.

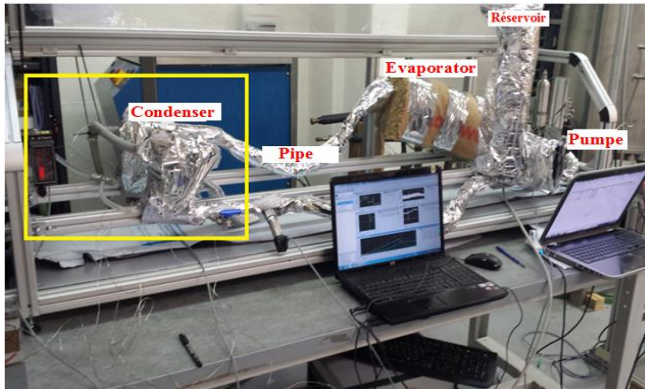


Figure 5: Design of the real loop

3.1. Hydraulic analysis

In view of validating the thermo-hydraulic model of the condenser, we consider here the following monophasic test:

$$\text{at: } t = 0s; \quad Q_{vCP} = 5.09 \text{ cm}^3/\text{s}.$$

$$\text{at: } t = 640s; \quad Q_{vCS} = 7.44 \text{ cm}^3/\text{s}.$$

Analysis of the Figure 6:

Simulation results are compared with experimental results for downstream liquid pressure in Fig.6 (1). These results show good agreement between the model and the real hydraulic behavior, with a discrepancy of

$$\frac{\Delta P_{exp} - \Delta P_{mod}}{\Delta P_{exp}} = 3\% \quad \text{Fig.6 (2)}. \text{ The minor discrepancies}$$

between the results could be explained by the approximate modeling of the real condenser geometry.

3.2. Thermal analysis

Effect of the total pressure losses:

It appears that for the actual monophasic test, the total pressure losses (about **900 Pa**) calculated by the model ($\Delta P_1 + \Delta P_2$) are leading to low heating \dot{Q} (about **0.0045W**) that could be totally ignored.

In fact, it can be argued that as long as the flow is purely monophasic, the heating \dot{Q} due to the friction may be omitted as shown in Fig.7 where wall temperatures are exactly the same with and without thermo hydraulic coupling in PC, Fig.7 (a) and in SC, Fig.7 (b).

However, a biphasic study of the condenser will need to take into account the thermal-hydraulic coupling.

Comparison between fluid and wall temperature:

At the steady-state the difference between the core working fluid temperature (model), Fig.8 (a) green curve, and wall temperature (model), Fig.8 (a) red curve, is about **1°C** while the difference between the secondary fluid (model), Fig.8 (b) green curve, and the wall temperature (model), Fig.8 (b) blue curve, is about **1.3°C**.

The temperature sensors on the set-up are fixed on the tube wall, which makes it impossible to have any information on the temperature inside the fluid. Thus in the following, the comparison between model and experiment results deal with the wall temperatures

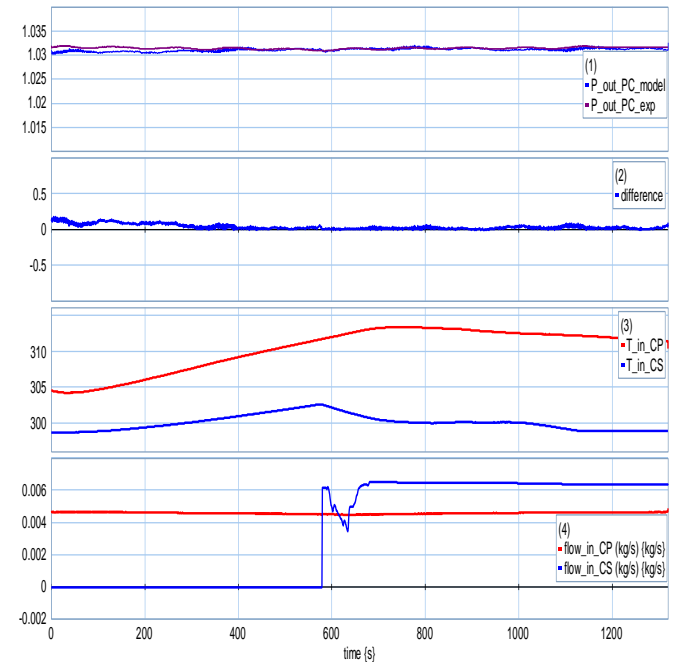


Figure 6: (a) Time evolution of the outlet pressure of the condenser.

(b) Discrepancy between experimental pressure drop and modeled one.

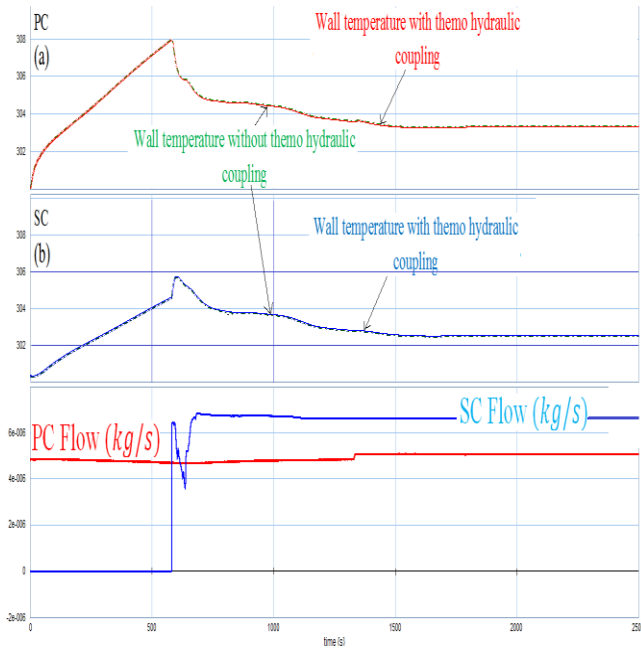


Figure 7: Temperatures; in the PC (Graph a), in the SC (Graph b), time evolution of input flow in PC and SC (Graph c).

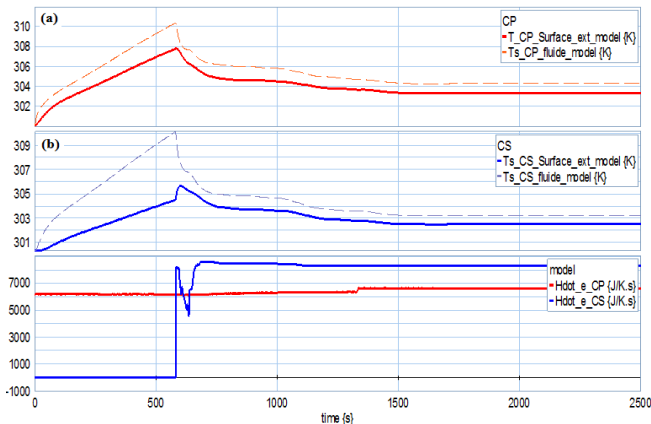


Figure 8: Time evolution of fluid temperature in PC (a), in SC (b), and flow evolution in both PC and SC.

4. Identification and optimization of the convective conductance

The accurate determination of the heat transfer coefficient “h” inside the condenser is very difficult because of the complexity of the corrugated geometry of the exchanger. However the dynamic BG model proposed in this study is equipped with a semi empirical model for its estimation. The objective of the current section is to optimize the thermal conductance in both compartments of the condenser PC and SC. Starting with the nominal value “ h_0 ” calculated by the proposed semi empirical model (eq.9) for each compartment, then an optimization is performed on “ h_0 ” to minimize the difference in temperatures between the model and experience.

The optimization used in this study is based on Broydon Fletcher Goldfarb Shanno method, which is already

integrated into the 20sim simulation software. This method uses both the gradient of a function and the second order gradient to determine the search direction. The search direction is kept for each new step until a minimum has been found. Then a new search direction is determined and the process goes on.

4.1. First test with a constant conductance value

The brazed-plate heat exchanger used in our study is delivered with data sheet where the manufacturer mentions a value of $h = 6530 \text{ w/m}^2\text{C}$. The idea here is to launch the simulation of the first test case (4.a) with this imposed value and compare the profile of simulating temperatures with experimental measurements (Fig.9).

The dynamic model simulated with this value of “h” shows a discrepancy of 2°C with the measured temperature in steady state. This means that the imposed value of conductance does not correspond to the right value.

4.2. Improvement of the convective conductance

The scientific literature describes very few models of the convective conductance specific to brazed-plate heat

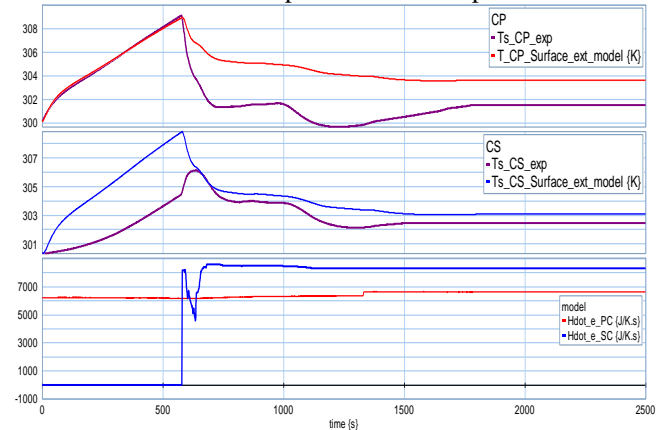


Figure 9: Temperatures profiles in both PC and SC with $h_{PC} = h_{SC} = 6530 \text{ w/m}^2\text{C}$.

exchanger. However, Alfa Laval is a condenser manufacturer which discloses a model adapted to our current application and whose formula is:

$$h = K \times \lambda \times P_r^{1/3} \times \left(\frac{\rho \times \Delta P}{\mu^2}\right)^{0,3274} \quad (9)$$

with:

- h : Heat transfer coefficient (in $\text{w/m}^2\text{K}$)
- K : Optimization parameter, initially equal to 234.
- Pr : Prandtl number (by definition $C_p \times \mu / \lambda$).
- ΔP : Drop pressure (in kPa)
- μ : Viscosity (in cP). ($1\text{N/s}^2 = 10^3 \text{cP}$).

Test I:

Simulation of the case detailed in paragraph (III.a), is run again, however, with the heat transfer coefficient “h” evaluated using AlfaLaval equation. The latter is then optimized according to Broydon method. Optimization of the

two coefficients “h” (PC and SC) converges to the following values:

$$h_{opt_PC} = 1062 \text{ w/m}^2\text{K}. \quad h_{opt_SC} = 4152 \text{ w/m}^2\text{K}.$$

Fig.10 shows a better concordance between numerical resolution (red and blue curves) and experience (purple curves). The difference being recorded is reduced from 2°C to 1.2 °C in primary circuit, and from 0.9°C to 0.2°C in secondary circuit, which is inside the precision domain of the temperature sensors. The result is slightly better for the SC because the fluid is pure water, even though the fluid in the hot circuit (PC) is not really pure water but contains a certain quality of oil for the pump lubrication.

Test 2:

Initial conditions:

- Cold mass flow rate = 4 cm3/s.
- Hot mass flow rate = 0 cm3/s.

At the hot circuit, we notice that at the steady state regime, the temperature difference between the curve from the model and the experimental is around 1 degree, which may correspond to the uncertainty of the thermocouples. Whereas at cold circuit, we clearly see that the two curves are superimposed (*fig.12*).

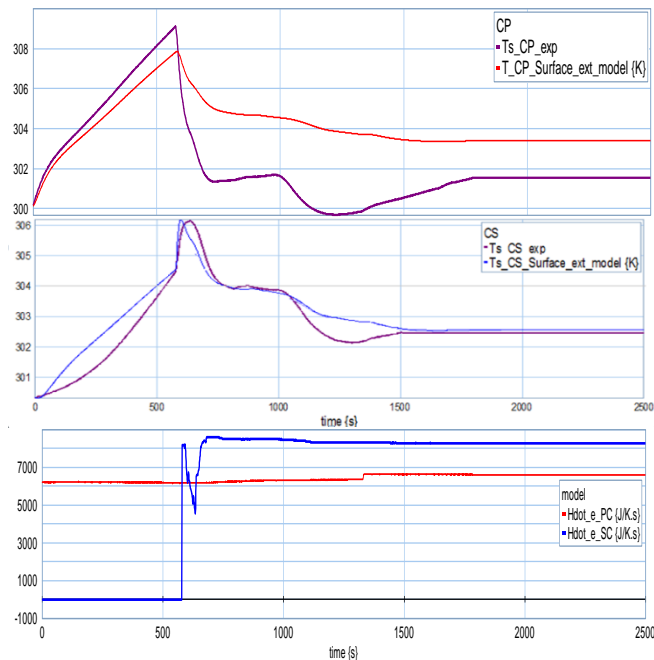


Figure 10: Temperatures profiles in both PC and SC with Optimized Alfa Laval “h”.

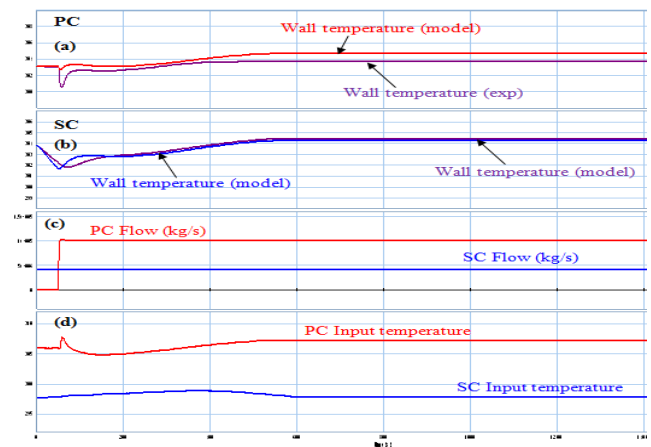


Figure 11: Time evolution of fluid temperature in PC (a), in SC (b), flow evolution in both PC and SC (c) and input temperature in both PC and SC (d).

5. CONCLUSION

In this paper we propose a Brazed-Plate heat exchanger model based on BG approach, taking into consideration the hydro-thermal exchanges that occur in the system. Due to simplified assumptions, the difference between theoretical and experimental results can be attributed to the uncertainty of the sensors. The model can be considered as reliable enough to represent the heat transfer in the heat exchanger in monophasic behavior. The model is parametrized in terms of device geometry, type of fluid, input variables (hot and cold sources and temperatures). The future research work is to model the two-phase regime and validate it through experiments.

MODEL VARIABLES

C_p	Specific heat	J/kg/K
C	Capacity	J/K
e	Channels thickness	m
H	Enthalpy	J
\dot{H}	Heat flow	J/s
H_e	Inlet enthalpy	J/kg
H_s	Outlet enthalpy	J/kg
L	Channels length	m
m	Mass	kg.
P	Pressure	Pa
q_m	Mass flow	kg/s
\dot{Q}_{exp}	Heat flow (Hot source)	J/s
R	Resistance.	
T	Temperature	K
V	Volume	m ³
ρ	Density of the fluid	kg/m ³
v	Velocity	m/s
μ	Viscosity	Pa.s
m	Mass.	kg
O	Initial state.	
<i>liq</i>	Liquid.	
<i>cond</i>	Condenser.	
λ	Thermal conductivity of water	
MSe:	Modulate source effort.	

ACKNOWLEDGMENTS

This paper describes results from research supported by the FUI 14 Program in the context of project ThermoFluid RT labeled by the competitiveness pole ASTech. The authors gratefully acknowledge Mr R. Albach from Atmosat company for his important contribution to the experimentation phase, and the members of the consortium for the multiple fruitful scientific discussions about heat exchanges.

REFERENCES

Kebdani M., Dauphin-Tanguy G., Dazin A., Dupont P., 2015. Bond Graph Model of a mechanically Pumped Biphasic Loop (MPBL), 23rd Mediterranean Conference on Control and Automation, 16-19 Juin, 2015, Meliá Costa del Sol, Torremolinos, Spain,

Sarraf K., Launay S., Tadriss L., 2006. Investigation des transferts thermiques locaux dans un échangeur à plaques par thermographie infrarouge, Aix-Marseille Université, Laboratoire IUSTI, UMR CNRS 7343, Marseille cedex 13, France.

Crevaschi L., Barve A., and Wu X., 2012. Effect of Condensation Temperature and Water Quality on Fouling of Brazed-Plate Heat Exchanger, ASHRAE Transactions. 1086-1100.

Focke W.W., Zachariades J., and Olivier I., 1985. Effect of the corrugation inclination angle on the thermohydraulic performance of plate heat exchangers, International Journal of Heat and Mass Transfer, 1469–1479.

Vlasogiannis, P., Karagiannis, G., Argyropoulos, P., Bontozoglou, V., 2002. Air-water two-phase flow and heat transfer in a plate heat exchanger, International Journal of Multiphase Flow, 28(5), pp. 757-772.

Volker, G. & Kabelac, S., 2010. Experimental investigations and modelling of condensation in plate heat exchangers, Washington.

Freund S., Kabelac s., 2010. Investigation of local heat transfer coefficients in plate heat exchangers, International Journal of Heat and Mass Transfer, vol. 53, p. 3764–3781.

Rong X., Kawaji M., Burgers J.G., 1995. Two-phase header flow distribution in a stacked plate heat exchanger, Proceedings ASME/JSME FED-Gas Liquid Flows 225, 115–122.

Cooper A., Usher J.D., 1983. Plate heat exchangers, In: Schlunder, E.U. (Ed.), Heat Exchanger Design Handbook, vol. 3. Hemisphere, Washington.

Raju K.S.N., Bansal J.C., 1983. Design of plate heat exchangers, In: Kakac, S., et al. (Eds.), Low Reynolds Number Flow Heat Exchangers. Hemisphere, Washington, pp. 913–932.

Focke W.W., Zachariades J., Olivier I., 1985. The effect of the corrugation inclination angle on the thermohydraulic performance of plate heat exchangers, Int. J. Heat Mass Transf, 1469–1497.

Focke W.W., Knibbe, P.G., 1986. Flow visualization in parallel-plate ducts with corrugated walls, J. Fluid Mech, 73–77.

Bansal B., Muller-Steinhagen H., 1993. Crystallization fouling in plate heat exchangers, ASME J. Heat Transfer, 584–591.

Ould Bouamama B., Thoma J. U., Cassar J.P., 1997. Bond Graph modelisation of steam condenser, Article IEEE. Automatic Control, Computer Engineering and Signal Laboratory.

GAIT MODELLING FOR A CONTEXT-AWARE USER-ADAPTIVE ROBOTIC ASSISTANT PLATFORM

Georgia G. Chalvatzaki¹, Xanthi S. Papageorgiou¹ and Costas S. Tzafestas¹

¹*School of Electrical and Computer Engineering, National Technical University of Athens, Greece*
gchal@central.ntua.gr, xpapag@mail.ntua.gr, ktzaf@cs.ntua.gr

ABSTRACT

For a context-aware robotic assistant platform that follows patients with moderate mobility impairment and adapts its motion to the patient's needs, the development of an efficient leg tracker and the recognition of pathological gait are very important. In this work, we present the basic concept for the robot control architecture and analyse three essential parts of the Adaptive Context-Aware Robot Control scheme; the detection and tracking of the subject's legs, the gait modelling and classification and the computation of gait parameters for the impairment level assessment. We initially process raw laser data and estimate the legs' position and velocity with a Kalman Filter and then use this information as input for a Hidden Markov Model-based framework that detects specific gait patterns and classifies human gait into normal or pathological. We then compute gait parameters commonly used for medical diagnosis. The recognised gait patterns along with the gait parameters will be used for the impairment level assessment, which will activate certain control assistive actions regarding the pathological state of the patient.

1. INTRODUCTION

The care of the constantly growing ageing population is a considerable problem for modern societies (Foundation, 2010; Center, 2010). One of the major issues we have to face is the mobility difficulties of the elderly, which can be caused either by age, or by certain pathologies. Walking problems affect not only the daily lives of the elderly but also their self-esteem, after they lose their ability to look after themselves. The lack of nursing staff, (Montemerlo et al., 2002), in relation to the increased demands of the elderly for care, led scientists to turn to robotic assistants, since robotics can incorporate features such as posture sup-

This research work was supported by the European Union under the project "MOBOT" with grant FP7-ICT-2011-9 2.1 - 600796.

port and stability, walking assistance, navigation in indoor and outdoor environments, health monitoring, etc.

Our motivation is to use intelligent robotic platforms (Fig.1), which can monitor and understand the patient's walking state and will autonomously reason on performing assistive actions regarding the patient's mobility and ambulation (X.Papageorgiou et al., 2014). We are working on the development of an Adaptive Context-Aware Robot Control architecture, when the robotic assistant is in front of the user and detects the patient's mobility state by using real-time laser data. We recognise specific gait patterns and also compute gait parameters that are indicative of particular pathologies. The recognised parameters

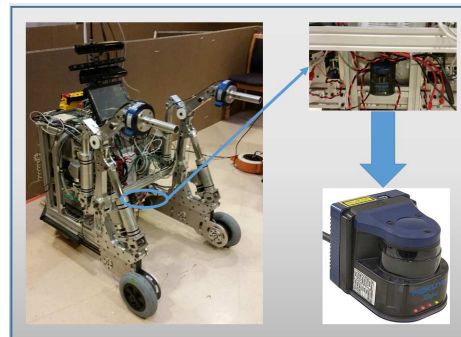


Figure 1: A robotic platform equipped with a Hokuyo Laser Sensor aiming to record the gait cycle data of the user (below knee level).

of the user are then used for the patient's mobility impairment assessment, and this indication will trigger certain control assistive actions and behaviours from the robotic assistant that follows the user. Such actions would be velocity adjustment of the platform, approach of the patient because of recognised changes in gait patterns due to fatigue, walking instability or due to the patient's will to perform another task (like approaching a chair to perform a stand-to-sit action).

In this paper we present our approach for the development of two procedures that are important for human gait modelling and their performance is nec-

essary for the Adaptive Context-Aware Robot Control architecture. Firstly, we analyse the detection and tracking of the patient's legs, based on a Kalman Filter (**KF**), for estimating the legs' kinematic parameters. This process has the potential to track the user while performing straight walking, but also can overcome leg occlusions and false detections. Also, this is an essential part of the preprocessing of the raw laser data and it actually provides the input signal for our control architecture. Secondly we describe the development of a non-invasive framework for pathological walking recognition, based on a Hidden Markov Model (**HMM**), used for gait modelling and classification. This framework is designed to actively incorporate many different gait patterns as a subsystem within a larger cognitive behaviour-based context-aware robot control framework (that embodies several walking morphologies, including turning and maneuvering motions). Furthermore, this framework has the potential to be used for the classification of various walking pathologies and related impairments, and for actively and cognitively being augmented with new patients with mobility difficulties.

2. RELATED WORK

As mobile robots are becoming more and more autonomous, the robot-following-human concept is getting popular in assistive robotics, and they are actually using various sensing technologies for monitoring human activity (Hirai and Mizoguchi, 2003; Luo et al., 2009). The automatic classification and modeling of specific physical activities of human beings is very useful for the development of smart walking support devices, aiming to assist motor-impaired persons and elderly in standing, walking and other mobility activities, as well as to detect abnormalities and to assess rehabilitation procedures (Dubowsky et al., 2000; Spenko et al., 2006; Jiang et al., 2011; Bachlin et al., 2010; Lin and Kulic, 2011). For the extraction of gait motions, different types of sensors have been used, from gyroscopes and accelerometers to cameras, etc., (Bae and Tomizuka, 2011; Nickel et al., 2011; Pappas et al., 2001; Bebis et al., 2008; Meng et al., 2010). Other approaches refer to human detection and tracking, or recognition of human activity utilizing laser sensors, and in some cases complementary with cameras, or force sensors, (Panangadan et al., 2010).

For the robot-following-human problem, there is a discrimination in positioning between human and mobile robot; robot following human from behind, or by the side of the human, or in front of the human. Towards this direction, the estimation of the legs' kine-

matic parameters with respect to the mobility aid is essential. Thus, the detection and tracking of humans is a common problem. Most research work focuses on detecting and tracking human legs from static sensors, as in pedestrian tracking, (Shao et al., 2006), or from laser scanners mounted on mobile robotic platforms for person following (K. Arras et al.,), where several tracking and control methods have been applied, (Kirby et al., 2007; Jung et al., 2012). The need for a substantial interaction between human and accompanying robotic platform led to the development of sophisticated control schemes for a high level understanding of the human behavior, presenting early research results in (Zender et al., 2007; Cosgun et al., 2013; Kruse et al., 2013; Ho et al., 2012). Most gait tracking methods use standard Kalman Filters, for which normal gait is modeled as an interchange of accelerative and decelerative motions of the two legs (Katsuyuki Nakamura and Shibasaki, 2012), with predefined filter inputs for the motion models. However, those models are had to be applied to pathological gait. Mobility impairment of different origin result in different gait patterns. In this work, we present a gait detection and tracking method that is easy to implement, that uses a standard Kalman filter, using acceleration as the system's noise, and also uses the predicted state vector as feedback of the tracking process for the detection of the user's legs for the next time frame.

A key issue for the development of a context-aware robotic assistant platform that monitors elderly people with mobility inabilities, is gait modelling, i.e. the extraction of specific gait patterns that correspond to specific pathologies, and will be necessary for the assessment of the mobility impairment level of the subject, that will trigger certain assistive actions from the robotic assistant. The dynamic properties of walking led to the usage of Hidden Markov Models (**HMMs**). Time series data can be modelled by HMMs, since they are not only easy to build and manipulate, but also to train and score them with optimal algorithms (e.g. maximum likelihood, Viterbi decoding). In HMMs only the output of the model is visible to the observer and the states of the model (corresponding to a physical event) are not observable, in other words are hidden, (Rabiner, 1990). The versatility of HMMs makes them useful in extracting human patterns. Apart from their prominent application in speech recognition, (Katsamanis et al., 2008), HMMs are also used in a number of pattern recognition applications, gesture recognition, (Theodorakis et al., 2009), human activity analysis, (Turaga et al., 2008) and biometric gait recognition, (Chen et al., 2006). The first attempts to model the normal walking

motion by using HMMs with respect to laser data features, were presented in (Papageorgiou et al., 2014; Chalvatzaki et al., 2014). In this work we extend this approach to model and characterize the pathological walking motion, in order to integrate it into a Context-Aware Robot Control.

3. SYSTEM OVERVIEW

An Adaptive Context-Aware Robot Control architecture is being developed for the intelligent robotic assistant platform, that will adapt and act according to the patient's needs. The system is driven by the sensory data of a 2D laser range scanner that detects the walking motion (Fig.1). An important step for performing behavior-based context aware control is the preprocessing of the system's input signal. This process incorporates the detection and tracking of the user's legs. This framework takes as input the noisy laser data, detects the patient's legs and estimates their actual position and velocity with respect to the robotic assistant. The estimated kinematic state of the subject's legs feed the cognitive context-aware control system as the environmental input signal, that is used to infer the context (i.e. state of the patient) and to perform specific actions in the detected context.

The control scheme consists of the typical three-layer architecture. The high level of this control scheme contains the Gait Modelling and Classification module. This is an HMM-based approach that can recognize sequences of gait patterns and also it can classify them into normal pathological ones, or non-walking activity. Given the spatiotemporal properties of those sequences, we compute particular gait parameters (such as step length, cadence), that are commonly used for medical diagnosis, (Arias-Enriquez et al., 2012), since differentiations in their values are indicative of specific pathological states. In that way, an impairment level assessment is performed, for completely knowing the context of the patient's walking motion (i.e. recognition of the patient's intention to walk, gait modelling, estimation of the subject's pathological status).

This context-awareness is used as input to the medium level control module. Medium level control contains specific behaviours and assistive actions, that are activated according to the subject's detected context. The robotic assistant should adaptively track and follow the subject during its walking motion. Also the platform should smoothly stop in front of the subject in cases when the subject freezes and stops abruptly. Furthermore, the platform should smoothly approach the user to provide possible support when instability in gaiting is detected.

All this information is used as input to the typical low level controller of the platform, in order to inherently translate the decision of performing a specific assistive action into motor commands.

4. PREPROCESSING OF CONTROL INPUT: LEG DETECTION AND TRACKING

For the detection and tracking of the patient's legs we use a combination of K-means clustering to detect the subject's legs and a Kalman Filter for tracking the user, and therefore estimate of the kinematic parameters of walking, i.e. the legs' positions and velocities. Our approach is a recursive system with a substantial forward-backward interaction between the detection and tracking of the user.

4.1. Data Processing and extraction of candidate legs

The raw laser data are processed at each time frame. Data processing consists of defining an observation window (a rectangle area) in the scanning plane of the laser scanner. The window's initial dimension is computed by the area in front of the rollator, where we expect the subject to be standing before performing the walking task. This initial search window is predetermined and wide enough, while in the subsequent frames it is adjusted. For the data inside the window we use a simple background extraction method based on thresholding criteria. The laser points that lie outside the observation window are discarded, while the remaining are separated into groups, corresponding to detected objects according to the Euclidean distance between consecutive laser points. In cases of discontinuities of laser points, due to fluctuations of the device, or due to the objects deformable surface (common in creasing pants), instead of having one laser group describing an object, we end up with more. In such cases the adjacent laser groups are merged according to an euclidian threshold. Finally, any laser group that contains less than a specific number of points is deleted. The remaining laser groups formulate the candidate legs. The candidate legs extraction is successful when we end up with two candidates, corresponding to the legs. The treatment in cases of less or more laser groups is described below.

4.2. Legs' Detection

The candidate legs feed the Legs' Detection subsystem, by using a K-means++ clustering algorithm (Arthur and Vassilvitskii, 2007), that classifies the

left and right leg. Instead of using the highly noisy centroid-mean of each cluster given by K-means, we take as consensus that the human limbs can be represented as cylinders, and therefore can be seen as circles in the scanning plane. We use nonlinear least squares circle fitting with a constant pre-computed radius, in order to approach the actual planar leg centers. In that way we have a compact representation of the legs, which is not influenced so much by the shape deformations of the laser groups. The detected legs' centers compose the observation vector z_k for the tracking process.

4.3. Kalman Filter Tracking

The tracking of the user's legs is performed by a discrete Kalman filter (**KF**) algorithm (Maybeck, 1979), using as observation vector z_k the detected leg centers at each time frame. For the description of the legs' motion we used a second order kinematic model, i.e. it incorporates the position and velocity of the legs, and subsequently the used state vector has eight parameters: $x_k = [x^L \ y^L \ x^R \ y^R \ v_x^L \ v_y^L \ v_x^R \ v_y^R]$ where $(x^L, y^L), (x^R, y^R)$ are the positions and $(v_x^L, v_y^L), (v_x^R, v_y^R)$ the velocities of the left and right leg along the axes. The Kalman Filter process equation has the form: $x_{k+1} = A_k \cdot x_k + B_k \cdot w_k$ where A_k is the transition matrix and it has the following form: $A_k = \begin{bmatrix} I_4 & A_1 \\ 0_4 & I_4 \end{bmatrix}$ where $A_1 = \Delta t \cdot I_4$, and I_4 is the 4x4 identity matrix. The gain matrix B_k is multiplied with the process noise w_k and is given by: $B_k = \begin{bmatrix} B_1 \\ B_2 \end{bmatrix}$ where $B_1 = (\Delta t^2/2) \cdot I_4$, $B_2 = \Delta t \cdot I_4$, I_4 is the 4x4 identity matrix. The uncorrelated process noise w_k is white and gaussian, and is given by the distribution $w_k \sim N(0, Q_k)$, where Q_k is the process noise covariance matrix. Since we have no known control inputs, we assume that acceleration is the effect of an unknown input and we treat the acceleration as the process noise. Therefore, it represents the influence of acceleration's variability at the state parameters at each time instant k. The process noise covariance matrix Q_k , which is an 8x8 square matrix, is computed by: $Q_k = B_k \cdot C_a \cdot B_k^T$ where C_a is the covariance matrix of the acceleration a , with $a \sim N(0, C_a)$ and C_a is a 4x4 diagonal matrix with diagonal elements: $std_{La_x}^2, std_{La_y}^2, std_{Ra_x}^2, std_{Ra_y}^2$ where $std_{La_x}, std_{La_y}, std_{Ra_x}, std_{Ra_y}$ are the standard deviations of the accelerations along the axes for both legs, that were experimentally defined and describe the acceleration uncertainty throughout the gait.

The observation vector z_k of the true state is

updated according to the equation: $z_k = H_k \cdot x_k + v_k$ where H_k is the observation matrix which maps the true state space into the observed space: $H_k = [I_4 \ 0_4]$ with 0_4 is the 4x4 zero matrix, and v_k is the observation noise, with normal probability distribution $p(v_k) \sim N(0, R_k)$, where R_k is the measurement noise covariance matrix, a 4x4 diagonal matrix with diagonal elements: $v_{x_k}^2, v_{y_k}^2, v_{x_k}^2, v_{y_k}^2$ where v_{x_k} and v_{y_k} for both legs are the standard deviations of the measurement noise v_k along the axes. KF is a recursive Bayesian estimator that consists of two phases, (i) the prediction and (ii) the update phase. During prediction phase the KF projects the state vector and the state covariance matrix forward in time according to the physical model of the process described by the input matrix A_k , and provides the *a priori* state estimate: $\hat{x}_{k|k-1} = A_k \cdot \hat{x}_{k-1|k-1}$ and the *a priori* estimate covariance: $P_{k|k-1} = A_k \cdot P_{k-1|k-1} \cdot A_k^T + Q_k$.

In the update phase, the observation vector serves as a feedback that corrects the *a priori* estimates. Thus, the observation innovation is computed by: $\tilde{y}_k = z_k - H_k \cdot \hat{x}_{k|k-1}$ and its innovation covariance: $S_k = H_k \cdot P_{k|k-1} \cdot H_k^T + R_k$.

Innovation is crucial for obtaining the Kalman gain. The Kalman gain is the solution to the minimum mean square error in the posterior state estimation, and is given by: $K_k = P_{k|k-1} \cdot H_k^T \cdot S_k^{-1}$. Kalman gain technically calculates the quota of the predicted state estimate and the measurement into the final *a posteriori* state estimation. In that way we get the *a posteriori* state estimate: $\hat{x}_{k|k} = \hat{x}_{k|k-1} + K_k \cdot \tilde{y}_k$ and the *a posteriori* estimate covariance: $P_{k|k} = (I - K_k \cdot H_k) \cdot P_{k|k-1}$.

At each time instant, the detection process provides the observations for the KF tracking, and the KF feeds the system back with the predicted state vector $\hat{x}_{k|k-1}$. Especially the legs' predicted positions are used as seed for the K-means++ algorithm, as an inference to where it should assign the leg clusters in the next frame. Around the predicted positions of the legs, leg-windows are set having initial constant dimensions proportional to the leg-circle's dimensions. The leg-windows dimensions are also adaptively adjusted, by enlarging or shortening them according to the variability of the predicted positions, provided by the *a priori* estimate covariance $P_{k|k-1}$ derived by the KF. From the two leg-windows, a wider search window is defined in the plane and the detected raw data inside it are ready to be processed. Thus, it results in an iterative interaction between detection and tracking processes. Finally, the estimated state vector $\hat{x}_{k|k}$ enters the HMM Gait Phases Recognition System as an observation at each time frame.

4.4. False Detection Treatment

False detections are the cases in which either one leg is occluded by the other or there is interference of another person's legs inside the search window that have not been successfully discarded. Those cases can interrupt or contaminate the detection and can result in losing track of the legs. To address such false detections, certain hypotheses are checked. If the detected leg centers violate a Euclidean distance constraint that we have set, relevant to an experimentally defined anatomical threshold, or when there are detected less or more than two laser groups, the corresponding detection is regarded false. In order to continue to the tracking phase, an only-prediction Kalman filter is applied. In that particular case, we perform only the prediction step and we use the prediction state vector $\hat{x}_{k|k-1}$ and the *a priori* estimate covariance $P_{k|k-1}$ as feedback for the detection of the next frame, without taking into consideration any observations for that particular time frame. This choice has been made, as it was noticed that between two consecutive frames the leg positions are not so prone to sharp or sudden shifts.

5. HMM GAIT MODELLING

Hidden Markov Models are well suitable for gait recognition because of their statistical properties and their ability to reflect the temporal state-transition nature of gait. An HMM is defined as a doubly embedded stochastic process with an underlying process that is not observable (it is hidden), but can only be observed through another set of stochastic processes that produce the sequence of observations, (Rabiner, 1990). This reveals that the states underlying the data generation process are hidden, and they could be inferred through observations.

This HMM based model is performed in the high level of the Adaptive Context-Aware Robot Control, which utilizes as observables several quantities that represent the motion of the subjects' legs (relative position w.r.t. the laser, velocities, etc.), which are estimated sequentially by the detection and tracking module, while the robotic assistant platform follows the subject's motion.

In this paper we have used the gait phases that characterize gait cycle. The gait cycle describes the period of time when one leg leaves the ground for the first time to perform a forward motion till when the same leg contacts the ground again, (Jacquelin Perry, 1992). Each gait cycle has two phases: stance and swing. In stance the foot is in contact with the ground. In swing the foot is in the air performing a ballistic

motion. The gait cycle is divided into eight events: 1. *IC* - Initial Contact: 0% of gc:¹ Heel strike initiates the gait cycle and represents the point at which the body's centre of gravity is at its lowest position. 2. *LR* - Loading Response: 0-10% of gc: The time when the plantar surface of the foot touches the ground. 3. *MS* - Midstance: 10-30% of gc: When the swinging (contralateral) foot passes the stance foot and the body's centre of gravity is at its highest position. 4. *TS* - Terminal Stance: 30-50% of gc: The heel loses contact with the ground and pushoff is initiated via the triceps surae muscles, which plantar flex the ankle. 5. *PW* - Preswing: 50-60% of gc: Toe-off terminates the stance phase as the foot leaves the ground. 6. *IW* - Initial Swing: 60-70% of gc: Acceleration begins as soon as the foot leaves the ground and the subject activates the hip flexor muscles to accelerate the leg forward. 7. *MW* - Midswing: 70-85% of gc: When the foot passes directly beneath the body, coincidental with midstance for the other foot. 8. *TW* - Terminal Swing: 85-100% of gc: Deceleration describes the action of the muscles as they slow the leg and stabilize the foot in preparation for the next heel strike.

Since the TW phase is characterized by heel strike that is an equivalent trigger to the IC phase, those phases are treated as identical. These seven states can define the hidden states of the HMM (Fig. 2). The state and observations at time t are denoted as s_t and O_t , respectively. The seven states at time $t = 1, 2, \dots, T$, where T is the total time, are expressed by the value of the (hidden) variable $s_t = i \in \mathbf{S}$, for $i = 1, \dots, 7$, where $1 \equiv IC/TW$ (since we treat IC and TW as identical), $2 \equiv LR$, $3 \equiv MS$, $4 \equiv TS$, $5 \equiv PW$, $6 \equiv IW$, and $7 \equiv MW$. Regarding observations at time t , we define nine signals denoted as x^m, y^m, v_x^m, v_y^m , for $m = \{R, L\}$, which are the coordinates and the velocities along the axis for right and left leg, respectively, and $Dlegs$ which is the distance between legs, that are represented by the vector $O_t = [o_t^1 \dots o_t^9]^T \in \mathbf{O}$, for $k = 1, \dots, 9$, where $o_t^1 \equiv x^R$, $o_t^2 \equiv y^R$, $o_t^3 \equiv x^L$, $o_t^4 \equiv y^L$, $o_t^5 \equiv v_x^R$, $o_t^6 \equiv v_y^R$, $o_t^7 \equiv v_x^L$, $o_t^8 \equiv v_y^L$, and $o_t^9 \equiv Dlegs$. The observation data (derived from the raw laser sensor data) are modeled using a mixture of Gaussian distributions. This is a natural way of representing these data, as the data vector takes values from a bounded set (recall that we use the relative position of the legs from a robot that follows the subject with his/her mean velocity) and is inherently repetitive (due to the cyclic nature of the human gait). Thus, by collecting many data for a normal gait, we can obtain the mean and the variance of the Gaussian distributions of the mixture. Since nine signals are measured and consti-

¹gc: abbreviation for gait cycle

tute the extracted features at each time instant, the distribution is a multivariate Gaussian distribution: $g(x|\mu_m, \Sigma_m) = \frac{1}{(2\pi)^{\frac{n}{2}} |\Sigma_m|^{\frac{1}{2}}} \exp\{-\frac{1}{2}(x - \mu_m)^T \Sigma_m^{-1} (x - \mu_m)\}$ where $x \in \mathbb{R}^n$ is the feature vector, $\mu_m \in \mathbb{R}^n$ denotes the mean vector and Σ_m denotes the $(n \times n)$ covariance matrix of the m^{th} Gaussian probability density, where in our case $n = 9$, and $m = 1, \dots, M$. The Gaussian Mixture Model (GMM) is then a weighted sum of these M component Gaussian densities, as given by the equation: $P(x) = \sum_{m=1}^M w_m \cdot g(x|\mu_m, \Sigma_m)$ where w_m are the mixture weights, for which it holds: $\sum_{m=1}^M w_m = 1$, $w_m \geq 0$.

In normal gait cycle the gait phases follow each other sequentially, while in pathological gait the sequence of gait phases may be different or some of them may disappear. Thus, this HMM is a left-to-right model.

6. GAIT PARAMETERS COMPUTATION FOR MEDICAL DIAGNOSIS

The analysis of gait patterns for medical diagnosis is presented in (Arias-Enriquez et al., 2012), by using different types of wearable and non-wearable sensors and by extracting and employing various gait parameters, (Muro-de-la Herran et al., 2014).

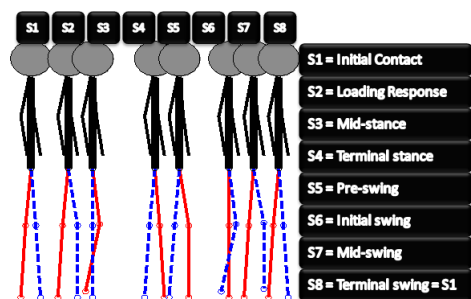


Figure 2: Internal states of normal gait cycle (Left Leg: blue dashed line, Right Leg: red solid line).

The recognized sequence of gait phases is indicative of the subject's underlying pathology, since it differs from the normal gait phase sequences. We can, also, take advantage of the segmentation in time that the recognition system provides, regarding the duration of each gait phase, in order to compute specific gait parameters from the range data, that are necessary to specialists to perform medical diagnosis of the subject, (Muro-de-la Herran et al., 2014). The recognized gait patterns along with the gait parameters will be used by the robotic platform for the assessment of the patient's impairment level, which will trigger specific behaviours and assistive actions by the robotic

assistant platform, in the medium level of the Adaptive Context-Aware Robot Control. For the impairment level assessment, we are computing the following gait parameters, (Muro-de-la Herran et al., 2014):

1. Step length (linear distance between two successive positions of the same leg)
2. Stride length (linear distance between the positions of both feet)
3. Cadence (number of steps per time unit)
4. Step width (lateral distance between the two legs)
5. Stance time (time from IC to TS)
6. Swing time (time from IW to TW).

7. EXPERIMENTAL RESULTS

7.1. Experiment Description and Dataset

The experimental data used in this work were collected in Agaplesion Bethanien Hospital/ Geriatric Center with patients that presented moderate to mild impairment according to clinical evaluation of the medical associates. We have used a Hokuyo rapid laser sensor (UBG-04LX-F01 with mean sampling period of about 28msec) mounted on the robotic platform.

For the evaluation of our algorithmic approach, we have used the recorded data of seven patients with moderate mobility impairment (aged over 65 years old), performing a scenario during which the subject walked unassisted, i.e. without any physical support of the carer or the robotic platform, the subject walked straight in a walkway, while the robotic platform moved in a near distance in front of the subject (following mode).

7.2. Detection and Tracking results

For the experimental evaluation of the Detection and Tracking system, we had experimentally defined the thresholds used in the preprocessing of the laser data. A crucial feature for the performance of the KF tracking is the fine tuning of the filter to achieve its convergence to the true state. Since we did not have any ground truth data, KF tuning was difficult to achieve. As far as it concerns the measurement noise, given that only three points are sufficient to define a circle, we conducted Markov Chain Monte Carlo sampling for the three point in the circle's contour, using the information about the nominal noise of the laser scanner (considered to be white and gaussian with standard deviation $\sigma_{laser} = 0.0025m$). With those random samplings we have simulated how the random disturbances of the three points on the circle's contour introduced by the laser's error can deviate the estimated

circle center through nonlinear circle fitting (given a known radius). On the other hand, the process noise statistics were trained by raw data.

However, the described experimentation led to an overestimation of the process noise parameters and an underestimation of the measurement noise statistics that resulted in overfitting problems. This seems quite reasonable, since human leg's locomotion cannot be accurately described by a linear motion model, and also measurement noise influenced by other parameters that cannot be simulated, e.g. the laser clusters deformable shapes due to the patient's clothing. In order to achieve the filter's convergence, we have followed the presented methodology of (Gamse et al., 2014). The resulted noise parameters are as follows:

- For the computation of the process noise covariance matrix, we need the acceleration's covariance matrix, where: $std_{La_x} = 4.62$, $std_{La_y} = 9.1$, $std_{Ra_x} = 2.63$, $std_{Ra_y} = 8.38$ (in m/sec^2).
- For the measurement noise covariance matrix, we resulted to the following standard deviations: $v_{x_k} = 0.05$ and $v_{y_k} = 0.01$ (in m).

In Fig. 3 and Fig. 4 the detected (magenta and green stars) and the estimated (solid blue and red lines) for the lateral and forward displacement of the left and right leg accordingly, are shown. For the evaluation

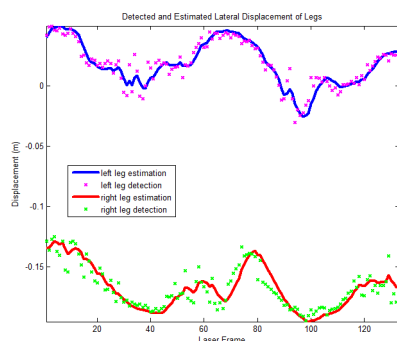


Figure 3: Detected and estimated legs' lateral displacement.

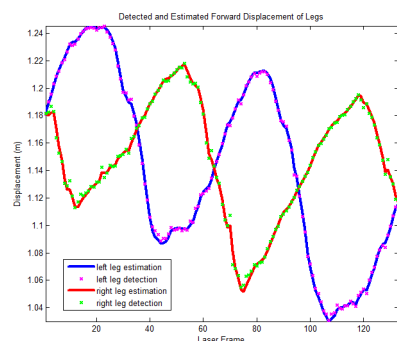


Figure 4: Detected and estimated legs' forward displacement.

of the KF performance, we have computed the root mean square errors (**RMSE**) between the estimated and detected positions of the legs. In the absence of ground truth data, we regard the computed RMSE a measure of how much the KF improves the noisy observations. The average RMSE computed over the results of the detection and tracking process of the 7 patients that performed the same task, were 0.0078m for the x coordinate (lateral motion) and 0.0018m for the y coordinate (forward motion). In the lateral plane there is greater uncertainty (about 4 times bigger), due to the leg clusters shape deformability and length variability. In the absence of ground truth data, we are not able to accurately evaluate the results of the computed RMSE. However, we observed that the deformability of the leg clusters caused greater variability in the lateral plane, which is generally not wanted (gaiting is mainly taking place in the forward direction towards the rollator, thus sudden lateral motions are artifacts), we can say that our method smooths out the noise in the lateral motion, rather than in forward motion, where we desire a smoother but closer tracking of the observations in that direction. In order to evaluate the results of our tracking method, we are working on extracting motion capture data to use as ground truth.

7.3. Gait Phases Recognition Results

HMM training procedure comprises only a part of subjects' data, excluding the recorded data of one subject. The testing procedure aims to test the performance of the proposed approach, validating its generalisation capacity over unseen data obtained by new subjects. The evaluation is based on an assessment of the estimated states provided by the constructed HMM, which represents the human gait cycle.

For testing and evaluation purposes of the constructed HMM, we have demonstrated an example of the real experimental data set which is depicted in Fig. 5. The goal of this evaluation phase is to unveil the hidden parts of the constructed models, i.e. to estimate the correct sequence of phase transitions that occur in the test data. This test dataset reflects the gait session of one elderly subject, and comprises about seven walking sections (about seven strides²). In this figure the displacement of each leg in the sagittal plane with respect to time is depicted on the top graph, while the bottom graph shows the evolution of the distance between legs within the same time frame. This figure is very useful to understand the exact subject's motion. The walking session is starting with the left leg, and it is obvious from the increasing of the

²Stride is the equivalent of gait cycle, i.e. two sequential steps define one stride, (Perry, 1992).

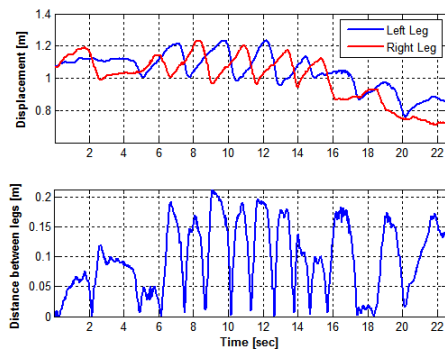


Figure 5: Real experimental data from one subject's walking motion that have been used in the testing and evaluation phase of the constructed HMM. Top: Left (blue data) and Right (red data) legs displacement. Bottom: legs distance in the sagittal plane.

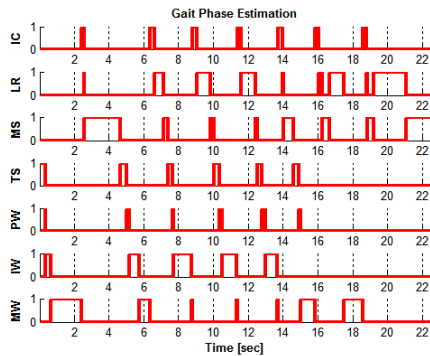


Figure 6: Estimated sequence of gait phases based on the constructed model with respect to time by testing the data depicted in Fig. 5, which represent an unknown walking section.

distance between the legs that the early gait phases are occurred, Fig. 5. While this distance is going to zero (crossing point) the right leg is moving forward until the next crossing point. It can be observed that the first complete stride is recognized to begin just after the 6sec. This is observable to the results of the constructed HMM in Fig. 6, since at the time instant just after the 6sec, a gait cycle is started by the recognized IC phase.

The estimated sequence of gait phases obtained using the trained model is depicted in Fig. 6. This figure shows the time instant at which each gait phase (hidden state of HMM) is activated. A first remark that can be made by observing these experimental results is that the evolution of the gait phases provided by the models matches the general evolution of the human gait model that is to be represented by the HMMs; i.e. the gait phases appear sequentially with the correct order, and the time frame of each phase is within the general bounds as have been mentioned

previously in Section 5. It is obvious that some of the gait phases are omitted, since these experimental data corresponds to a subject with walking difficulties related to an underlying pathology.

There is an assumption, without loss of generality, that at the beginning of each gait cycle the initial contact refers to the left leg, while a complete stride is concluded when the right leg is again in front of the left leg, ready for a new initial contact and therefore for the next stride. By observing the results depicted in Fig. 6, it can be seen that the model manages to successfully recognize that (for the recorded experimental data of Fig. 5, used in this case study for model testing) the subject starts the motion with the right leg. Thus, the first estimated gait phase in Fig. 6 is the Terminal Stance (TS).

Another remark concerns the abnormal walking motion. At some point of the recorded test data of Fig. 5 (after 16sec), it can be seen that the motion is characterized by abnormal behaviour, and therefore the gait phase evaluation procedure has typical abnormal exports. Although the walking motion starts a new stride with the left leg, due to the abnormal nature of the data, the model could not recognize a complete stride. The results show that the constructed model recognizes the pathological gait.

7.4. Gait Parameters Computation Results

In order to perform the assessment of the impairment level of each patient, it is necessary to compute the appropriate gait parameters from which we can infer the pathological state. We have used the recognized sequence of gait phases and therefore the timestamps of each gait phase along with the estimated positions of the legs from the laser data to compute these parameters. The data are presented as the mean quantity plus/minus its standard deviation and refer to the patient's motion depicted and analysed in Fig. 5, 6. The presented gait patterns refer to a female patient, aged 77 years old with height 159cm, weight 60kg and knee height 45.5cm. Medical partners performed cognitive and mobility evaluation, in which this patient was categorised in cognitive level 1, i.e. no cognitive impairment and in mobility level 2, i.e. mild/moderate impairment - gait speed < 0.6m/sec for unassisted walking.

The respective gait parameters for this patient are presented in Table 1. The gait parameters will be useful for the formulation of a pathology recognition system based on the recognised gait patterns. We are currently working along with clinicians for the evaluation of those parameters and their categorization according to certain pathologies that result in mobility

Parameters	
Right Step Length (m)	0.0565 ± 0.0147
Left Step Length (m)	0.1298 ± 0.0245
Stride Length (m)	0.1863 ± 0.0376
Step Width (m)	0.1688 ± 0.058
Cadence (step/min)	53.38
Stance time % of gait cycle	57.5
Swing time % of gait cycle	42.5

Table 1: Gait Parameters computed using the range data and the segmentation in time of the recognised gait phases

inabilities. The information about the patient's pathological state will then be used in the Context-Aware Robot Control for the assessment of the impairment level of the patient, and thus the inference of the patient's pathological status will trigger certain control assistive behaviors to be executed by the robotic assistant platform.

8. CONCLUSIONS AND FUTURE WORK

In this paper we have presented the basic concept of an Adaptive Context-Aware Robot Control architecture for a robotic assistant platform, that is moving in front of the the user, and will adapt to the user's needs in order to act assistively whenever in case. We have analysed the parts of the proposed control scheme. Firstly, we have described the processing of the raw data from a laser range scanner mounted on the robotic platform. We have analysed the usage of a Kalman Filter for the tracking of the subject's legs and therefore the estimation of the legs' position and velocity, which are the input signal of the control scheme. Then, a Hidden Markov Model based framework have been represented in order to analyse the pathological walking motion, by detecting sequences of gait phases, constituting a completely non-invasive approach, since we have used a non-wearable device. The resulted sequence of the gait phases and the time segmentation are appropriate in order to compute specific gait parameters, necessary for clinical diagnosis.

For further research, we are working on a new detection and tracking system based on particle filtering, fusing also other sensorial data like RGB data, for a whole body tracking approach. Particle filters will perform better in more complicate motion scenarios including also turnings, that are not easy to track with Kalman Filter, which is a linear estimator. Moreover, particle filters can be better used for hierarchical tracking of the human body parts. Furthermore, we are working on the classification approach of normal/pathological gait or non-walking activity. Moreover, in assistance with clinicians, we are elaborating on the computed gait parameters from vari-

ous patients, in order to organize and classify them according to certain pathologies. In that way, a complete automatic pathology recognition system will be developed in order to assess the impairment level of the patient, and particular levels of mobility impairment will indicate the need for specific control assistive actions for the robotic platform in order to adapt to the user's needs.

REFERENCES

- Arias-Enriquez, O., Chacon-Murguia, M., and Sandoval-Rodriguez, R. (2012). Kinematic analysis of gait cycle using a fuzzy system for medical diagnosis. In *NAFIPS 2012*.
- Arthur, D. and Vassilvitskii, S. (2007). K-means++: The advantages of careful seeding. In *Proc. of the 18th Annual ACM-SIAM Symposium on Discrete Algorithms, SODA '07*.
- Bachlin, M., Plotnik, M., Roggen, D., Maidan, I., Hausdorff, J., Giladi, N., and Troster, G. (2010). Wearable assistant for parkinson's disease patients with the freezing of gait symptom. *IEEE Trans. on Information Technology in Biomedicine*, 14(2):436–446.
- Bae, J. and Tomizuka, M. (2011). Gait phase analysis based on a hidden markov model. *Mechatronics*, 21(6):961–970.
- Bebis, G., Nicolescu, M., Nicolescu, M., Tavakkoli, A., King, C., and Kelley, R. (2008). An architecture for understanding intent using a novel hidden markov formulation. *Int'l Journal of Humanoid Robotics*, 05(02):203–224.
- Center, S. (2010). Stroke statistics.
- Chalvatzaki, G., Pavlakos, G., Maninis, K., Papageorgiou, X., Pitsikalis, V., Tzafestas, C., and Maragos, P. (2014). Towards an intelligent robotic walker for assisted living using multimodal sensorial data. In *Mobihealth*.
- Chen, C., Liang, J., Zhao, H., and Hu, H. (2006). Gait recognition using hidden markov model. In Jiao, L., Wang, L., Gao, X.-b., Liu, J., and Wu, F., editors, *Advances in Natural Computation*, volume 4221 of *Lecture Notes in Computer Science*, pages 399–407. Springer Berlin Heidelberg.
- Cosgun, A., Florencio, D., and Christensen, H. (2013). Autonomous person following for telepresence robots. In *Robotics and Automation (ICRA), 2013 IEEE International Conference on*, pages 4335–4342.
- Dubowsky, S., Genot, F., Godding, S., Kozono, H., Skwersky, A., Yu, H., and Yu, L. S. (2000). Pamm - a robotic aid to the elderly for mobility assistance and monitoring: A 'helping-hand' for the elderly. In *IEEE Int'l Conf. on Robotics and Automation*, pages 570–576.
- Foundation, P. D. (2010). Statistics for parkinson's disease.
- Gamse, S., Nobakht-Ersi, F., and Sharifi, M. A. (2014). Statistical process control of a kalman filter model. *Sensors*, 14(10):18053–18074.
- Hirai, N. and Mizoguchi, H. (2003). Visual tracking of human back and shoulder for person following robot. In

- Advanced Intelligent Mechatronics, 2003. AIM 2003. Proceedings. 2003 IEEE/ASME International Conference on*, volume 1, pages 527–532 vol.1.
- Ho, D., Hu, J.-S., and Wang, J.-J. (2012). Behavior control of the mobile robot for accompanying in front of a human. In *Advanced Intelligent Mechatronics (AIM), 2012 IEEE/ASME International Conference on*, pages 377–382.
- Jacquelin Perry, M. (1992). *Gait Analysis: Normal and Pathological Function*. SLACK Incorporated, first edition.
- Jiang, S., Zhang, B., and Wei, D. (2011). The elderly fall risk assessment and prediction based on gait analysis. In *IEEE 11th Int'l Conf. on Computer and Information Technology (CIT), 2011*, pages 176–180.
- Jung, E.-J., Yi, B.-J., and Yuta, S. (2012). Control algorithms for a mobile robot tracking a human in front. In *Intelligent Robots and Systems (IROS), 2012 IEEE/RSJ International Conference on*, pages 2411–2416.
- K.Arras, S.Grzonka, M.Luber, and W.Burgard. Efficient people tracking in laser range data using a multi-hypothesis leg-tracker with adaptive occlusion probabilities. In *Trans. of IEEE ICRA. IEEE Int'l Conf. on Robotics and Automation*.
- Katsamanis, A., Papandreou, G., and Maragos, P. (2008). Audiovisual-to-articulatory speech inversion using active appearance models for the face and hidden markov models for the dynamics. In *ICASSP*, pages 2237–2240. IEEE.
- Katsuyuki Nakamura, Huijing Zhao, X. S. and Shibasaki, R. (2012). *Human Sensing in Crowd Using Laser Scanners, Laser Scanner Technology*.
- Kirby, R., Forlizzi, J., and Simmons, R. (2007). Natural person-following behavior for social robots. In *Proceedings of Human-Robot Interaction*, pages 17–24.
- Kruse, T., Pandey, A. K., Alami, R., and Kirsch, A. (2013). Human-aware robot navigation: A survey. *Robotics and Autonomous Systems*, 61(12):1726 – 1743.
- Lin, J. F.-S. and Kulic, D. (2011). Automatic human motion segmentation and identification using feature guided hmm for physical rehabilitation exercises. In *IEEE Int'l Conf. on Intelligent Robots and Systems*.
- Luo, R., Chang, N.-W., Lin, S.-C., and Wu, S.-C. (2009). Human tracking and following using sensor fusion approach for mobile assistive companion robot. In *Industrial Electronics, 2009. IECON '09. 35th Annual Conference of IEEE*, pages 2235–2240.
- Maybeck, P. S. (1979). *Stochastic models, estimation and control*, volume 1 of *Mathematics in science and engineering*. Academic Press NYC.
- Meng, M., She, Q., Gao, Y., and Luo, Z. (2010). Emg signals based gait phases recognition using hidden markov models. In *Information and Automation (ICIA), 2010 IEEE Int'l Conf. on*, pages 852–856.
- Montemerlo, M., Pineau, J., Roy, N., Thrun, S., and Verma, V. (2002). Experiences with a mobile robotic guide for the elderly. In *Proc. of National Conf. on AI*.
- Muro-de-la Herran, A., Garcia-Zapirain, B., and Mendez-Zorrilla, A. (2014). Gait analysis methods: An overview of wearable and non-wearable systems, highlighting clinical applications. *Sensors*.
- Nickel, C., Busch, C., Rangarajan, S., and Mobius, M. (2011). Using hidden markov models for accelerometer-based biometric gait recognition. In *Signal Processing and its Applications (CSPA), 2011 IEEE 7th Int'l Colloquium on*, pages 58–63.
- Panangadan, A., Mataric, M., and Sukhatme, G. (2010). Tracking and modeling of human activity using laser rangefinders. *Int'l Journal of Social Robotics*, 2(1):95–107.
- Papageorgiou, X., Chalvatzaki, G., Tzafestas, C., and Maragos, P. (2014). Hidden markov modeling of human normal gait using laser range finder for a mobility assistance robot. In *Proc. of the 2014 IEEE Int'l Conf. on Robotics and Automation (ICRA)*.
- Pappas, I., Popovic, M., Keller, T., Dietz, V., and Morari, M. (2001). A reliable gait phase detection system. *IEEE Trans. on Neural Systems and Rehabilitation Engineering*, 9(2):113–125.
- Perry, J. (1992). *Gait Analysis: Normal and Pathological Function*. Slack Incorporated.
- Rabiner, L. R. (1990). Readings in speech recognition. chapter A tutorial on hidden Markov models and selected applications in speech recognition, pages 267–296. Morgan Kaufmann Publishers Inc., San Francisco, CA, USA.
- Shao, X., Zhao, H., Nakamura, K., Shibasaki, R., Zhang, R., and Liu, Z. (2006). Analyzing pedestrians' walking patterns using single-row laser range scanners. In *Systems, Man and Cybernetics, 2006. SMC '06. IEEE Int'l Conf. on*, volume 2, pages 1202–1207.
- Spenko, M., Yu, H., and Dubowsky, S. (2006). Robotic personal aids for mobility and monitoring for the elderly. *IEEE Trans. on Neural Systems and Rehabilitation Engineering*, 14(3):344–351.
- Theodorakis, S., Katsamanis, A., and Maragos, P. (2009). Product-hmms for automatic sign language recognition. In *ICASSP*, pages 1601–1604. IEEE.
- Turaga, P., Chellappa, R., Subrahmanian, V. S., and Udrea, O. (2008). Machine recognition of human activities: A survey. *Circuits and Systems for Video Technology, IEEE Trans. on*, 18(11):1473–1488.
- X.Papageorgiou, C.Tzafestas, and et al (2014). Advances in intelligent mobility assistance robot integrating multimodal sensory processing. *Lecture Notes in Computer Science, Universal Access in Human-Computer Interaction. Aging and Assistive Environments*, 8515:692–703.
- Zender, H., Jensfelt, P., and Kruijff, G. (2007). Human- and situation-aware people following. In *Robot and Human interactive Communication, 2007. RO-MAN 2007. The 16th IEEE International Symposium on*, pages 1131–1136.

USER FRONT-FOLLOWING BEHAVIOUR FOR A MOBILITY ASSISTANCE ROBOT: A KINEMATIC CONTROL APPROACH

George P. Moustris^(a), Athanasios Dometios^(b), Costas S. Tzafestas^(c)

Intelligent Robotics & Automation Laboratory
School of Electrical & Computer Engineering,
National Technical University of Athens

^(a)groustri@mail.ntua.gr, ^(b)athdom@mail.ntua.gr, ^(c)ktzaf@cs.ntua.gr

ABSTRACT

We present a robot following behavior, which enables a mobility assistance robot to follow the user from the front. Although this behavior is desirable in various circumstances, it has received scarce attention. Our proposed solution consists of a kinematic control scheme, tied to a human position estimator based on a Laser Range Finder. Experiments have been performed in an indoor environment with ten users, and the results have been analyzed and presented. We show that the control is feasible but inserts a cognitive load on the users, who tend to “drive” the robot to the optimal paths they would take under normal conditions.

Keywords: kinematic control, front following, gait, assistance robot

1. INTRODUCTION

Human-robot interaction has received increasing attention in the past decade, especially for service robots. Human-aware navigation involves scenarios where the robot must navigate in public places e.g. libraries, hospitals, warehouses, and avoid collision with humans and obstacles (Kruse et al. 2013). Another typical task is human-following, where the robot must assist the user in various tasks by following him/her through the environment. This mode can be seen for example, in telepresence robots (Cosgun, Florencio, and Christensen 2013), assistance robots in hospitals (Gockley, Forlizzi, and Simmons 2007), companion robots (Ohya and Muneakata 2002) and other. The main assumption in human tracking is that the user resides always in front of the robot. However, in general we can discern three cases for human following (Ho, Hu, and Wang 2012):

1. “behind the leader”
2. “side-by-side”
3. “in front of the leader”

The vast majority of the research volume addresses only the first case; that is, following the user from behind. This eases the control problem as the user intention can be discerned from his/hers trajectory. However, it also presents shortcomings in the interaction. Jung, Yi, and Yuta (2012) have noticed that when the robot tracks the human from behind, the human looks backs to see where the robot is. This imposes a cognitive load and

causes the human to pay attention to the robot either from curiosity e.g. see where the robot has gone, or even from fear of the robot bumping onto the human. To alleviate this problem, recently the “side-by-side” and “following from the front” tasks has been addressed by some researchers. From a control-theoretic point of view, the “following from behind” task needs only to know the position of the human relative to the robot. As a control problem, the robot has but to retrace the human’s path in order to stay behind the user. In a more general case, the problem can be classified as a *pursuit* problem, which has received ample attention in the literature. However, in the “side-by-side” and “following from the front” tasks, the difficulty increases significantly. Specifically, in the first, the user orientation must also be taken into account in order for the robot to stay by the side of the human. In the second, prediction of the user’s intention must also be incorporated, while in some cases the problem might be undecidable, requiring user feedback to escape deadlocks.

Here we present a kinematic control strategy for enabling a mobility assistance robot to follow the user from the front. This behavior has been developed in the settings of the “MOBOT” project (www.mobot-project.eu). MOBOT is an active mobility assistance robot for indoor environments that provides user-centered, context-adaptive and natural support (Papageorgiou et al. 2014).



Figure 1: The MOBOT assistance robot

The “front-following” behavior is intended to allow the robot to oversee the patient, walk along with him/her and provide assistance either on demand or autonomously.

2. PROBLEM CLASSIFICATION

The problem of following from the front can be divided into two general cases; following the human in free space i.e. in an obstacle-free space with no objects and, following the human in a structured environment e.g. in an office building, corridor etc. The two problems have different complexity with the former being substantially simpler than the latter. Specifically, in *free space following*, the problem can be cast as a control problem where the goal is to minimize some error measures e.g. minimize the distance and orientation errors between the human and the robot. This approach is singularly treated in the current literature. In the *structured environment* case, the task involves avoiding obstacles, either static or moving, as well as deciding where the human actually wants to go; a possibly undecidable problem. See for example Figure 2.

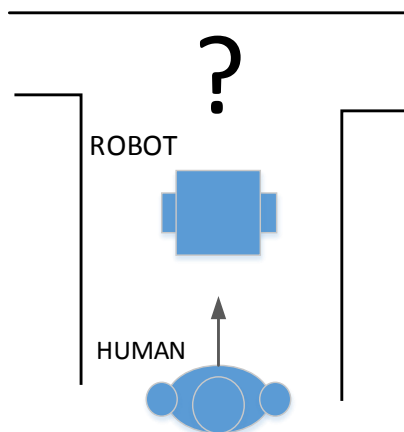


Figure 2: Undecidability of the front-following problem in structured environments

It is clear that the robot has no way of knowing where the human wants to turn by examining solely the human motion. This problem requires the addition of further information into the control loop by letting the human show the robot to turn left/right using some kind of feedback e.g. audio, posture, gestures etc. Thus, the human must also “steer” the robot and not just act as an observable for the robot. The control strategy for this problem is radically different from the *free space* following problem, and has received no attention in the literature.

3. RELATED WORK

As mentioned above, the front-following problem has received scarce attention from the research community. Our survey has produced only three papers dealing with subject. All three deal with the free-space following problem. In (Jung, Yi, and Yuta 2012) the authors use a Laser Range Finder (LRF) to scan the human torso, which serves as a more robust scanning target than the

legs. Using a particle filter employing a constant velocity model, they track the pose of the human during motion. The control algorithm uses a *virtual target* based on the human and robot poses. The aim is for the robot to track the target, which lays in the approximate direction of the human velocity vector. (Ho, Hu, and Wang 2012) use an RGBD sensor (Microsoft Kinect) to track the human position relative to the robot. Following, they use the nonholonomic human model (Arechavaleta et al. 2008; Arechavaleta et al. 2006) to calculate the human’s orientation, combined with an Unscented Kalman Filter to provide a smooth estimate of the human orientation, linear velocity and angular velocity. The controller is an ad-hoc solution aiming to align the human-robot poses while putting the robot in front. Simulation and experimental results are promising, although not very extensive.

(Cifuentes et al. 2014) use a different approach. They combine readings from a wearable IMU sensor on the human, along with LRF data of the legs in order to provide an estimate of the human pose and linear/angular velocities. They use an inverse kinematics controller to exponentially stabilize a position and orientation error between the human and the robot. In this setup, they perform experiments in straight line tracking, as well as in tracking the human along an 8-shaped path.

4. HUMAN POSITION ESTIMATION

The first step towards human following is the detection/estimation of the human pose. A basic assumption is that the human is detected by a LRF located on the robot, which scans the user legs. Furthermore, the kinematic controller only needs the position of the human, not the orientation and velocity. This simplifies the control and is more robust to estimation errors.

To filter out environment artefacts and obstacles, we borrow the idea of a Human Interaction Zone (HIZ) from (Cifuentes et al. 2014), which consists of a parallelogram of width 2m and length 2m, centered at the LRF (Figure 3).

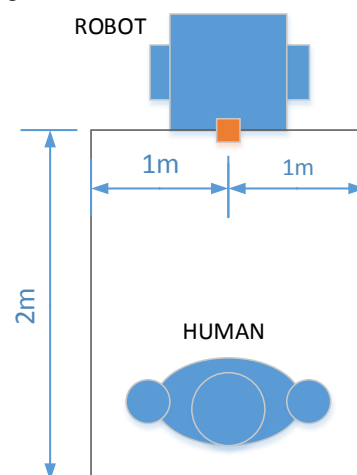


Figure 3: Definition of the Human Interaction Zone

Based on the laser scans inside the HIZ, a *centroid* is calculated by taking the average in each x, y coordinates. Thus, if k scans lay inside the HIZ, the centroid coordinates are,

$$\begin{bmatrix} x_H \\ y_H \end{bmatrix} = \begin{bmatrix} 1/k \sum_k x_L^i \\ 1/k \sum_k y_L^i \end{bmatrix} \quad (1)$$

To enable more valid detection results, in order to exclude false positives from walls, furniture etc. we have inserted an adaptive algorithm based on the previous valid centroid position. Specifically, in the beginning, the robot considers only scans inside an *initial window*, similar to the HIZ but with a width of 0.8m. This implies that the human who is intended to be followed, approaches the robot in a narrow region. Following, the algorithm estimates the centroid coordinates x_H^i, y_H^i at loop “ i ”. In the next loop “ $i+1$ ”, the algorithm scans inside a small *leg window*, of width 0.3m and height 0.2m. Thus the detection area is the rectangle $[x_H^i \pm 0.3, y_H^i \pm 0.2]$. In this way, the algorithm tracks the human as he/she moves inside the HIZ, and discards other unrelated objects.

5. KINEMATIC CONTROLLER

The proposed solution for the front-following problem, is a *virtual pushing* approach through a kinematic controller. We define an equilibrium distance x_0 where the system is at rest. If the human passes the equilibrium point and approaches the robot, then the robot starts to move depending on the human-robot distance.

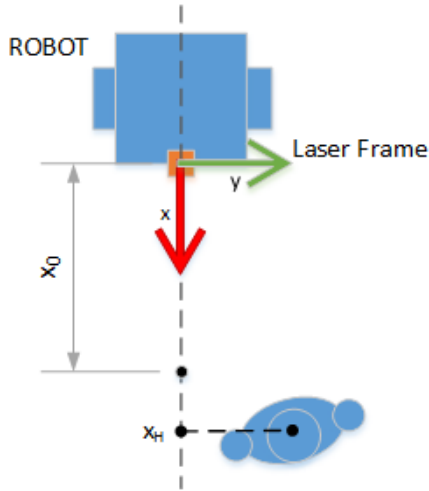


Figure 4: Depiction of the Laser Frame and the Equilibrium distance x_0

The robot model used is the Unicycle robot (Figure 5), described by the equations,

$$\begin{bmatrix} \dot{x}_R \\ \dot{y}_R \\ \dot{\theta}_R \end{bmatrix} = \begin{bmatrix} \cos \theta_R \\ \sin \theta_R \\ 0 \end{bmatrix} v_R + \begin{bmatrix} 0 \\ 0 \\ 1 \end{bmatrix} \omega_R \quad (2)$$

where x_R, y_R are the coordinates of robot with respect to a *world frame*, and θ_R its orientation. The inputs v_R, ω_R are the linear and angular velocities respectively.

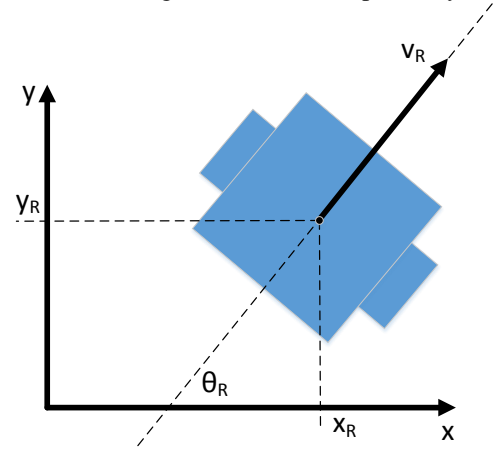


Figure 5. The unicycle robot model

Rigidly attached to the robot is the *laser frame*, in which the user centroid x_H, y_H is calculated. The robot's linear velocity is given by,

$$v_R = \lambda(y_H) v(x_H) \quad (3)$$

where,

$$v = \begin{cases} 0 & , x_H > x_0 \\ k_1(x_H - x_0) & , x_2 \leq x_H \leq x_0 \\ v_{\text{walk}} & , x_1 \leq x_H \leq x_2 \\ v_{\text{max}} - k_2 x_H & , 0 \leq x_H \leq x_1 \end{cases} \quad (4)$$

$$k_1 = \frac{v_{\text{walk}}}{x_2 - x_0}, \quad k_2 = \frac{v_{\text{max}} - v_{\text{walk}}}{x_1}$$

The term λ is a velocity modulating term (see next page for a more thorough analysis). Equation (4) defines a piece-wise linear velocity profile, consisting of three regions; the *approach region*, the *walking region* and the *collision region*.

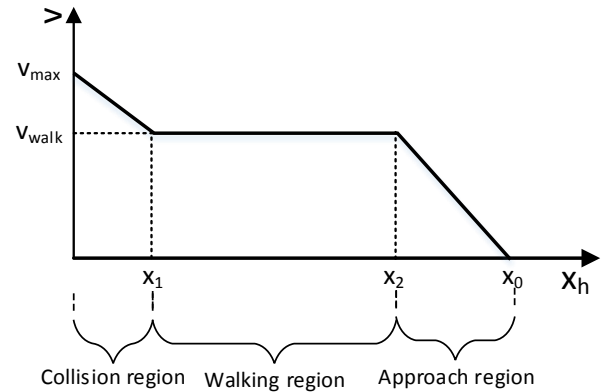


Figure 6: Profile of the linear velocity input

The *walking region* is the set on the x -axis of the LRF frame, within which the robot has a constant velocity, namely the *walking velocity* v_{walk} . In this region the robot moves synchronously with the user. If the human moves very close to the robot, he/she enters into the *collision region*, in which the robot accelerates up to a maximum velocity v_{max} . Conversely, if the human falls behind (or enters the HIZ from a distance greater than the Equilibrium distance x_0), the *approach region* is considered, where the robot accelerates from halt up to the walking velocity. The second robot input, the angular velocity ω_R , is described by the following equations,

$$\omega_R = \begin{cases} 0 & , |y_H| < \varepsilon \\ k_\omega \operatorname{sgn}(y_H)(|y_H| - \varepsilon_0) & , |y_H| > \varepsilon \end{cases} \quad (5)$$

$$k_\omega = \frac{\omega_{max}}{HIZ_w / 2 - \varepsilon}$$

Here ω_{max} is the maximum angular velocity, HIZ_w is the width of the HIZ and ε is a deadband about the x -axis. The deadband is inserted in order to filter out natural gait oscillations during walking, as well as noise from the centroid estimator. In our experiments ε was set to 10cm.

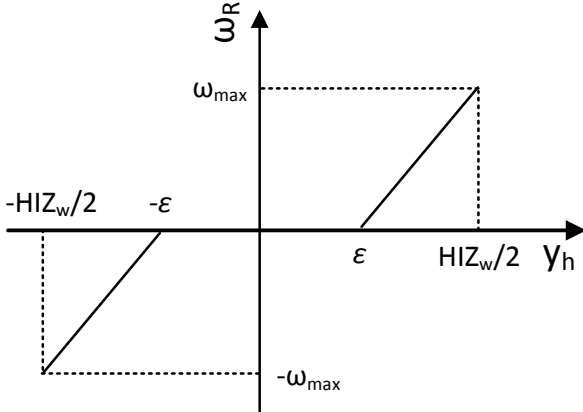


Figure 7: Profile of the angular velocity input

Using Eq.(5), the robot essentially turns in such a way as to always face the user. During experiments it was observed that in corners the users place themselves on the outer limits of the y -axis to make the robot turn fast enough. This oversteers the robot and in order to correct its heading, they must swiftly move on the other end of the axis. At the same time the robot is moving forward with a linear velocity, making the reaction time rather short and leading to unstable behaviors. To prevent this situation, we have inserted a velocity modulating term $\lambda(y_h)$ in Eq.(3). The term is given by,

$$\lambda = \begin{cases} 1 & , |y_H| < y_a \\ \frac{y_b - |y_H|}{y_b - y_a} & , y_a \leq |y_H| \leq y_b \\ 0 & , y_b < |y_H| \end{cases} \quad (6)$$

$$y_b = \varepsilon + b(HIZ_w / 2 - \varepsilon)$$

$$y_a = \varepsilon + a(HIZ_w / 2 - \varepsilon)$$

The parameters $0 < a < b < 1$ are percentages with respect to the deadband. A graphical depiction of λ can be seen in Figure 8.

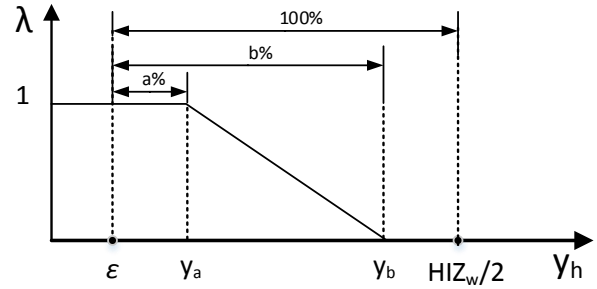


Figure 8: Illustration of the λ function

The λ term reduces the linear velocity as the user increases his/hers lateral displacement. On the outer regions, the robot halts and turns on the spot to face the human. For our experiments the parameters were set to $a=0.3$ and $b=0.6$.

6. EXPERIMENTAL RESULTS

The control scheme presented in the previous, has been implemented on a Pioneer 3DX differential drive robot, with a Hokuyo UBG-04LX-F01 laser range finder. The experiments considered here, aim to assess the gait pattern of the users with and without the robot following them from the front.

Ten healthy subjects were asked to walk naturally from an initial predefined position, around a corner and stop at a designated target position. Each subject performed two runs, thus in total 20 paths were collected as a baseline. The subjects were tracked with the laser scanner on top of the robot, which in turn was placed statically at the head of the corner, overseeing the experimental field. In post processing, using the detection algorithm, the centroid traces were extracted, as seen in Figure 9.

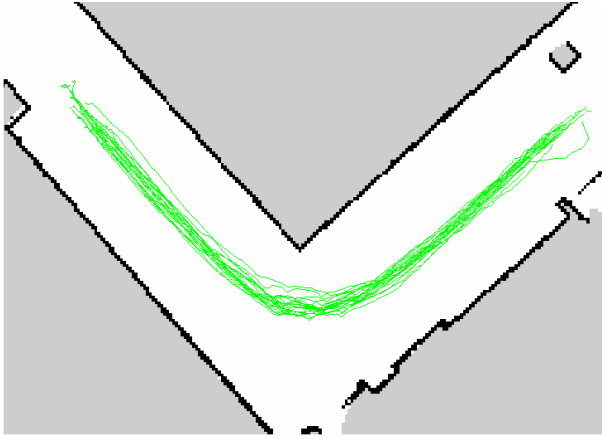


Figure 9: Traces of the baseline experiments (green). The subjects started on the right and progressed to the left.

Following, the subjects were asked to perform the experiment again, but with the robot following them from the front. Each subject did two test runs in order to get acquainted with the robot behavior. Then, they performed the experiment twice. The total collected paths are again 20.

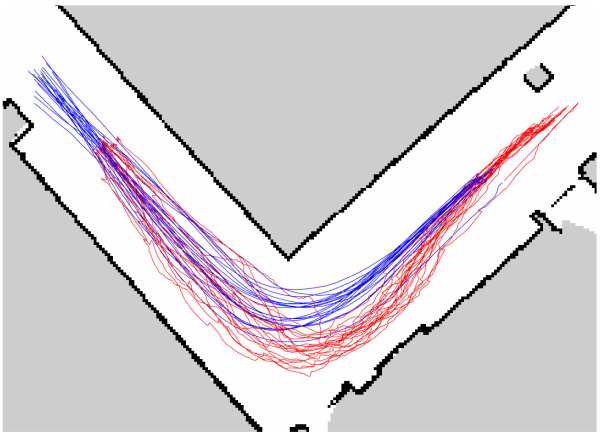


Figure 10: Traces of the following experiments (Human-red, Robot-blue). The subjects started on the right and progressed to the left

To analyze the paths, we have divided the plane into a grid of 48×26 square cells with an edge of 20 cm each. Then, for each path we collected the binary mask consisting of those cells that the path has traversed. By counting the number of masks each cell appears in, we have produced a 2D histogram of those masks. Apparently, since we have 20 paths in each case, the count of each cell goes from zero up to twenty. The three histograms are,

$$\begin{aligned}
 H_B(i, j) &: \text{Baseline paths} \\
 H_U(i, j) &: \text{User paths} \\
 H_R(i, j) &: \text{Robot paths} \\
 i \in [1, 48] \quad , \quad j \in [1, 26]
 \end{aligned} \tag{7}$$

The histograms are presented in the following figures.

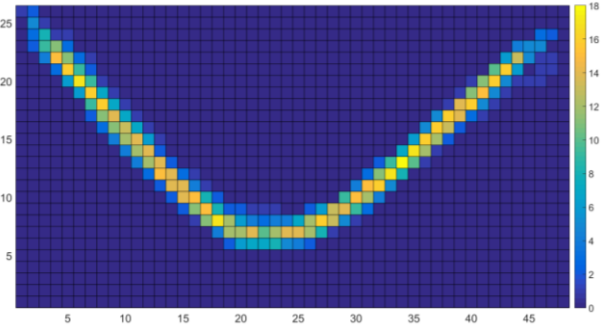


Figure 11: Histogram of the baseline paths

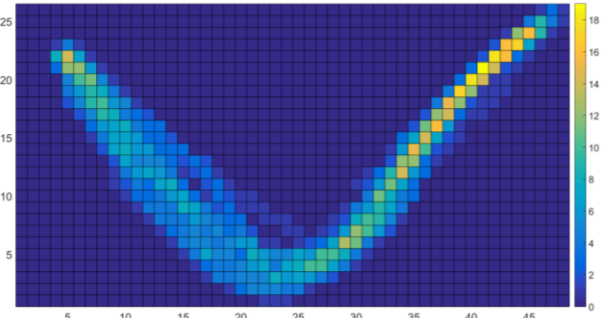


Figure 12: Histogram of the users' paths (following)

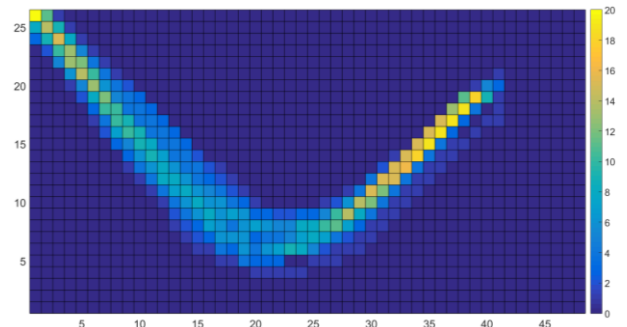


Figure 13: Histogram of the robot paths (following)

From the three histograms we can produce two new sets of distributions. By dividing the count of each cell with the total number of paths, we produce the probability of each cell being traversed by a path, viz.

$$\begin{aligned}
 T_B(i, j) &= H_B(i, j) / 20 \\
 T_U(i, j) &= H_U(i, j) / 20 \\
 T_R(i, j) &= H_R(i, j) / 20
 \end{aligned} \tag{8}$$

Thus a cell with high such a probability means that it is traversed by most of the paths. Note that these are not probability distributions as they don't sum up to one. Another set of distributions can be produced by dividing each cell with the total count of its respective histogram, i.e.

$$\begin{aligned}
 P_B(i, j) &= H_B(i, j) / \sum_{i,j} H_B(i, j) \\
 P_U(i, j) &= H_U(i, j) / \sum_{i,j} H_U(i, j) \\
 P_R(i, j) &= H_R(i, j) / \sum_{i,j} H_R(i, j)
 \end{aligned} \tag{9}$$

These express the probability of a user/robot being on a specific cell and are probability density functions. Equations (7)(8)(9) are similar up to a scaling factor (for each group “B”, “U”, “R”), thus all three have the same shape.

To compare the three groups, we resort to the *Hellinger distance* (Pollard 2002) which is a measure of statistical distance between two distributions P, Q given by.

$$H(p, q) = \frac{1}{\sqrt{2}} \sum_k (\sqrt{p_k} - \sqrt{q_k})^2 \quad (10)$$

The Hellinger distance ranges from zero to one, with zero being identical distributions and one completely disjoint. The distances of P_U to P_B and P_R to P_B are,

$$H(P_U, P_B) = 0.6265 \quad , \quad H(P_R, P_B) = 0.4907 \quad (11)$$

We see that the Robot path distribution is more similar to the Baseline distribution than the Users’ distribution. This means that the users actually tend to “drive” the robot to the path they consider “optimal” i.e. the one that *they* would take under normal conditions (the baseline paths). Doing so, they deviate from their normal gait patterns.

To further compare the three groups, we resort to Eq.(8) which describes the probability of each cell being traversed by a path. Taking the histogram of each T divided by the total number of cells *being traversed in the grid*, we get the probability of a cell being traversed by a specific fraction (or percentage if multiplied by 100%) of the paths, denoted by $TP(a)$. For example, if the total number of cells being traversed by paths in the grid is N , and there are M cells being traversed by K out of 20 paths, then $TP(K/20)=M/N$. Mathematically,

$$\begin{aligned} TP_B(a) &= \text{hist}(T_B) / \text{count}(T_B) \\ TP_U(a) &= \text{hist}(T_U) / \text{count}(T_U) \\ TP_R(a) &= \text{hist}(T_R) / \text{count}(T_R) \end{aligned} \quad (12)$$

where $\text{count}()$ returns the number of non-zero element, and a is the fraction of paths with the given probability.

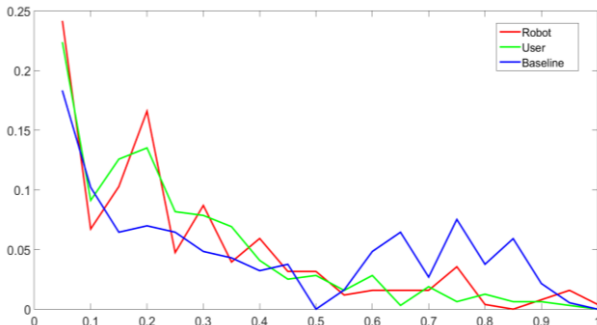


Figure 14: The distributions TP_B, TP_U and TP_R

High probabilities for small fractions, means that most of the cells being traversed have been traversed by few paths, and so, the paths are “spread out” (large

variance). On the other hand, if we have high probabilities for high fractions, most of the cells that have been traversed, are done so by many paths and so the paths are localized.

We see that both the “user” and “robot” distributions are skewed towards small fractions whereas the “baseline” group is skewed towards large ones. The table with the standard deviations is given below:

Table 1: Standard Deviation of TP_B, TP_U and TP_R

Standard Deviation		
TP_B	TP_U	TP_R
0.0412	0.0584	0.0608

As expected, we see that the “User” and “Robot” groups have higher standard deviation than the “Baseline” group. Another measure of dispersion is the relative differences between $\text{count}(TP_R) - \text{count}(TP_B)$ and $\text{count}(TP_U) - \text{count}(TP_B)$, since the *count* function measures the number of cells a distribution contains. Thus the relative difference is a measure of the *extent* of a group with respect to the baseline group.

Table 2: Measure of the *extent* of the “User” and “Robot” groups with respect to the “Baseline” group

Results		
	<i>Count()</i>	<i>% rel.diff.</i>
TP_B	186	-
TP_U	318	70.96%
TP_R	253	36.02%

From Table 2 we see that the users cover almost 71% more cells trying to steer the robot, than when walking normally, which is almost twice the cells the robot covers. This can be regarded as a measure of cognitive load since it shows that the users walk through a wider area.

7. CONCLUSION

We have described a simple kinematic control strategy for enabling a non-holonomic mobile robot to follow a user from the front. The controller is simple and robust, based on a *virtual pushing* principle. This enables the following behavior to be incorporated into a structured environment, by including the human in the loop. Experimental results have shown the feasibility of our approach, albeit the users tend to deviate from their normal walking patterns trying to “steer” the robot around. Results have shown that the actual robot paths are closer to the optimal human paths (without the robot following them), than the path produced by the humans “steering” the robot. This implies that the controller inserts a cognitive load on the user by shifting a large control effort to him/her.

Future work will focus on refining the control strategy by inserting more intelligent features on the robot e.g. obstacle avoidance, undecidability detection, human intent recognition and prediction etc. These features will

aim to alleviate the control burden of the human and shift it to the robot. Our ultimate goal is to develop a successful “front-following” behavior in structured environment, in order to enable the mobility assistance robot follow the patient from the front, and provide help when needed.

ACKNOWLEDGMENTS

This work is supported by 7th Framework Program of the European Union, ICT Challenge 2, Cognitive Systems and Robotics, contract "EU-FP7-ICT-2011-9 2.1 - 600796 - MOBOT: Intelligent Active MObility Assistance RoBOT Integrating Multimodal Sensory Processing, Proactive Autonomy and Adaptive Interaction".

REFERENCES

- Evans W.A., 1994. Approaches to intelligent information retrieval. *Information Processing and Management*, 7 (2), 147–168.
- Arechavaleta G., Laumond J.-P., Hicheur H., and Berthoz A., 2006. “The Nonholonomic Nature of Human Locomotion: A Modeling Study.” In *The First IEEE/RAS-EMBS International Conference on Biomedical Robotics and Biomechanics, 2006. BioRob 2006*, 158–63.
- Arechavaleta G., Laumond J.-P., Hicheur H., and Berthoz A., 2008. “On the Nonholonomic Nature of Human Locomotion.” *Auton. Robots* 25 (1-2): 25–35.
- Cifuentes C. A., Frizera A., Carelli R., and Bastos T., 2014. “Human–robot Interaction Based on Wearable IMU Sensor and Laser Range Finder.” *Robotics and Autonomous Systems* 62 (10): 1425–39.
- Cosgun A, Florencio D. A., and Christensen H. I., 2013. “Autonomous Person Following for Telepresence Robots.” In *2013 IEEE International Conference on Robotics and Automation (ICRA)*, 4335–42.
- Gockley R., Forlizzi J., and Simmons R.. 2007. “Natural Person-Following Behavior for Social Robots.” In *Proceedings of the ACM/IEEE International Conference on Human-Robot Interaction*, 17–24. HRI '07. New York, NY, USA.
- Ho D-M., Hu J-S., and Wang J-J. 2012. “Behavior Control of the Mobile Robot for Accompanying in Front of a Human.” In *2012 IEEE/ASME International Conference on Advanced Intelligent Mechatronics (AIM)*, 377–82.
- Jung E-J., Yi B-J., and Yuta S., 2012. “Control Algorithms for a Mobile Robot Tracking a Human in Front.” In *2012 IEEE/RSJ International Conference on Intelligent Robots and Systems (IROS)*, 2411–16.
- Kruse T., Kumar A. P, Alami R., and Kirsch A., 2013. “Human-Aware Robot Navigation: A Survey.” *Robotics and Autonomous Systems* 61 (12): 1726–43.

Ohya A., and Munekata T., 2002. “Intelligent Escort Robot Moving Together with Human-Interaction in Accompanying Behavior.” In *Proceedings of the 2002 FIRA Robot Congress*, 31–35.

Papageorgiou X.S., Tzafestas C.S., Maragos P., Pavlakos G., Chalvatzaki G., Moustiris G.P., Kokkinos I., et al. 2014. “Advances in Intelligent Mobility Assistance Robot Integrating Multimodal Sensory Processing.” In *Universal Access in Human-Computer Interaction. Aging and Assistive Environments*, edited by C. Stephanidis and M. Antona, 692–703. Lecture Notes in Computer Science 8515. Springer International Publishing.

Pollard, D.E., 2002. "A user's guide to measure theoretic probability". Cambridge, UK: Cambridge University Press

AUTHORS BIOGRAPHY

George P. Moustiris received his M.Eng. in electrical & computer engineering (2003) from the ECE school at the Aristotle University of Thessaloniki (AUTH) and his Ph.D. in robotics and control at ECE/NTUA (2010). From 2011-2013 he carried out his Post-Doctoral research at the Intelligent Robotics & Automation Lab (IRAL) of ECE/NTUA in medical/surgical robotics. He is currently a Research Associate at the Institute of Computers & Communications Systems and member of IRA. His current research interests are focused on medical, surgical and assistive robots, aiming towards automating various functions of their operation. He has authored more than 15 publications and has been involved in many national and international research projects. He is a member of IEEE/RAS and the Technical Chamber of Greece.

Athanasios Dometios graduated from the School of Electrical and Computer Engineering (ECE) of the National Technical University of Athens (2013). He completed his Bachelor thesis in the Institute of Automatic Control Engineering (LSR) of the Technical University of Munich (TUM). From 2014 he has joined the Intelligent Robotics and Automation Laboratory of at ECE/NTUA as a Ph.D. Student. His research interests include 3D mapping, path-planning, sensor fusion, SLAM, control of mobile robots and robotic manipulators.

Costas S. Tzafestas holds an Electrical and Computer Engineering Degree (1993) from the National Technical University of Athens (NTUA, Greece), as well as a D.E.A. (1994) and Ph.D. (1998) degrees on robotics from the Université Pierre et Marie Curie (Paris 6, France). He is currently an Assistant Professor on Robotics at the School of Electrical and Computer Engineering of NTUA. He has previously served as a Research Fellow at the Institute of Informatics and Telecommunications of the Hellenic National Center for Scientific Research “Demokritos”. His main research interests include human/robot interaction, telerobotics, and haptics, also spanning robust, adaptive and

intelligent control methods with applications in dextrous robotic manipulation, as well as in walking and mobile robots. He has authored and co-authored more than 90 scientific publications and has been a principal investigator and/or technical manager in several national and international research programs. He currently serves as an Associate Editor of the Journal of Intelligent and Robotic Systems. Dr. Tzafestas is a member of the IEEE and of the Greek Technical Chamber.

Author's Index

Aguiar	55	
Austin	1	
Azevedo	115	
Baliño	115	
Borutzky	29	
Breedveld	39	
Bru	63	
Burr	115	
Cabello	63	
Canonico	55	
Carignano	48	
Chalvatzaki	132	
Chui	79	
Cohodar	89	
Dalla	105	
Damic	89	
Dauphin-Tanguy	125	
Dazin	125	
de Toledo Fleury	71	
Dometios	142	
Dupont	125	
Fleury	79	
Gonzalez-A	39	
Guimond	1	
Ilinca	1	
Junco	48	63
Kebdani	125	
Lacressonniere	63	
Leonardi	55	
Louca	12	
Makhbouche	97	
Martins F.	79	
Martins M.	22	
Moustris	142	
Nigro	48	
Núñez-Hernández	39	
Odloak	22	
Papageorgiou	132	
Pathak	105	
Ramdenee	1	
Roboam	63	
Santoro	22	

Trigo	79	
Trindade	71	
Turki	125	
Tzafestas	132	142
Weustink	39	
Yamashita	22	
Zennir	97	